Decomposition Mechanism of Lignin Models on Pt(111) : Combining Single Crystal Experiments and First-Principles Calculations

By

Cherif Aghiles Ould Hamou

Thesis submitted to the University of Ottawa
in partial fulfillment of the requirements for the
Doctorate in Philosophy degree in Physics

Department of Physics
Faculty of Science
University of Ottawa

Abstract

The world energy and product consumption keep increasing steadily over the years as the world population keeps growing and more countries become industrialized. As the world reserves deplete it becomes a necessity to find an alternative way to meet the population's demand. Biomass conversion seems to be the future of a clean and sustainable world. Lignin is the second most abundant polymer in the biomass. Given the unique structure and chemical properties of lignin, a wide variety of bulk and fine chemicals can be obtained and be used for goods and biofuels production. Catalysis, with its selective bond cleavage and lower energy activation, is considered as a potential key solution in the process of lignin conversion into valuable chemicals. To gain insights into that catalytic system, we performed surface science experiments (X-ray Photoelectron Spectroscopy, Temperature Programmed Desorption and Reflection Absorption Infrared Spectroscopy) under Ultra-High Vacuum conditions (UHV). Due to lignin's physical properties limitation under UHV conditions, lignin models with the same chemical structure such as phenol, anisole, 2-phenoxyethanol and veratrol were used to gain a better understanding of the reactivity of lignin itself.

Dosing anisole and 2-phenoxyethanol on Pt(111) surprisingly gave benzene, carbon monoxide and hydrogen as the main desorbing products of decomposition. With the help of Density Functional Theory (DFT), we successfully explain the unexpected selectivity. In the present work, we show in particular that phenoxy PhO stands as a key intermediate. Although the UHV conditions do not allow the hydrogenation of phenoxy into phenol, *i.e.* the catalytic product, they reveal the key role of both hydrogen and carbonaceous species. Under UHV conditions, anisole and 2-phenoxyethanol are extensively dehydrogenated: it results in the formation of carbonaceous fragments, which can actually perform the deoxygenation of phenoxy into benzene.

The reactivity of veratrol on Pt(111) hindered the formation of benzene and only gave carbon monoxide and hydrogen as the main desorbing products of decomposition. Although carbonaceous fragments were formed on the surface, the deoxygenation of the two oxygenated arm moieties does not occur without the total decomposition of the aromatic ring, hence the formation of coke.

This detailed work opens the door to a rational design of metal-based catalysts and a route towards lignin valorization.

Résumé

La consommation mondiale d'énergie et de produits ne cesse d'augmenter au fil des ans, à force que la population mondiale continue de croître et que de plus en plus de pays s'industrialisent. Au fur et à mesure que les réserves mondiales s'épuisent, il devient nécessaire de trouver un autre moyen de satisfaire la demande de la population. La conversion de la biomasse semble être l'avenir d'un monde propre et durable. La lignine est le deuxième polymère le plus abondant dans la biomasse. Compte tenu de sa structure et de ses propriétés chimiques uniques, une grande variété de produits chimiques fins peut être obtenue et utilisée pour la production de biens et de biocarburants. La catalyse, avec sa sélectivité dans la rupture de liaison et sa faculté de baisser énergie d'activation, est considérée comme une solution clé potentielle dans le processus de conversion de la lignine en produits chimiques de valeur. Pour mieux comprendre ce système catalytique, nous avons réalisé des expériences scientifiques (spectroscopie de photoélectron par rayons X, désorption programmée par température et spectroscopie infrarouge à absorption par réflexion) dans des conditions ultravide (UHV). En raison de la limitation des propriétés physiques de la lignine dans des conditions UHV, des modèles de lignine ayant la même structure chimique tel que le phénol, l'anisole, le 2-phénoxyéthanol et le veratrol ont été utilisés pour mieux comprendre la réactivité de la lignine elle-même.

Le dosage de l'anisole et du 2-phénoxyéthanol sur la surface de Pt (111) a, de manière surprenante, donné du benzène, du monoxyde de carbone et de l'hydrogène comme principaux produits de la décomposition. Avec l'aide de la théorie de la fonctionnelle de la densité (DFT), nous expliquons avec succès la sélectivité inattendue. Dans le présent travail, nous montrons en particulier que le phénoxy PhO est un intermédiaire clé. Bien que les conditions UHV ne permettent pas l'hydrogénation du phénoxy en phénol, c'est-à-dire le produit catalytique, elles révèlent le rôle clé de l'hydrogène et des fragments carbonées. Dans des conditions UHV, l'anisole et le 2-phénoxyéthanol subissent une déshydrogénation poussée : il en résulte la formation de fragments carbonés, qui à leur tour permettent la désoxygénation du phénoxy en benzène.

La réactivité du veratrol sur la surface de Pt (111) entrave la formation de benzène et ne donne que du monoxyde de carbone et de l'hydrogène comme principaux produits de désorption à la suite de la décomposition. Bien que des fragments carbonés se soient formés à la surface, le

processus de désoxygénation pour la formation du benzène ne se ne se produit pas sans la décomposition totale du cycle aromatique, d'où la formation de coke.

Ce travail détaillé, ouvre la voie à une conception rationnelle des catalyseurs à base de métal et à une valorisation de la lignine.

In the Memory of My beloved Father, Ould Hamou Mohamed Cherif

"Sometimes in life you have to run on faith, you have to run…not seeing the outcome, but just knowing that there will be the results that you desire. As you feel, as you believe…You will receive! Because after all, that what you seek, that what you desire, that what you long for…is equally seeking you" - D Ivan Young

Acknowledgments

It all started in a small village called Taourit Amrane in mountains of Kabylie, in the North of Algeria. My great-grandfather Belkacem was a farmer and had 3 sons, among them was my grandfather Cherif who was born in 1881. At that time Algeria was a French colony and made school mandatory to young children. My great-grandfather did not have enough money to pay the officer, in order to keep my grandfather Cherif working on the field. Also, given his feeble build it was better to let him go to school than having him on the field. It turned out that he was a quick learner, but pursuing further studies required money. My great-grandmother had to sell her wedding gift and only object of value she had, a handmade bed cover tapestry, to be able to cover the cost of the boarding school. This is how my grandfather Cherif became the first teacher in the village and was the first member in my family to not be illiterate. My grandfather sacrificed everything he had to make sure that my father could gain access to school and seek knowledge. My father Mohamed Cherif was the first one in the family to obtain a master's degree. In his turn, he also sacrificed his career and most of his belongings to be able to immigrate to Canada, hoping for a better future for my siblings and me.

I would not have made it here today without the sacrifice of the generations before me and the help, and constant support of Javier, my family, my fiancée and my friends.

Javier, I still remember the first day that I sat down in your office and I still do not know what you saw in me…You never said what it was, but your eyes clearly spoke for you. During all my PhD, you supported me, guided me and was patient with me (God knows it takes a lot of patience with me!). But most importantly, you believed in me more than I believed in myself. I cannot call you "my supervisor", because what we share is more than that, it is the same relationship between a father and a son. I am more than proud to say that this life has gifted me with a second father. I will never be thankful enough. Even though I am walking out of the lab, I am clearly not walking out of your life.

To my Mother, Malika Hired, you sacrificed as much as dad and even more to make sure I was fed and healthy. You took the time to prepare my lunchbox (yes I was that lucky!) to make sure the only thing I could focus on was my studies. I hope this degree will make you proud, because I know deep inside of me, there is no better recognition than bringing you this degree.

To my siblings Zahoua and Abderrahmane, we fight, we laugh and we do it all over again. We are always close to each other, I could not ask for better siblings and all I care now is to keep growing old with you two.

To my fiancée Manele, one more reason to get it all done is to finally get married. You gave me all the time and space to be able to finish my thesis, you were supportive all along and I could never ask for a better person to build my life with.

To my friends, I do not have so many but you recognize yourselves. I rethink about our childhood and the time we spent together, and the amazing solidarity that we have along these years. Thank you for being there for me and guiding me during my toughest moments and decisions.

I would like to thank Carine Michel and Philippe Sautet for opening my eyes on the modelling field. You helped me gain a greater understanding of surface chemistry and will always be grateful for that. I would also like to thank Romain Réocreux who made my journey in Lyon memorable.

Thanks to Tom Baker, who was my guru in choosing the most promising molecules for the lignin models.

I thank all my past and present lab mates who made these last 5 years one of the best experiences in my life. I especially thank Jeffrey Sims, Mohammed Asiri and Virginna Kusuma. You guys worked with me on the UHV chamber and we all shared the same struggles! Making the bond between us somewhat special. Thank you for your help and collaboration along this journey.

I would also like to thank all the members of the Physics department. Especially Béla Joós, Peter Piercy and Yazid Braik. We had several fruitful discussions whether it is science, career path or life in general. You contributed to my development starting from my 1st year as an undergraduate and I will never forget all the help that you provided me.

I also thank the Machine Shop people. Especially, Hervé Beaudoin, Olivier Demers and Rock Thibault. You guys are always willing to help, and without your exceptional work the RAIRS chamber would never see light (Infrared). Your work made a huge difference in my advancement and for this I will always be grateful. At the same time, I would like to thank Ian, who was very kind to always come to our rescue when we had electrical problems with the water chiller and the UHV system.

To all my family around the globe, that are excited for me to finally finish my thesis: thank you because as time flies by, I realize the only richness that I have is to be blessed with the beautiful people that surround me.

Above all, thanks to God for making this journey on earth a blessing.

Table of Contents

Statement of Contributions of Collaborators

During my PhD studies I have coauthored several peer reviewed publications:

1) Ould Hamou, C. A.; Asiri M.; Kusuma V. A.; Giorgi, J.B. Adsorption and Decomposition of a lignin β-O-4 Linkage Model: Reactivity of Veratrol on Pt(111) by Combination of XPS, TPD and RAIRS Experiments. *In Progress*
2) Ould Hamou, C. A.; Giorgi, J.B. Direct observation of phenoxy as the key and common intermediate for the decomposition of lignin fragments containing the beta-O-4 linkage. S*ubmitted to J. Phys. Chem. C*
3) Sims, J. J.; Ould Hamou, C. A.; Réocreux, R.; Michel, C.; Giorgi, J. B. Adsorption and Decomposition of Formic Acid on Cobalt (0001). *J. Phys. Chem. C* ***2018****.122 (35), 20279-20288.*
4) Ould Hamou, C. A.; Réocreux, R.; Sautet, P.; Michel, C.; Giorgi, J. B. Adsorption and Decomposition of a Lignin B-O-4 Linkage Model, 2-Phenoxyethanol, on Pt(111): Combination of Experiments and First-Principles Calculations. *J. Phys. Chem. C* **2017**, *121*, 9889–9900.
5) Réocreux, R.; Ould Hamou, C. A.; Michel, C.; Giorgi, J. B.; Sautet, P. Decomposition Mechanism of Anisole on Pt(111): Combining Single-Crystal Experiments and First-Principles Calculations. *ACS Catal.* **2016**, *6*, 8166–8178.

I hereby declare that I am the sole author of this thesis.

1) I performed all the XPS and TPD experiments and XPS prediction by density functional theory calculations for the reactivity of Anisole and 2-Phenoxyethanol on Pt(111). It can be found in Chapter 3 and 4.
2) I performed all the RAIRS experiments and analysis for the reactivity of Phenol, Anisole and 2-Phenoxyethanol on Pt(111). It can be found in Chapter 5.
3) I initiated and supervised the project related with the reactivity of Veratrol on Pt(111). Kusuma Virginna Adiningtyas helped me perform the XPS and TPD experiments as part of fulfillment of her coop term. I trained Mohammed Asiri in performing the RAIRS experiments and analysis. I interpreted all the results and wrote the draft article. It can be found in Chapter 6. This draft paper opens subsequent research studies that Mohammed Asiri will be taking on as part of his master's degree requirements.
4) I started the project of formic acid on Co(0001) where I performed XPS and TPD experiments, and initial DFT calculations (Slab optimisation, adsorption geometry and XPS calculations). Jeffery Sims took over as it was part of his master's thesis. Jeffrey conducted further investigation of the reactivity of formic acid on Co(0001), performed all the analysis and interpretation. Javier Giorgi pushed further the Density functional theory calculations where he calculated the transition states and the adsorption geometries of the byproducts, and finalized the project. It can be found in Appendix J.
5) I designed and built the sample stage for the reflection adsorption infrared spectroscopy technique. I also prepared the UHV chamber to be compatible with the RAIRS system. The technique is currently used by Mohamed Asiri as part of his master's project but will also be used by future students.
6) I spent two months in France to learn how to perform core level binding energy calculations and how to correlate them to XPS results. I developed a methodology that still now days used by students. I learned how to perform Infrared calculations, energy minimization calculations for the bulk structure and the molecules adsorption geometry. I also learned how to generate thermodynamic profiles and Infrared/XPS spectra.

List of Figures

Chapter 1

Chapter 2

Chapter 3

Appendix G

Appendix I

Appendix J

List of Tables

List of Symbols and Abbreviations

Symbol/Abbreviation	Definition
$\vec{a}$	Acceleration
$\vec{B}$	Magnetic field
E_b	Binding energy
$\mathrm{E_{des}}$	Energy of desorption
$\mathrm{E_{gap}}$	Bandgap energy
E_p'	Reflected Electric field with a perpendicular polarization
E_p	Electric field with a perpendicular polarization
E_{pass}	Pass energy
E_s'	Reflected Electric field with a parallel polarization
E_s	Electric field with a parallel polarization
$\mathrm{E_{xc}}$	Energy exchange-correlation
$\vec{E}$	Electric field
$\vec{F}$	Force
k_b	Boltzmann constant
m_{ar}	Molecular weight of argon
n_0	Number of molecules per unit volume
n_d	Vibrational frequency factor
n_x	atomic concentration
R_0	Mean radius
S_{gas}^0	Entropy of the gas at standard pressure
T_0	Initial temperature
T_{max}	Maximum temperature
$\mathrm{U_{quad}}$	Quadrupole voltage
$\mathrm{V_{xc}}$	Potential exchange-correlation
λ_{max}	Cut-off frequency
φ_{i}	Orbital wave function
ΔE_{an}	Analyzer resolution

ΔE_{level}	Atomic level linewidth
ΔE_{photon}	Photon linewidth
ΔE_{res}	Spectral resolution
O	Area from which photoelectrons are detected
A	Pre-exponential factor
a,q	Stability parameters
AFM	Atomic force microscopy
Al	Aluminium
B-A	Bayard Alpert ion gauge
C_i	Concentration of atomic species
CPS	Counts per second
dT	Derivative of temperature
E_k	Kinetic energy
FAT	Fixed analyzer transmission
FT-IR	Fourier-transform Infrared
FWHM	Full width at half-maximum
HREELS	High-resolution electron energy-loss spectroscopy
hv	Photon energy
I	Area of the photoelectron peak
IR	Infrared
Ir	Iridium
J	Photon flux
K	Coulomb constant
k	Desorption rate constant
KBr	Potassium bromide
LEED	Low-energy electron diffraction
m	Molecular weight
MCT	Mercury Cadmium Telluride
Mg	Magnesium
n	Number of scans
P	Pressure

Q	Charge
QMS	Quadrupole mass spectrometer
R	Gas constant (J/mol K)
r	Temperature rate of change
RAIRS	Reflection adsorption infrared spectroscopy
RGA	Residual gas analyzer
RSF	Relative sensitivity factor
S	Mean slits width
SEM	Secondary electron multiplier
STM	Scanning tunnelling microscopy
T	Temperature (K)
t	Time (s)
TPD	Temperature programmed desorption
TSP	Titanium sublimation pump
U	Voltage of direct current
UHV	Ultrahigh vacuum
UPS	Ultraviolet photoelectron spectroscopy
V	Amplitude of alternative current
v	Mean speed
XPS	X-ray photoelectron spectroscopy
y	Relative excitation probability
Z	Beam intensity
α	Half angle of the dispersion direction
β	Heating rate (K/s)
δ	Optical path difference
ΔV	Potential difference
ε	Ground state energy
ϑ	Photonelectron emission angle
θ	Surface coverage
λ	Mean free path
ρ	Electron density

σ	Cross section
ϕ	Flux incident on surface
φ	Instrument work function
χ	Instrument constant
ω	Frequency (s^{-1})

Chapter 1:
Introduction

1 Research context and project approach

1.1 Energy consumption

The world energy consumption keeps increasing steadily over the years as the world population keeps growing and more countries become industrialized. Fossil fuels including oil, coal and natural gas are the major resource and constitute up to 85% of the provided world energy (Figure 1.1).[1,2] In 2016 the world oil reserve has been estimated to be 240.7 thousand million tons, given the world consumption to be 4418.1 million ton / year it has been estimated that oil reserves will not last more than 55 years. For the natural gas reserves, the remaining time is estimated to be 52 years. Canadian energy consumption is slightly different from the world average, as it strongly relies on hydro-electricity to reduce its fossil fuel consumption.[1] Nevertheless, Fossil fuels still constitute the major source for the energy consumption for Canadians at 67%. In Canada the oil and gas reserves are estimated to last for 273 and 22 years respectively. Moreover, the pollution and toxic gas emissions from fossil fuels add to the greenhouse effect and increases global warming. The contribution of Carbon dioxide emission from fossil fuels has been estimated to be 65%.[3] As the world reserves deplete it becomes a necessity to find an alternative way to meet the energy demand. Biomass conversion seems to be the future of a clean and sustainable world.[4]

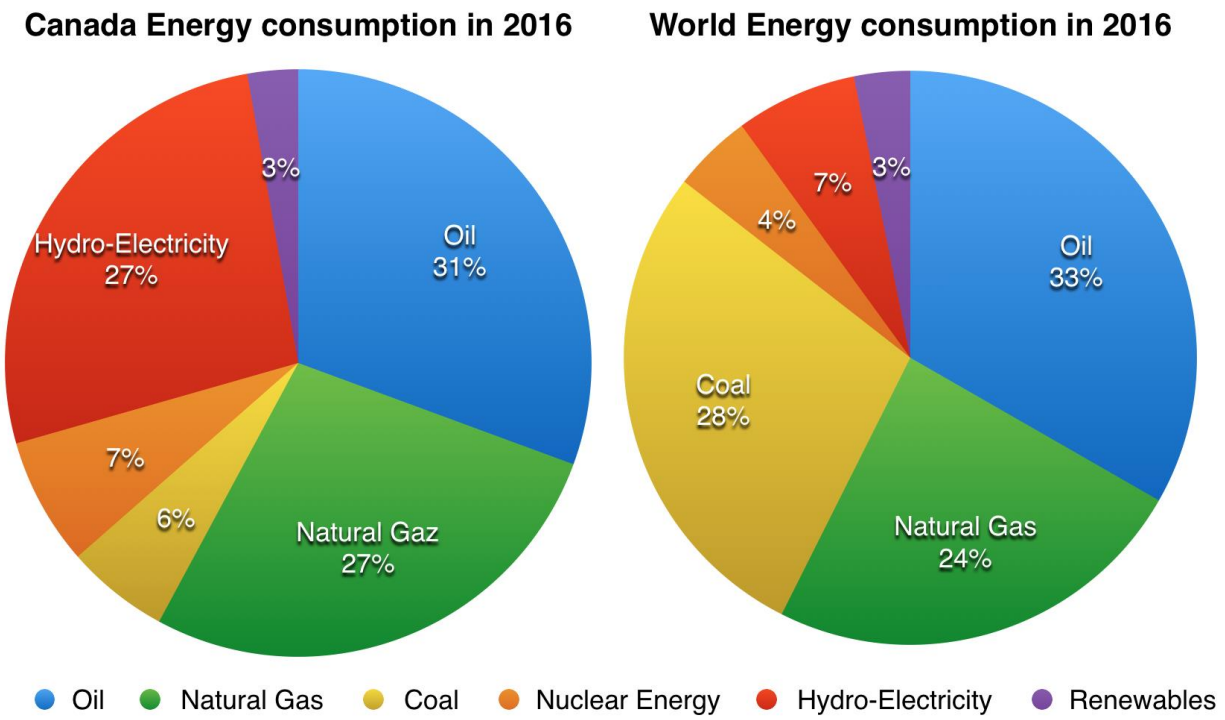

Figure 1.1: Canadian and world energy consumption in 2016. Plotted from data published by BP.[1]

Biomass is a term for all organic material that stems from plants including seaweeds, trees, crops and animal wastes. Low moisture content biomass is called "dry" biomass or lignocellulosic biomass and it is constituted of agricultural residues, herbaceous crops, trees, etc. Many advantages can be attributed to biomass exploitation: It is a renewable source of energy, carbon neutral and very abundant. At a global scale, lignocellulosic biomass has the potential to provide up to 450 EJ/yr which represents 61% in comparison to the projected global primary energy consumption of 732 EJ by 2030.[5–7] Biomass seems to be an ideal candidate to succeed fossil fuels.

In Canada only 3% of the energy consumption comes from renewable resources.[1] The potential and use of biomass as an energy source depends on several aspects such as energy crop yields, land availability and competing uses for feedstocks. In Canada the forest area is estimated to be 347 million hectares which represents approximately 35% of Canada's surface area and it has been quite stable over the past years (Figure 1.2).[8] Wood from trees is considered as a Lignocellulosic biomass that does not compete with the food industry which motivates its development as an alternative biofuel that is not produced from food crops.[7] Increasing Canada's biofuels mandate could add 31,000 jobs and $5.6 billion to the economy.[9] Although, the production

of biofuels has increased by 10 times in the last decade (Figure 1.3), it is still not enough to replace fossil fuels.

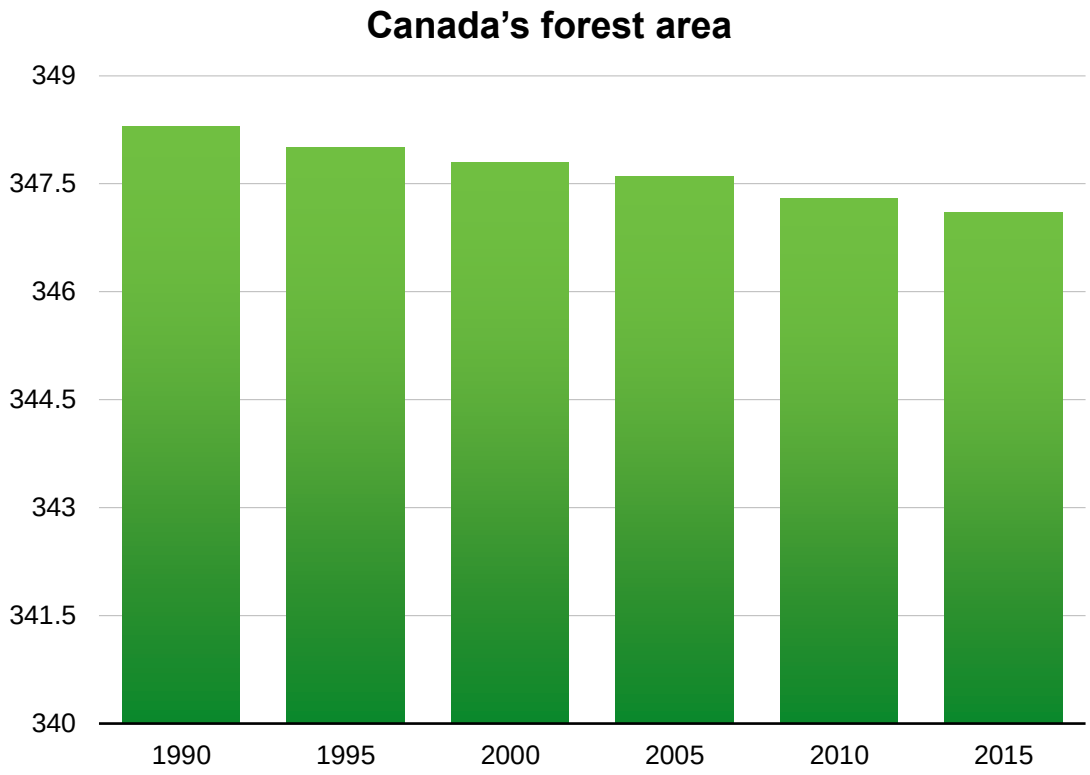

Figure 1.2: Canada's forest area in million hectares has been stable over the last 25 years. A decrease of 0.34% has been reported. Plotted from published data by Natural Resources Canada.[8]

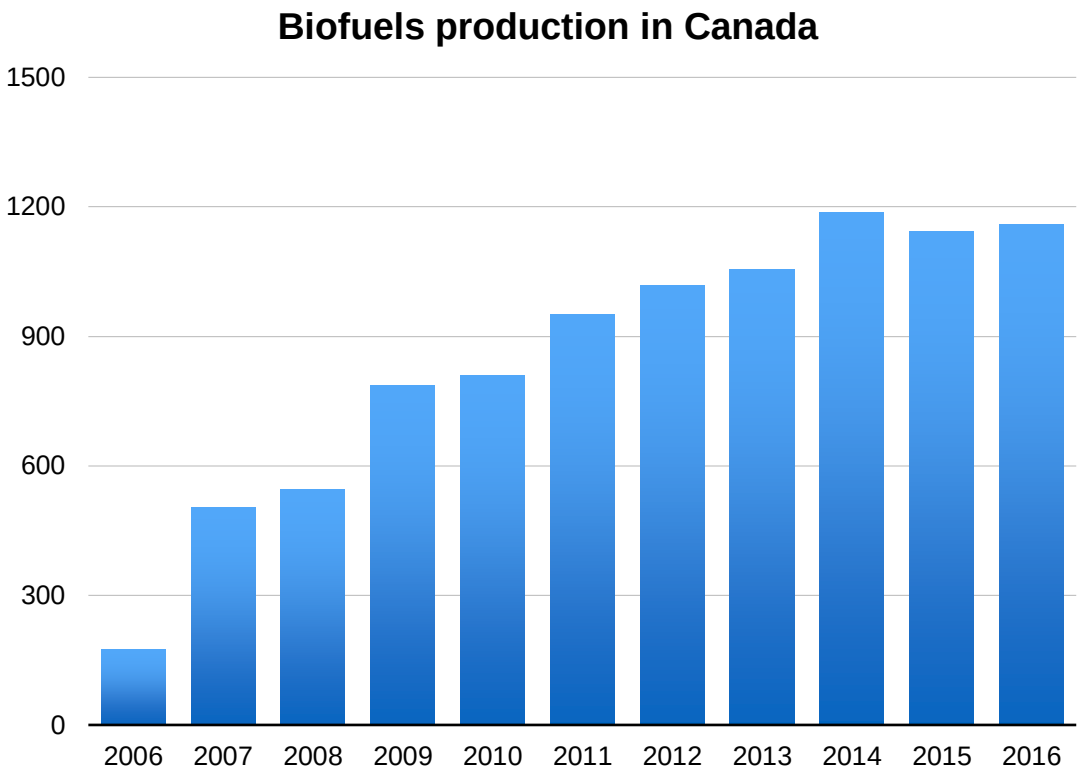

Figure 1.3: Biofuels production in thousand tonnes oil equivalent in Canada over the last decade. Plotted from data published by BP. [1]

1.2 Lignocellulosic Biomass

Lignocellulosic biomass consists of three major polymers: cellulose, hemicellulose, lignin and a small amount of extraneous material.[10] Typical compositions of several lignocellulosic biomass feedstocks are shown in Table 1.1.

Table 1.1: The abundance of cellulose, hemicelluloses and lignin in different biomass feedstock.[11–16]

Feedstock	Cellulose (%)	Hemicellulose (%)	Lignin (%)
Hardwood	40-55	18-36	15-22
Softwood	42-55	11-27	20-28
Agricultural waste	25-47	12-36	7-25
Grasses	25-40	25-50	10-30
Newspaper	24-40	44-55	18-30

Cellulose is the most abundant polymer in the biomass and it is the structural component of plant cell walls, which gives mechanical strength and shape to plants. Cellulose composition consists of linear chains of (1,4)-D-glucopyranose units, in which the units are linked 1–4 in the β-configuration (Figure 1.4).[10,17,18] In simpler terms, it consists of long linear chains of polysaccharide, exclusively glucose units, that are held together by hydrogen bonds. Cellulose is mainly used to produce paper products. Smaller quantities are converted into a wide variety of derivative products such as cotton, linen and rayon for clothes, as blood purification membranes for biomedical applications and as a fat substitute, texturizer, emulsifier in the food industries.[19]

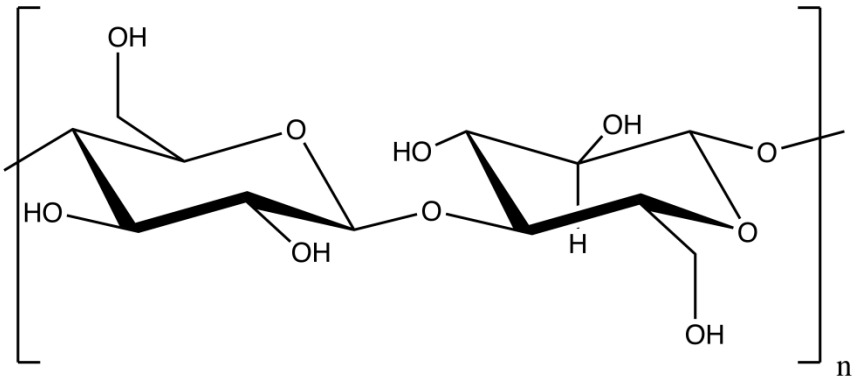

Figure 1.4: Chemical structure of (1,4)-D-glucopyranose unit that forms cellulose.

Hemicellulose comes second/third as the most abundant polymer in the biomass. Hemicellulose consists of mixed chains of polysaccharide such as pentoses (xylose and arabinose), hexoses (mannose, glucose, and galactose), and sugar acids (Figure 1.5).[10,16,18,20] The primary role of hemicellulose is to help to strength the cell wall by interaction with cellulose and lignin. In contrast to cellulose, hemicellulose has shorter chains and does not form chemical bonds between the different polysaccharides.

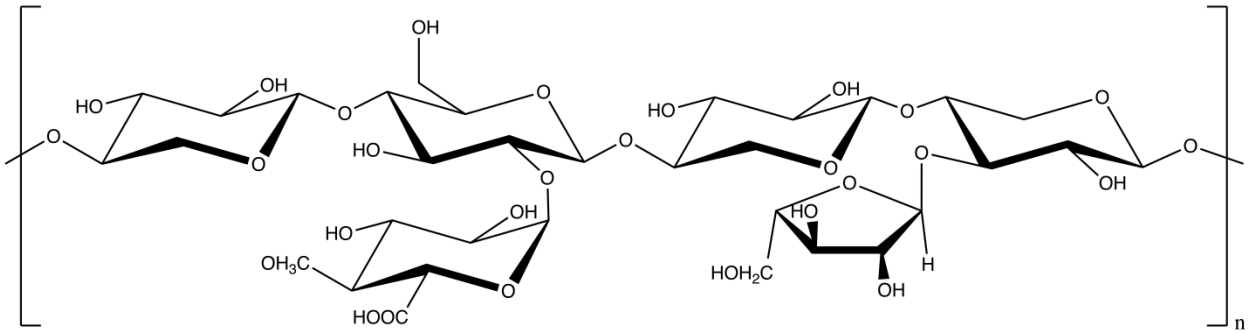

Figure 1.5: Chemical structure of a glucoronoxylan unit that is part of the chain that forms hemicellulose.

Lignin is also part of the nature's most abundant polymers in biomass and it consists of three types of substituted phenols : coniferyl, sinapyl, and p-coumaryl alcohols (Figure 1.6).[18,21,22] The polymer linkages consist of ether bonds (β-O-4, α-O-4, 4-O-5, α-O-γ) and carbon-carbon bonds (5-5, β-5, β-1, β-β) (Figure 1.7).[13,23] The β-O-4 ether linkage is the most dominant one and constitutes up to 60% of the lignin (Table 1.2). Lignin functions as the cellular glue which provides compressive strength to the plant tissue, stiffness to the cell wall and retains water and nutrients in the fibers.

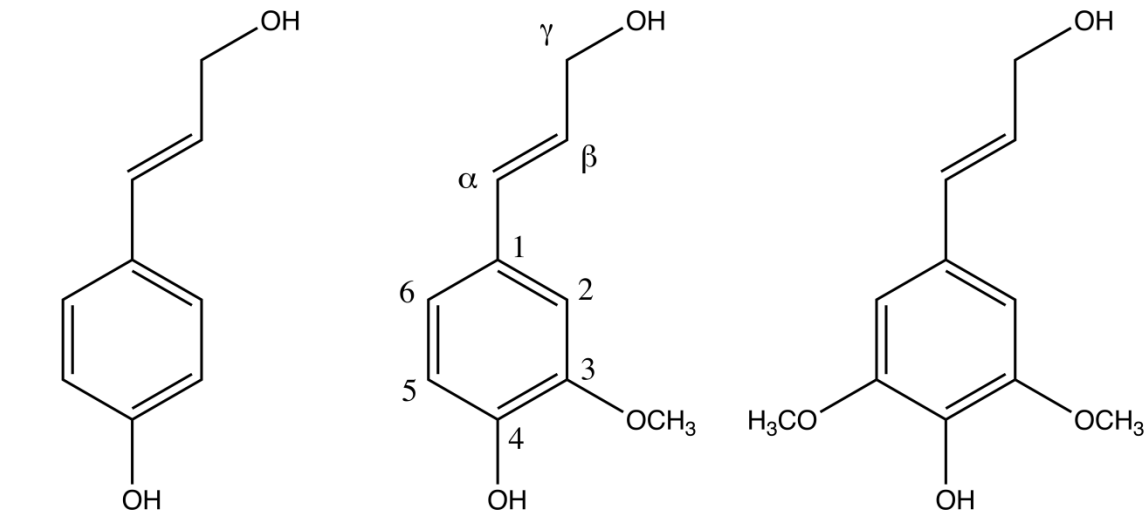

p-coumaryl alcohol Coniferyl alcohol Sinapyl alcohol

Figure 1. 6: Chemical structure of the three main monolignols that forms lignin.

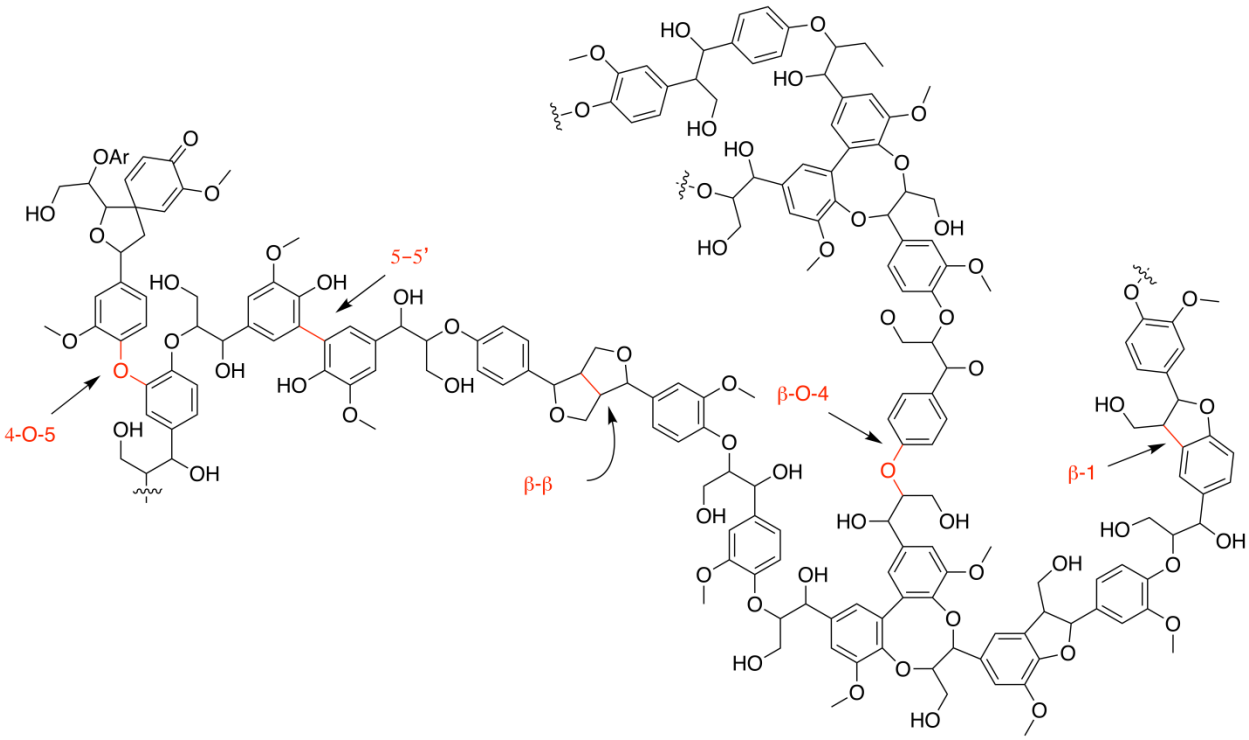

Figure 1.7: Chemical structure of lignin with the most dominant linkages.[24]

Table 1.2: The abundance of different lignin linkages in softwood and hardwood. From Pandey et al.[11] Copyrights © 2010 John Wiley & Sons, Inc. Reprinted by permission of John Wiley & Sons, Inc.

Linkage type	Softwood (Spruce) (%)	Hardwood (Birch) (%)
β-O-4 Aryl ether	46	60
α-O-4 Aryl ether	6 – 8	6 – 8
4-O-5 Diaryl ether	3.5 – 4	6.5
β-5 - phenylcoumaran	9 – 12	6
5-5 - Biphenyl	9.5 – 11	4.5
β-1 (1,2-Diarylpropane)	7	7
β-β (Resinol)	2	3
Others	13	5

1.3 Extraction process of cellulose, hemicellulose and Lignin

Extraction and isolation methods of cellulose, hemicellulose and lignin strongly depend on the plant tissue that is used.[25] Given the variable composition of these polymers in the different type of biomass, the isolation procedure will differ in certain steps. Numerous studies have been reported in literature about extraction of lignocellulosic polymers, the methods mainly depend on the targeted polymer. Hemicellulose extraction has been carried out by hydrolysis[26,27], acid treatments[20,24] and alkaline treatments[20,28]. On the other hand cellulose has been extracted by alkaline medium treatments[29], ultrasound[30] and acid treatments[24]. For lignin, the extraction has been done with ionic liquid[31], extraction of pulp[21], hydrolysis[27], kraft and sulphite[32,33], organosolv (solvent treatments)[34], alkaline treatments, etc. All the extraction methods used in lignin are drastic and will eventually cause a change in its chemical structure, it is almost impossible to extract lignin unaltered.[35]

Figure 1.8 represents an example of the organosolv process of the extraction of cellulose and lignin from wheat straw. The first step is treating the raw material by acid treatment to be able to break it down. In this case a mixture of formic acid and acetic acid that has been added to the raw material and left it to boil for 2h before allowing it to cool down at room temperature. After isolating the fibers and washing it with formic acid and distilled water, a pulp is obtained. The second step of the process is to use strong oxidizing agents such as performic acid and peracetic

acid to separate the lignin and hemicellulose from the cellulose. At this step, delignified fibers and black liquor are obtained. The black liquor consists of a mixture of lignin fragments and carbohydrates from the breakdown of hemicellulose. In the third step, the delignified fibers are bleached with hydrogen peroxide to remove the residual lignin and isolate cellulose. In the last step, the black liquor is heated in a formic acid solution to precipitate the lignin.[21]

Figure 1.8: Schematic diagram of the organosolv process of lignin extraction. From Watkins et al.[21]

1.4 Lignin

Currently, there is a great interest for the lignocellulosic biofuels industry to develop valuable co-products that can improve the overall economics of a biofuel production process. Cellulose has already several traditional applications in the paper, pharmaceutical, and textile industries and it is also used to produce biofuels. The most common way to transform cellulose into biofuels is to use enzymes to break it down into simple glucose sugars then use fermentation process followed by distillation to produce bioethanol.[15] Hemicellulose in contrast is very difficult to convert into ethanol. Due to its heterostructure of different sugars, it is difficult for traditional enzymes to break it down efficiently to be able to ferment it to ethanol. Instead, hemicellulose is

degraded to lactic acid, a valuable chemical that is used in the food, cosmetic and in other industrial applications.[36,37] In contrast to its cousins, lignin is considered as a waste product during the extraction process of cellulose. Lignin is usually a byproduct of paper and wood pulp industries, and it is mainly recycled as low grade fuel to generate heat. As of today, 95% of the worldwide lignin production is simply burned to produce heat and approximately 5% his used in the production of adhesives, dispersants, rubbers and artificial vanilla.[38,39] Given the unique structure and chemical properties of lignin, a wide variety of bulk and fine chemicals, particularly phenols, aldehydes and aliphatic compounds are potentially obtainable from lignin (Figure 1.9). It can technically constitute an infinite supply of chemicals that can be use in the transport, pharmaceutical, textile, chemical and manufacturing industries.

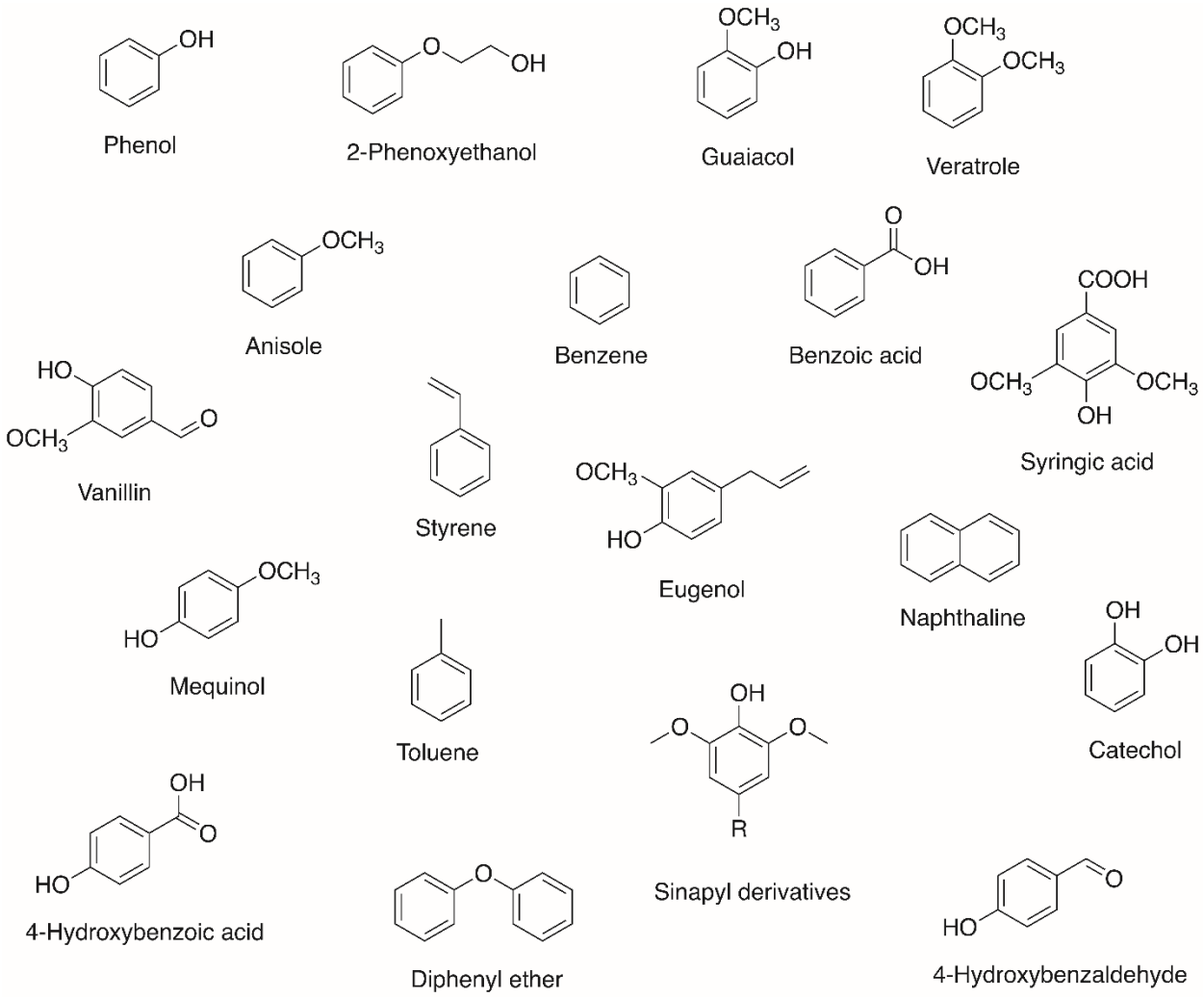

Figure 1.9: List of some chemicals that are potentially obtainable from lignin.

Lignin exploitation with selective bond cleavage is the major challenge for converting it into valuable chemicals. In addition, its 3-D amorphous complex structure and its physical-chemical properties (High viscosity, low vapor pressure, insolubility and heat resistivity) make it even more difficult to handle.[40] Therefore, it requires advanced conversion technologies, which are not yet at a commercial scale, but are undergoing rapid development. The main developments in the degradation of lignin into value added compounds has been studied by hydrothermal conversion[41–47], pyrolysis[11,48–54], catalysis[23,55–58], enzymatic degradation[59–61], ionic liquids[31,57], etc (Figure 1.10).

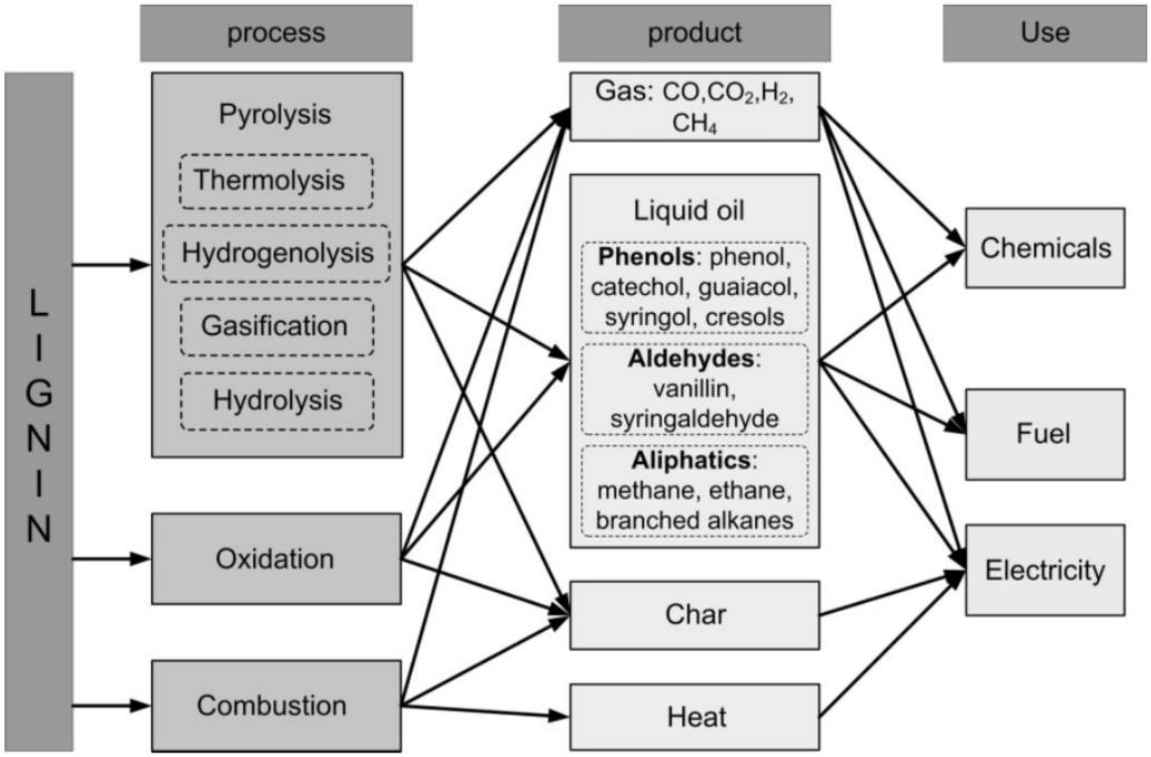

Figure 1. 10: Potential products obtainable from lignin and their uses. From Pandey et al. [11] Copyrights © 2010 John Wiley & Sons, Inc. Reprinted by permission of John Wiley & Sons, Inc.

1.4.1 Pyrolysis

Pyrolysis is the most studied method for the conversion of biomass. Pyrolysis represents the thermal treatment of organic materials in the absence of oxygen. Depending on the temperature and heating rate, pyrolysis converts organic materials into solids, liquid oil and/or gases.[11,50,53,62] The composition of the product and the yield of individual compounds depends strongly on the lignin source and the isolation methods.

Lignin degradation by pyrolysis occurs between 400 and 1100K. The final product of lignin pyrolysis is called char which constitute of the formation of benzene rings that recombines to form an aromatic polycyclic structure (Figure 1.11).[11,63] This process can be separated into two steps. The first one occurs at lower temperature (400-700K) where the weak bonds are cleaved to separate the monomers, and the second step is the cleavage of stronger bonds at higher temperatures which leads the formation of the char residue.

At lower temperatures, the alkyl chains that hold the monomer units are the first ones to start to react. The main observed products are monomers, phenolics, formic acid, formaldehyde, CO_2, CO, and water.[11,63,64] Starting at 400K, the cleavage of hydroxyl groups on the *β and γ* carbons releases water, while the cleavage of the *β*-*γ*-carbon bonds releases formaldehyde. *β*-O-4 and *α*-O-4 ether linkages can also cleave between 470 and 520K. The cleavage of *β*-O-4 and *α*-O-4 bonds release oxygenated compounds such as CO_2, CO, and water.[54] Above 580K , the C-C bonds cleavage in the alkyl chains become accessible and leads to the formation of monomers and phenolics such as anisole, guaiacol, cresol, syringol, etc.[54] At 700 K, methoxy groups of the aromatics start to fragment and eventually lead to the formation of methanol and methane.[65] At 750K and above, most of the linkages between the monomers are cleaved except the 4-O-5 and the 5-5 linkages that are persistent. The 4-O-5 will eventually cleave and release CO and H_2. Upon reaching 1100K, the aromatic rings rearrange in a polycyclic structure, and H_2 is released during the process.[66,67]

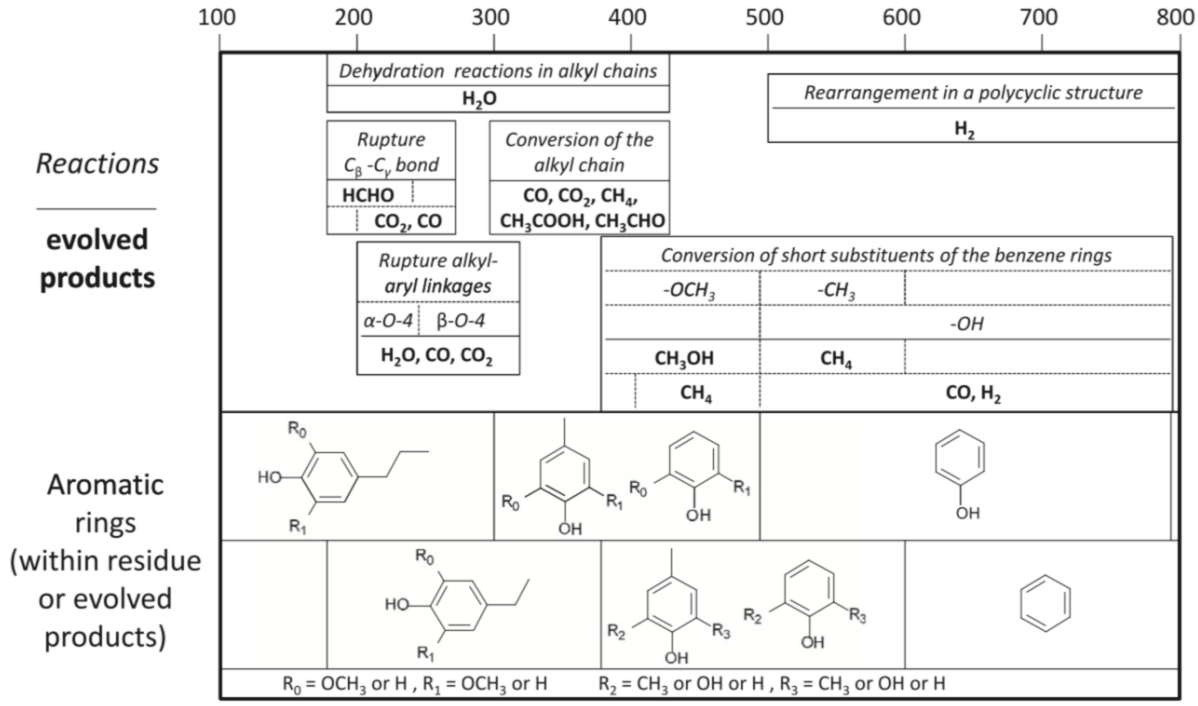

Figure 1.11: Summary of the bonds cleavage and formed products as a function of temperature from lignin pyrolysis process. Reprinted from Collard et al.[63] Copyright (2014) with permission from Elsevier.

1.4.2 Hydrothermal conversion

Hydrothermal conversion is a physical and thermo-chemical technique that uses high pressure liquid or supercritical water to decompose the biomass polymers.[41,68] Three main methods have been widely studied: wet oxidation[42,43], liquefaction[11,45,69] and gasification[41,44,46,70,71]. Depending on the method water is used in its normal form or as supercritical water. The main advantage of using water is that it acts as hydrogen donor during the reaction processes. On the other hand, supercritical water is achieved when water is heated to 647K and maintained at a pressure of 22Mpa. These conditions are above the critical point where the water is neither in liquid nor in gas phase. The water behaves like a fluid to dissolve molecules and at the same time it effuses through solids like a gas. The main advantage of using it in hydrothermal technique for lignin conversion is that the supercritical water has total miscibility with organic material and oxygen species.[72]

Hydrothermal gasification is a process that converts lignin into gas. The gasification of lignin under supercritical water condition mainly led the formation of CO_2 and CH_4 , a considerable amount of H_2 and CO, and small amount of C_2H_4, C_2H_6.[44,46,71] Lignin degradation takes place into two steps reaction pathway. The first step of the cleavage of the Ether bonds and cleavage of *β and γ* carbons of the alkyl chains to form the volatile compounds and phenolics. The phenolics will keep decomposing further by C-C bond cleavage in the aromatic to form more volatile compounds.

Hydrothermal liquefaction is process that converts lignin into bio-oils. The major products of the liquefaction are phenolics such as phenol, m-cresol, p-cresol and catechol, and they represent up to 80% of the derived bio-oils.[47,69,73] The conversion yield of lignin to bio-oils is between is between 32.6% and 90.2% and it strongly depends on the nature of the lignin and its pretreatments. The decomposition process of lignin under these conditions was mainly through the *β*-O-4 linkage. Aromatic rings are not affected by the hydrothermal conditions.

Wet oxidation is a process that uses the oxygen in the water to oxidize the lignin polymer.[42] The process is operated between 370K and 600K and at very high pressure. The major products of the wet oxidation are aromatic aldehydes such as vanillin, benzaldehyde, syringaldehyde, etc. The degradation of the lignin into aldehydes starts with the cleavage of the ether bonds, followed by the oxidation of the *alpha* carbons.

All the hydrothermal conversion methods will not yield a total of lignin conversion into value added chemicals. The residual byproduct of these techniques is hydrochar. In contrast to the char produced by pyrolysis, hydrochar has a higher hydrogen/carbon ratio and is lower in aromaticity with almost no fused aromatic ring structure.

1.4.3 Enzymatic conversion

Enzymatic conversion consists of using enzymes produced by living organism as a catalyst to break down the lignin. There are several types of different enzymes that have been studied for lignin degradation.[60,61] The preference in the bond cleavage in the lignin strongly depends on the type of enzyme that is used but also on the type of linkage in the lignin models. For example, in *β*-1 lignin models, laccase enzymes dehydrogenate phenolic-OH groups of phenolic lignin model compounds to form phenoxy radicals that can eventually undergo alkyl-aryl bond cleavage, α and *β* carbons bond cleavage and α carbon oxidation.[60,74] The major products formed by alkyl-aryl

bond cleavage are aldehydes and quinones, while α and β carbons bond cleavage forms aldehydes and ketones, and α carbon oxidation formed ketones. In β-O-4, it is the ring cleavage, α and β carbons bond cleavage and α carbon oxidation that occur.[75] The major products formed by ring cleavage bond cleavage are cyclic carbonates, while α and β carbons bond cleavage forms acids and alcohols, and α carbon oxidation formed ketones. In both models, the formation of phenoxy radicals undergo polymerization via radical coupling. Breaking down lignin selectively and efficiently remains a challenge as it requires the use of several and different enzymes.[60]

1.4.4 Catalysis

Catalysis is considered to be the most promising method in biomass and lignin conversion. Catalysts usually are required to assist selective bond cleavage, leading to high selectivity values for a particular compound.[76–78] Various catalysts have been tested in combination with several processes such as pyrolysis, hydrothermal treatment, hydrodeoxygenation, etc. These studies used both lignin and lignin models (Table 1.3).

Table 1.3: Summary of several studies in attempt of lignin and lignin model conversion by using catalysis

Feedstock	Process	Catalyst	Conversion (%)	Major products
Organosolv Lignin	Pyrolysis	HZSM-5[79]	43	benzene, toluene and xylene
Alkaline lignin	Pyrolysis	MCM-48[49]	17.01	benzene, toluene and xylene
Alkaline lignin	Pyrolysis	Al/MCM-48[49]	32.45	benzene, toluene and xylene
Alkaline lignin	Pyrolysis	Zr/MCM-48[49]	49.39	benzene, toluene and xylene
Kraft Lignin	Hydrogenolysis	Metal oxides[77]	37.5	p-ethylphenol, p-

				propylphenol and m-cresol
Kraft Lignin	Hydrogenolysis	ammonium heptamolybdate[80]	74	Phenols, cyclohexane, benzenes, naphtalenes and phenanthrenes
Phenol	Hydrogenolysis	Pt/HY[81]	100	Cyclohexane
Anisole	Hydrogenolysis	Pt/HBeta[82]	100	Benzene, toluene and xylene
Anisole	Hydrogenolysis	Pt/Al_2O_3[83]	----	Phenols
Guaiacol	Hydrodgenolysis	Rh/ZrO[84]	100	Benzene
Pyrolitic oil	Hydrothermal	$Pt/Al_2O_3/SiO_2$[85]	----	Phenols, aromatics, alkanes
Oranosolv lignin	Hydrothermal	Cu/PMO[86]	100	2-Ethycylohexanol, methylethycyclohexanol
4-Propylphenol	Hydrogenolysis	Pt/AC(N)[87]	100	Propylcyclohexane
2-Phenoxyethanol	Oxidation	Dipicolinate[88] Vanadium	20	Phenol and formic acid
1-phenyl-2-phenoxyethanol	Oxidation	Dipicolinate[88] Vanadium	95	Benzoic acid, phenol and 2-phenoxyacetophenone

1.5 Approach

The separation of the products formed by homogeneous catalysis, hydrothermal treatments and pyrolysis can be challenging and costly. By contrast, heterogeneous catalysis seems to be the key solution for the conversion of lignin, as the products and the catalyst can be easily separated. In addition, since pyrolysis and hydrothermal treatments requires high temperatures and lead to a

variable and often uncontrolled range of target products, catalysis plays an essential role in making biomass conversion viable for valorization by reducing activation energies for reaction and guiding product selectivity.

The choice of a catalyst plays a critical role in development of technologies for selective lignin conversion. In order to do so, the need to understand fundamental interactions of lignin with catalysts at a molecular level is a necessity. The surface science approach consists on probing surface interactions at the molecular level and this requires maintaining a clean and a well characterized surface.[89] The use of ultrahigh vacuum (UHV) in the range of $1x10^{-9}$ torr and below allows us to create an isolated system in order to probe the interaction of the lignin (lignin models) on the catalyst surface without the interference of the surrounding environment. Also, by achieving ultrahigh vacuum the experiments determine properties of the relevant species on the surface without interaction of the same species in the gas phase.

Platinum catalysts have shown very high conversion rates and selectivity in the valorization of lignin and lignin models (Table 1.3). This makes it convenient to choose Pt(111) as model catalyst. The main advantage of using single crystals is that they have a well defined surface which makes it easier to characterize.[90,91,93] The choice of the <111> orientation is mainly because it is thermodynamically stable but it is also a very reactive surface. This falls in the line of Sabatier's principle which state that for optimal reactivity, the interaction between the catalyst and the molecules should neither be too strong nor be too weak. Further literature, specific to the reactivity of relevant molecules on Pt(111) is presented in the introduction section of chapter 3, 4 and 5.

Targeting the functional groups in the lignin could be the key to converting lignin regardless of source. Since the β-O-4 ether linkage is the most dominant one in lignin composition, it will be the one targeted in the next chapters. Starting with lignin itself or a small fragment of lignin can be very challenging, due to the physical properties of lignin (High viscosity, low vapor pressure, insolubility and heat resistivity). These properties make it impossible to handle under UHV conditions. The approach proposed in this work, is to use model molecules that have a chemical structure similar but without the inconvenience of the physical properties. The reactivity of these model molecules on the Pt(111) surface will provide a better understanding of the eventual reactivity of the lignin itself. In this work, we start with simple lignin models such as phenol and gradually increase the complexity towards anisole and 2-phenoxyethanol. Once we have a better understanding of the behavior of one complex functional group, we can increase the complexity

by having a secondary functional groups on the ortho, meta and para sites (Figure 1.12). The build up towards understanding the reactivity of the complex lignin structure will guide the valorization of lignin step by step.

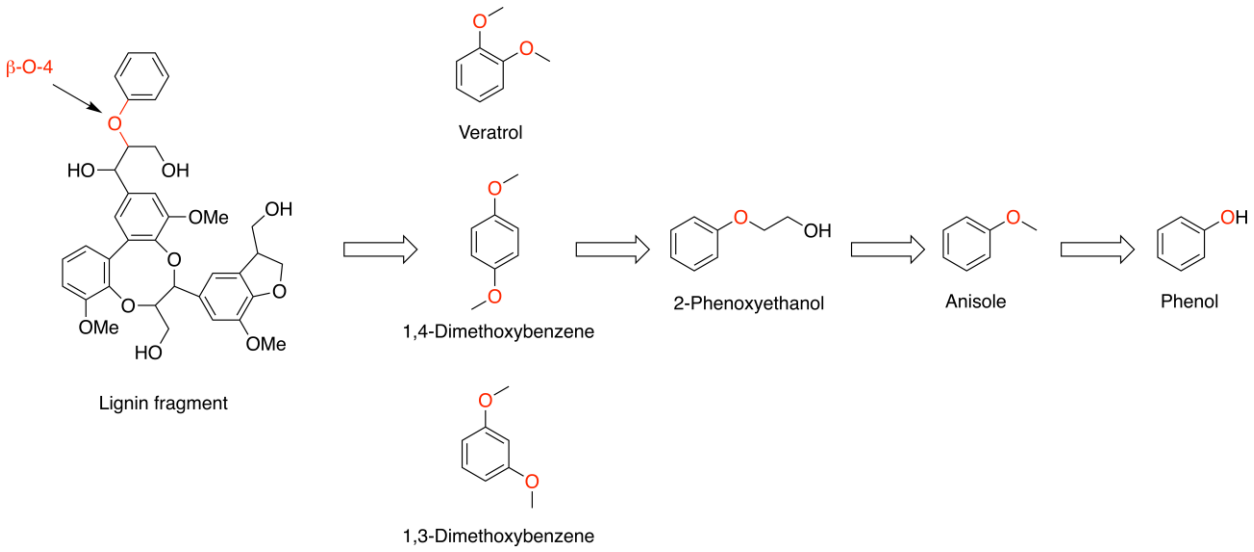

Figure 1.12: Starting with simple lignin models and gradually increasing the complexity towards lignin.

The main techniques that will be used are X-ray photoelectron spectroscopy (XPS) to identify the elemental composition of the model molecules and intermediate species; low energy electron diffraction (LEED) to determine the surface structure, temperature programmed desorption (TPD) to identify the desorbed reaction products; and reflection absorption infrared spectroscopy (RAIRS) to have insights about the adsorption geometry and the intermediate species of the decomposition. The studies combine surface science and first principle calculations to investigate the reactivity of the lignin models on the platinum Pt(111) model surface as a model catalyst in order to compare the facility of the C-H vs. C-O vs. C-C vs. O-H bonds cleavage (Figure 1.13).

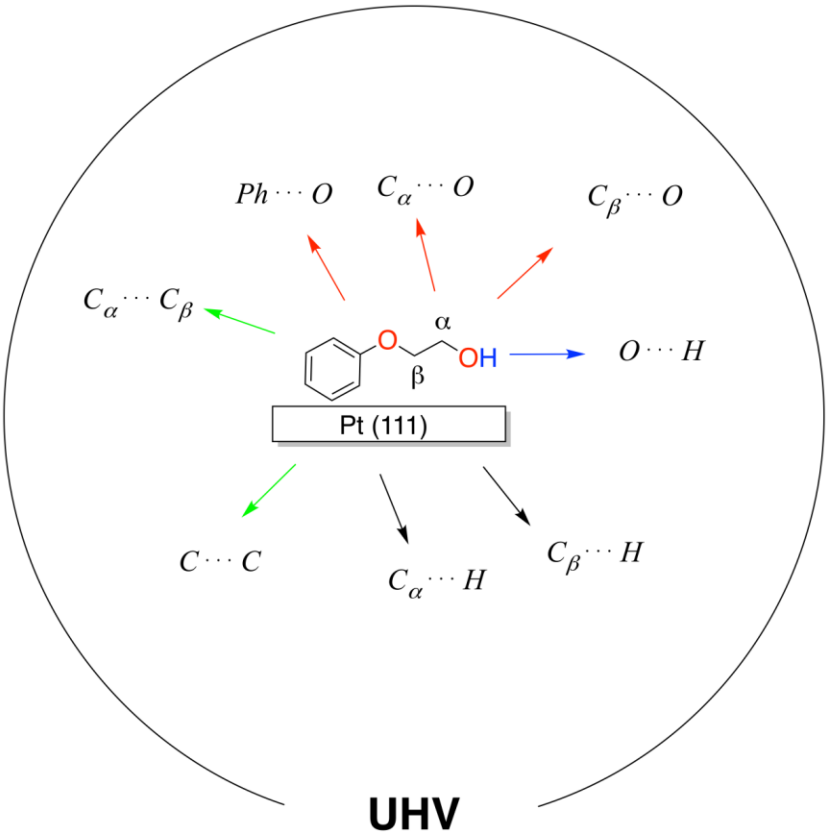

Figure 1.13: Study of lignin models such as 2-Phenoxyethanol under UHV conditions to investigate the reaction pathway and the order of bond cleavage.

References

(1) British Petroleum. BP Statistical Review of World Energy 2017. *Br. Pet.* **2017**, 1–52.

(2) Mohr, S. H.; Wang, J.; Ellem, G.; Ward, J.; Giurco, D. Projection of World Fossil Fuels by Country. *Fuel* **2015**, *141*, 120–135.

(3) Nejat, P.; Jomehzadeh, F.; Taheri, M. M.; Gohari, M.; Muhd, M. Z. A Global Review of Energy Consumption, CO2emissions and Policy in the Residential Sector (with an Overview of the Top Ten CO2emitting Countries). *Renew. Sustain. Energy Rev.* **2015**, *43*, 843–862.

(4) Popp, J.; Lakner, Z.; Harangi-Rákos, M.; Fári, M. The Effect of Bioenergy Expansion: Food, Energy, and Environment. *Renew. Sustain. Energy Rev.* **2014**, *32*, 559–578.

(5) Berndes, G.; Hoogwijk, M.; Van Den Broek, R. The Contribution of Biomass in the Future Global Energy Supply: A Review of 17 Studies. *Biomass and Bioenergy* **2003**, *25*, 1–28.

(6) Gronowska, M.; Joshi, S.; MacLeana, H. L. A Review of U.S. and Canadian Biomass Supply Studies. *BioResources* **2009**, *4*, 341–369.

(7) Demirbaş, A. Biomass Resource Facilities and Biomass Conversion Processing for Fuels and Chemicals. *Energy Convers. Manag.* **2001**, *42*, 1357–1378.

(8) *Canada - Global Forest Resources Assessment 2015 – Country Report*; 2015.

(9) Renewable Industries Canada. facts-dont-lie http://ricanada.org/.

(10) Pettersen, R. The Chemical Composition of Wood. *Chem. solid wood* **1984**, 1–9.

(11) Pandey, M. P.; Kim, C. S. Lignin Depolymerization and Conversion: A Review of Thermochemical Methods. *Chem. Eng. Technol.* **2011**, *34*, 29–41.

(12) Shahzadi, T.; Mehmood, S.; Irshad, M.; Anwar, Z.; Afroz, A.; Zeeshan, N.; Rashid, U.; Sughra, K. Advances in Lignocellulosic Biotechnology : A Brief Review on Lignocellulosic Biomass and Cellulases. *Adv. Biosci. Biotechnol.* **2014**, *5*, 246–251.

(13) Isikgor, F. H.; Becer, C. R. Lignocellulosic Biomass: A Sustainable Platform for the Production of Bio-Based Chemicals and Polymers. *Polym. Chem.* **2015**, *6*, 4497–4559.

(14) Mosier, N.; Wyman, C.; Dale, B.; Elander, R.; Lee, Y. Y.; Holtzapple, M.; Ladisch, M. Features of Promising Technologies for Pretreatment of Lignocellulosic Biomass. *Bioresour. Technol.* **2005**, *96*, 673–686.

(15) Limayem, A.; Ricke, S. C. Lignocellulosic Biomass for Bioethanol Production: Current Perspectives, Potential Issues and Future Prospects. *Prog. Energy Combust. Sci.* **2012**, *38*, 449–467.

(16) Musule, R.; Alarcón-Gutiérrez, E.; Houbron, E. P.; Bárcenas-Pazos, G. M.; del Rosario Pineda-López, M.; Domínguez, Z.; Sánchez-Velásquez, L. R. Chemical Composition of Lignocellulosic Biomass in the Wood of Abies Religiosa across an Altitudinal Gradient. *J. Wood Sci.* **2016**, *62*, 537–547.

(17) Peter, M. Energy Production from Biomass (part 1): Overview of Biomass. **2002**, *83*, 37–46.

(18) Vander Wielen, L. C. The Structure and Physical Properties of Pulpwood Fibers. **2005**, 1–31.

(19) Lavanya, D.; Kulkarni, P. K.; Dixit, M.; Raavi, P. K.; Krishna, L. N. V. International Journal of Drug Formulation and Research Sources of Cellulose and Their Applications –. **2011**, 19–38.

(20) Peng, F.; Ren, J. L.; Xu, F.; Sun, R. Chemicals from Hemicellulose: A Review. *Sutainable Prod. Fuels, Chem. Fibers from For. Biomass* **2011**, 219–259.

(21) Watkins, D.; Nuruddin, M.; Hosur, M.; Tcherbi-Narteh, A.; Jeelani, S. Extraction and Characterization of Lignin from Different Biomass Resources. *J. Mater. Res. Technol.* **2015**, *4*, 26–32.

(22) A. Sluiter, B. Hames, R. Ruiz, C. S.; Slui, J.; ter, D. Templeton, and D. C. Determination of Structural Carbohydrates and Lignin in Biomass: Laboratory Analytical Procedure (LAP); Issue Date: April 2008; Revision Date: July 2011 (Version 07-08-2011) - 42618.pdf. *Tech. Rep. NREL/ TP -510 -42618* **2008**, 1–15.

(23) Zakzeski, J.; Bruijnincx, P. C. A.; Jongerius, A. L.; Weckhuysen, B. M. The Catalytic Valorization of Ligning for the Production of Renewable Chemicals. *Chem. Rev.* **2010**, *110*, 3552–3599.

(24) Galbe, M.; Zacchi, G. A Review of the Production of Ethanol from Softwood. *Applied Microbiology and Biotechnology*, 2002, *59*, 618–628.

(25) Harmsen, P.; Huijgen, W.; Bermudez, L.; Bakker, R. *Literature Review of Physical and Chemical Pretreatment Processes for Lignocellulosic Biomass*; 2010.

(26) Farhat, W.; Venditti, R.; Quick, A.; Taha, M.; Mignard, N.; Becquart, F.; Ayoub, A. Hemicellulose Extraction and Characterization for Applications in Paper Coatings and Adhesives. *Ind. Crops Prod.* **2017**, *107*, 370–377.

(27) Sun, Y.; Cheng, J. Hydrolysis of Lignocellulosic Materials for Ethanol Production : A Review Q. *Bioresour. Technol.* **2002**, *83*, 1–11.

(28) Egüés, I.; Sanchez, C.; Mondragon, I.; Labidi, J. Effect of Alkaline and Autohydrolysis Processes on the Purity of Obtained Hemicelluloses from Corn Stalks. *Bioresour. Technol.* **2012**, *103*, 239–248.

(29) Sun, R.; Lawther, J. M.; Banks, W. B. Influence of Alkaline Pre-Treatments on the Cell Wall Components of Wheat Straw. *Ind. Crops Prod.* **1995**, *4*, 127–145.

(30) Bussemaker, M. J.; Xu, F.; Zhang, D. Manipulation of Ultrasonic Effects on Lignocellulose by Varying the Frequency, Particle Size, Loading and Stirring. *Bioresour. Technol.* **2013**, *148*, 15–23.

(31) Binder, J. B.; Gray, M. J.; White, J. F.; Zhang, Z. C.; Holladay, J. E. Reactions of Lignin Model Compounds in Ionic Liquids. *Biomass and Bioenergy* **2009**, *33*, 1122–1130.

(32) Radotić, K.; Mićić, M. Methods for Extraction and Purification of Lignin and Cellulose from Plant Tissues BT - Sample Preparation Techniques for Soil, Plant, and Animal Samples. In; Micic, M., Ed.; Springer New York: New York, NY, 2016; pp. 365–376.

(33) Carvajal, J. C.; Gómez, Á.; Cardona, C. A. Comparison of Lignin Extraction Processes: Economic and Environmental Assessment. *Bioresour. Technol.* **2016**, *214*, 468–476.

(34) Zhao, X.; Cheng, K.; Liu, D. Organosolv Pretreatment of Lignocellulosic Biomass for Enzymatic Hydrolysis. *Appl. Microbiol. Biotechnol.* **2009**, *82*, 815–827.

(35) Pu, Y.; Hu, F.; Huang, F.; Ragauskas, A. J. Lignin Structural Alterations in Thermochemical Pretreatments with Limited Delignification. *Bioenergy Res.* **2015**, *8*, 992–1003.

(36) Garde, A.; Jonsson, G.; Schmidt, A. S.; Ahring, B. K. Lactic Acid Production from Wheat Straw Hemicellulose Hydrolysate by Lactobacillus Pentosus and Lactobacillus Brevis. *Bioresour. Technol.* **2002**, *81*, 217–223.

(37) Walton, S. L.; Bischoff, K. M.; Van Heiningen, A. R. P.; Van Walsum, G. P. Production of Lactic Acid from Hemicellulose Extracts by Bacillus Coagulans MXL-9. *J. Ind. Microbiol. Biotechnol.* **2010**, *37*, 823–830.

(38) Laurichesse, S.; Avérous, L. *Chemical Modification of Lignins: Towards Biobased Polymers*; 2013; Vol. 39.

(39) Silva, E. A. B. Da; Zabkova, M.; Araújo, J. D.; Cateto, C. a.; Barreiro, M. F.; Belgacem, M. N.; Rodrigues, a. E. An Integrated Process to Produce Vanillin and Lignin-Based Polyurethanes from Kraft Lignin. *Chem. Eng. Res. Des.* **2009**, *87*, 1276–1292.

(40) Krutov, S. M.; Voznyakovskii, a. P.; Gribkov, I. V.; Shugalei, I. V. Lignin Wastes: Past, Present, and Future. *Russ. J. Gen. Chem.* **2014**, *84*, 2632–2642.

(41) Kang, S.; Li, X.; Fan, J.; Chang, J. Hydrothermal Conversion of Lignin: A Review. *Renew. Sustain. Energy Rev.* **2013**, *27*, 546–558.

(42) Mishra, V. S.; Mahajani, V. V.; Joshi, J. B. Wet Air Oxidation. *Ind. Eng. Chem. Res.* **1995**, *34*, 2–48.

(43) Luck, F. A Review of Industrial Catalytic Wet Air Oxidation Processes. *Catal. Today* **1996**, *27*, 195–202.

(44) Naqvi, M.; Yan, J.; Dahlquist, E. Black Liquor Gasification Integrated in Pulp and Paper Mills: A Critical Review. *Bioresour. Technol.* **2010**, *101*, 8001–8015.

(45) Vuori, B. A.; Bredenberg, J. B. Liquefaction of Kraft Lignin. *Holzforschung* **1988**, *42*, 155–161.

(46) Sricharoenchaikul, V. Assessment of Black Liquor Gasification in Supercritical Water. *Bioresour. Technol.* **2009**, *100*, 638–643.

(47) Zhang, B.; Huang, H. J.; Ramaswamy, S. Reaction Kinetics of the Hydrothermal Treatment of Lignin. *Appl. Biochem. Biotechnol.* **2008**, *147*, 119–131.

(48) Giudicianni, P.; Cardone, G.; Ragucci, R. Cellulose, Hemicellulose and Lignin Slow Steam Pyrolysis: Thermal Decomposition of Biomass Components Mixtures. *J. Anal. Appl. Pyrolysis* **2013**, *100*, 213–222.

(49) Elfadly, A. M.; Zeid, I. F.; Yehia, F. Z.; Rabie, A. M.; aboualala, M. M.; Park, S. E. Highly Selective BTX from Catalytic Fast Pyrolysis of Lignin over Supported Mesoporous Silica. *Int. J. Biol. Macromol.* **2016**, *91*, 278–293.

(50) Brebu, M.; Vasile, C. Thermal Degradation of Lignin- a Review. *Cellul. Chem. Technol.* **2010**, *44*, 353–363.

(51) Jiang, G.; Nowakowski, D. J.; Bridgwater, A. V. A Systematic Study of the Kinetics of Lignin Pyrolysis. *Thermochim. Acta* **2010**, *498*, 61–66.

(52) Jiang, G.; Nowakowski, D. J.; Bridgwater, A. V. Effect of the Temperature on the Composition of Lignin Pyrolysis Products. *Energy & Fuels* **2010**, *24*, 4470–4475.

(53) Bridgwater, a. V. Review of Fast Pyrolysis of Biomass and Product Upgrading. *Biomass and Bioenergy* **2012**, *38*, 68–94.

(54) Wang, S.; Wang, K.; Liu, Q.; Gu, Y.; Luo, Z.; Cen, K.; Fransson, T. Comparison of the Pyrolysis Behavior of Lignins from Different Tree Species. *Biotechnol. Adv.* **2009**, *27*, 562–567.

(55) Díaz-Urrutia, C.; Hurisso, B. B.; Gauthier, P. M. P.; Sedai, B.; Singer, R. D.; Baker, R. T. Catalytic Aerobic Oxidation of Lignin-Derived Bio-Oils Using Oxovanadium and Copper Complex Catalysts and Ionic Liquids. *J. Mol. Catal. A Chem.* **2016**, *423*, 414–422.

(56) Yan, N.; Zhao, C.; Dyson, P. J.; Wang, C.; Liu, L. T.; Kou, Y. Selective Degradation of Wood Lignin over Noble-Metal Catalysts in a Two-Step Process. *ChemSusChem* **2008**, *1*, 626–629.

(57) Dai, J.; Patti, A. F.; Saito, K. Recent Developments in Chemical Degradation of Lignin: Catalytic Oxidation and Ionic Liquids. *Tetrahedron Lett.* **2016**, *57*, 4945–4951.

(58) Huber, G. W.; Iborra, S.; Corma, A. Synthesis of Transportation Fuels from Biomass: Chemistry, Catalysts, and Engineering. *Chem. Rev.* **2006**, *106*, 4044–4098.

(59) Pérez, J.; Muñoz-Dorado, J.; De La Rubia, T.; Martínez, J. Biodegradation and Biological Treatments of Cellulose, Hemicellulose and Lignin: An Overview. *Int. Microbiol.* **2002**, *5*, 53–63.

(60) Pollegioni, L.; Tonin, F.; Rosini, E. Lignin-Degrading Enzymes. *FEBS J.* **2015**, *282*, 1190–1213.

(61) Xia, Z.; Yoshida, T.; Funaoka, M. Enzymatic Degradation of Highly Phenolic Lignin-Based Polymers (lignophenols). *Eur. Polym. J.* **2003**, *39*, 909–914.

(62) McKendry, P. Energy Production from Biomass (part 2): Conversion Technologies. *Bioresour. Technol.* **2002**, *83*, 47–54.

(63) Collard, F. X.; Blin, J. A Review on Pyrolysis of Biomass Constituents: Mechanisms and Composition of the Products Obtained from the Conversion of Cellulose, Hemicelluloses and Lignin. *Renew. Sustain. Energy Rev.* **2014**, *38*, 594–608.

(64) Shen, D. K.; Gu, S.; Luo, K. H.; Wang, S. R.; Fang, M. X. The Pyrolytic Degradation of Wood-Derived Lignin from Pulping Process. *Bioresour. Technol.* **2010**, *101*, 6136–6146.

(65) Asmadi, M.; Kawamoto, H.; Saka, S. Thermal Reactions of Guaiacol and Syringol as Lignin Model Aromatic Nuclei. *J. Anal. Appl. Pyrolysis* **2011**, *92*, 88–98.

(66) Hosoya, T.; Kawamoto, H.; Saka, S. Role of Methoxyl Group in Char Formation from Lignin-Related Compounds. *J. Anal. Appl. Pyrolysis* **2009**, *84*, 79–83.

(67) Sharma, R. K.; Wooten, J. B.; Baliga, V. L.; Lin, X.; Chan, W. G.; Hajaligol, M. R. Characterization of Chars from Pyrolysis of Lignin. *Fuel* **2004**, *83*, 1469–1482.

(68) Peterson, A. a.; Vogel, F.; Lachance, R. P.; Fröling, M.; Antal, Jr., M. J.; Tester, J. W. Thermochemical Biofuel Production in Hydrothermal Media: A Review of Sub- and Supercritical Water Technologies. *Energy Environ. Sci.* **2008**, *1*, 32.

(69) Tymchyshyn, M.; Xu, C. C. Liquefaction of Bio-Mass in Hot-Compressed Water for the Production of Phenolic Compounds. *Bioresour. Technol.* **2010**, *101*, 2483–2490.

(70) McKendry, P. Energy Production from Biomass (part 3): Gasification Technologies. *Bioresour. Technol.* **2002**, *83*, 55–63.

(71) Rönnlund, I.; Myréen, L.; Lundqvist, K.; Ahlbeck, J.; Westerlund, T. Waste to Energy by Industrially Integrated Supercritical Water Gasification - Effects of Alkali Salts in Residual by-Products from the Pulp and Paper Industry. *Energy* **2011**, *36*, 2151–2163.

(72) Galkin, A. A.; Lunin, V. V. Subcritical and Supercritical Water: A Universal Medium for Chemical Reactions. *Russ. Chem. Rev.* **2005**, *74*, 21–35.

(73) Kang, S.; Li, X.; Fan, J.; Chang, J. Classified Separation of Lignin Hydrothermal Liquefied Products. *Ind. Eng. Chem. Res.* **2011**, *50*, 11288–11296.

(74) Kawai, S.; Nakagawa, M.; Ohashi, H. Degradation Mechanisms of a Nonphenolic ␣ - O -4 Lignin Model Dimer by Trametes Versicolor Laccase in the Presence of. **2002**, *30*, 482–489.

(75) Christopher, L. P.; Yao, B.; Ji, Y. Lignin Biodegradation with Laccase-Mediator Systems. *Front. Energy Res.* **2014**, *2*, 1–13.

(76) Pineda, A.; Lee, A. F. Heterogeneously Catalyzed Lignin Depolymerization. *Appl. Petrochemical Res.* **2016**, *6*, 243–256.

(77) Bozell, J. J. Approaches to the Selective Catalytic Conversion of Lignin: A Grand Challenge for Biorefinery Development. In *Selective Catalysis for Renewable Feedstocks and Chemicals*; Nicholas, K. M., Ed.; Springer International Publishing: Cham, 2014; pp. 229–255.

(78) Kobayashi, H.; Ohta, H.; Fukuoka, A. Conversion of Lignocellulose into Renewable Chemicals by Heterogeneous Catalysis. *Catal. Sci. Technol.* **2012**, *2*, 869.

(79) Luo, Z.; Wang, S.; Guo, X. Selective Pyrolysis of Organosolv Lignin over Zeolites with Product Analysis by TG-FTIR. *J. Anal. Appl. Pyrolysis* **2012**, *95*, 112–117.

(80) Oasmaa, A.; Johansson, A. Catalytic Hydrotreating of Lignin with Water-Soluble Molybdenum Catalyst. *Energy and Fuels* **1993**, *7*, 426–429.

(81) Hong, D.-Y.; Miller, S. J.; Agrawal, P. K.; Jones, C. W. Hydrodeoxygenation and Coupling of Aqueous Phenolics over Bifunctional Zeolite-Supported Metal Catalysts. *Chem. Commun.* **2010**, *46*, 1038–1040.

(82) Zhu, X.; Lobban, L. L.; Mallinson, R. G.; Resasco, D. E. Bifunctional Transalkylation and Hydrodeoxygenation of Anisole over a Pt/HBeta Catalyst. *J. Catal.* **2011**, *281*, 21–29.

(83) Runnebaum, R. C.; Nimmanwudipong, T.; Block, D. E.; Gates, B. C. Catalytic Conversion of Anisole: Evidence of Oxygen Removal in Reactions with Hydrogen. *Catal. Letters* **2011**, *141*, 817–820.

(84) Gutierrez, a.; Kaila, R. K.; Honkela, M. L.; Slioor, R.; Krause, a. O. I. Hydrodeoxygenation of Guaiacol on Noble Metal Catalysts. *Catal. Today* **2009**, *147*, 239–246.

(85) Sheu, Y. H. E.; Anthony, R. G.; Soltes, E. J. Kinetic Studies of Upgrading Pine Pyrolytic Oil by Hydrotreatment. *Fuel Process. Technol.* **1988**, *19*, 31–50.

(86) Barta, K.; Matson, T. D.; Fettig, M. L.; Scott, S. L.; Iretskii, A. V.; Ford, P. C. Catalytic Disassembly of an Organosolv Lignin via Hydrogen Transfer from Supercritical Methanol. *Green Chem.* **2010**, *12*, 1640.

(87) Ohta, H.; Kobayashi, H.; Hara, K.; Fukuoka, A. Hydrodeoxygenation of Phenols as Lignin Models under Acid-Free Conditions with Carbon-Supported Platinum Catalysts. *Chem. Commun.* **2011**, *47*, 12209.

(88) Hanson, S. K.; Baker, R. T.; Gordon, J. C.; Scott, B. L.; Thorn, D. L. Aerobic Oxidation of Lignin Models Using a Base Metal Vanadium Catalyst. *Inorg. Chem.* **2010**, *49*, 5611–5618.

(89) Goodman, D. W. Catalysis: From Single Crystals to the "Real World." *Surf. Sci.* **1994**, *299-300*, 837–848.

(90) Woodruff, P. *Modern Techniques of Surface Science*; Cambridge University Press: Cambridge, 2016.

(91) Somorjai, G. A.; Mujumdar, A. S. Introduction to Surface Chemistry and Catalysis. *Dry. Technol.* **1995**.

(92) Kolasinski, K. W. *Surface Science: Foundations of Catalysis and Nanoscience*; 2012.

(93) Schirmer, W. Introduction to Surface Chemistry and Catalysis. *Zeitschrift für Phys. Chemie* **1995**.

Chapter 2:
Experimental

2 Experimental

This chapter provides a detailed description of the ultrahigh vacuum chamber and the experimental techniques used in this thesis. In the first section we will address how to achieve ultrahigh vacuum in the chamber, then we will delve into the physical basis behind the characterization techniques and how to operate them. The techniques that will be covered in this chapter are X-ray photoelectron spectroscopy (XPS), low-energy electron diffraction (LEED), temperature programmed desorption (TPD) and reflection adsorption infrared spectroscopy (RAIRS).

2.1 The need for Ultrahigh Vacuum

Surface science consists on probing surface interactions at the molecular level and this requires maintaining a clean and a well characterized surface.[1] From the kinetic theory of ideal gases, the number of molecules that hits the surface per unit of time derived from Maxwell-Boltzmann distribution is $\frac{1}{4}n_0 v$ and it mainly depend on the pressure P and temperature T.[1–3] They can be described by these two equations,

$$P = n_0 k_b T \tag{2.1}$$

$$v = \sqrt{\frac{8k_b T}{\pi m}} \tag{2.2}$$

Where n_0 is the number of molecules per unit volume, v is the mean speed of the molecules, m is the molecular weight of the molecule and k_b Boltzmann constant. Substituting equations 2.1 and 2.1, we can rewrite the flux incident on the surface ϕ as

$$\phi = \frac{P}{\sqrt{2\pi m k_b T}} \tag{2.3}$$

Which corresponds to the Hertz-Knudsen equation.

The atomic density of a solid surface is approximately ~ 10^{15} atoms cm^{-2}. Assuming that the sticking probability is one, the time necessary to cover the surface can be estimated. For example, the flux incident on the surface for carbon monoxide (28 amu) at a room temperature of 298 K and a pressure of $1x10^{-6}$ torr, is $3.88x10^{14}$ atoms cm^{-2} s^{-1}. It would only take few seconds to cover the surface. In contrast, at pressures of $1x10^{-9}$ and $1x10^{-10}$ torr it would take 42 min and 7 hours respectively to cover the surface. Thus, the use of ultrahigh vacuum is a necessity to maintain those surfaces contamination-free state for the duration of the experiment.

Moreover, from the kinetic theory of gases, the mean free path λ for any molecule or particle can be described as,

$$\lambda = \frac{1}{n_0 \sigma} \tag{2.4}$$

Where n_0 is the number of molecules per unit volume, σ ($\sigma = 2\pi r$) is the collision cross section of the molecule[4]. By substituting equation 2.1, the mean free path equation becomes

$$\lambda = \frac{k_b T}{\sqrt{2}\sigma P} \tag{2.5}$$

For example, the collision cross section of carbon dioxide is σ = 0.52 nm^2. Assuming that the temperature is at 298 K and the pressure is at 1 torr, the mean free path is 41 μm. Compared to a pressure of $1x10^{-10}$ torr, the mean free path is approximately 410 km. On average the particle will travel a distance of 410 km before a collision occurs. The same analogy can be applied to ions and electrons. The use of probe techniques based on electron spectroscopy and electron beam require ultrahigh vacuum in order to maintain a large mean free path of the electrons to avoid collisions and scattering events that would result in loss of electron kinetic energy. The typical distance travelled by the ions and electrons in the UHV system is between a few centimeters up to 1 m. By achieving ultrahigh vacuum, we ensure that the mean free path is higher than λ > 0.01-1 m which avoids scattering effects and also helps to achieve a better signal to noise ratio.

2.2 Chamber description and how to achieve Ultrahigh Vacuum

The main ultrahigh vacuum chamber is custom built by Specs GmbH and RHK (Figure 2.1). The chamber is made of stainless steel and consists of a combination of three chambers separated by gate valves.

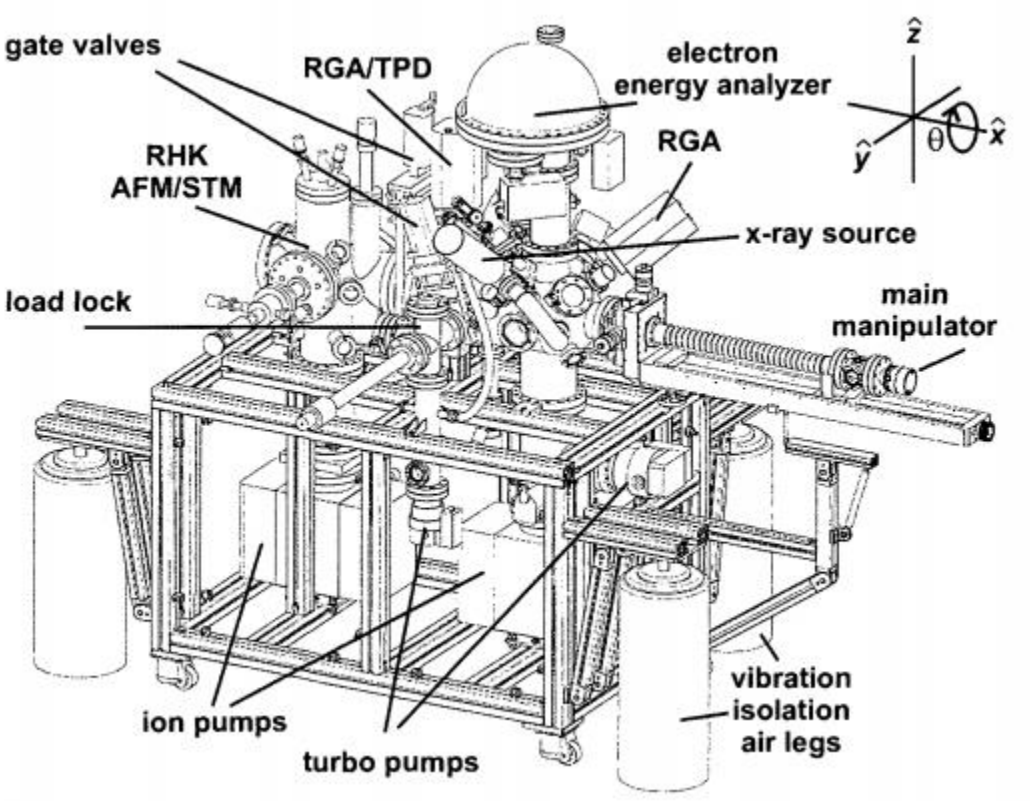

Figure 2.1: Diagram of the UHV chamber. Picture provided by Specs GmbH.

The first chamber is called load-lock and it is where samples can be loaded in or out. It is the first entry point of the sample from ambient pressure into the vented chamber. The load-lock is connected to the analysis chamber and they are separated by a gate valve to avoid breaking the vacuum in the analysis chamber during the loading/unloading processes. It is equipped with a transfer arm and a manipulator in X-Y directions to be able to transfer the sample into the analysis chamber. A full compact range gauge is used for pressure reading from UHV to atmosphere. The ultimate pressure in the load-lock is $1x10^{-8}$ torr and it is achieved by a combination of a mechanical pump and a turbo molecular pump. The mechanical pump is a rotary vane pump type (Edwards RV3) that consists of sliding vanes that rotates to generate a positive volume displacement by

compressing and ejecting the gas to atmosphere (Figure 2.2). This type of pump has a very high throughput and its ultimate pressure is in the order of $2x10^{-3}$ torr. Once the rough vacuum is reached we can turn on the turbo molecular pump which has a low throughput (especially for lighter gases such as H_2) but can achieve an ultimate pressure of $1x10^{-9}$ torr. The turbo molecular (TMU 071P) consist of multiple stages of fast rotating blades and a static stator (Figure 2.3).[5] The basic physical phenomenon relies on momentum transfer. The inlet gas goes through several collisions with the blades and acquires momentum, then it is pushed into the gas transfer holes in the stator that directs the molecules to the next stage of rotating blades and stator. The gas acquires energy by collision through several stages before reaching the exhaust. The turbo molecular pump requires a mechanical pump that acts as a "backing" pump to reduce the pressure at its outlet to be able to maintain a very low pressure at its inlet. This is why the mechanical pump is attached to the turbo molecular pump that is attached to the load-lock chamber. A detailed description about the models and specifics of the pumps used in each chamber can be found in Appendix A.

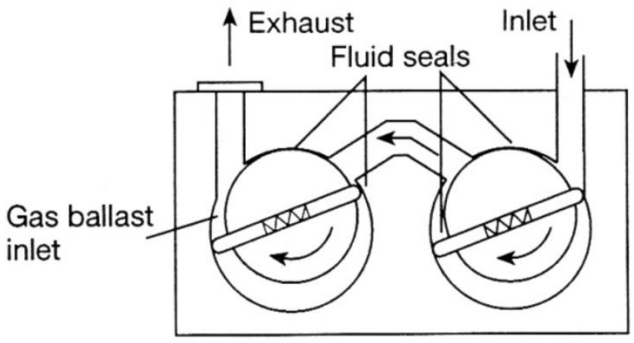

Figure 2.2: Cross section Diagram of a double stage displacement pump. Picture provided by Edwards vacuum.

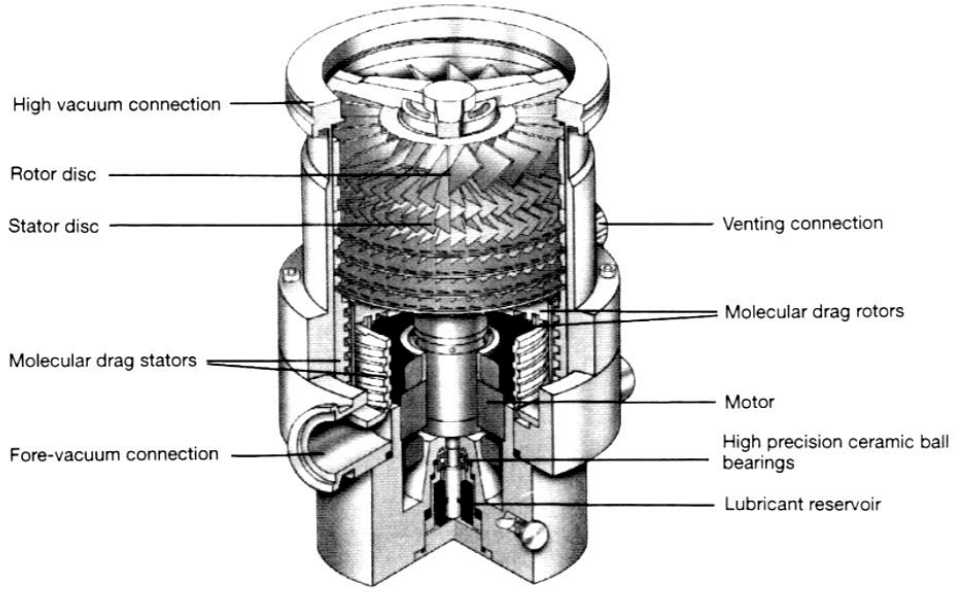

Figure 2.3: Cross section Diagram of a turbomolecular pump. Picture provided by Pfeiffer vacuum.

The second chamber is called the analysis chamber and it is where samples can be transferred from the load-lock the main manipulator arm. The analysis chamber is connected to the RHK chamber and they are separated by a gate valve to avoid unnecessary molecule deposition during the cleaning and dosing processes. The chamber houses a low energy electron diffractometer (LEED) to verify surface cleanness; an X-ray photoelectron spectrometer (XPS) to provide information on the elemental composition of the surface and to verify surface cleanness; an ultraviolet photoelectron spectrometer (UPS) to provide information on the surface electronic structure; a quadrupole mass spectrometer for residual gas analysis and to perform temperature programmed desorption (TPD); a sputtering gun used in sample cleaning; a Bayard Alpert ion gauge to measure the pressure and finally a metal evaporator to allow thin film deposition. This chamber is made of mu-metal, a type of stainless steel that is an alloy of nickel, iron and molybdenum. This alloy provides a high magnetic permeability for low magnetic fields and this shielding is necessary to avoid field interaction with electron-based techniques.

The Analysis chamber is equipped with a main manipulator allowing 70 cm linear transfer of the sample in the x direction with 360° rotational range. The manipulator is also mounted on an y-z stage which allows the arm to move within 25 mm range in the y and z directions. The ultimate

pressure in the analysis chamber is typically $2x10^{-10}$ torr and it is achieved by a combination of a mechanical pump, a turbo molecular pump, an ion pump and a titanium sublimation pump (TSP). In the previous paragraphs we covered the basic principle behind the mechanical and turbo molecular pumps, and these two can be categorized as displacement pumps. On the other hand, ion and TSP pumps can be categorized as entrapment pumps.

Once the vacuum is achieved by the mechanical and turbo molecular pump, the ion pump can be turned on to be able to achieve an ultimate pressure of $1x10^{-11}$ torr.[6] The Varian ion pump (Valcon plus 300 starcell) uses permanent magnets located outside the vacuum to generate a strong magnetic field (Figure 2.4). Then a high voltage between 3 to 7 kV is applied to the element assembly to pull electrons into the anode tube assembly. By doing so, the electrons become trapped by the high magnetic field and a spinning electron cloud is generated. As gases move into the anode assembly, they are struck by electrons and become ionized. These positive ions are then accelerated by the high voltage field toward the cathode plate (sputtering). Upon reaching the cathode surface the ions can undergo a chemical or a physical reaction with the cathode material. The chemical reaction occurs when the ions react with cathode material to form a new solid compound. For example, an ionized oxygen molecule will take an electron from and readily react with a metal cathode atom creating a solid metal oxide. In the physical reaction, the ions (especially heavier ions) that that hits the cathode surface acquire an electron and bounce back with enough energy to implant themselves physically on the pump surfaces. Both reactions ensure that the ions do not contribute to the surrounding pressure.

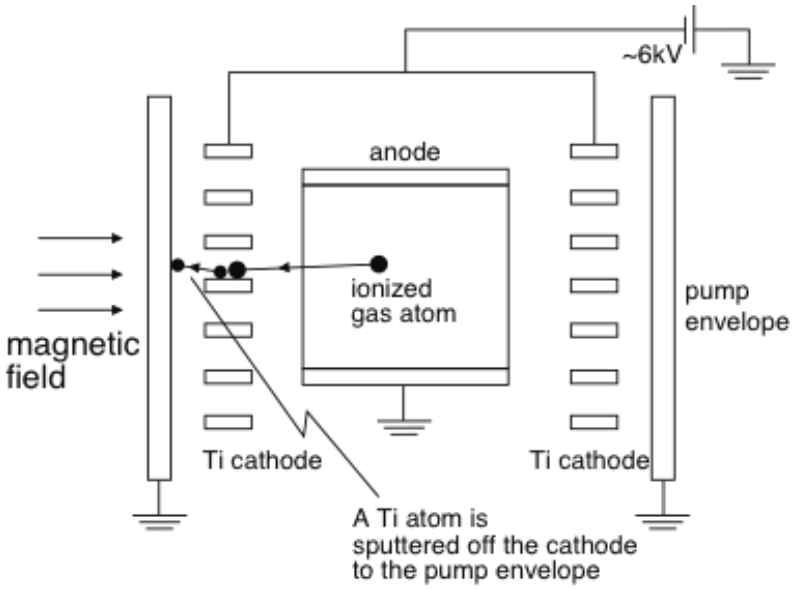

Figure 2.4: Schematic Diagram of an ion pump and its sections. Picture provided by Varian.

Titanium sublimation pumps are mainly used to remove residual gas in the ultrahigh vacuum chamber. The operating concept behind the Varian TSP pump (919-0180) consists of passing a high current, typically between 5 and 50 A through a titanium filament. The filament temperature increases until sublimation occurs and surrounding UHV chamber walls get coated with clean layers of titanium. Since clean titanium is very reactive, it is more likely that the surrounding molecules that hit the walls will react with the titanium to form a solid residue. It is efficient to entrap H_2, CO, H_2O and O_2 but it is totally ineffective for noble gases. Titanium films are more efficient at lower temperatures by ensuring that the sticking probabilities are close to 1 and for this reason the TSP pump is surrounded by a cryopanel that can be cooled down with liquid nitrogen.

The third chamber is called the RHK chamber and the samples can be transferred from the analysis chamber by using the main manipulator arm. The RHK chamber is equipped with scanning tunneling microscopy (STM) that uses tunneling effect of electron to obtain topography images of the surface with an atomic resolution, an atomic force microscopy (AFM) that uses Vander Waals forces to obtain topography images with a nanometer resolution, a sample/tips storage elevator, a Bayard Alpert ion gauge to measure the pressure and a wobble stick that allows the transfer of the sample from the main manipulator to the STM/AFM stage and to the storage

unit. The ultimate pressure in the RHK chamber is below 10^{-10} torr. It is achieved in two steps. The first one consists on using the combination of a mechanical pump, a turbo molecular pump of the analysis chamber through the gate valve to reach a pressure of $2x10^{-10}$ torr. In the second step, by closing the gate valve between the analysis and RHK chambers, the 2nd set of ion and TSP pumps takes the lead to maintain a low pressure and bringing it down below 10^{-10} torr.

Besides the main chamber, RAIRS experiments were performed in a dedicated "RAIRS chamber". The RAIRS chamber is equipped with its own electronics and it is setup to work independently. This chamber is dedicated for reflection absorption infrared spectroscopy (RAIRS) and it consists of a coupled Fourier transform infrared spectrometer (FT-IR) and a UHV chamber. The RAIRS is a convenient technique for verifying molecular integrity and orientation at metal surfaces. The UHV chamber contains a low energy electron diffraction (LEED) to verify surface cleanness, a quadrupole mass spectrometer for residual gas analysis and a sputtering gun used in sample cleaning. The chamber is equipped with a main manipulator allowing 500 mm linear transfer of the sample in the z direction with 360° rotational range. The manipulator is also mounted on an x-y stage which allows the arm to move within 25 mm range in the x and y directions. The ultimate pressure in the analysis chamber is $7x10^{-10}$ torr and it is achieved by a combination of a mechanical pump and a turbo molecular pump. Two differentially pumped windows are mounted on opposite sides of the UHV chamber to allow the infrared (IR) beam to pass through. These windows have 2.75" CF flanges and use KBr 38 x 6mm optical crystals with a 1/4" tube for differential pumping. Fluorocarbon O-rings are used as seals between the chamber and the windows.

In principle the optimal pressure of the pumping systems is in the UHV region, to achieve such low pressure, molecules must be removed from the inside surfaces of the chamber which would produce an eternal virtual leak. In order to achieve the UHV condition faster, "baking" the chamber is a necessity. The bake-out of the chamber consists of removing the impurities (especially water) from the walls of the UHV system by heating the walls uniformly while pumping down the system. For the main UHV chamber, an aluminium metal frame can be set around the UHV system and fiber glass insulating blankets are wrapped around it to create a tent. Two radiative heaters on opposite side of the frame are used to provide a uniform heating. The bake-out temperature is gradually increased to a maximum of 115° C and left at this temperature for at least 72 hours. The UHV windows and feedthroughs are gently wrapped in aluminium foil

to avoid thermal shocks which may result in the development of leaks. During the bake-out, the ion pumps are turned off to avoid high gas load in order to preserve them. Close to the end of the bake-out period, heating collards are used to bake the turbo pumps as well and at the end of the bake-out titanium sublimation pumps are turned for two minutes to achieve much lower pressures. For the RAIRS chamber, the setup is a bit different where heating tapes are used to heat the chamber. The tapes are wrapped around the chamber and the whole chamber walls are covered by aluminium foil to ensure that the heating is uniform. The bake-out temperature is gradually increased to a maximum of 115° C; because the chamber is smaller it requires less time to achieve ultrahigh vacuum conditions (36-48 hours).

2.3 Pressure measurement

The pressure reading in the chambers is mainly done by two types of gauges : Full compact gauge and Bayard Alpert ion gauge (B-A gauge).

The full compact gauge consists of a combination of a pirani gauge and an inverted magnetron gauge that allows a reading between 10^{-10} torr to atmosphere. It is to be noted that no gauge alone is able to perform a wide range reading from UHV to atmosphere, a combination of two different principles (gauges) is necessary.

Pirani gauge is a type of thermal conductivity gauge. It consists of a filament that is connected to an electrical circuit from which a pressure reading can be taken. The basic principle consists of heating the filament by flowing a current through it. As the surrounding molecules collide with the filament, heat exchange occurs, and the filament starts to transfer its heat to the surrounding gas. As the pressure drops down, less molecules are present in the background which results in a decrease of heat exchange between the molecules and the filament. The heat conductivity is proportional to the surrounding number of molecules. Hence, with a proper calibration an indirect pressure reading can be obtained. The limit of pressure reading does not go below 10^{-3} torr as the thermal conductivity of the gas will be relatively low comparted to the thermal transfer over the wire ends. At this point it is the inverted magnetron gauge that takes the lead.

An inverted magnetron gauge consists of a circular magnet and two electrodes: a pin anode and circular cathode that surrounds it (Figure 2.5).[7] The basic principle consists of setting high voltage between the anode and the cathode. By doing so, electrons are accelerated from the cathode

towards the anode and along the path they ionize the surrounding gas. Due to the magnetic field the electrons travel in a spiral trajectory which extends the electron path and increases the ionisation probability. Those ions are collected and an ion current which is proportional to the density of the molecules (pressure) can be measured. The lowest pressure reading is around 10^{-10} torr. The advantage of this type of gauge is that it does not need a filament and no heating occurs, but in order to achieve very low-pressure readings a strong magnet is required.

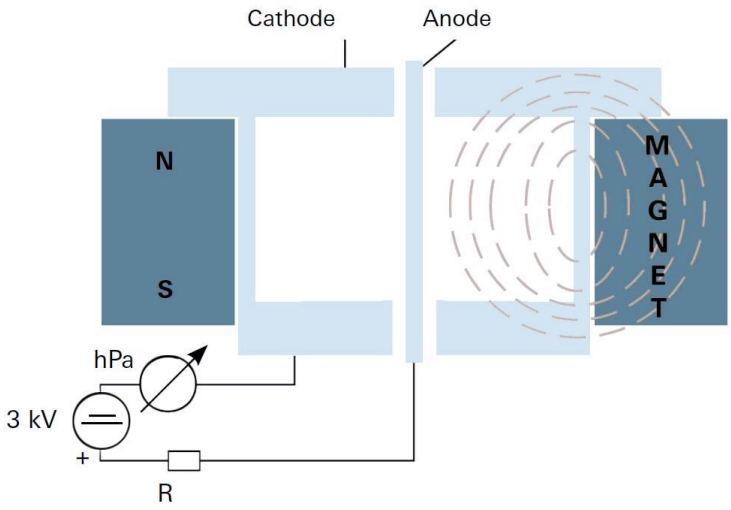

Figure 2.5: Schematic Diagram of inverted magnetron gauge and its components. Picture provided by Pfeiffer vacuum.

The B-A gauge operates between pressures of 10^{-3} and 10^{-11} torr.[8] The basic principle behind the B-A gauge relies on a heated filament (cathode) that emits electrons (Figure 2.6). Those electrons are accelerated towards a positively charged grid (anode). Upon collision of these electrons with the molecules inside of the grid, ions are generated and are collected by the ion collector. The ion collector is at nearly ground potential, which is negative with respect to the grid. The rate at which these positive ions are collected is directly proportional to the density of molecules (below 10^{-3} torr). Hence, the ion current is calibrated to give a reading in pressure units.

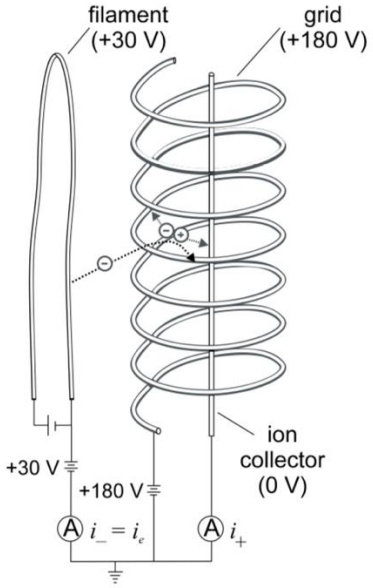

Figure 2.6: Schematic Diagram of a Bayard-Alpert ion gauge and its operation. Picture provided by Granville Phillips.

2.4 Sample holder, Heating and cooling

2.4.1 Main UHV chamber

2.4.1.1 Sample holder

The sample holder or commonly called the "puck", is specially designed by RHK to hold the sample and make it easier to transfer from one chamber to another. The puck consists of two parts, a grooved copper base and a titanium nitride coated molybdenum top that are held together by screws (Figure 2.7). The copper base has two grooves, the top one is used to grab the puck to be able to transfer it and the bottom groove is used to slide inside the sample stage clips to hold the puck on the main manipulator. The coated top part has a hollow well into which the sample can be placed, three molybdenum leaf clips to hold the sample in place, two holes on two different sides to hold the thermocouple and to provide grounding possibilities, and three ramps on its surface to allow the landing of the STM probe legs. The uniform coating provides chemical, mechanical and thermal stability, and also provides smoothness to allow the STM probe legs to slide down the ramp without friction during the tip approach process.

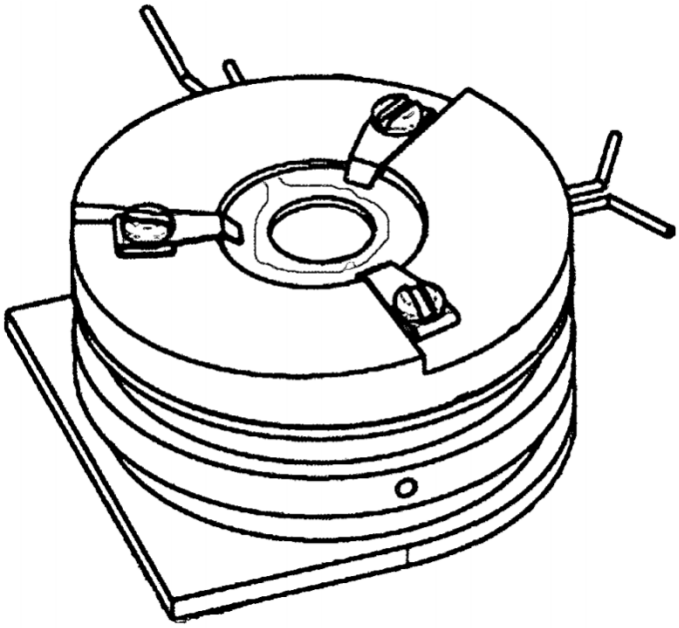

Figure 2.7: A Schematic of the sample holder "Puck". Picture provided by RHK.

2.4.1.2 Sample mounting

The sample mounting, starting from the bottom to the top consist of a sapphire washer, K-type thermocouple, Pt sample and a sapphire washer. Molybdenum clips apply the same pressure on the sapphire washer to maintain the sample relatively flat and in place, and to provide a better contact for heat exchange during the cooling process.

The 8 mm diameter and 0.5 mm thick Platinum single crystal sample with purity of 99.999% was purchased from Princeton scientific. The platinum sample has one polished side with a roughness below 0.03 micron and a (111) orientation with an accuracy below 0.1 degree.

The sapphire washers that are used have an inner and outer diameter of 6 and 10 mm respectively. They fit perfectly inside the well. Two advantages can be associated with the use of sapphire. The first one is the cooling, sapphire is an excellent thermal conductor at low temperatures and poor thermal conductor at high temperatures. During the cooling process, sapphire helps to cool down the sample faster and during the heating process the sapphire slows down the heat transfer to the puck and main manipulator. The second advantage is electrical insulation, sapphire is a poor electrical conductor and this helps to electrically isolate the sample

from the puck during the heating process so that current passes only through the Pt sample and does not resistively heat up the entire puck assembly.

The thermocouple that is used to measure the temperature of the sample is a K-type thermocouple. A K-type thermocouple is made of two types of metal alloys: chromel (90% nickel and10% chromium) and alumel (95% nickel, 2% manganese, 2% aluminium and 1% silicon). The advantage of using to use this type of thermocouple is that it provides a wide range of temperature readings from 3 K up to 1533 K with accuracy of ± 2.2 K from 172 to 566 K and ± 0.75% T from 566 to 1533 K.[9] The temperature reading is achieved by measuring the potential voltage at the junction. When there is a change of temperature at the junction, a measurable current flows through the circuit (Seebeck effect) and a voltage can be measured. The measured voltage potential is proportional to the temperature. The thermocouple that is used is handmade and consists of spot-welding alumel and chromel in a shape of a loop that has 6-7 mm diameter and a wire thickness of 0.005" (Figure 2.7). Each side of the open loop are again spot-welded to its respective alumel and chromel pins of 0.02". Grooved ceramic pieces are used to hold the thermocouple pins and isolate them from the puck.

2.4.1.3 Heating and cooling

Once the sample is mounted properly, the sample holder can be transferred on the sample stage where heating and cooling can be performed (Figure 2.8). The heating is performed by a retractable filament heater. The filament is hand made in the laboratory and it is made with a 0.005" tungsten wire that has a 3N8 (99.98%) purity. The filament consists of 11 loops of 1.5 mm diameter and is shielded by a ceramic tube. The choice of tungsten is due to its high melting point, low vapor pressure, high resistance to chemicals and above all its good thermionic emission. The basic principle behind the heating consists on applying a negative voltage on the filament with respect to the sample. By increasing the current, the filament heats up and starts emitting electrons. Due to the generated electric field those electrons are accelerated toward the sample and upon collision their kinetic energy is transferred to the sample. This heating method is called electron bombardment heating.

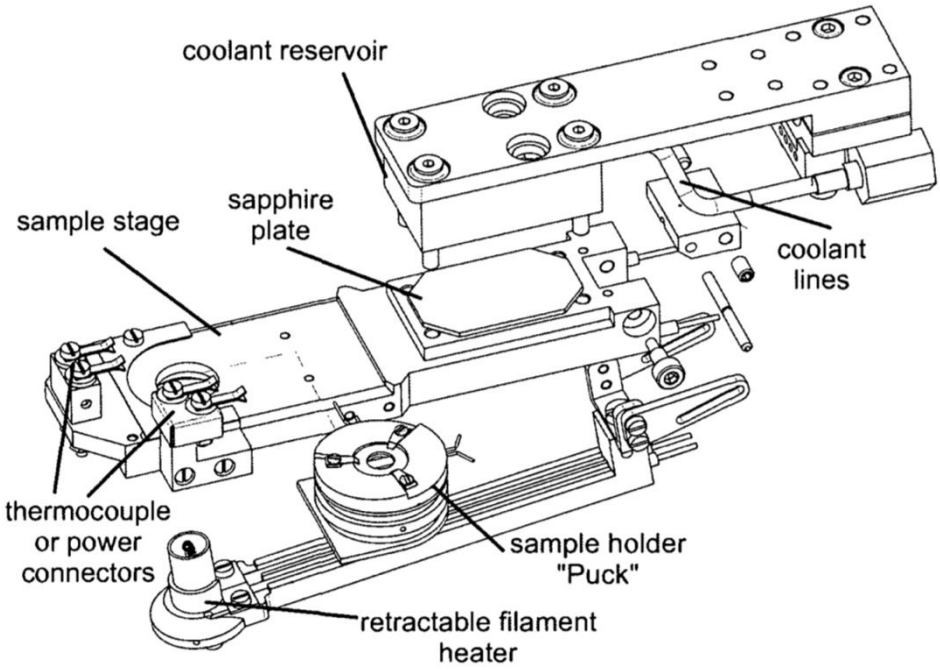

Figure 2.8: A Schematic of the sample stage connected to the coolant reservoir and the filament heater. Once the sample holder slides in placed on the sample stage the thermocouple pins slides in the thermocouple clips to be able to read the temperature. Picture provided by RHK.

The cooling is performed by flowing liquid nitrogen through the main manipulator coolant lines into a reservoir (Figure 2.8). The reservoir is made of copper and is separated from the sample stage by a sapphire plate. Sapphire is again used to ensure a good thermal conductivity and to maintain an electrical insulation. The cooling of the sample is performed indirectly. First, the heat is exchanged between the liquid nitrogen and the copper reservoir, then between the reservoir the sample stage and finally between sample stage and the sample holder. All these steps create a gradient in temperature due to the mismatch between the different components. The typical liquid nitrogen temperature is 77 K, the lowest temperature measured on the sample stage is 90 K and on the sample is 110 K.

The liquid nitrogen is carried from a dewer to the manipulator by a laboratory designed coolant tube (Figure 2.9). The tube consists of a counter current shell and tube heat exchanger using an inner tube of 1/8" tubing and an outer shell tube of 1/4". The design of the coolant tube and its insulator sleeve cover ensures the minimization of heat loss to the surrounding environment.

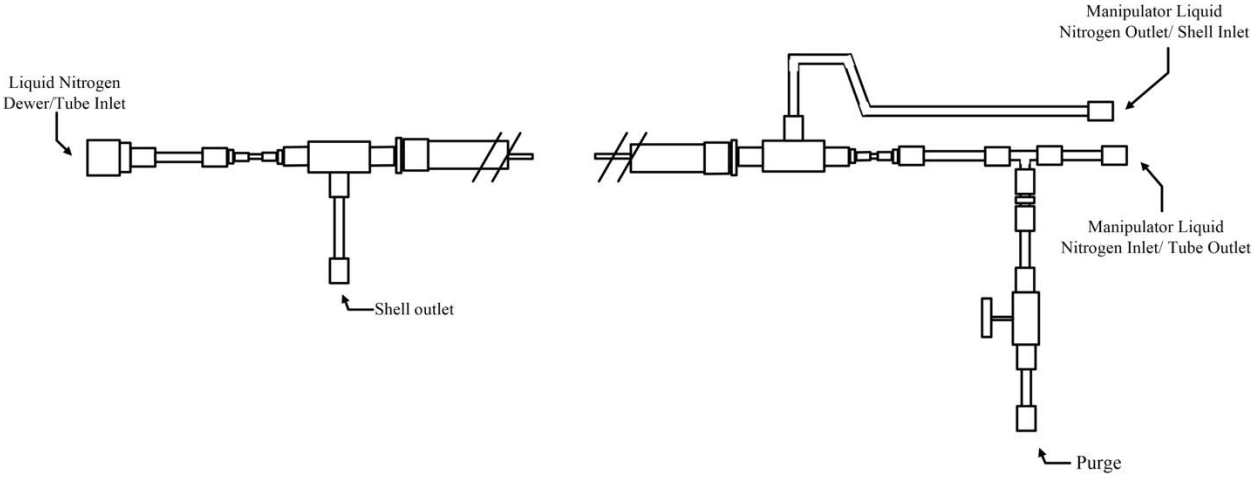

Figure 2.9: A Schematic of the cooling lines showing the inlet and outlet of the liquid nitrogen.[10]

The temperature range that can be measured on the sample strongly depends on a number of factors including the sample mounting, cooling power of the arm and the elemental composition, thickness and number of loops of the filament. With the design described above, the maximum heating temperature that can be reached is 1200 K (while cooling the manipulator) and the limiting factor in this case is the low melting point of surrounding material. For the cooling, the lowest temperature that can be reached is 110 K and it takes about 45 min to an hour. Procedure and information about the heating and cooling methods can be found in Appendix B.

2.4.2 RAIRS UHV chamber

Setting up a new characterization technique adds value to the published papers as it provides further insights of the studied phenomena. In this case, the reference is made to the set-up of the reflection adsorption infrared spectroscopy (RAIRS) technique. Although the setup will seem to be simple, you need to take my word for it, that it is extremely challenging as it requires a meticulous planning and patience, but I must admit that it is quite exciting at the same time. There are several design constraints and restrictions that must be considered. The trial of different designs and materials is often a necessity to be able to achieve the desired functions. In the next paragraphs, I will only focus on the final and properly working design and explain step by step the choices that were made.

The restrictions and the functionalities of the RAIRS chamber need to be equivalent to the main chamber to have the same experimental condition for the sake of consistency. The design of the RAIRS chamber needs to take into account these following functionalities:

- The sample temperature needs to be able to reach 1100 K in order to clean the sample
- The cooling needs to reach 110-130 K to be able to absorb the molecules on top of the Platinum surface and allow heating to high temperature
- The shape of the sample holder needs to allow the reflection of the IR beam from the sample by passing through the 2.75 inches Potassium Bromide (KBr) windows.
- The material used need to be compatible with UHV systems (low vapor pressure and heat resistant)
- The optical path needs to be purged in dry air or nitrogen.

2.4.2.1 Sample holder Design and mounting

The self-designed sample holder consists of a "Z" shape molybdenum plate with of 0.02" thickness and 99.95% purity (Figure 2.10 and Figure 2.12). The choice of the "Z" shape is mainly to allow an incidence angle between 2 and 10° on the sample due to geometry limitation of the chamber. The choice of molybdenum is due to its high melting point, low thermal expansion, low vapor pressure, hardness and high resistance to corrosive chemicals. The dimensions of the sample holder have been minimized to ensure an efficient and fast heat transfer (Figure 2.11). The sample positioning is brought as close as possible from the reservoir to be able to achieve the lowest temperature possible due to the temperature gradient.

The sample mounting is the same setup used in the main chamber. Starting from the bottom to the top consists of a sapphire washer, Pt sample, K-type thermocouple and sapphire bits. Molybdenum clips are used to press the sapphire bits hold the sample in place and to provide a better contact for heat exchange during the cooling process. The sapphire washer has an inner and outer diameter of 6 and 10 mm respectively. The K-type thermocouple wires have a 0.05" diameter thickness and their junction is sandwiched between the sapphire bit and the sample by the clip on the right. The shape of the thermocouple consists of two parallel alumel and chromel wires that are spot-welded at one end. The whole wires are covered with insulating ceramic tubes to avoid

any physical contact with manipulator or the sample holder. These measures ensure that the sample is electrically insulated from the sample holder. The choice of the materials is for the same reasons stated in section 1.5.1.2.

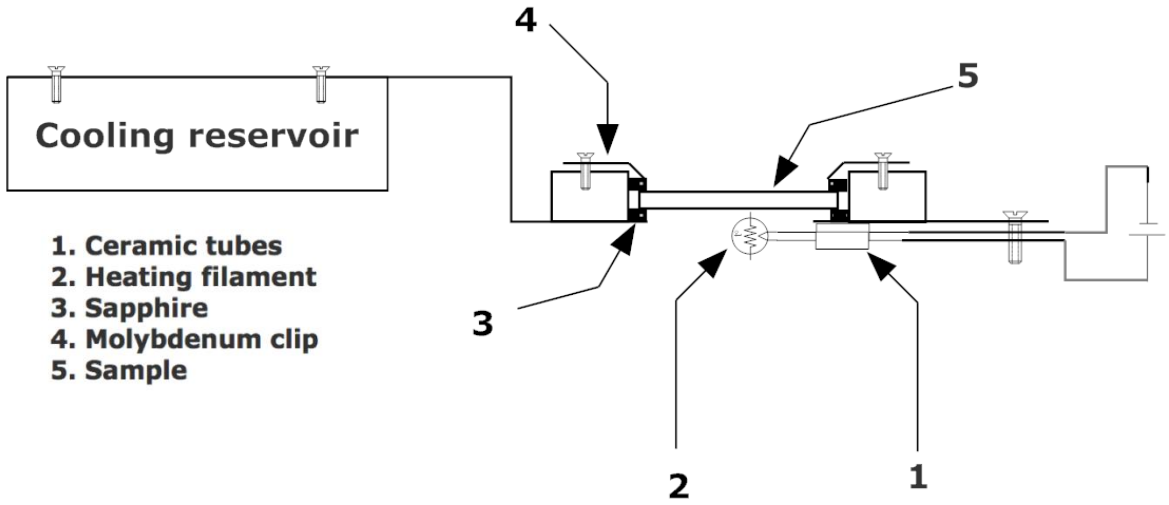

Figure 2.10: A side view diagram of the RAIRS sample holder with a properly mounted sample.

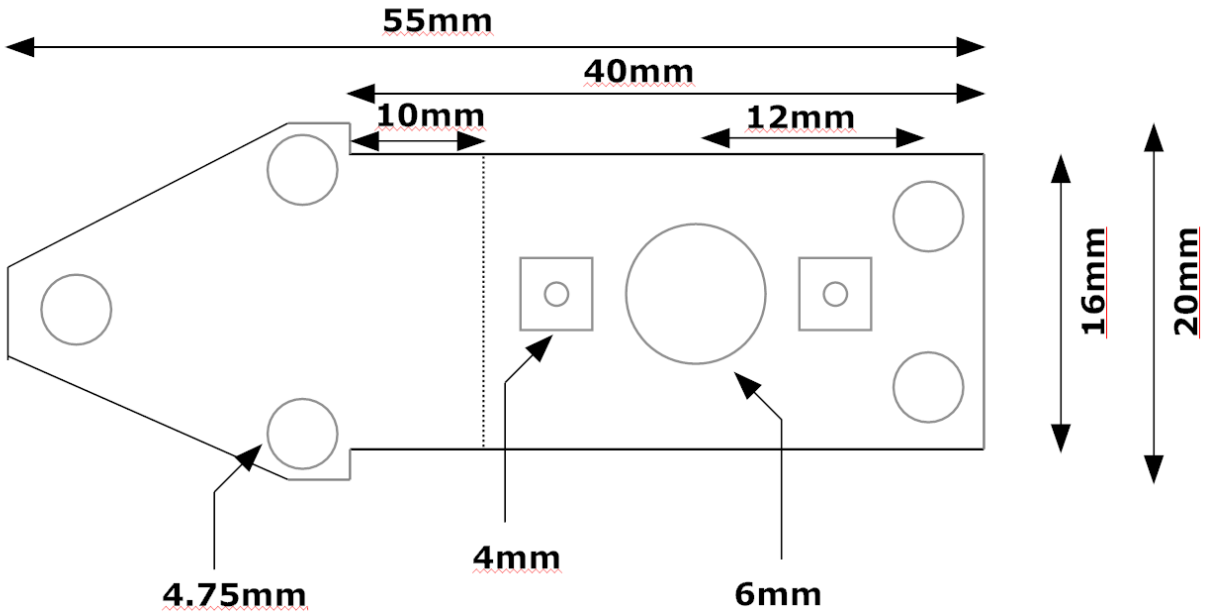

Figure 2.11: A top view diagram of the RAIRS sample holder with its proper dimensions.

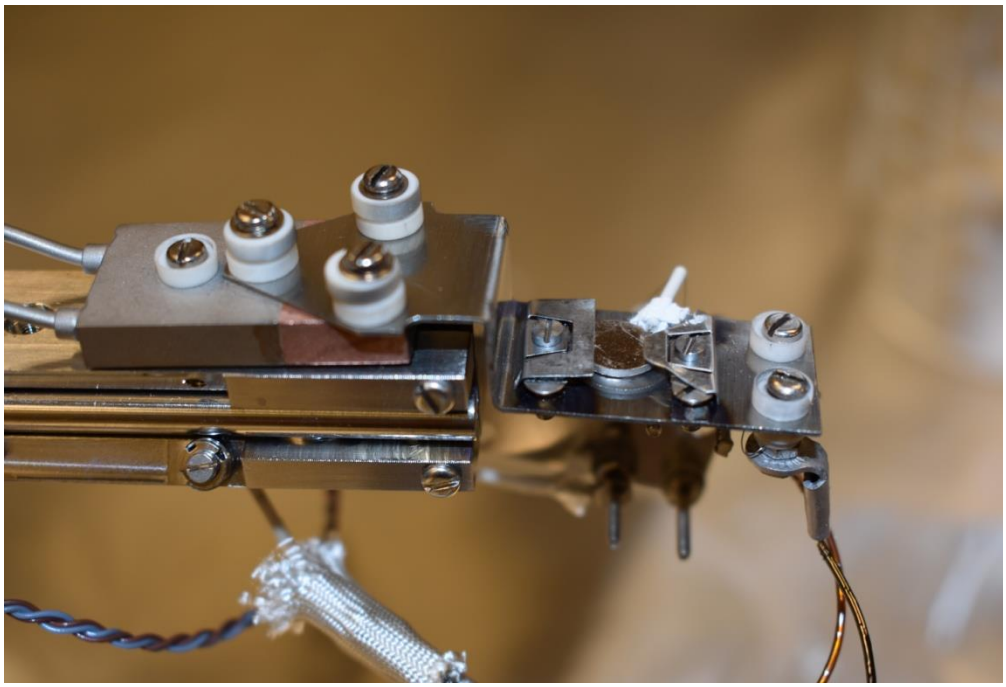

Figure 2.12: Photography of the RAIRS sample holder.

2.4.2.2 Heating and cooling

The heating is performed by a fixed filament that is attached on the back of the sample holder by two ceramic tubes of 0.005" inner diameter (Figure 2.10). The ceramic tubes themselves are held in place by using an alumina ceramic paste. The filament is made with a 0.005" tungsten wire that has a 3N8 (99.98%) purity and consists of 11 loops of 1.5 mm diameter. The heating can be performed by either putting a positive voltage on the sample with respect to the filament or by putting a negative voltage on the filament with respect to the sample.

The cooling is performed by flowing liquid nitrogen through a coolant coil into a reservoir (Figure 2.13). The cooling lines are wrapped around the main manipulator without any physical contact. The reservoir is made of copper and is separated from main manipulator by a sapphire disk. Sapphire in this case is used as an electrical insulator. The sample holder itself is sitting on top of the reservoir to have a direct heat exchange and optimize the cooling power.

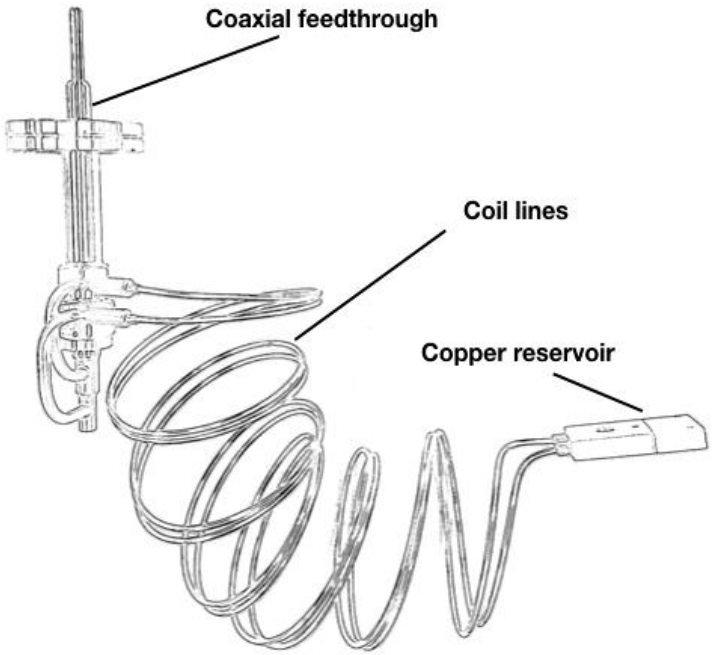

Figure 2.13: A side view diagram of the cooling lines and the attached reservoir.

The temperature range that can be measured on the sample strongly depends on a number of factors including the sample mounting, size of the reservoir and the coolant lines, shape and thickness of the sample holder, and the thickness and number of loops of the filament. With the design described above, the maximum heating temperature that was reached is 1200 K, the heating can go at much higher temperature as the surrounding materials have a high melting point. For the cooling, the lowest temperature that can be reached is 125 K in less than 30 min.

Further details on the resistance readings, the operation steps and how to mount the ceramics on the back of the sample can be found in Appendix B.

2.5 Sample cleaning

Surfaces are continually exposed to gases in the UHV and will eventually become covered with a layer of atoms or molecules. Cleaning the surface is mandatory if we want to perform experimental studies without worrying about the interference of the contaminants. A surface is considered "clean" if the surface contaminants is below 1% of the monolayer which is actually the detection limit of the current surface science techniques.[1,3] Also, a contamination below 1% is considered unlikely to affect the experimental results.[11]

The surface cleaning is performed by ion sputtering and high-temperature treatments.[12] Ion sputtering is an efficient way to clean the surface by physically removing layers from the surface. It consists of generating ions and accelerating them towards the surface. Upon collision on the surface, ions transfer their kinetic energy to the surface which causes chemical bond cleavage of the surface species, and ejection of atoms and molecules from the surface. The ion sputtering gun is an IQE 11-A model and is provided by specs. The sputtering gun can go up to a 3 KeV kinetic energy and uses argon with a 99.999% purity as a gas source to generate a collimated ion beam. The argon gas is directly fed into the ionization chamber through a leak valve in order to minimize the pressure increase and the typical operating pressure is between 10^{-6} and 10^{-5} mbar. Preferential atomic removal may occur during sputtering which results in a distorted surface that contains vacancies, kinks and adatoms.[1,13] Annealing to high temperature provides enough energy to allow enough mobility to the atoms at the sample surface in order to obtain flat terraces and reach an optimal orientation. In addition, annealing to high temperatures will also help to desorb the unwanted molecules from the surface.

The major and common impurities that can be observed on the platinum surface are carbon, calcium, phosphorus, oxygen, silicon, chlorine and sulfur.[11] For the Pt(111) single crystal used in this thesis, the only observed impurities are carbon and oxygen. Cleaning the surface for the first time requires several argon-ions (1.5 keV, 1 x 10^{-5} mbar Ar^{+}) sputtering cycles for 30 min without annealing, otherwise the existing impurities generated during the fabrication process can form dislocations and ruin the surface. Later on, it is followed by another argon sputtering cycle but this time at a temperature of 600 K for 30 min. This followed by annealing to 1100 K for 2 minutes, then heating in oxygen at a pressure of 1 x 10^{-7} mbar and at a temperature of 900 K for 2 minutes. During the annealing process the carbon diffuses from the bulk to the surface and an oxygen treatment is recommended to remove the excess carbon that eventually desorbs as CO and CO_2. The surface cleanness is verified by XPS and LEED. It takes several days with repetitive cleaning cycles to clean the platinum surface for the first time (Figures C1and C2).

The subsequent recleaning can be achieved with less time and only the ion bombardment and high temperature treatment are required. The Pt (111) crystal surface is usually recleaned by repetitive cycles of 15 min of argon-ion sputtering at a pressure of 1 x 10^{-5} mbar and with an energy of 1.5 keV at 600 K, followed by annealing to 1100 K for 2 minutes. Generally, it takes 3 cycles to clean the surface.

Further information on how to operate the equipment and a typical cleaning procedure can be found in Appendix C.

2.6 X-ray photoelectron spectroscopy

2.6.1 Basic principle

X-ray photoelectron spectroscopy is a powerful technique for surface chemical analysis. It provides important information about the elemental surface composition, the oxidation state of these elements and the relative abundance of the atom species at the surface.[14–17] The technique was developed in the 1940-1950's by Kai Siegbahn and coworkers which led him to win the Nobel prize in physics in 1981. The Basic principle behind the XPS relies on the photoelectric effect. It consists of irradiating the specimen with X-rays (Figure 2.14). The X-ray photon interacts with a core level electron by transferring its energy to the core electron which is ejected from the atom with a certain kinetic energy (E_k). The kinetic energy of this electron can be measured by an electron analyzer. Hence, the binding energy (E_b) of the photoelectron can be determined by the following equation :

$$E_b = h\nu - E_k - \varphi \tag{2.6}$$

Where $h\nu$ is the energy of the incident photon and it is well known because it is specific to the radiation source, and φ is the work function of the material.

The binding energy of the photoelectrons is an intrinsic material property which leads to chemical identification of the elemental surface composition. Moreover, the shift in the binding energy is related to a change in the chemical environment. For example, the binding energy of the electrons from the 1s orbital of elemental carbon is 284.8 eV and is shifted by 4.2 eV with respect to the 289 eV of the carbon monoxide. The shifts of the core electrons binding energy are mainly caused by the charge redistribution of valence electrons, thus providing information about the valence state.

The simplest method to determine the relative abundance of the atomic species is by comparing the peak area of the species of interest to the peak areas of the all the other elements present in the sample. The assumption in this method is that the number of recorded photoelectrons is proportional to the number of atoms on the surface. Thus, the concentration of the atomic

species, i, (C_i) can be determined by the following equation:

$$C_i = \frac{I_i / S_i}{\sum_{j=1}^{n} I_j / S_j} \tag{2.7}$$

Where I is the integrated area of the photoelectron peak and S is the relative sensitivity factor (RSF). The RSF values are experimentally determined and are usually implemented in the analysis software tools.

The intensity or integrated peak area of the photoelectron peaks can be described by the following equation,

$$I = n_x \sigma \lambda J \vartheta y \chi O \tag{2.8}$$

Where σ is the photoelectric cross section of the element, λ is electron mean free path in the sample, J is the photon flux, ϑ is the photoelectron emission angle, y is the relative excitation probability, O is the sample area from which photoelectrons are detected, n_x is the atomic concentration of the element and χ is the instrument constant (transmission function of the analyzer and detector efficiency).

It is to be noted that due to the mean free path of the outgoing photoelectron is few nanometers (between 3-10 nm for Al X-ray source), which makes the XPS very sensitive only to surface species.

2.6.2 XPS components

The XPS used in the laboratory is made by SPECS and its major components consist of an X-ray source, electron energy analyser, focusing lenses and the electron detector (Figure 2.15).

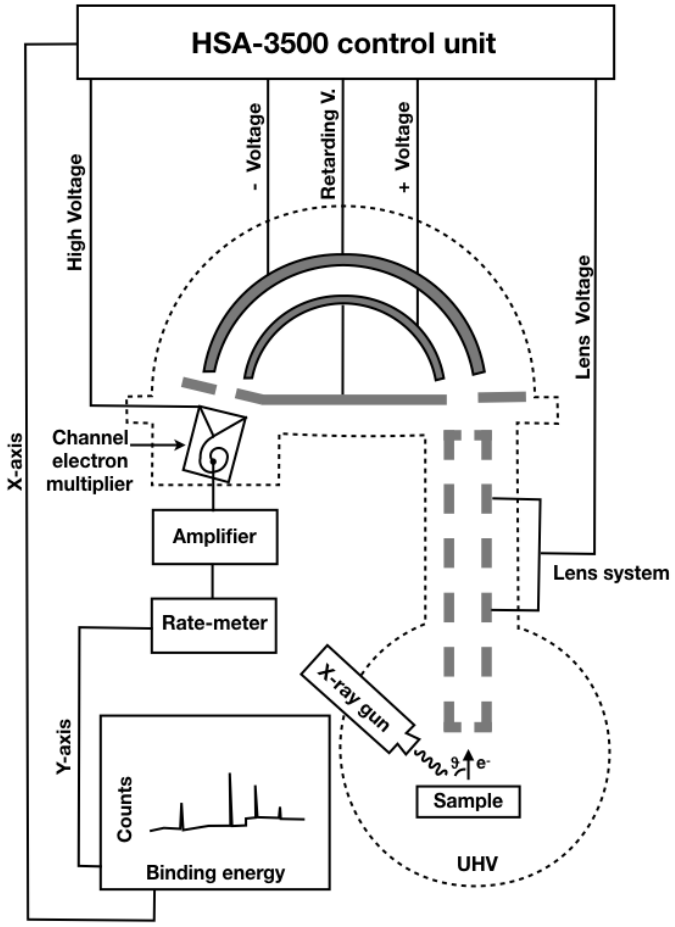

Figure 2.14: Schematic Diagram of the X-ray photoelectron spectrometer with all its principle components.

2.6.2.1 X-ray source

The choice of an anode is very important when it comes to performing the experiment, the quality of the results mainly depends on the following factors : X-ray energy and linewidth. The X-rays emitted from the anode need to have high enough energy to generate the photoelectrons in the region of interest, the linewidth should not be too large otherwise it broadens the peaks. The use of a monochromated source can improve the resolution.

Our X-ray source is non-monochromatic and is equipped with a twin anode configuration allowing the choice of generated X-ray from aluminium (Al) or magnesium (Mg) (Figure 2.15). The energies of the K_α emitted X-rays are 1486.6 eV for the Al with a full width at half-maximum (fwhm) of 0.85 eV and 1253.6 eV for the Mg with a fwhm of 0.7 eV.[1]

The basic principle behind the X-ray source consists of passing a high current through

tungsten filament which will eventually emit electrons. These electrons are accelerated towards a high voltage positively biased anode (with respect to the filament). Upon collision with the anode, core electrons can be exited and emits photons (X-rays) when they go back the ground state. The anode is water-cooled to dissipate the heat generated by the electron bombardment. A thin Al window and shielding covers the source. The Al window allows the transmission of the X-ray but cuts off the stray electrons and minimize Bremsstrahlung, and the shielding is necessary to avoid sample contamination from the filament.

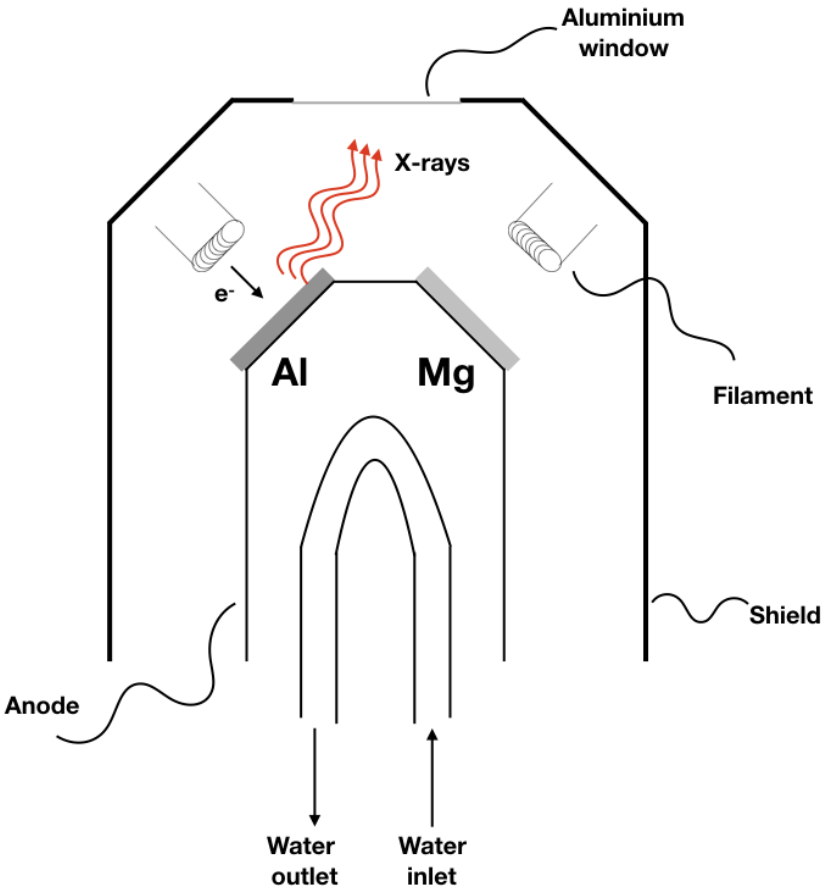

Figure 2.15: Cross section Diagram of a twin anode X-ray source.

2.6.2.2 Energy Analyzer and lens system

Once photoelectrons are ejected from the sample, they travel through a lens system that is positioned at an optimum distance of 40 mm on top of the sample. The lens system is a set of 10 electrostatic lenses and was designed to yield ultimate transmission by focusing the electron beam

into the entrance slit of the hemispherical energy electron analyzer (HSA) (Figure 2.14).[18] The lens system allows several acquisition modes to define the analysis area and angular acceptance in order to optimize the results depending on the application. all the lenses are controlled electronically. The lens system is also equipped with an iris that can be manually controlled and by closing it the photoelectrons from the surroundings can be eliminated.

The HSA PHOIBOS 100 is used to disperse the photoelectrons. It consists of two 180° concentric hemispheres that are mounted on a common center with a mean radius of 100 mm. An entrance slit connected to the lenses systems and an exit slit connected to the detector are equally distant from the centre. A negative potential voltage is applied on the outer hemisphere and a positive potential voltage is applied on the inner hemisphere to generate an inverse squared ($1/R^2$) electrostatic field in the region in-between. For a fixed electrical field gradient, only electrons with the right kinetic energy can make it from the entrance slit to the exit slit . Electrons arriving with very high kinetic energies are deflected on the negatively biased hemisphere and the electrons arriving with low kinetic energies are deflected on the positively biased hemisphere. The energy necessary to allow the electron to pass through the energy analyzer and make it to the detector is called the pass energy (E_{pass}) and it can be defined by the following equation :

$$E_{pass} = (-Q)K\Delta V \tag{2.9}$$

Where ΔV is the potential difference applied to the hemisphere, Q is the charge of the electron and K is the calibration constant related to the geometry of the analyzer.

2.6.2.3 Electron Detector

The electron detector type used is a single channel electron multiplier and commonly called channeltron. The channeltron consists of a square-shaped glass box that is shaped inside as a funnel connected to a small curved glass tube (Figure 2.15). The inner walls are coated with a high resistance material and when a potential is applied at the ends of the tube, the coating becomes a continuous dynode. The collision of the photoelectron with the dynodes results in the emission of secondary electrons. These electrons are accelerated by the high voltage connected to the chaneltron which results in further collision with the dynode along the glass tube. These successive

collisions result in a cascade of electrons (pulse). At the end of the glass tube, the electrons are intercepted by the collector electrode and are counted in the preamplifier channel. On average for one incident electron, about 10^8 electrons make it to the collector.

2.6.2.4 Operational mode

The XPS spectrum is typically plotted as electron counts or electron counts per second (CPS) versus binding energy or kinetic energy. We operated the system in a fixed analyzer transmission (FAT) mode. It consists of setting a constant voltage on the analyzer such that the pass energy of the analyzer is held at a constant value. The electrostatic lens system will be responsible to retard or accelerate the given kinetic energy of the electrons to the range accepted by the analyzer, and by doing so the lens voltage is recorded and converted to the appropriate electron kinetic energy (x axis). The advantage of using this mode is to allow the acquisition of the spectra with a constant resolution.

The spectral resolution (ΔE_{res}) observed in the XPS spectra depends on three major factors: the analyzer resolution (ΔE_{an}), the inherent linewidth of the of the atomic level (ΔE_{level}) (e.g. O 1s, C 1s), and the natural linewidth of the incident photon radiation ΔE_{photon}. The spectral resolution equation is given by the convolution of these three factors

$$\Delta E_{res} = \sqrt{\Delta E_{an}^2 + \Delta E_{level}^2 + \Delta E_{photon}^2} \tag{2.10}$$

The analyzer resolution depends mainly on geometrical factors and can be described by the following equation

$$\frac{\Delta E_{an}}{E_{pass}} = \frac{\mathrm{S}}{2\mathrm{R}_0} + \frac{\alpha^2}{4} \tag{2.11}$$

Where S is the mean slits width, R_0 is the mean radius of the hemisphere and α is the half angle of the dispersion direction. Maintaining the pass energy constant results in a constant analyzer resolution.

Besides the physical parameters we also have the software parameters that can be tuned

such as the dwell time, energy step and number of scans to improve the quality of the collected spectrum. The dwell time is the time spent per energy step acquiring the intensity. The higher the dwell time the higher intensity that can be obtained. The energy steps play an important role especially in resolution as you obtain a smooth continuum spectrum; the lower energy step the better. The increase of the number of scans increases the S/N ratio by a factor of $\sqrt{n}$, where n is the number of scans. To double the S/N ratio 4 scans are necessary, but to triple the S/N ratio it requires 9 scans. The paid price for all these improvements is time. Optimizing these parameters to improve the quality of the spectrum often means that more time needs be spent for spectrum acquisition. A summary of the parameters that were used in this thesis can be found in Table 2.1 and guidelines on how to operate the XPS step by step can be found in Appendix D.

Table 2.1: Acquisition parameters set for the acquisition of XPS spectra.

Physical Parameters				
Source			Aluminium	
Voltage (eV)			1462.8	
Anode Current (mA)			26.5	
Filament Current (A)			2.23	
Operation Mode			Fixed Analyzer Transmission	
Lens Mode			Small Area	
Iris (mm)			28	
Entrance Slit (mm)			7 x 20	
Pass Energy (eV)			30-75	
Software Parameters				
	Survey	**C1s**	**O1s**	**Pt(4f)**
Dwell Time	0.2	1	1	0.5
Energy Step	0.5	0.05	0.05	0.1
Pass Energy (eV)	75	30	30	30
Scans	1	6	6	1

2.7 Low Energy Electron Diffraction

2.7.1 Basic principle

Low energy electron diffraction is a technique for surface structure determination. It is generally used to determine the surface structure of clean and adsorbate covered crystal surfaces.[3,19–22] The basic principle of the LEED relies on Bragg's diffraction. It consists of bombarding the sample with a collimated electron beam (Figure 2.16). The incident electrons behave like a wave and upon collision with atoms they can undergo elastic collision and are scattered from the lattice planes. These back-scattered electrons interfere constructively and are observed as bright spots on the fluorescent screen forming a diffraction pattern.

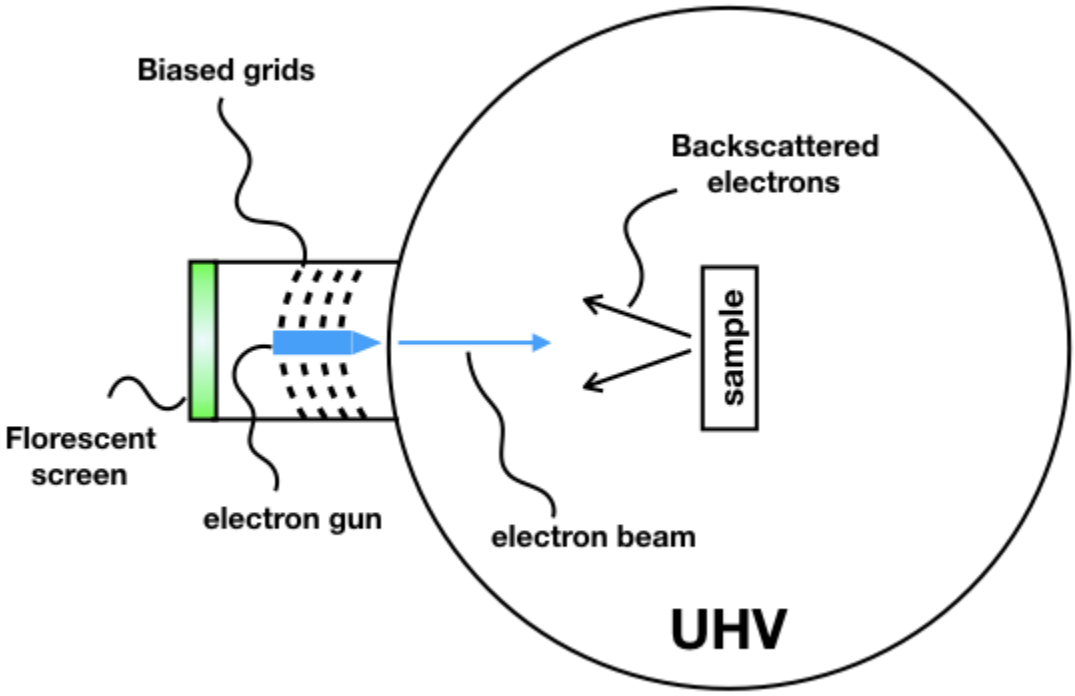

Figure 2.16: Side view diagram of the Low Energy Electron Diffraction technique.

The inelastic mean free path of the electrons in a solid depends strongly on the incident energy of the electrons. For this reason, the incident electrons energy should be between 10 and 400 eV where the inelastic mean free path is ~ 2-4 layers (Figure 2.17). This will allow the incident electrons to penetrate only the few first layers before undergoing inelastic collisions, thus making the LEED a very sensitive surface technique.

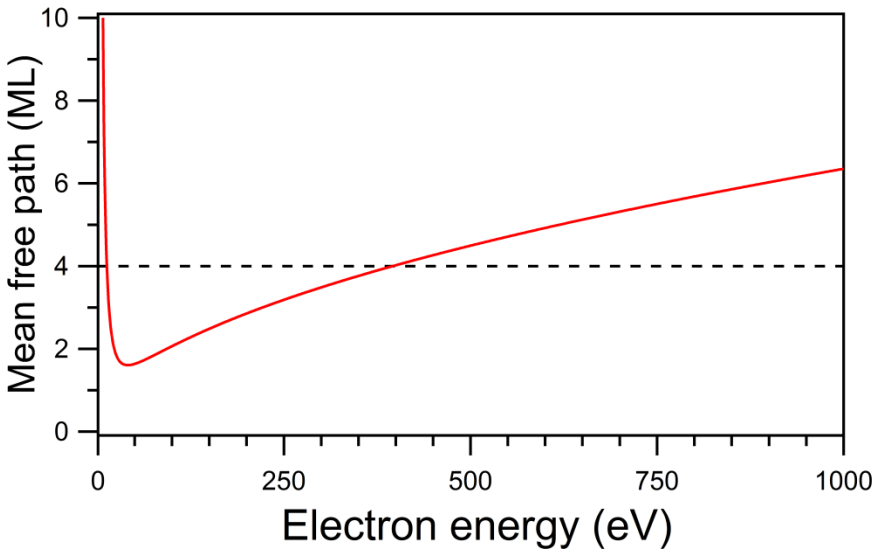

Figure 2.17: Electron mean free path in platinum(111) Where the mean free path distance is expressed in number of platinum layers. Spectrum was generated by using the mean free path equation provided by Seah.[23]

The information that can be extracted on the LEED pattern relies on the position and the intensity of the diffraction spots. From the position of the spots, the surface, size and shape of the reciprocal lattice the unit cell can be determined; hence, its corresponding unit cell of the real space can also be obtained. Furthermore, the symmetry, the number and sharpness of the spots can provide information about the presence of adsorbates and their preferential orientation compared to the substrate. From the intensities of the diffraction spots, the exact atomic coordinates can be obtained. The spot intensities are recorded as function of the incident kinetic energy of the electron to generate the I-V curves and additional computer modelling is necessary.[19]

In this work, LEED was only used as a standard method for the characterization of the surface quality in order verify the cleanliness of the Pt(111) surface prior to performing the other experimental techniques. Qualitatively, sharp spots were associated with a well ordered surface ready for usage. A LEED image of the clean Pt(111) surface is show in the cleaning process section in appendix C. Guidelines on how to operate the LEED step by step can be found in Annex D.

2.7.2 LEED components

The LEED used in the laboratory is made by SPECS and its major components consist of an electron gun, grids and a fluorescent screen.

The electron gun consists of a cathode, a Wehnelt cylinder, a double anode, an electrostatics single lens and a drift tube. The used filament is made of iridium (Ir). The advantage of using Ir is that it emits electrons at much lower temperatures and is more resistant than tungsten. The anode is positively biased with respect to the cathode. So once electrons are emitted, they are accelerated by the anode towards the elements of the electrostatic single lens which has the responsibility to focus and shape the electron beam. The Wehnelt cylinder surrounds the cathode and acts as an electrostatic aperture by narrowing the electron beam. It generally has a control over the sharpness of the diffractions spots.

The hemispherical grids are made of molybdenum and are gold coated. The grids act as suppressors. By applying a negative voltage to them, the reflected inelastic and secondary electrons from the sample can be blocked allowing only the elastically scattered electrons to go through.

The fluorescent screen is placed after the grids and a positive high voltage between 5 and 7 kV is applied to it. Once the elastically scattered electrons make it through the grids they are accelerated towards the fluorescent screen and upon collision a diffraction spot appears.

Table 2.2: Initial Parameters used for the LEED prior the incidence of the electron.

Parameters	
Filament Current (A)	2.4
Energy (eV)	0
Wehnelt Voltage	-7
Anode Voltage	359
Lens 1/3 Voltage	5
Lens 2 Voltage	85
Suppressor Voltage	0

2.8 Temperature programmed desorption

2.8.1 Basic principle

Temperature programmed desorption is a powerful technique that probes surface kinetics of the gas phase molecules with surfaces.[24–26] It provides important information about the adsorption/desorption energies and the mechanism of catalytic reactions of molecules on the surface.[24] The technique consists of dosing molecules on top of a sample and approaching it towards a mass spectrometer (Figure 2.18). By gradually increasing the temperature as a function of time, the adsorbed parent molecules can either molecularly desorb from the surface or decompose into byproducts that can also desorb from the surface. The mass spectrometer monitors the pressure of the desorbed species from the surface as a function of time. Hence, the temperatures of desorption of the parent molecule and byproducts can be determined, providing information about the adsorbed state of the molecule (chemisorbed or physisorbed). The order of desorption of the species gives information about the reaction pathways.

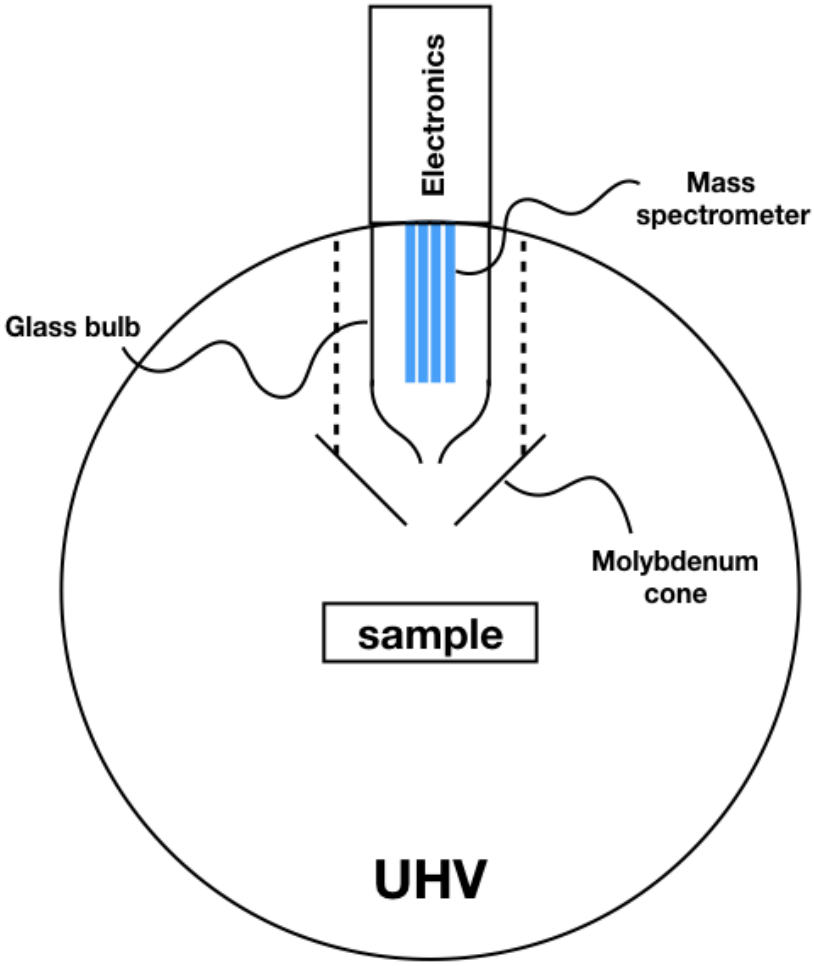

Figure 2.18: Side view diagram of the Temperature programmed technique

The experiments are monitored by a computer that records the pressure (rate of desorption) and temperatures as a function of time. The time between the two sets of data can be correlated with a designed macro and a spectrum of pressures as a function of temperature can finally be obtained. The determination of the energetic barriers is performed by applying the redhead analysis which mainly depends on the heating rate (β) and the desorption rate (r).[27]

The temperature of the sample (T) is linearly increased as a function of time (t) and can be determined by the following equation:

$$T = T_0 + \beta t \tag{2.12}$$

Where T_0 is the initial temperature of the sample.

Equation (2.12) can be rewritten as

$$\beta = \frac{\partial T}{\partial t} \tag{2.13}$$

The desorption rate is the rate of change in the coverage (θ) as a function of time and can be described by the following equation :

$$r = -\frac{\partial \theta}{\partial t} = k\theta^n \tag{2.14}$$

Where k is the desorption rate constant and n is the order of desorption.

The rate of change in the coverage as a function of temperature can be obtained by dividing equation (2.14) by (2.13)

$$-\frac{\partial \theta}{\partial T} = \frac{k\theta^n}{\beta} \tag{2.15}$$

The rate constant for desorption obeys Arrhenius equation

$$k = A * \exp\left(\frac{-E_{des}}{RT}\right) \tag{2.16}$$

Where E_{des} is the desorption energy and R is the gas constant. Replacing k in the equation (2.15) leads us to the so-called Polanyi-Wigner equation

$$-\frac{\partial \theta}{\partial T} = \frac{A\theta^n}{\beta} \exp\left(\frac{-E_{des}}{RT}\right) \tag{2.17}$$

The maximum intensity of the desorption peak of the molecules occurs at the maximum temperature (T_{max})

$$\left.\frac{\partial^2\theta}{\partial T^2}\right|_{T_{max}} = 0 \tag{2.18}$$

Assuming that A and E_{des} are independent of coverage and by substitution of equation (2.17) in equation (2.18), the Redhead equation can be obtained.

$$\frac{E_{des}}{RT_{max}^2} = \frac{An\theta^{n_d-1}}{\beta}\exp\left(\frac{-E_{des}}{RT_{max}}\right) \tag{2.19}$$

A first order desorption is when the molecule desorbs from the surface by itself and the value attributed to n_d is equal to 1. For example, the molecular desorption of methanol from the surface. A second order desorption is often called associative desorption and it happens when two adsorbed molecules recombine to desorb from the surface as one. For example, two hydrogen atoms (H) in the adsorbed phase recombine to desorbs as dihydrogen (H_2). In this latter case, n equals to 2.

Use of the Redhead equation is the simplest method to determine the desorption energy as it can be obtained from one spectrum. More complex and accurate methods exist for TPD analysis[28], but the complexity of the chemical systems and the overlap of peaks make the Redhead method more suitable for our experiments. In order to determine the desorption energy, we need to know the pre-exponential factor, the maximum temperature of the desorption peak and the heating rate. The T_{max}, and the ramp can be easily determined from the spectrum and experimental setting. The pre-exponential factor A is usually simplified and estimated to be 10^{13} s^{-1}. This value is often underestimated which leads to non- accurate results. For example, taking T_{max} = 300K, β= 3K/s and A= 10^{13}, 10^{14} and 10^{15} s^{-1} results in the following energies ~77, 83 and 89 kJ/mole respectively. A difference of 6 kJ/mole in the energies results in a change of one order of magnitude in the pre-exponential factor.

The determination of the pre-exponential factor can be determined experimentally in two ways. The first one consists of acquiring several TPD spectra with different heating rates and then plotting the $ln\left(\beta/T_{max}^2\right)$ versus $1/T_{max}$. The desorption energy can be determined form the slope of the linear plot. Hence, the pre-exponential factor can be obtained. The second one consists of using Charlie Campbell approach and it is the one used in this thesis.[29] This approach takes into account the entropy of adsorbed and gas phase species to provide more accurate results.[30]

Campbell compared over 30 different adsorbates/substrate combination and concluded that the desorption prefactor after nonactivated molecular adsorption with attractive adsorbate− adsorbate interactions can be obtained by the following equation

$$A = \frac{k_b T}{h} \exp\left\{ (0.3 S^0_{gas}/R \ + 3.3 - 9.31 \ ln\left[\left(\frac{m}{m_{Ar}}\right)^{\frac{3}{2}} \left(\frac{T}{298K}\right)^{\frac{5}{2}} \right] \right\} \qquad (2.20)$$

Where, k_b is Boltzmann constant, S^0_{gas} is the entropy of the gas phase molecule at standard pressure, m_{Ar} is the mass of argon, m is the mass of the desorbed specie and T is the desorption temperature.

2.8.2 TPD components

The main component in the TPD technique used in the laboratory is the quadrupole mass spectrometer (QMS) also called the residual gas analyzer (RGA). The model used is a Prisma TM 80 and is provided by Pfeiffer vacuum. It has a detection range varying from 1 to 200 mass to charge (m/z) ratio with a detection limit below 10^{-12} torr. The RGA resolution is adjustable between 0.5 to 2.5 m/z, typically a lower resolution results in higher signal sensitivity and a higher resolution results in a lower signal sensitivity. The RGA is composed of three important parts: an ionizer, a quadrupole mass filter and an ion detector (Figure 2.19).

The residual gas analyzer parts are encased in a glass bulb that has a 1mm hole at the bottom and is differentially pumped by the ion pump in the RHK chamber. A molybdenum cone with a 5 mm tip hole is attached to the glass bulb bottom and acts as a first stage filter for the molecules take of angle from the surface. It allows only the molecules that perpendicularly desorb from the surface to make it into the glass blub and this helps to increase the signal to noise ratio. The small diameter of the cone and the bulb ensures that we are only detecting the molecules that desorb from the sample surface. Once the molecules pass through the bulb hole, they reach the ionization region (Ionizer). It relies on the same principle as in the ion gauge (section 1.4), where the entering gas molecules get ionized upon collision with the emitted electrons from the filament. Once the ions are formed they are focused and accelerated towards the quadrupole mass filter region. The quadrupole mass filter, as its name suggests, acts as filter for the ions, based on their

mass to charge ratio (m/z). It consists of four parallel rods in which an alternating and direct currents are coupled to generate an oscillating electric field. For a given alternating and direct current, the ion entering the oscillating electric field follows a helical trajectory and if it has the right mass to charge ratio it makes it to the detector region otherwise it collides with the rods or the walls and is discharged.[31–34]

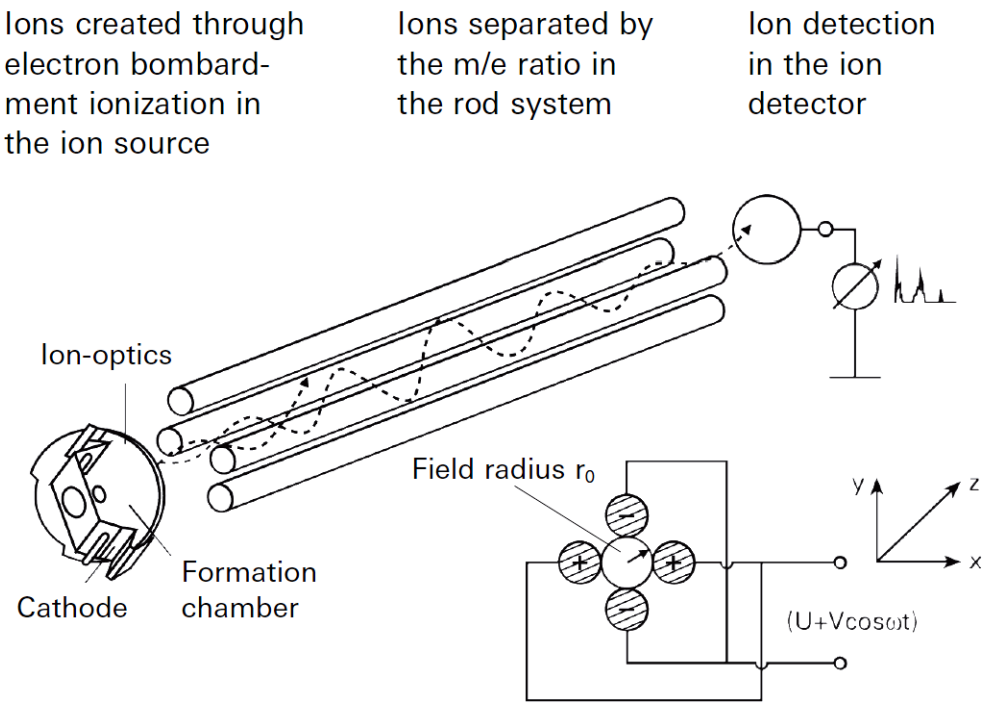

Figure 2.19: Schematic diagram of the components of the quadrupole mass spectrometer. Picture provided by Pfeiffer.

The quadrupole voltage (U_{quad}) can be described by following equation

$$U_{quad} = U + V\cos(\omega t) \tag{2.21}$$

Where U_{quad} represents the voltage of direct current and V is the amplitude of the alternative current oscillating at frequency ω.

The motion of the ions inside the mass inside the quadrupole mass filter can be described by starting with Newton's second law and Lorentz's force law

$$\vec{F} = m\vec{a} \tag{2.22}$$

$$\vec{F} = Q\vec{E} + Q\vec{v}\vec{B} \tag{2.23}$$

Where F is the force, m is the mass of the ion, Q is the ion charge, E is the electric field, v is the speed of the moving ion and B is the magnetic field.

Knowing that the magnetic field B=0 and that the $\vec{E} = -\nabla\vec{V}$,and by combining 2.21, 2.22 and 2.23, the differential equations of motion can be obtained[35]

$$\frac{\partial^2 x}{\partial t^2} = -\frac{Q}{m}\frac{[U + V\cos(\omega t)]}{r_0^2}\, x \tag{2.24}$$

$$\frac{\partial^2 y}{\partial t^2} = \frac{Q}{m}\frac{[U + V\cos(\omega t)]}{r_0^2}\, y \tag{2.25}$$

$$\frac{\partial^2 z}{\partial t^2} = 0 \tag{2.26}$$

Where r_0 is the field radius. These equations are an example of Mathieu's equation and can be numerically solved. To perfectly fit Mathieu's equation, the substitution of these two parameters is necessary

$$a = \frac{8QU}{mr_0^2\omega^2} \tag{2.27}$$

$$q = \frac{4QV}{mr_0^2\omega^2} \tag{2.28}$$

These parameters are called the stability parameters and by plotting a versus q, the cross section of the curves in the x and y directions give us the stability region (which is represented by the area under the red triangle (Figure 2.20). The load line is obtained by dividing parameter a/q which gives us 2U/V. In Figure 2.20, for a given value of U, V, ω, and r_0 the intersection of the load-line with the stability region delimits the acceptance region of the ions. All the ions of the same mass to charge ratio have the same "a" and "q" parameters. Hence, only those specific atoms with a "a" and "q" parameters inside the triangle between the load-line and the apex will make it to the detector. All the other ions outside of this region will be deflected towards the rod or the walls and will be discharged.

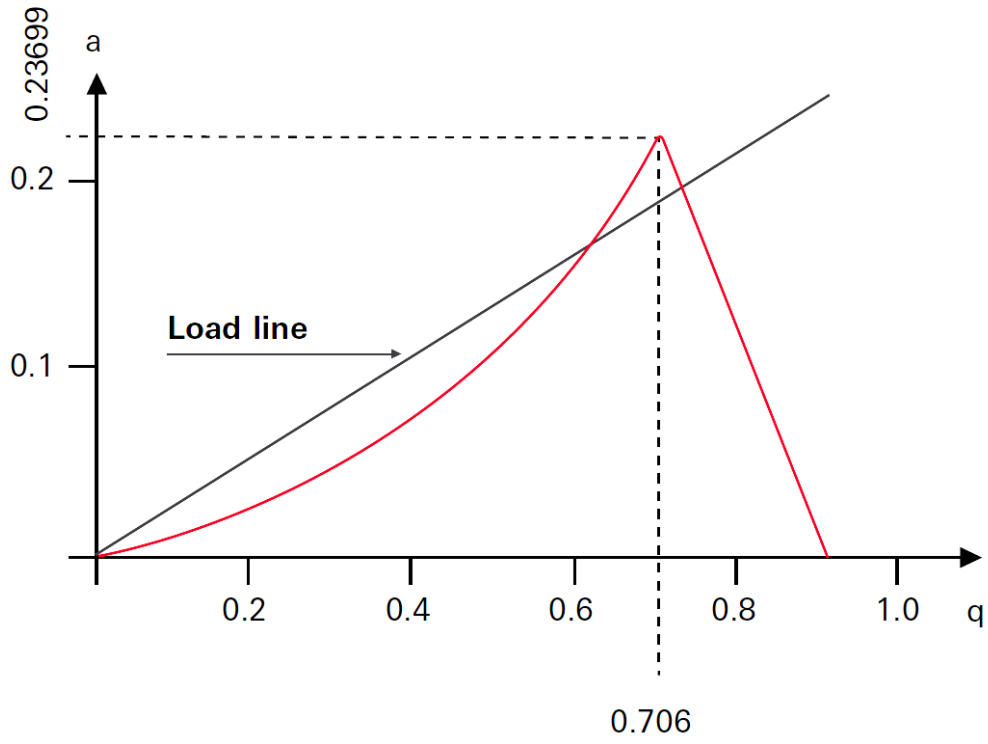

Figure 2.20: Stability region Diagram of the quadrupole mass spectrometer at fixed U, V, ω, and r_0 parameters. Diagram provided by Pfeiffer.

The resolution in this case can be improved by simply increasing the slope of the load line U/V ratio. The closer the load line is to the apex the better the resolution will be (Figure 2.21). Comparing the solid line and the dashed line, the solid line has a lower slope and is far from the

apex which results in broader peak but a higher detected signal. In contrast, the dashed line is closer to the apex allowing a better resolution, but the signal is weaker as fewer ions makes it to the detector. The scanning of different mass number can be achieved by varying the amplitude of U and V but maintaining the U/V ratio constant. The lower m/z ions trajectory are more stable at low of U and V amplitudes, and the higher m/z ions trajectory is more stable at higher U and V amplitudes.

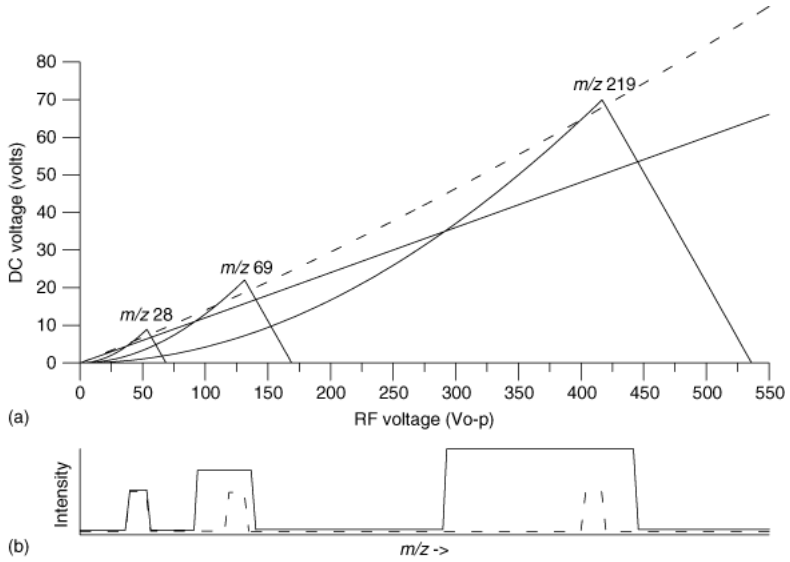

Figure 2.21: a) Stability region Diagram of m/z 28, 69 and 219. The dashed line and the solid line represent the load line with different slopes to show the stability region of the collected ions .b) Simulated intensities and the resolutions of the mass spectrometer depending on the load line slope. *From Kero et al.[31] Copyrights © 2005 John Wiley & Sons, Inc. Reprinted by permission of John Wiley & Sons, Inc.*

The primsa mass spectrometer in the laboratory is equipped with a dual ion detector. The first one is a Faraday cup and the second one in a secondary electron multiplier (SEM).[36,37] The farday cup consists of a metallic cup on which the ions get discharged upon collision with its surface. A current proportional to the number of ion captured by the cup can be measured. The ion current is then converted into a reading of pressure with proper calibration. The Faraday cup can detect partial pressures up to 10^{-11} torr but the measurement is slow especially at the detection limit. To measure lower ion current the use of the SEM is necessary. SEM can detect partial pressures up to 10^{-14} torr. The SEM detector relies on the same principle as the channeltron seen in section

1.6.2.3 except that the setup is different. The SEM consists of consecutive semi-cylindrical dynodes facing each other with a certain offset. Upon the collision of the ion with the first dynode, secondary electrons are emitted and are accelerated towards the second dynode that will emit at his turn more secondary electrons. A cascade of electrons is generated and at the end a collector collects those electrons to measure a current that is proportional to the number of incident ions. For each incident ion about 10^7 electrons make it to the collector which makes very sensitive. The SEM has the advantage that it has a fast response time and the noise to level ratio is much better compared to the Faraday cup.

The number of detected ions is proportional to the number of molecules in the gas phase. It is also to be noted that during the ionization process the molecules can break down into fragments that are taken into account during the acquisition process. A typical plot of pressure versus temperature will include the partial pressure of the parent molecule and the partial pressure of its fragmentation pattern as well. For example, when CO_2 (44 amu) is ionized, the signal with m/z ratio of 44 will be measured but it will also measure the intensity of m/z ratio of 14, 16, 28 and 32 corresponding to Carbon, Oxygen, CO and O_2 respectively.

The RGA is not only used for TPD technique but is also used to monitor the partial pressures of the gases inside the chamber. It also helps to detect leaks when performing check-ups with helium gas.

A procedure on how to perform a TPD experiment can be found in Appendix D.

2.9 Reflection adsorption infrared spectroscopy

2.9.1 Basic principle

Reflection adsorption infrared spectroscopy is a powerful technique that is used to probe the vibrations of the molecules on the surface with a sensitivity of one thousandth of a monolayer. It provides important information about the adsorption geometry and the integrity of the adsorbed molecule.[38] The basic principle behind the technique consists of exciting the vibrational modes of the molecules by irradiating the surface with infrared light. The infrared light is initially generated by the FT-IR (Bruker Equinox 55) spectrometer and is incident on a flat mirror that reflects the beam at a 90° angle to a parabolic mirror (90° off-axis, 30 cm focal length) which focuses the beam on the sample with an angle of incidence of 7° onto the surface inside of the UHV chamber (Figure 2.22). The energy of the incident infrared light is absorbed by the molecule only if it

matches its vibrational frequencies, otherwise the infrared beam is simply reflected from the surface. After reflection from the surface of the sample, a second parabolic mirror focuses the beam to a liquid-nitrogen cooled mercury-cadmium-telluride (MCT) detector (InfraRed associates, model D315/6). By measuring the reflected infrared light, the absorbed frequencies can be determined. The frequency at which a given vibration occurs depends on the strengths of the bond and the mass of the atoms. This means that every molecule has its own vibrational modes; thus, providing us with information about the chemical nature of the adsorbates.

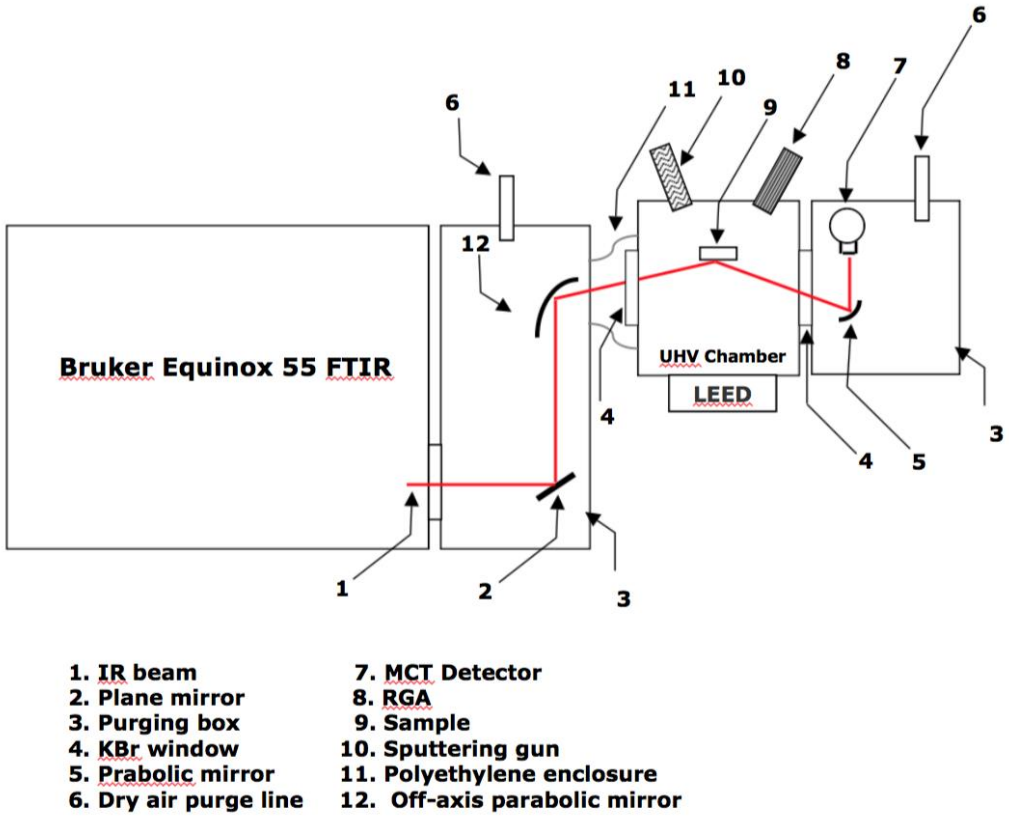

Figure 2.22: Top view schematic diagram of the RAIRS system setup with its components.

The vibrational modes of the molecules can be excited by the interaction of the electric field with the dipole moment of the molecule. The behaviour of the electric field changes when a metal is involved. Consider an electric field incident with a polarisation s parallel (E_S) to the surface and a polarisation p perpendicular (E_p) with an angle to the surface (Figure 2.23). Upon

reflection from the surface, the electric field components (E_p and E_S) are reversed in opposite direction with almost the same magnitude given the fact that the reflection factor is close to 1 for metals. At the reflection boundary, the parallel components of the electric field of the s polarisation E_S and E_s' almost cancel out while the perpendicular component of the electric field of p polarisation is enhanced.

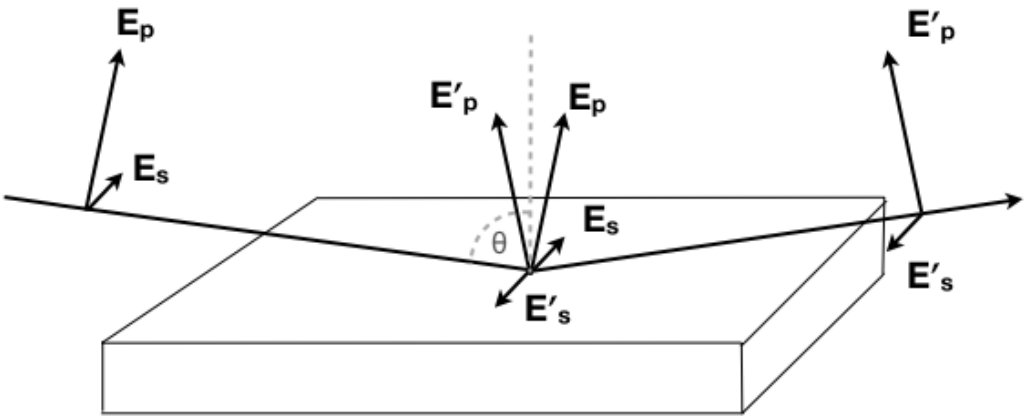

Figure 2.23: Reflection of the electric field from a metallic surface at the boundary. The incident s and p polarisations of the electric field are represented by E_S and E_p respectively with their corresponding reflections E_s' and E_p'.

This means that it is only the perpendicular component of the electric field that interacts with the dipole moments of the molecule and this is called the metal-surface selection rule.[39,40]

The intensity of the measured peaks depends on the strength of the electric field, the change in the dipole moment of the molecule and the angle between the perpendicular electric field and the dipole moment. The intensity of the perpendicular component of the electric field strongly depends on the incident angle. In figure 2.24, for incident angle around 80 and 88°, $E_{p_\perp}$ intensity is almost doubled. This angle is called a grazing angle where the sensitivity of the RAIRS is at a maximum.

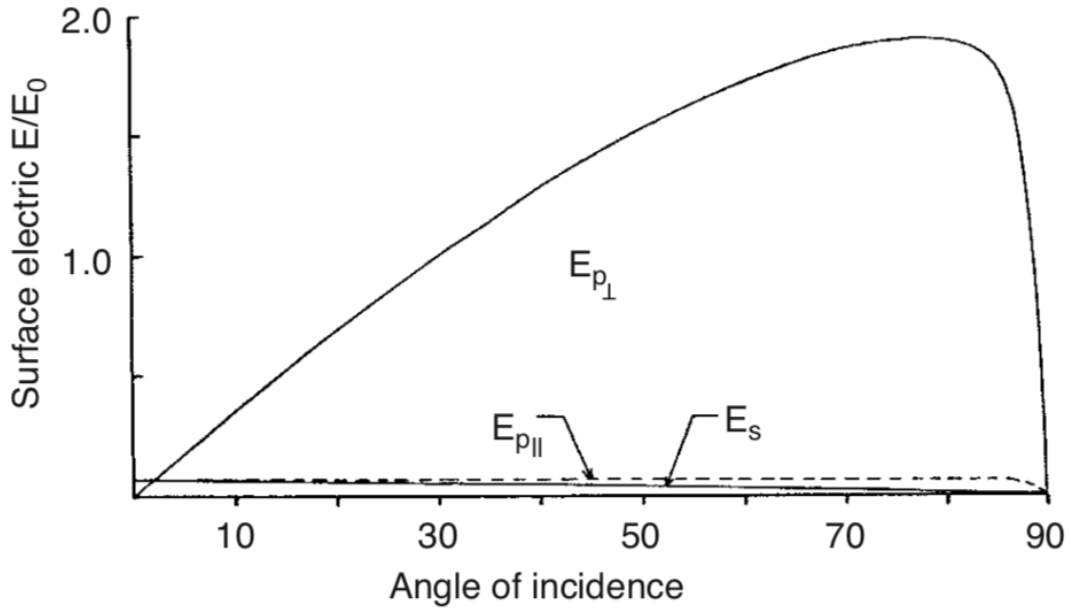

Figure 2.24: Resultant electric field from the surface with varying incident angles. The incident electric field for the infrared radiation is represented by E_0 while s and p polarisations of the electric field are represented by E_S and E_p. Given that the intensity $I \propto E^2$, the contribution from the parallel components of the Electric field is almost zero.Reprinted from Hollins et al.[41] Copyright (1985) with permission from Elsevier.

2.9.2 RAIRS components

Figure 2.22 shows that the major components for the setup of the RAIRS chamber are: the infrared source, the FT-IR spectrometer, the MCT detector and purging boxes. All the other components of the UHV chamber are discussed in sections 1.3 and 1.5.2.

2.9.2.1 Infrared Source

The infrared source used in the equinox 55 is a silicon carbide heat source (commonly known as a globar) that generates mid-infrared radiation $(2 - 25\mu m)$.[42] The basic principle relies on black body radiation. A current is passed through the silicon carbide rod to raise its temperature. The intensity of the black body radiation mainly depends on the temperature, this is why the silicon carbide is operated at 1200 K. The source is air cooled to maintain the temperature constant.

2.9.2.2 Fourier Transform Infrared Spectrometer

The basic principle of the FTIR relies on the Michelson interferometer.[43–45] An interferometer is used to measure the wavelength of the optical beam through the creation of interference patterns. A Michelson interferometer consists of a fixed mirror, a movable mirror and a beam splitter. The emitted infrared beam from the source is partially reflected to the fixed mirror and partially transmitted to the movable mirror by the beam splitter. When they return to the beam splitter they recombine, then leave the interferometer to interact with the sample and then the signal is measured by a detector. The intensity of the signal depends on the interference of the waves and their path difference. For a given wave length, if the path difference (δ) is zero or an integer number of wavelengths, the two beams are in phase and the interference is constructive and a maximum intensity is measured, but if δ is not zero and is not an integer number of wavelengths then a total or a partial destructive interference occurs. Each wave length undergoes constructive and destructive interference at a different path differences δ and this is how the interferometer distinguishes the different frequencies. The measured intensity of all the IR beam wavelengths ($I(\delta)$) by the detector as a function of δ gives rise to an interferogram which represents an addition of each interferogram arising from each different wavelength (Figure 2.25 a). It is typically performed by moving the movable mirror back and forth at constant speed. The highest intensity is measured at zero path difference, where all the wavelengths of the IR beam are in phase and constructively interfere. This high band intensity is called the centerburst. Moving the path difference causes some of the wavelengths to be out of phase and results in signal drop due to destructive interference. By taking the Fourier transform of the interferogram we obtain the calculated spectrum of the infrared absorbance intensity versus wavenumber (cm^{-1}) (Figure 2.25 b). This spectrum is generally called the single beam spectrum and its shape is mainly due to the globar of the infrared source, the sensitivity of the detector and properties of the optics.

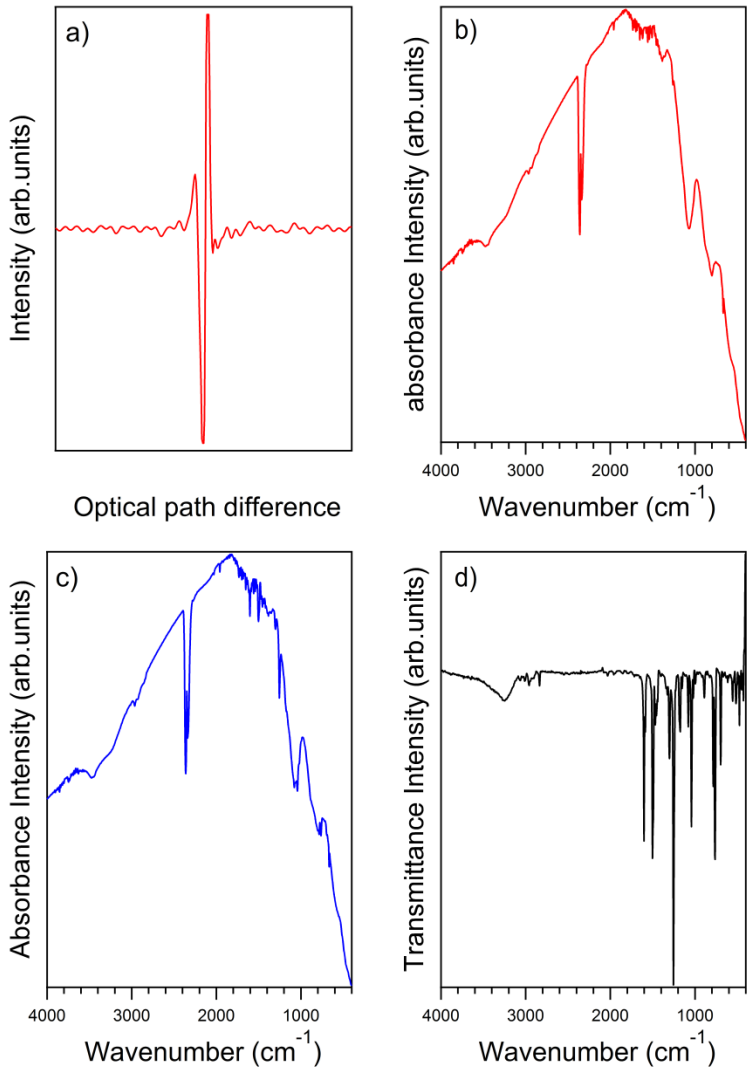

Figure 2.25: a) Interferogram obtained after reflection from a clean Pt(111) surface. b) Background single beam spectrum. c) Single beam spectrum after depositing 100L of anisole on Pt(111). d) Transmittance spectrum obtained by dividing spectrum c by spectrum b.

Prior dosing the molecules, a single beam spectrum of the clean surface is acquired and is referred to as the background. The background will generally contain absorbance peaks of the surrounding molecules in the environment such as water vapour and carbon dioxide. Upon adsorption of the molecules, a single beam spectrum is acquired and will contain peaks specific to the vibrational modes of the dosed molecule but also undesired peaks from the molecules present in the surrounding environment (Figure 2.25 c). To eliminate these peaks a transmittance spectrum can be obtained by dividing the intensity of the molecule's absorbance spectrum by the intensity

of the background spectrum (Figure 2.25 d).

The collected interferogram is performed by multiple scans (moving the mirror back and forth) to increase the signal to noise ratio (S/N). The relation between them is described by the following equation $S/N \propto (n)^{1/2}$ where n is the number scans. Increasing the number increases the S/N in the other hand increases the acquisition time as well. This leads us to the next important parameter which is the resolution. The resolution is proportional to $1/\delta$, meaning that the higher the path difference the better the resolution becomes. To obtain a higher path difference, the mirror will have to be displaced at a longer distance. The drawback in doing so, is that the spectrum will be noisier $S/N \propto resolution$. Depending on the experiment and what we want to probe a trade-off between the S/N, the time and the resolution needs to be taken into account to achieve high quality spectra.

2.9.2.3 Mercury cadmium telluride (MCT) Detector

Mercury cadmium telluride detector used in the laboratory consists of a crystal made of these three elements, a thallium bromoiodide (KRS-5W) window to protect the crystal, electronics to measure the current and a liquid nitrogen reservoir to cool down the detector. MCT detectors are very sensitive to infrared light and the model used can detect wavelengths between 2-24 μm with a peak at 22 $\mu m(\lambda_{max})$. When the infrared light interacts with the crystal, electrons from the valence band are excited to the conduction band. By applying a voltage, a current can be measured, and it is proportional to the number of photons hitting the detector. Hence, the measured current gives the measure of the infrared intensity.

MCT detectors have the advantage of being very sensitive and having a tunable bandgap. The sensitivity (D*) of the detector is at least 10 times higher than the conventional ones such as deuterated triglycine sulfate (DGTS).[46]In order to achieve this, cooling down the detector with liquid nitrogen is necessary to avoid the excitation of the electrons by thermal agitation which results in a noise decrease. Depending on the compositions of the alloy elements the bandgap can be tuned (Figure 2.26). A lower bandgap will allow infrared waves of lower energies (lower frequencies) to excite the electron from the valence band to the conduction band. The limit at which the infrared wave frequencies cannot excite the electron to the conduction band is called a cut-off frequency and generally falls just above the value of λ_{max} . The cut-off frequency of the D315/6 model, is around 700 cm^{-1} and below. This is the reason why metal-atom vibrational

modes cannot be observed, because their frequencies lie in region below 400 cm^{-1}. Typical specifications of the 315/6 model and acquisition parameters can be found in Table 2.3. For the operation mode of the RAIRS technique, please see Appendix D.

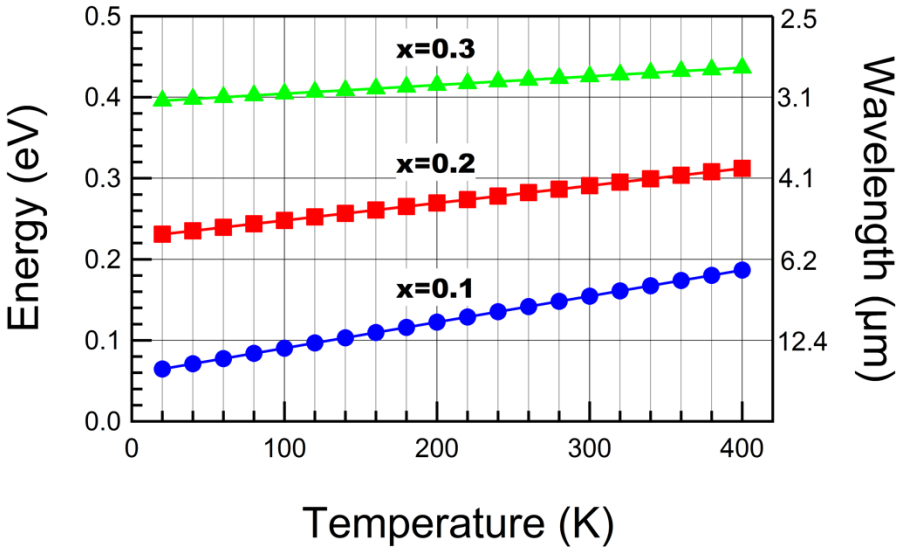

Figure 2.26: This graph summarises the behaviour of the band gab and the cut-off frequency as a function of the alloy composition Hg_{1-x} Cd_x Te and temperature. The bandgap energy (E_{gap}) as a function of alloy composition is modelled from the following equation $E_{gap} = -0.302 + 1.93x - 0.81x^2 + 0.832x^3 + 5.35(1-2x)10^{-4}\,T$. *Replotted from P. Norton.*[47]

2.9.2.4 Purging

The presence of water along the optical path leads to the appearance of undesired sharp peaks in the IR spectrum. These peaks may obscure peaks that provide important information about compounds in the sample. One way to eliminate these undesired peaks is by purging the optical path with dry air or nitrogen. To ensure that the optical path is purged, two plexiglass boxes have been built by using screws and silicone as a sealant. The first plexiglass box is the intermediate between the FT-IR spectrometer and the UHV chamber (Figure 2.22). The box holds a dessicant to absorb water moisture, a flat mirror and a parabolic mirror to reflect the IR beam. The box also protects the KBr windows, KBr is soluble in water. Over time exposure of the windows to water vapor causes the widows to become opaque and eventually they will stop transmitting the IR beam. A second plexiglass box is also used on the opposite side of the chamber, this box holds a dessicant, a parabolic mirror and a detector. The box is purged with dry air as well and on top of the reasons

stated above, the detector is usually cooled down with liquid nitrogen and any presence of vapor water can condensate on detector lens which results in signal saturation.

Table 2.3: Acquisition parameters set for the RAIRS spectra and specifications of D315/6 MCT model.

Physical Parameters	
Source	Silicon carbide
Voltage (eV)	1462.8
Crystal width (mm)	1
Crystal length (mm)	1
window	KRS-5W
Operating temperature (K)	77
D* (cm $Hz^{1/2}W^{-1}$) at 10KHz	$8.47x10^{9}$
Software Parameters	
Resolution (cm^{-1})	4
Scans	1000
Sample signal gain	4

2.10 First principles calculations

Determining the reaction pathways and the intermediate species experimentally is very challenging as consecutive reactions can occur quickly and the resolution of the equipment makes it difficult to track the exact reaction pathways without assumptions. Applying DFT methods in computational chemistry helps us to determine the relative stability of intermediates and the transition states without worrying about the experimental constraints, and thus providing us with a complete picture of the catalytic mechanism. In this work, first principles calculations based on density functional theory (DFT) were performed with the Vienna Ab Initio Simulation Package (VASP). This work was part of a collaboration between École normale supérieure de Lyon and the University of Ottawa. I performed all the work related to XPS simulations and the determination of the core level binding energy. The work related to the surface optimisation, adsorption geometry of the molecules, transition states and kinetic analysis have been performed

by Romain Réocreux, specific details about his work can be found in his published thesis.[48] In this section, I will cover an introduction of the first principles calculations and present an optimal guide on how to perform XPS calculations to estimate the core electron binding energy.

2.10.1 Introduction to density functional theory

The first principles calculations approach is based on density function theory. DFT technique assumes that the ground state energy (ε) is only determined by the electron density (ρ). The density itself is a function of position, hence its name "functional".[49–51] From Schrödinger's equation the energy functional as a function of denstity can be described by the kinetic energy (T), the interaction with external potential (V_{ext}) and the electron-electron interaction (V_{ext}):

$$E[\rho] = T[\rho] + V_{ext}[\rho] + V_{ext}[\rho]$$

The kinetic and electron-electron functionals are unknown. In order to solve Schrödinger's equation an approximation has to be made. In this case we introduce a ficticious system of n non-interacting electrons where each electron can be described by a single determinant orbital wavefunction φ_i. The electron-electron interaction will be approximated as the classical coulomb interaction. The ground state energy can be obtained by the Schrodinger equation :

$$\left[-\underbrace{\frac{\boldsymbol{p}^2}{2m}}_{Kinetic\ Energy} - \underbrace{V_{ext}(\boldsymbol{r}_1)}_{external\ potential} - \underbrace{\int \frac{\rho(\boldsymbol{r}_2)}{4\pi\varepsilon_0 r_{12}} d\boldsymbol{r}_2}_{\substack{electron\ electron \\ repulsion}} + \underbrace{V_{XC}(\boldsymbol{r}_1)}_{\substack{exchange\ correlation \\ potential}} \right] \varphi_i(\boldsymbol{r}_1) = \varepsilon_i \varphi_i(\boldsymbol{r}_1) \quad (2.29)$$

Where V_{ext} represents the external potential applied to the system. For example, for molecules and solids it would be the attraction of the electron to the nucleus.

The density $\rho(\boldsymbol{r})$ is described by the wavefunctions $\varphi_i(\boldsymbol{r})$:

$$\rho(\boldsymbol{r}) = \sum_{i=1}^{n} |\varphi_i(\boldsymbol{r})|^2 \quad (2.30)$$

The exchange-correlation energy (E_{XC})is the sum of the error made using n non-interacting electrons and treating the electron-electron interaction classically. The exchange-correlation potential (V_{XC}) is obtained by applying the gradient of the density to the exchange-correlation energy :

$$V_{XC}[\rho] = \frac{\delta E_{XC}[\rho]}{\delta \rho} \tag{2.31}$$

Unfortunately, the exchange correlation energy functional ($E_{XC}[\rho]$) is not known and it relies on an approximation. This approximation itself is a research field which is out of the scope of this thesis. There are many different functionals and each one of them is suited for a certain type of study. The exchange correlation energy functional used is this thesis is a generalized gradient approximation (GGA, optPBE) that depends on the density and its gradient. This functional was shown to correctly describe both chemisorption bonds and dispersive interactions, and to give adsorption energies in close agreement with experimental results.

$$E_{XC} \approx \int \rho(r)\varepsilon_{xc}(\rho, \nabla\rho)d\boldsymbol{r} \tag{2.32}$$

The Kohn-Sham equations are solved self-consistently (Figure 2.27). It starts by guessing the density of electrons. Then the density is used to estimate the exchange correlation energy which at its turn is used to obtain the exchange correlation potential. The exchange correlation potential is then used in the Kohn-Sham equations to solve for a new set of wavefunctions. Then the new set of wavefunctions is used to estimate the new density of electrons. The process is repeated until convergence is achieved where the density of electrons and the exchange correlation potential are constant.

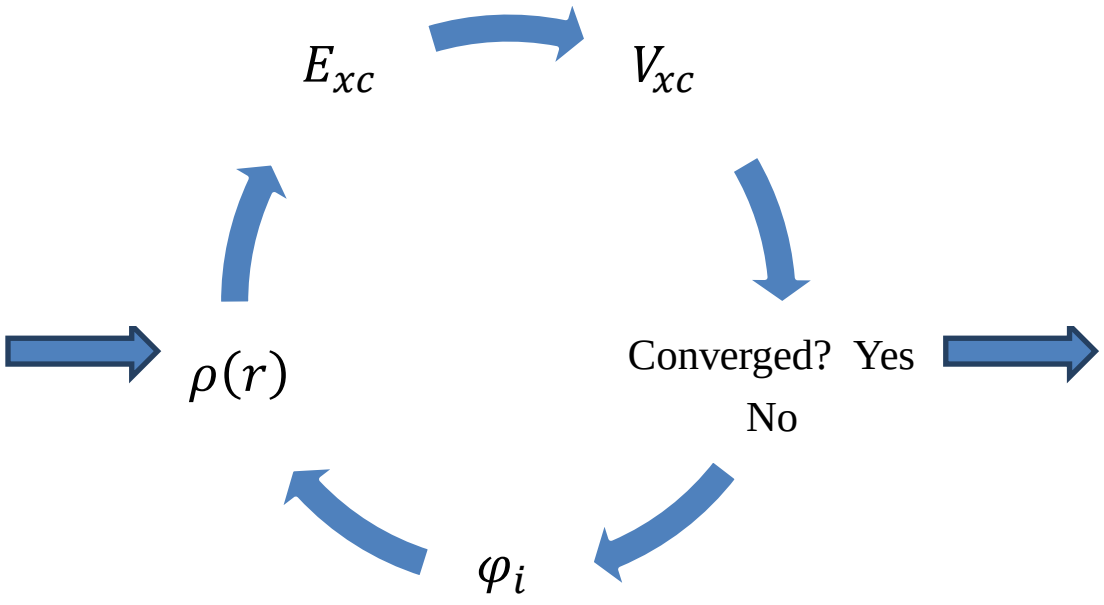

Figure 2.27: Diagram representing the logical pathway in density functional theory calculations.

2.10.2. XPS Simulations

To perform XPS simulations a methodology had to be implemented to accurately estimate the core level binding energies. The project started by calculating core level binding energies of simple molecules such as CO on Pt(111) surface and by varying different parameters such as the number of adsorbed species, the number of K-points, the adsorption sites and the number of excited electrons. Once a better understanding of the influence of these parameters has been achieved, we increased the complexity towards ethanol to be able to study the influence of the adsorption geometry, and the individual/simultaneous excitations of the atoms. The overall understanding of the influence of all these parameters enabled us to determine the optimal parameters that were used to calculate the core level binding energies of phenol, anisole and 2-Phenoxyethanol. The successful agreement between the theoretical predictions and the experimental results led to the implementation of the methodology (how perform XPS simulations) in the research group for future use. The details of calculations and spectra simulations can be found in Appendix E.

The XPS simulations are carried with a code implemented by Kresse in the Vienna Ab Initio Simulation Package.[52,53] The simulation consists of 3D-cell where a molecule and /or slab

can be implemented. The cell system is periodically reproduced to generate an "infinite" surface. Although the code provides a good description of the surface potential of transition metals and their interaction with molecules, it still lacks proper determination of the core electron binding energies. The core hole is simulated with a pseudopotential rather than the full electronic description of core electrons.[54,55] In addition, simulating a real XPS process where the core electron is completely removed from the atom is impossible. The Coulomb potential of an ionized atom cannot be treated under the assumption of periodicity due to Coulombic divergence. For these reasons, the method cannot provide absolute core level energies but the binding energy shifts ΔE_b is accurate and can be compared to experimental values.[56,57]

XPS simulations are carried by specifying the following parameters implemented in VASP : ICORELEVEL, CLNT, CLN, CLL, CLZ.[58]

The ICORELEVEL can take two values either 1 or 2. If ICORELEVEL is set to 1, it will only provide core level binding energy in the initial state approximation which involves recalculating the Kohn-Sham eigenvalues of the core states after a self-consistent calculation of the valence charge density. If it is set to 2, an electron from the core shell will be removed and placed into the conduction band. The final state approximation process is closely related to the XPS process.

The CLNT corresponds the concerned atom. The position number corresponding to the atom in the POSCAR file should be entered here.

The CLN and CLL corresponds to the principal quantum number (n) and angular quantum number (l) to specify from which core shell the electron should be excited.

The CLZ corresponds the number of electrons that are removed from the core. The choices are 1 or 0.5 electron (Derived from Janak's theorem).[59]

Table 2.4 contains the optimal parameters to calculate core level energies that can be compared to experimental results. Further details about the determination of the right parameters can be found in Appendix E.

Table 2.4: Initial Parameters used for the calculation of core electron binding energy of the C1s.

Parameters	
ICORELEVEL	2
CLNT	2
CLN	1
CLL	0
CLZ	0.5

References

(1) Somorjai, G. A.; Mujumdar, A. S. Introduction to Surface Chemistry and Catalysis. *Dry. Technol.* **1995**.

(2) Reif, F. *Fundamentals of Statistical and Thermal Physics*; Waveland Pr Inc, 1965.

(3) Chung, Y. W. *Practical Guide to Surface Science and Spectroscopy*; 2001.

(4) Atkins, P.; De Paula, J. *Physical Chemistry for the Life Sciences*; 2006.

(5) Bottauscio, O.; Casaro, F.; Chiampi, M.; Giors, S.; Maccarrone, C.; Zucca, M. High-Speed Drag-Cup Induction Motors for Turbo-Molecular Pump Applications. *IEEE Trans. Magn.* **2006**, *42* (10), 3449–3451.

(6) Foster, J. S.; Lawrence, E. O.; Lofgren, E. J. A High Vacuum High Speed Ion Pump. *Rev. Sci. Instrum.* **1953**, *24* (5), 388–390.

(7) Hobson, J. P.; Redhead, P. A. OPERATION OF AN INVERTED-MAGNETRON GAUGE IN THE PRESSURE RANGE 10−3 TO 10−12 MM. Hg. *Can. J. Phys.* **1958**, *36* (3), 271–288.

(8) Helmer, J. C.; Hayward, W. H. Ion Gauge for Vacuum Pressure Measurements below 1×10^{-10} Torr. *Rev. Sci. Instrum.* **1966**, *37* (12), 1652–1654.

(9) Kollie, T. G.; Horton, J. L.; Carr, K. R.; Herskovitz, M. B.; Mossman, C. A. Temperature Measurement Errors with Type K (Chromel vs Alumel) Thermocouples due to Short-Ranged Ordering in Chromel. *Rev. Sci. Instrum.* **1975**, *46* (11), 1447–1461.

(10) Sims, J. J. Formic Acid Decomposition on Cobalt Surfaces. Université d'Ottawa/University of Ottawa 2015.

(11) Musket, R. G.; McLean, W.; Colmenares, C. A.; Makowiecki, D. M.; Siekhaus, W. J. Preparation of Atomically Clean Surfaces of Selected Elements: A Review. *Appl. Surf. Sci.* **1982**, *10* (2), 143–207.

(12) Yonts, O. C.; Harrison Jr, D. E. Surface Cleaning by Cathode Sputtering. *J. Appl. Phys.* **1960**, *31* (9), 1583–1584.

(13) Moslemzadeh, N.; Tamara, M.; Raval, R.; Prior, D.; Preston, M. R. Improved Efficiency of the Sputtering Technique for Pyrite Surface and Its Effect on Reduction of Electron Beam Damage. *Surf. Interface Anal.* **2009**, *41* (1), 1–5.

(14) Siegbahn, K. From X-Ray to Electron Spectroscopy. In *Nishina Memorial Lectures: Creators of Modern Physics*; Springer Japan: Tokyo, 2008; pp 137–228.

(15) Hollander, J. M.; Jolly, W. L. X-Ray Photoelectron Spectroscopy. *Acc. Chem. Res.* **1970**, *3* (6), 193–200.

(16) Swartz, W. E. X-Ray Photoelectron Spectroscopy. *Anal. Chem.* **1973**, *45* (9), 788A – 800a.

(17) Seah, M. P. The Quantitative Analysis Gf Surfaces by XPS : *Surf. Interface Anal.* **1980**, *2* (6), 222–239.

(18) Walls, J. M.; Smith, R. Surface Science Techniques. *Vacuum* **1994**.

(19) Karas, I.; Houfek, J.; Matol, V. A Low Energy Electron Diffraction Study of Surface Structures. **2005**, *1*, 580–583.

(20) Pendry, J. B. *Low Energy Electron Diffraction*; Academic Press London, 1974.

(21) Somorjai, G. A.; Farrell, H. H. Low-Energy Electron Diffraction. *Adv. Chem. Phys* **1971**, *20*, 215.

(22) Vanhove, M. A.; Weinberg, W. H.; Chan, C.-M. *Low-Energy Electron Diffraction: Experiment, Theory and Surface Structure Determination*; Springer Science & Business Media, 2012; Vol. 6.

(23) Seah, M. P.; Dench, W. A. Quantitative Electron Spectroscopy of Surfaces : *Surf. Interface Anal.* **1979**, *1* (1), 2–11.

(24) Cvetanović, R. J.; Amenomiya, Y. Application of a Temperature-Programmed Desorption Technique to Catalyst Studies. *Adv. Catal.* **1967**, *17* (C), 103–149.

(25) Falconer, J. L.; Schwarz, J. A. Temperature-Programmed Desorption and Reaction: Applications to Supported Catalysts. *Catal. Rev. Sci. Eng.* **1983**, *25* (2), 141–227.

(26) Cvetanović, R. J.; Amenomiya, Y. A Temperature Programmed Desorption Technique for Investigation of Practical Catalysts. *Catal. Rev.* **1972**, *6* (1), 21–48.

(27) Redhead, P. A. Thermal Desorption of Gases. *Vacuum* **1962**, *12*, 203–211.

(28) Nieskens, D. L. S.; Van Bavel, a. P.; Niemantsverdriet, J. W. The Analysis of Temperature Programmed Desorption Experiments of Systems with Lateral Interactions; Implications of the Compensation Effect. *Surf. Sci.* **2003**, *546* (2-3), 159–169.

(29) Campbell, C. T.; Árnadóttir, L.; Sellers, J. R. V. Kinetic Prefactors of Reactions on Solid Surfaces. *Zeitschrift für Phys. Chemie* **2013**, *227* (9-11), 1–20.

(30) Campbell, C. T.; Sellers, J. R. V. The Entropies of Adsorbed Molecules. *J. Am. Chem. Soc.* **2012**, *134*, 18109–18115.

(31) Kero, F. A.; Pedder, R. E.; Yost, R. A. Quadrupole Mass Analyzers: Theoretical and Practical Considerations. *Encycl. Genet. Genomics, Proteomics Bioinforma.* **2005**.

(32) Dawson, P. H. *Quadrupole Mass Spectrometry and Its Applications*; Elsevier Scientific Publishing Company, 1976.

(33) Hoffmann, E. De; Stroobant, V. *Mass Spectrometry - Priniples and Applications.*; 2007; Vol. 29.

(34) William Reusch. Mass Spectrometry. *Iocd* **2013**.

(35) Miller, P. E.; Denton, M. B. The Quadrupole Mass Filter: Basic Operating Concepts. *J. Chem. Educ.* **1986**, *63* (7), 617.

(36) Mohanty, S. R.; Bhuyan, H.; Neog, N. K.; Rout, R. K.; Hotta, E. Development of Multi Faraday Cup Assembly for Ion Beam Measurements from a Low Energy Plasma Focus Device. *Jpn. J. Appl. Phys.* **2005**, *44* (7R), 5199.

(37) Allen, J. S. The Detection of Single Positive Ions, Electrons and Photons by a Secondary Electron Multiplier. *Phys. Rev.* **1939**, *55* (10), 966.

(38) Hoffmann, F. Infrared Reflection-Absorption Spectroscopy of Adsorbed Molecules. *Surf. Sci. Rep.* **1983**, *3* (2-3), 107.

(39) Greenler, R. G. Infrared Study of Adsorbed Molecules on Metal Surfaces by Reflection Techniques. *J. Chem. Phys.* **1966**, *44* (1), 310–315.

(40) Lang, N. D.; Kohn, W. Theory of Metal Surfaces: Induced Surface Charge and Image Potential. *Phys. Rev. B* **1973**, *7* (8), 3541.

(41) Hollins, P.; Pritchard, J. Infrared Studies of Chemisorbed Layers on Single Crystals. *Prog. Surf. Sci.* **1985**, *19* (4), 275–349.

(42) Spitzer, W. G.; Kleinman, D.; Walsh, D. Infrared Properties of Hexagonal Silicon Carbide. *Phys. Rev.* **1959**, *113* (1), 127.

(43) Ferraro, J. R.; Basile, L. J. *Fourier Transform Infrared Spectra: Applications to Chemical Systems*; Academic Press, 2012.

(44) Smith, B. C. *Fundamentals of Fourier Transform Infrared Spectroscopy*; CRC press, 2011.

(45) Bell, R. *Introductory Fourier Transform Spectroscopy*; Elsevier, 2012.

(46) Hasegawa, T.; Taniguchi, K.; Sato, Y. Selection of Modulation Frequency of FT-IR Equipped with an MCT Detector for Thin-Film Analysis. *Vib. Spectrosc.* **2009**, *51* (1), 76–79.

(47) Norton, P. HgCdTe Infrared Detectors. *Opto-Electronics Rev.* **2002**, *10* (3), 159–174.

(48) Reocreux, R. Biomass Derivatives in Heterogeneous Catalysis : Adsorption, Reactivity and Support from First Principles, Universit{é} de Lyon, 2017.

(49) Ziegler, T. Approximate Density Functional Theory as a Practical Tool in Molecular Energetics and Dynamics. *Chem. Rev.* **1991**, *91* (5), 651–667.

(50) Harrison, N. M. An Introduction to Density Functional Theory. *Nato Sci. Ser. Sub Ser. III Comput. Syst. Sci.* **2003**, *187*, 45–70.

(51) Sholl, D.; Steckel, J. A. *Density Functional Theory: A Practical Introduction*; John Wiley & Sons, 2011.

(52) Kresse, G.; Furthmüller, J. Efficient Iterative Schemes for Ab Initio Total-Energy Calculations Using a Plane-Wave Basis Set. *Phys. Rev. B* **1996**, *54*, 11169–11186.

(53) Hafner, J. Ab-initio Simulations of Materials Using VASP: Density-functional Theory and beyond. *J. Comput. Chem.* **2008**, *29* (13), 2044–2078.

(54) Cramer, C. J.; Truhlar, D. G. Density Functional Theory for Transition Metals and Transition Metal Chemistry. *Phys. Chem. Chem. Phys.* **2009**, *11* (46), 10757–10816.

(55) Gautier, S.; Steinmann, S. N.; Michel, C.; Fleurat-Lessard, P.; Sautet, P. Molecular Adsorption at Pt(111). How Accurate Are DFT Functionals? *Phys. Chem. Chem. Phys.* **2015**, *17*, 28921–28930.

(56) Pueyo Bellafont, N.; Viñes, F.; Hieringer, W.; Illas, F. Predicting Core Level Binding Energies Shifts: Suitability of the Projector Augmented Wave Approach as Implemented in VASP. *J. Comput. Chem.* **2017**, *38* (8), 518–522.

(57) Ozaki, T.; Lee, C.-C. Absolute Binding Energies of Core Levels in Solids from First Principles. *Phys. Rev. Lett.* **2017**, *118* (2), 26401.

(58) Kresse, G.; Furthmuller, J. Vienna Ab-Initio Simulation Package (VASP): The Guide. *VASP Group, Inst. fur Mater. Univ. Wien, Sensengasse* **2002**, *8*.

(59) Sanna, S.; Frauenheim, T.; Gerstmann, U. Validity of the Slater-Janak Transition-State Model within the LDA+U Approach. *Phys. Rev. B - Condens. Matter Mater. Phys.* **2008**, *78* (8), 1–7.

Chapter 3:
Decomposition Mechanism of Anisole on Pt(111): Combining Single-Crystal Experiments and First-Principles Calculations

I performed all the XPS and TPD experiments, and XPS prediction by density functional theory calculations for the reactivity of Anisole on Pt(111). I performed all the analysis and interpretation related to the experimental results. Romain Réocreux performed all the DFT calculations (except the XPS predictions) and related analysis.

3 Decomposition Mechanism of Anisole on Pt(111): Combining Single-Crystal Experiments and First-Principles Calculations.

Romain Réocreux,[‡] Cherif A. Ould Hamou,[†,§] Carine Michel,[‡] Javier B. Giorgi,[†,‖,*] Philippe Sautet[‡,&,*]

[‡] Univ Lyon, Ens de Lyon, CNRS UMR 5182, Université Claude Bernard Lyon 1, Laboratoire de Chimie, F-69342, Lyon, France
[†] Centre for Catalysis Research and Innovation, [§] Department of Physics, [‖] Department of Chemistry and Biomolecular Sciences, University of Ottawa, 10 Marie Curie Pvt., Ottawa, Ontario, Canada. K1N 6N5.
[&] Department of Chemical and Biomolecular engineering, University of California, Los Angeles, Los Angeles, CA 90095, United States

Abstract

To valorize lignin as a renewable source of aromatics, it is necessary to develop selective heterogeneous catalysts for the hydrodeoxygenation reaction of aromatic oxygenates such as anisole. Most of the metal supported catalysts tested so far exhibit a high conversion but a low selectivity towards valuable aromatic hydrocarbons, yielding mainly phenolic compounds. To gain insights into that catalytic system, we performed surface science experiments (X-ray Photoelectron Spectroscopy and Temperature Programmed Desorption) under Ultra-High Vacuum conditions (UHV). Dosing anisole on Pt(111) surprisingly gave benzene, carbon monoxide and hydrogen as the main desorbing products of decomposition. With the help of Density Functional Theory (DFT) we successfully explain the unexpected selectivity. In the present work we show in particular that phenoxy PhO stands as a key intermediate. Although the UHV conditions do not allow the hydrogenation of phenoxy into phenol, *i.e.* the catalytic product, they reveal the key role of both hydrogen and carbonaceous species. Under UHV conditions, anisole gets extensively dehydrogenated: it results in the formation of carbonaceous fragments, which can actually perform the deoxygenation of phenoxy into benzene, but also, more importantly, coke. This detailed study opens the door to a rational design of hydrodeoxygenation catalysts based on supported metals.

Keywords: Lignin, Pt(111), anisole decomposition mechanism, phenol, benzene, DFT, TPD, XPS

3.1 Introduction

Within the context of biomass conversion, lignin has received intense research for about a decade concerning its extraction and decomposition into upgradable aromatic fragments.[1–3] Lignin is indeed nature's most abundant aromatic polymer (10% to 30% of biomass) and therefore represents an extraordinary sustainable source of high valuable aromatic compounds, which are currently produced from oil fractions. Among those target molecules, the so-called BTX platform (benzene, toluene, and xylene) is of great interest. Their production however requires the deoxygenation of the aromatic monomers and oligomers obtained from preliminary lignin depolymerization. Decreasing the oxygen content of such recalcitrant phenolic compounds still remains a very difficult task. The required reduction of the oxygen containing functional groups (ethers, phenols, etc) indeed competes with the undesired reduction of the aromatic moieties into cyclic, or worse, linear alkanes.

Albeit quite challenging, many heterogeneous catalysts have been designed to reduce the amount of oxygenated functional groups using moderate to large pressures of hydrogen. This so-called hydrodeoxygenation (HDO) reaction can be catalyzed using molybdenum sulfide catalysts promoted with cobalt or nickel (CoMoS or NiMoS).[4–7] To maintain their catalytic activity, *extra* sulfur-containing species must however be added to the system, leading to an undesired increase of the sulfur content in the products.[8] The HDO of lignin fragments has also been attempted on noble metals. Ru and Pd show higher conversion for HDO than CoMoS and NiMoS.[9] Pt shows even higher conversions but the products are not as deoxygenated as with the other noble metals. This singularity of Pt has been investigated a great deal using anisole and guaiacol as model compounds. Under HDO conditions they mainly undergo demethylation or transalkylation reactions, leading to different phenolic compounds.[10–12] In spite of the very reducing environment, only very small amounts of BTX – resulting from demethoxylation – have been detected. Even if reaction networks have been proposed,[10,13,14] the full mechanism remains difficult to elucidate experimentally since both the conditions and the support can have effects on the selectivity.[15,16]

To gain insights into the reactivity of aromatic oxygenates on noble metal surfaces, many DFT studies have been performed and published.[13,17–24] Honkela *et al.* showed in particular that the dissociation of phenol into phenoxy was endothermic on Pt(111) and exothermic on Rh(111) and suggested that it may explain the higher propensity of Rh to deoxygenate aromatics.[19] Vlachos *and co-workers* recently proposed the first DFT-elucidated mechanism of guaiacol

decomposition.[20] Based on electronic energies, they showed that guaiacol could indeed be demethylated to catechol but was recalcitrant to further deoxygenation. Heyden *and co-workers* enhanced this model taking entropy and pressure effects into account and confirmed Vlachos's work.[25] However it is very difficult to get experimental evidence that support the proposed mechanism since many parameters remain quite challenging to model (e.g. support effects, state of surfaces, …).

Fortunately, single crystal experiments can help investigating the intrinsic reactivity of the metal catalyst by isolating the different parameters like in particular the environment and the shape of the catalyst. Using TPD experiments, the reactivity of simpler aromatics has already been reported in the literature and has shown different preferences in C-H, C-O and C-C bond cleavages. Phenol has been extensively studied on various metals. On Rh(111)[26] it decomposes into phenoxy via O-H bond cleavage at temperatures below 300 K, while C-H bond cleavage is observed at 350 K and above. Observable products of desorption are CO and H_2. On Mo(110)[27] phenoxy is also formed below 300 K but it decomposes into H_2, surface oxygen and hydrocarbon fragments. All C-O bond cleavages occur by 450 K (no molecular desorption of CO is observed). On Pt(111), the O-H bond cleavage occurs even earlier, below 200 K. Above 0.7 monolayer (ML) coverage phenoxy is subject to a competitive reaction pathway, it either generates benzene and surface oxygen, or it decomposes into CO, H_2 and carbonaceous species. Below 0.5 ML coverage, no CH-containing adsorbates can be observed on the surface: C-C and C-H bond cleavages are more favorable than the C-O bond cleavage. This leads to hydrogen and carbon monoxide as the main desorbing products.[28]

The only fundamental investigation of anisole decomposition on platinum was carried out by King *and co-workers*. They studied the adsorption of anisole on Pt(100)-hex by reflection adsorption infrared spectroscopy (RAIRS) and temperature programmed desorption (TPD).[29] King's group has found that the multilayer of adsorbed anisole molecularly desorbs at 175 K. The monolayer decomposes on the surface by the cleavage of the O-Me bond around 250 K to form phenoxy and methyl. Above 350 K the phenoxy species decomposes into CO, O, and H_2. The methyl group undergoes either hydrogenation to form methane that desorbs at 325 K or dehydrogenation to form surface carbon. No formation of benzene or phenol was reported.

In this manuscript, we provide a detailed description of the interaction and decomposition pathways of anisole on a Pt(111) surface. The fundamental approach involves the combination of

detailed DFT calculations with experimental techniques focusing on the monolayer and submonolayer regimes of anisole on the surface. Experimental results will be presented for X-ray photoelectron spectroscopy (XPS) and temperature programmed desorption (TPD). In combination with a kinetic analysis of the reaction energy profiles obtained from DFT, we propose a mechanism to understand the selectivity of benzene over phenol in the desorption products. Finally, we will discuss how we can rationalize the reverse selectivity observed under HDO reaction conditions.

3.2 Experimental

The 8 mm diameter and 0.5 mm thick platinum single crystal sample with purity of 99.999% was purchased from Princeton scientific. Experiments were carried out in a multi-technique UHV chamber (Specs GmbH) with a base pressure of 4 x 10^{-10} mbar. The Pt (111) crystal surface was cleaned by repetitive cycles of 15 min of sputtering (1.5 keV, 1 x 10^{-5} mbar Ar^{+}) at 600 K, followed by annealing to 1100 K for 2 min. The sample cleanness was confirmed by LEED and XPS. The sample was cooled via a liquid nitrogen reservoir and heated by electron bombardment as needed. The temperature was measured by a chromel-alumel (K-type) thermocouple in contact with the back of the sample.

Anisole (+99% purity, Sigma Aldrich) was introduced to the UHV chamber through a leak valve that was connected to a gas manifold with an anisole reservoir. The reservoir was heated to 350 K to increase the vapor pressure and ensure the purity of the deposition. The gas manifold was heated accordingly to prevent condensation and allow a constant, stable flux of anisole gas into the chamber. Exposure of anisole to the surface was typically performed at $1x10^{-8}$ torr pressure and the dosage measured in Langmuirs (1L = $1x10^{-6}$ torr.s).

All doses were subsequently converted to surface coverage and reported as layers on the platinum surface. The coverage was determined by calibration with the C 1s XPS signal of the CO saturation coverage at 300 K[30]. At 300 K, CO is known to saturate producing a uniform monolayer with coverage of 0.49 ± 0.02 (1 CO molecule for every 2 Pt atoms). Comparison of this saturation with the intensity dependence of the carbon signal from anisole allowed us to determine the saturation coverage of anisole and hence the coverage of every other dose. Dosage of anisole on Pt(111) shows a saturation plateau in the C 1s area corresponding to 1 anisole molecule for every 10 Pt atoms (Appendix F, Figure F1). We define this coverage as one monolayer (1 ML).

XPS

XPS spectra were recorded on a Specs GmbH system (XR50 X-ray source and Phoibos 100 SCD analyzer) using a standard Al Kα source (1486.7 eV) operated at 380 W (14.6 kV, 26 mA). Selected peaks were obtained in high-resolution spectra using 0.05 eV step size, 1 second dwell time, and a pass energy of 30 eV. For the C 1s and O 1s regions 8 and 6 scans respectively were acquired to increase the signal to noise ratio. The spectra were then fit using CasaXPS analysis software using a mixed Gaussian-Lorentzian function and Shirley background subtractions for the C 1s region while a linear background subtraction was used for the O 1s region.

For the experiments, anisole was dosed on the clean sample at 115 K and then heated up to the desired temperature of observation to acquire the spectrum. Once the acquisition was done, the sample was subject to a cleaning cycle (Ar sputtering followed by annealing to 1100 K) to remove all the residual carbon on the surface. The cleanness of the sample surface was verified by LEED and XPS. This process was repeated for each dosage of interest.

TPD

The TPD experiments require placing of the sample in front of a differentially pumped quadrupole mass spectrometer (QMS) and ramping the sample temperature while monitoring the fragments of interest. For our experiments, the Pt(111) sample was dosed with varying exposures of anisole at 110 K and placed 1 mm below a 1 mm diameter hole leading to the differentially pumped QMS. The temperature controlled heating ramp was programmed in LabView and designed to provide and record a linear temperature ramp in the range of 120 K to 800 K, with a ramp rate of 7 K/s. The sample was subject to one cleaning cycle (Ar sputtering followed by annealing to 1100 K) to insure the cleanness of the surface before each dosage. A total of 11 channels corresponding to m/z values of 108, 94, 78, 77, 65, 45, 32, 28, 16, 15 and 2, were monitored for the anisole TPD experiments. The selected m/z values correspond to the main peaks of the fragmentation pattern of the expected species.

3.3 Computational Details

The DFT calculations were performed using the Vienna Ab Initio Simulation Package[31–33] (version 5.3) with the optPBE non local functional.[34,35] This functional was recently shown to correctly describe both chemisorption bonds and dispersive interactions and to give adsorption energies in close agreement with single-crystal calorimetry for unsaturated hydrocarbon molecules on Pt(111).[36,37] The electron-ion interactions were treated using the Projected Augmented Wave (PAW) method.[38] The plane wave basis set was truncated at a cut-off energy of 400 eV. The geometric structures were considered as converged when the forces were less than 0.02 eV/Å.

When a metal surface was involved, a 4 layer p(4x4) slab model was considered, with 5 other equivalent layers of vacuum between slabs and the integration over the Brillouin zone was performed using a 3x3x1 Monkhorst-Pack k-points mesh.[39] For gas phase calculations, the energy was calculated at the gamma point in a cubic cell of 20×20×20 $Å^3$.

The local minima were located using the conjugated gradient method. The transition states were identified using the Nudged Elastic Band (NEB) method[40,41] and/or the dimer method.[42–44] To accurately locate the transition states, the structures were optimized using the Quasi-Newton method. For each optimized structure, a frequency calculation was finally performed to check its first order saddle point property.

All the frequency calculations were performed relaxing only the coordinates of the adsorbates and the upmost platinum layer. They were performed to calculate the ZPE correction as well as the vibrational entropy at 400 K within the harmonic oscillator approximation. For each structure involving a slab, the two softest modes of the bare slab were identified and removed for the evaluation of the entropy, keeping the number of vibrational modes constant from one structure to another. For gas phase hydrogen, both the rotational (free rigid rotator approximation) and the translational (free particle in a box model, pressure of 10^{-10} mbar *i.e.* roughly the pressure of the chamber) contributions were also calculated. For the other gas phase products (carbon monoxide, benzene and phenol), the free energy was not calculated since the partial pressures are very ill defined. Being mainly interested in barriers though, we associated to each desorption process a fictitious *desorbing transition state* meant to estimate the free energy barrier of desorption. The corresponding electronic energy and vibrational entropy were calculated from gas phase structures, and, to that, a 2D-translational entropy contribution (free particle on a 2D surface, the area of which equals the slab area) was added as earlier suggested by Campbell and co-workers.[45]

The XPS calculations were performed using the final state approximation, excitation of half a core electron to a virtual orbital. The excited electrons are allowed to relax after the core hole has been removed; all the remaining core hole electrons are frozen. Each atom was excited independently whatever its chemical nature. This method cannot provide absolute core level binding energies; only shifts of the core electron binding energy are relevant.[46,47]

3.4 Experimental Results.

XPS

The identification of surface species was initially performed by monitoring the carbon and oxygen environment of surface species as a function of temperature.

Figure 3.1 shows C 1s photoelectron spectra after deposition of 8.1 L of anisole on Pt(111), acquired at varying temperatures. This dosage corresponds to an overly saturated layer, perhaps better described as the onset of overlayers of anisole on the surface (see Appendix F, Figure F1) and hence we refer to it as a multilayer regime. Upon deposition at 110 K, anisole shows two peaks in the C 1s spectra, one at 285.3 eV, which is attributed to carbon bound to an oxygen atom (labeled C-O) and the other one at 283.7 eV, which is attributed to carbon atoms bound only to other carbons (labeled C-C).[28] After flashing to 240 K, the C-C and C-O areas decrease in intensity as some desorption takes place. At 360 K, the C-O peak area vanishes while the C-C peak area decreases only slightly in intensity. This is consistent with the decomposition and desorption of oxygen containing species. Upon heating to 550 K, the remaining C 1s peak shifts to lower energy, 283.3 eV, as adventitious carbon accumulates during the time of the experiment.

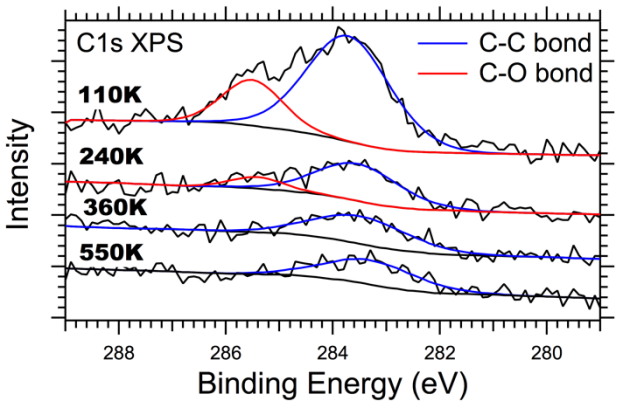

Figure 3.1: XPS spectra acquired at different temperatures starting from a multilayer of anisole deposited at 110 K

A closer look at the sub-monolayer regime is provided in Figure 3.2 where the Pt – anisole interactions are dominant. Upon deposition of 0.5 ML of anisole on Pt(111), the spectrum at 115 K shows the two characteristic peaks (C-C and C-O) in the C 1s region. The monolayer was determined as described in the experimental section and it is defined as one anisole molecule per 10 Pt surface atoms. Upon heating to 200 K and then 300 K, we notice no difference in the intensity of the peaks or in the electron binding energies. At 400 K, the C-O peak vanishes completely while the C-C peak intensity remains constant, and at the same binding energy of 283.5 eV. The extinction of the O 1s XPS signal (see Appendix F, Figure F2) further corroborates the disappearance of the oxygen containing species.

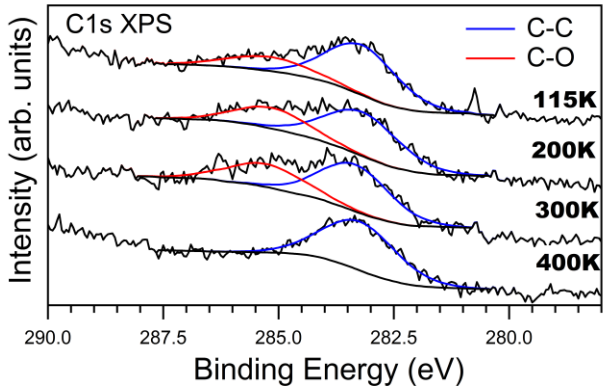

Figure 3.2: XPS C 1s spectra acquired at different temperatures starting from 0.5 ML of anisole deposited at 115 K

Temperature Programmed Desorption

Molecular desorption of the parent anisole molecule was monitored for multiple values of coverage as a function of temperature (Figure 3.3, top panel). The data shows no molecular desorption of anisole at low coverages (0.6 ML and below). As we increase the coverage and reach 0.9 ML we notice that a part of anisole molecularly desorbs with a broad peak at ~400 K. This peak keeps shifting to low temperatures as we increase the coverage stabilizing at 360 K. For very high coverages a growing desorption peak at 260 K is observed and it corresponds to the multilayer desorption. This temperature appears to be higher than what was determined by XPS experiments (<240 K), however taking into account the XPS experimental time (~1h vs. seconds for TPD) and the residence time of species on the surface, the two experiments are consistent. For example, the desorption of anisole from a physisorbed layer has a half-life of 1.79×10^{-17} h at 115 K so that the

physisorbed layer can be considered as kinetically stable. When the temperature increases around 220-240 K, the half-life drops drastically to a fraction of an hour. Since the XPS experiment lasts one hour, the desorption actively occurs and this results in a change in the XPS spectrum at 240 K. This agreement holds for other species observed to desorb at higher temperatures where the apparent discrepancy is bigger but the residence time of species on the surface is lower (see Table F1 for the half-lives of different species as a function of temperature).

The primary desorbing product of anisole decomposition is benzene as observed by TPD (Figure 3.3, middle panel). No other aromatic species were observed. The TPD spectrum for the benzene fragment (mass 78) shows that, for all coverages below 1 ML, benzene molecularly desorbs from the surface in a broad feature from 360 K to 500 K. As we increase the coverage above the monolayer the benzene desorption temperature centers to 400 K and we start seeing a growing peak at 260 K. Based on the measured fragmentation pattern of anisole in our QMS, this peak (marked with * in Figure 3.3) is not a reaction product, but rather due to the fragmentation of the molecularly desorbed anisole (see Appendix F, Figure F3). The peak at 400 K does not seem to saturate, suggesting a different reactivity.

H_2 and CO are the only other observed reaction products (Figure 3.3, bottom panel). Hydrogen shows peaks at 325 K and 460 K, with two shoulders at 425 K and 510 K. For comparison, the associative desorption of pure hydrogen from Pt(111) has been previously observed in the temperature interval between 290 and 375 K.[48,49] The dot-dash line in Figure 3.3 that matches the observed peak in these experiments, corresponds to the reported dosage of 2 L of H_2 on clean Pt(111).[48] The additional high temperature hydrogen peaks have been assigned to subsequent surface reactions yielding H_2 as a product (see discussion below). Only one peak of CO is observable at 470 K. This desorbing molecular CO matches the temperature range of molecular desorption of CO from clean Pt(111) (dashed line on Figure 3.3).[50] The reactivity of anisole on Pt(111) surface is coverage dependent. The main goal of this study is to focus on the monolayer regime to correlate the experimental data to DFT calculations. The 0.9 ML, 1 ML and > 1ML exposures of anisole show the same behavior in the evolution of H_2 and CO.

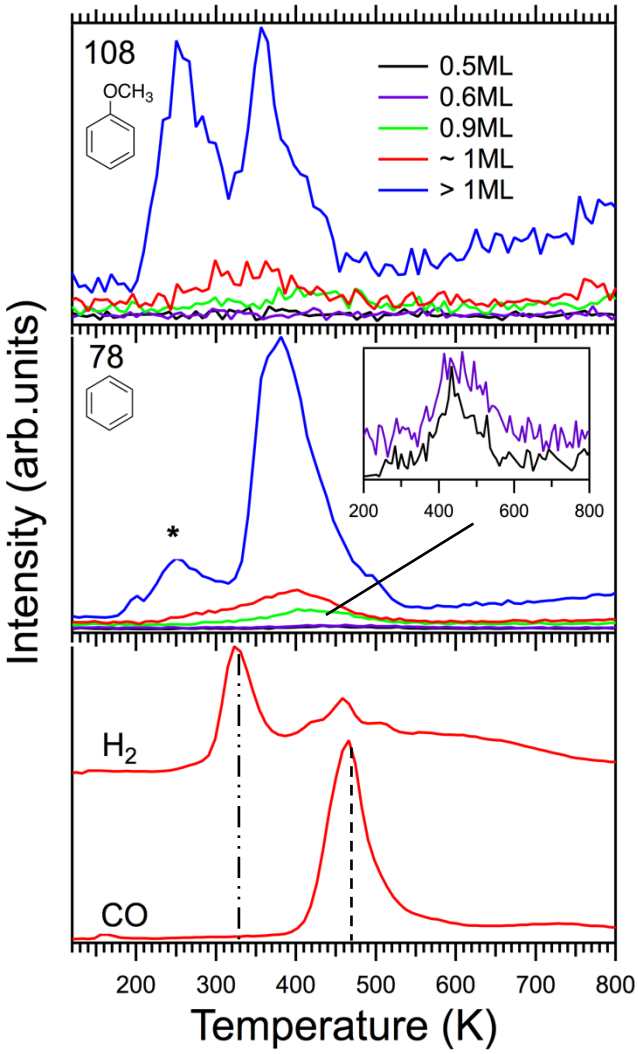

Figure 3.3: TPD spectra after anisole exposure on Pt(111) and selecting Anisole and formed byproducts (Benzene, Hydrogen and Carbon-monoxide). Different exposures of anisole have been dosed at 115 K on Pt(111) and desorption rates are measured using a linear temperature ramp of 7 K/s. (*) corresponds to benzene produced by the gas phase fragmentation pattern of anisole in the mass-spectrometer. The dashed line for CO corresponds to molecular desorption of pure CO from Pt(111) with 0.3 ML coverage.[51] The dot-dashed line for H_2 corresponds to the expected desorption temperature of Hydrogen from Pt(111).[49]

Analysis of the TPD data allows the experimental determination of desorption energies for each species (Table 3.1). The approach taken is based on the general rate law for desorption, the

Polanyi-Wigner equation (eq. 3.1), where ν is the frequency factor and $\Delta_{des}E$ is the desorption activation energy for an nth order process.

$$-\frac{d\theta}{dt} = \nu\theta^{n} \exp\left(-\frac{\Delta_{des}E}{RT}\right) \tag{3.1}$$

We use the simple approach of Redhead to obtain the general expression shown in equation 2. More complex and accurate methods exist for TPD analysis,[52] but the complexity of the chemical systems and the overlap of peaks make the Redhead method more suitable. Traditionally in the Redhead approach, the frequency factor ν takes the standard value of ~10^{13} s^{-1}. However Campbell *and co workers*[53–55] have demonstrated that a more accurate value can be calculated using the entropy of the adsorbed and gaseous species. The calculated frequency factors are presented in Table 3.1 as obtained using the Campbell approach for molecular or associative desorption and temperature corrected entropy values from the Yaw's Handbook.[56] With these appropriate frequency factors and using the TPD data, the desorption activation energy $\Delta_{des}E$ was calculated from the peak temperature T_p of each species of interest using (eq. 3.2).

$$\frac{\Delta_{des}E}{RT_p^2} = \frac{n\nu\theta^{n-1}}{dT/dt} \exp\left(-\frac{\Delta_{des}E}{RT}\right) \tag{3.2}$$

The TPD spectra also provide effective information of the activation energy associated with surface reactions. The high temperature peaks in the hydrogen TPD correspond to H_2 generated at a temperature above its normal desorption temperature and hence the associated activation energy calculated corresponds to the process that generates the additional H atoms. This quantity, calculated also using equation 3.2, is labeled as the apparent activation energy, $\Delta^{\ddagger}E_{app}$. It is important to note, however, that because hydrogen desorbs molecularly but is produced on the surface as an atomic species, desorption spectra can be analyzed as a first order molecular process or as a second order associative process. Both analyses are presented in Table 3.1 for comparison and the validity of the appropriate activation energies will be discussed in comparison with DFT computed values.

Table 3. 1: Desorption energies of observed species, calculated by the Redhead analysis

Species	Observations	Temperature K	$\nu^{(a)}$ s^{-1}	$\Delta_{des}E$ kJ/mol	$\Delta^{\ddagger}E_{app}$ kJ/mol
Anisole	Multilayer	260	5.4×10^{16}	83	-------
	Saturated 1st ML	360	2.4×10^{17}	121	-------
	1st layer (low coverage)	400	4.2×10^{17}	136	-------
Benzene	Molecular desorption	400	4.3×10^{16}	125	-------
	Literature	400-550[57]	-------	133-200[57]	
Carbon monoxide	Molecular desorption	470	8.3×10^{14}	137	-------
	Literature	470[58]	-------	-------	-------
Hydrogen	Analyzed as molecular desorption	325	1.7×10^{14}		89
		425	1.8×10^{14}		118
		460	1.8×10^{14}		128
		510	1.8×10^{14}		142
	Analyzed as associative desorption	325	9.7×10^{8}	-------	52
		425	5.9×10^{8}	-------	67
		460	5.5×10^{8}	-------	73
		510	4.9×10^{8}	-------	81
	Literature	293-375[48]	-------	-------	39.7[48]
		330[49]	-------	-------	73[49]

(a) *Desorption frequency factors*

Analyzing the XPS and TPD results together allows us to determine the ratio of decomposition vs. desorption processes. In the XPS spectra at 240 K we can assume that the C-C peak corresponds to the monolayer coverage of anisole. At 550 K, all the anisole, benzene and CO has desorbed from the surface. Quantifying the remaining carbon left on the surface shows that 80% of the monolayer decomposes into carbon and only 20% desorbs from the surface. Taking a

closer look to the TPD spectra of the saturated monolayer, mass 78 corresponds to the fragmentation pattern of anisole and benzene. Knowing the fragmentation ratio of anisole in the gas phase we can determine its contribution to mass 78. From the 20% desorption of the multilayer, 16% corresponds to the molecular desorption of benzene and 4% of anisole.

3.5 DFT Results

Anisole adsorption

We first studied the adsorption of anisole at different coverages and different geometries. The most stable structure of chemisorbed anisole was found at the so-called bri30 site, as earlier reported in the literature.[29,59,59–61] We computed the associated desorption energy on a p(4x4) slab and a p(3x3) slab in order to assess the coverage effect. On a p(4x4) slab (~0.6 ML with the definition given above), its desorption energy is 174 kJ/mol while on a p(3x3) slab (surface almost twice as covered, ~1.1 ML) it is about 140 kJ/mol showing a clear coverage dependence effect (see Figure 3.4). According to the experimental evaluation of saturation at one anisole for ten Pt, the p(3x3) slab models a close-to-saturation situation (one anisole for nine Pt).

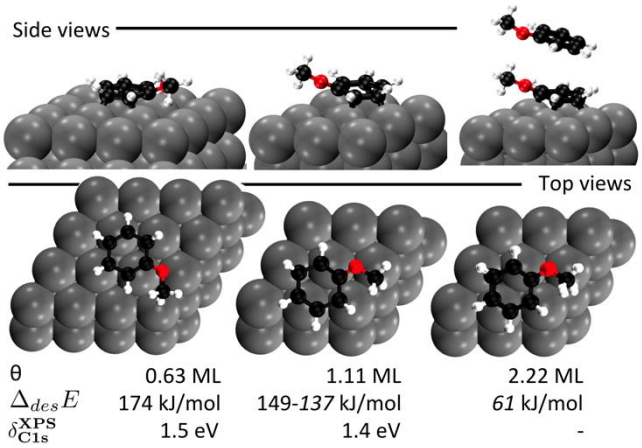

Figure 3.4: Structures of anisole at different coverages θ with their computed integral desorption energies $\Delta_{des}E$. One monolayer (ML) is defined as one molecule of anisole for ten surface platinum atoms. The energies in italics were computed with 14 layers of void between two slabs instead of 5. δ_{C1s}^{XPS} is the computed energy difference between the core level of carbon in the two environments, namely close to other carbons or close to an oxygen atom.

We went further and tried to model the situation corresponding to the bi-layer regime. We started from anisole on a p(3x3) slab and added another anisole molecule on top of the chemisorbed one with the same orientation of the methoxy MeO group (see Figure 3.4, right panel). In order to get rid of any non-physical interaction, we performed – only for this particular calculation – the geometry optimization with a larger void between the metallic slab and its periodic image, equivalent to 14 layers. The obtained structure and desorption energy (61 kJ/mol) must be compared with care to any experimental data. Static DFT is indeed usually not a method of choice to sample the phase space of such a flexible system. Nonetheless the potential energy surface should be rather flat since it is mainly based on weak van der Waals interactions. Therefore the energy should be quite reliable. Additionally, the carbon 1s electron binding energies were calculated for anisole on the p(3x3) and the p(4x4) slab and an XPS spectrum was simulated. The obtained separation $\delta_{\mathrm{C\ 1s}}^{\mathrm{XPS}}$ between the C 1s signal for the C-C and C-O environments was 1.4 eV and 1.5 eV respectively, in good agreement with the measured separation of 1.6 eV.

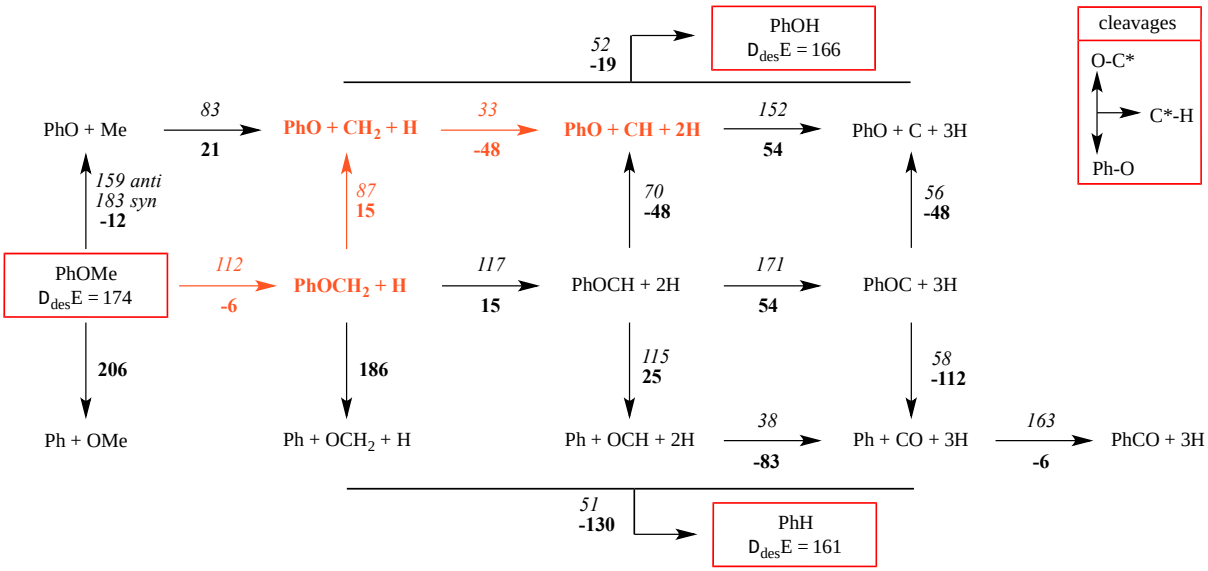

Figure 3.5: Sorted reaction network for the decomposition of anisole on Pt(111): rightward, upward and downward arrows show C-H, C*-O, Ph-O cleavages respectively. We assigned to each arrow the activation energy (in italics) and the reaction energy (in bold) of the elementary step. The reported energies are given in kJ/mol and are not ZPE-corrected. For the demethylation step, anti and syn precise the transition state of interest (see Figure 3.6, for the structures of the transition states).*

To investigate the anisole decomposition mechanism, we have first focused on the reactivity of the methoxy substituent, the carbon atom of which is referred to as C*. We therefore assumed that the phenyl moiety remains intact during the decomposition process. This fair assumption, considering that benzene derivatives are the main desorbing products experimentally, will be discussed later on in the present work. Despite the simplification resulting from this assumption, the decomposition mechanism still involves many bond cleavages: C-O scissions, namely Ph-O and C*-O, on the one hand, and C*-H scissions on the other hand. The resulting reaction network is therefore quite dense and shows many intermediates and transition states. To represent all the ensuing possibilities, we built the sorted reaction network given in Figure 3.5. This diagram gives the reaction and activation energies (except when the reaction is too endothermic) of each elementary step from anisole. For the sake of efficiency, the energies have not been ZPE-corrected since many intermediates have appeared to be chemically irrelevant. In spite of all, the raw data presented here invite interesting comments concerning the reactivity of

anisole on Pt(111). In Figure 3.5, vertical arrows show C-O cleavages: should they point downwards, it is a Ph-O cleavage process otherwise it is a C*-O cleavage. Rightward arrows are associated to C*-H cleavages. Moving to the right in the diagram therefore corresponds to an increase of the dehydrogenation level of C*. If we focus on the Ph-O cleavages (downward arrows), we notice that the reaction gets more and more favored thermodynamically when moving to the right of the diagram with reaction energies going from +206 kJ/mol (for the fully hydrogenated methoxy substituent) to -112 kJ/mol (for the fully dehydrogenated substituent). The Ph-O cleavage is particularly endothermic for anisole and phenoxymethylene $PhOCH_2$: this comes from the associated products, namely methoxy and formaldehyde, that adsorb through an oxygen atom to the not especially oxophilic Pt(111) surface. When the dehydrogenation level of the substituent increases (see Appendix F, Figure F6, for the structures), the resulting products, namely formyl CHO and carbon monoxide CO, start strongly interacting with the Pt(111) surface through their carbon atom: the reaction energies drastically drop then. The activation energies follow the same trend: increasing the dehydrogenation level lowers the barriers. That was also reported in the literature for other oxygenates such as ethanol on Pt(111).[62,63]

The same trends can be observed for the C*-O cleavages (upward arrows) but these steps tend to be kinetically easier and thermodynamically more favored than the Ph-O cleavages (except when the strongly chemisorbed carbon monoxide is formed). This is related to the production of carboradical intermediates CH_x ($x = 1 - 3$) that are particularly stable on platinum. Even phenoxy on Pt(111) can be seen as a carboradical: it has already been reported in the literature[28] that it has an oxocyclohexadienyl structure and it corroborates with the infrared spectrum we computed (see Appendix F, Figure F4). It also explains its particular stability on Pt(111). One C*-O cleavage elementary step shows up as an exception (upper left hand corner): the direct demethylation of anisole into phenoxy and methyl is particularly difficult. Albeit thermodynamically slightly downhill (-12 kJ/mol), the activation barrier is huge (183 kJ/mol) considering a syn-demethylation (Figure 3.6a). Nonetheless we were able to significantly lower this barrier (to 159 kJ/mol) when considering anti-demethylation with an S_N2-like mechanism involving a Walden inversion (Figure 3.6b). As far as we know, this is the first time such a transition state has been reported in the literature for surface platinum catalyzed reactions. Its stability might be addressed to its tighter geometry (bonds about 0.3 Å shorter) that makes the methyl group better interact with both the oxygen atom and the surface. Although that transition state is too high in energy to be of any

relevance later in this work, it might play an important role on other metallic surfaces or with other substituents that might stabilize further more the planar transition state.

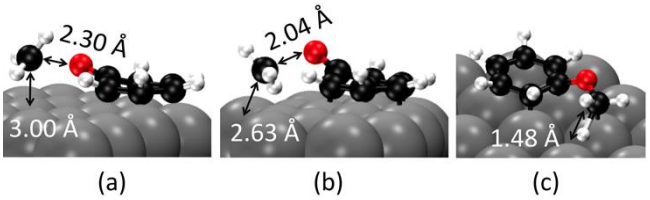

Figure 3.6: Selected transition states from anisole. (a) syn-demethylation ($\widehat{CPtO} = 86°$), (b) anti-demethylation with an SN2-like transition state structure ($\widehat{CPtO} = 123°$), and (c) first dehydrogenation of the methoxy MeO group.

PhO as a pivotal intermediate.

From the previous reactivity screening (Figure 3.5), we extracted the most favorable pathways yielding phenol and benzene and added the ZPE-corrections to build the corresponding free energy profiles at 0 K given in Figure 3.7.

As shown in Figure 3.7, the C*-O cleavage becomes the easiest process after the first dehydrogenation at C*. It leads to phenoxy PhO and methylene CH_2 on the surface, the latter evolving to methylidene CH, which is particularly stable on Pt(111). This agrees, at least qualitatively, with the experimental data of the group of Campbell[64,65] on the methyl-methylene-methylidene equilibrium. Phenoxy PhO is a pivotal intermediate. Its reactivity on the Pt(111) surface can yield either benzene or phenol. First, phenoxy can be very easily hydrogenated to phenol[19] (red path in Figure 3.7): the activation barrier is pretty low ($\Delta^{\ddagger}F = 27$ kJ/mol) and the reaction is thermodynamically favored ($\Delta_r F = -8$ kJ/mol). While phenol is easily formed on the surface, its desorption is rather difficult ($\Delta^{\ddagger}F = 164$ kJ/mol). An alternative consists in deoxygenating phenoxy into phenyl using methylidene CH (blue path in Figure 3.7) or atomic carbon C (green pathway in Figure 3.7). The key transition states towards the formation of phenyl are shown on Figure 3.8. The two overall barriers for benzene formation from phenoxy ($\Delta^{\ddagger}F = 144 - 153$ kJ/mol) are still higher than the one leading to adsorbed phenol, but slightly lower than that for the overall process including the phenol desorption ($\Delta^{\ddagger}F = 156$ kJ/mol). Although this 0 K study seems to support the selectivity for benzene over phenol, it is very delicate to compare barriers of a reaction at the surface and a desorption step since they involve quite different

activation entropies resulting in rates that can be three orders of magnitude different.[53] A more detailed comparison therefore requires including the temperature and entropic contributions.

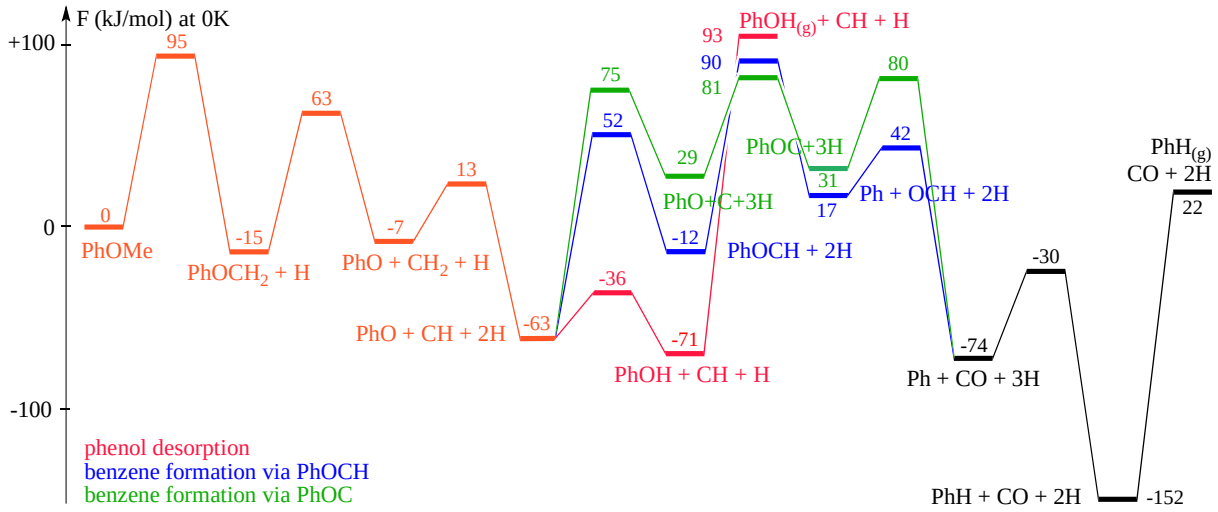

Figure 3. 7: Energy profile (E+ZPE, in kJ/mol) on Pt(111) for the most favored anisole decomposition pathway forming the pivotal PhO (orange) followed by three possible pathways for its further transformation, namely phenol desorption, benzene formation via PhOCH (blue), and benzene formation via PhOC (green).

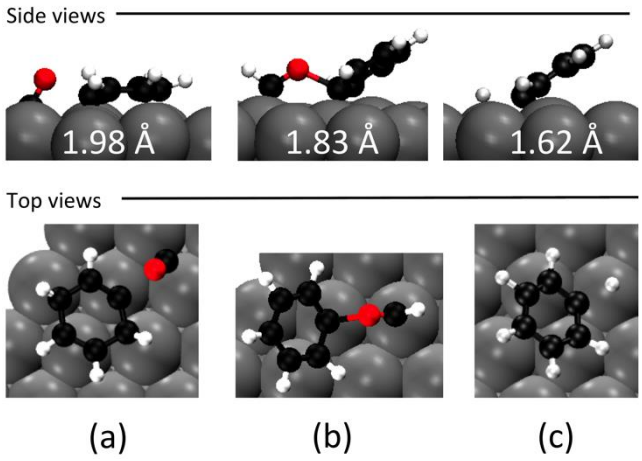

Figure 3.8: Transition states associated to phenyl formation from (a) PhOC and (b) PhOCH and (c) its hydrogenation to benzene. The distance of the bonds that undergoes cleavages are also given.

Entropic contributions

Modeling UHV conditions requires particularly special attention regarding the description of the desorption processes. Albeit endothermic, all the desorption processes become indeed extremely exergonic at higher enough temperature under these conditions. This is all the more important when trying to compare reactions with different amounts of gas phase molecules produced $\Delta_r n_g$:

$PhOMe_{(g)} = PhOH_{(g)} + ½\ H_{2(g)} + CH_{(ads)}$ $\Delta_r n_g = +0.5$ (3.3)

$PhOMe_{(g)} = PhH_{(g)} + H_{2(g)} + CO_{(g)}$ $\Delta_r n_g = +2$ (3.4)

With the stronger increase in the number of gas molecules, benzene is clearly entropically favored, especially at low pressures. We assumed that the UHV chamber atmosphere mainly consists in hydrogen: its partial pressure is therefore well defined and we can calculate its desorption entropy. It is a key parameter since hydrogen is produced on the surface all along the three different pathways described in Figure 3.7. Albeit endothermic ($\Delta_{des}E = 89\ kJ/mol$), hydrogen desorption becomes exergonic – because of the entropic contribution ($\Delta_{des}S(H_2) = 433\ J.mol^{-1}.K^{-1}$) – for temperatures above 206 K. Below this temperature, the decomposition pathways should not change much. Above 206 K, we have to reconsider the steps that involve adsorbed hydrogen: each time hydrogen is produced, an extra exergonic step appears, namely hydrogen desorption, that stabilizes the system by 42 kJ/mol at 400 K. We end up with the free energy profile at 400 K given in Figure 3.9.

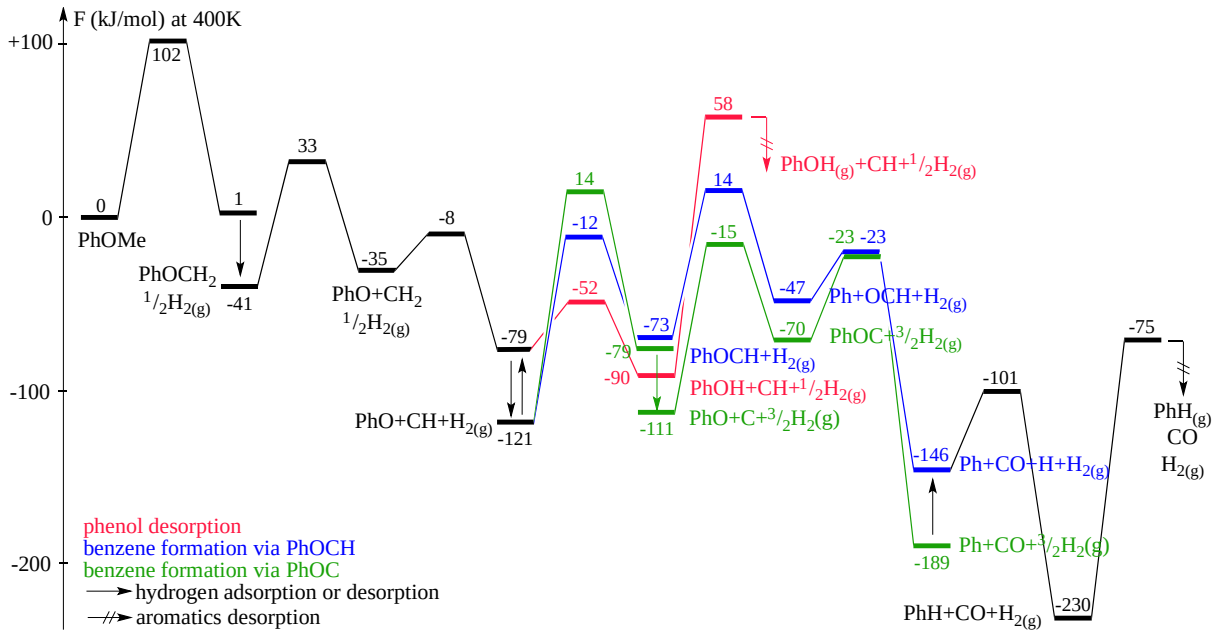

Figure 3.9: Free energy profiles at 400 K in kJ/mol using adsorbed anisole as a reference. Gas phase species are indicated with a (g) label. The barriers for phenol PhOH and benzene PhH desorptions have been estimated with the desorbing transition state model described in the computational section.

As we can see in Figure 3.9, vibrational entropy slightly increases the barrier of the first dehydrogenation step from 95 kJ/mol to 102 kJ/mol. This results likely from the immobilization of the methoxy group with the proper conformation to perform the dehydrogenation with the optimal C-H-Pt alignment (see associated transition state given in Figure 3.6c). Then, with hydrogen desorption, the states {$PhOCH_2$+½$H_{2(g)}$} and {PhO+CH+$H_{2(g)}$} become highly stabilized: this is a consequence of Le Châtelier's principle. These hydrogen desorption processes do not drastically change the barrier involved in the production of benzene via PhOCH (blue path) since the rate determining transition state (Ph-OCH scission, lying at +14 kJ.mol^{-1}) does not involve any hydrogenation or dehydrogenation reactions. The production of benzene via PhOC (green path) is, on the other hand, more impacted by the hydrogen pressure. The dehydrogenation of methylidene CH to carbon C, which was energetically demanding ($\Delta_r E = +92\ kJ/mol$), becomes more favorable ($\Delta_r F = +10\ kJ/mol$) with the help of hydrogen desorption. With a rate determining transition state[66] lying at +14 kJ/mol, the green path becomes as easy as the blue path for the production of benzene. This can be directly related to the number of hydrogen released in

the gas phase: 3/2 $H_{2(g)}$ in the case of the green path and 1 $H_{2(g)}$ for the blue path. With the release of only ½ $H_{2(g)}$, the production of phenol is clearly limited by the increase of the temperature: the desorption of phenol becomes much more difficult to reach ($\Delta^{\ddagger}F = 179\ kJ/mol$) from the rate determining intermediate {PhO+CH+$H_{2(g)}$}. The desorbing transition state associated to phenol desorption is admittedly stabilized by its 2D translational entropy but not as much as the intermediate {PhO+CH+$H_{2(g)}$}. Under TPD conditions, benzene formation is therefore easier than phenol production, with an overall effective activation barrier of 135 kJ/mol vs. 179 kJ/mol at 400 K, even though the conditions are much less reductive (low hydrogen pressure) than under catalytic conditions (large pressures of hydrogen).

Reactivity of the aromatic ring

So far, we have assumed that the aromatic ring remains intact while the methoxy group of anisole undergoes several bond cleavages. As stable as the aromatic moieties might be, the drastic conditions of the UHV chamber favors all the dehydrogenation steps by generating gas phase hydrogen, as we have already mentioned in the previous part. In our attempt to understand the intrinsic reactivity of the most representative aromatic intermediates, we have therefore screened the reactivity of several aromatic oxygenates, namely phenoxy, phenol, and anisole, toward C-H cleavages. The energetics (no ZPE-correction) of the first dehydrogenation step is given in Table 3.2. As a result of the adsorption of the aromatic ring at the bri30 site on Pt(111), no aromatic hydrogen atoms are equivalent. We labeled them with the usual *o*, *m*, and *p* tags (for *ortho*, *meta* and *para*) and we added the π/σ distinction (defined in Figure 3.10) to indicate whether the considered hydrogen is bound to a π or a σ bonded-to-Pt carbon atom. Strikingly, all the aromatic dehydrogenation reactions are endothermic and most of them involve huge barriers. The lowest barriers were computed for the *meta-σ* position, and, among the aromatic oxygenates studied, phenoxy shows the lowest energetic barrier ($\Delta^{\ddagger}\mathrm{E} = 128\ \mathrm{kJ/mol}$). This *meta* dehydrogenation was also reported by Ihm *et al.*[28] as being a key step in the aromatic ring decomposition of phenoxy. Along with another dehydrogenation in *ortho* (or *para*, but less likely scenario) they mention two C-C bond cleavages (*ipso-ortho* and *meta-para*) to form carbon monoxide CO and carbonaceous species on Pt(111). Using the same approach as in Figure 3.5, we studied the different C-C cleavages as a function of the hydrogen content of the aromatic ring (see Appendix F, Figure F5). Two routes have appeared to be chemically relevant: the first one consists of two *ipso-ortho* C-C

cleavages followed by the aforementioned *meta*-dehydrogenation while the second one starts with the *meta*-dehydrogenation to afford an intermediate that decarbonylates with two subsequent *ipso-ortho* C-C cleavages (see Figure 3.11). At 0 K, the first mechanism shows a lower barrier ($\Delta^{\ddagger}F = 162\ \mathrm{kJ/mol}$) than the second one ($\Delta^{\ddagger}F = 186\ \mathrm{kJ/mol}$). Although the first mechanism should be preferred at lower temperatures, the barrier is far too big to be affordable. Increasing the temperature has almost no impact on the first mechanism ($\Delta^{\ddagger}F = 159\ \mathrm{kJ/mol}$) but drastically changes the free energy landscape of the second one: the overall barrier of the latter strongly declines to $\Delta^{\ddagger}F = 113\ \mathrm{kJ/mol}$. This second route, which was locked at lower temperatures, opens up with the help of hydrogen desorption. The associated rate-determining step switches to the meta-dehydrogenation at temperatures above 600 K. The full decomposition of phenoxy becomes therefore extremely efficient at higher temperatures.

Table 3. 2: First aryl dehydrogenation energetics for adsorbed phenoxy PhO, phenol PhOH and anisole PhOMe. The reaction energies are given in bold and followed by the activation energy in italics. The energies are not ZPE-corrected.

$\mathbf{\Delta_r E}$, $\Delta^{\ddagger}E$ (kJ/mol)	*m*-π	*m*-σ	*o*-π	*o*-σ	*p*-π
PhO	**160**	**70**, *128*	**143**, *204*	**117**, *184*	**116,** *192*
PhOH	**155**	**68**, *150*	**157**, *208*	**82,** *174*	**116,** *163*
PhOMe	*not isolated*	**77**, *141*	**165**, *215*	**110,** *186*	**93,** *161*

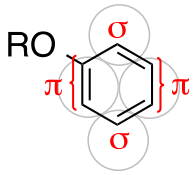

Figure 3.10: Labeling of the aromatic carbons for the flat-lying geometry of the organic species adsorbed at the bri30 site on Pt(111). Underlying Pt atoms shown as grey circles.

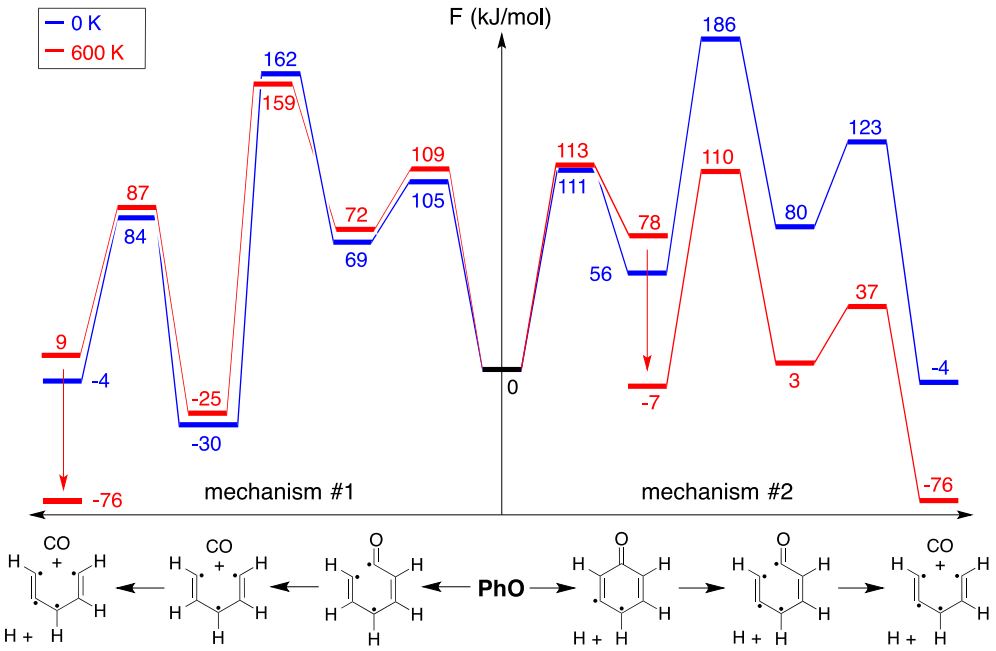

Figure 3.11: Decarbonylation of phenoxy into carbon monoxide and carbonaceous species.

3.6 Discussion

In our surface science experiments, anisole is deposited on a Pt(111) surface under Ultra High Vacuum (UHV) conditions at 110 K under higher and lower exposure conditions. Upon heating, four products desorb molecularly, namely anisole, hydrogen, benzene, and carbon monoxide. Interestingly enough, phenol has not been observed, while it is one of the main products in the hydrodeoxygenation reaction of aromatic oxygenates over the Pt/Al_2O_3 catalyst. Our approach, that combines results from TPD and XPS experiments on the one hand and DFT calculations on the other hand, allows us to address this selectivity for benzene over phenol under TPD conditions. We propose the reaction scheme given in Figure 3.12. Under higher exposure conditions, the XPS spectra shows two C 1s peaks one for carbon atoms bound to other carbon atoms and the other for carbon atoms bond to oxygen atoms. The concurrent intensity decrease of the two C 1s peaks at 240 K, *ie*. at a rather low temperature, suggests that part of the anisole molecules are weakly bound to the surface and desorb easily. The TPD experiments estimate their desorption energy at 83 kJ/mol. This is in fair agreement with the DFT computed energy of 61 kJ/mol for a physisorbed layer on top of the flat-lying chemisorbed layer as shown in Figure 3.4.

Those desorption energies are slightly higher than the vaporization enthalpy of anisole (which is about 40 kJ/mol[67]), as expected. Above 260 K, we end up with a mono or sub-monolayer chemisorbed system that is not necessarily equivalent to a submonolayer deposited directly. Evidence of the likely difference in the submonolayer regime can be found by the different ratio of reaction pathways. That is, upon initial adsorption of multilayers, the fraction of reaction leading to benzene products becomes dominant (see Figure 3.3).

Under lower exposure conditions ($\leq$ 1 ML), the chemisorbed layer can keep desorbing molecularly. TPD experiments show indeed a molecular desorption peak at 360 K for a coverage about 1 ML and another one at 400 K at a coverage of 0.9 ML. This temperature shift reflects a variation of the experimental desorption energies from 121 kJ/mol to 131 kJ/mol that likely results from a decrease of the lateral interactions on a less crowded surface. DFT depicts well the desorption process with an energy of about 140 kJ/mol for a coverage of 1 ML that increases to 170 kJ/mol at 0.6 ML. No corresponding anisole desorption TPD signal could be observed at such a low coverage since desorption has become energetically too difficult to happen, and other reaction processes can take place.

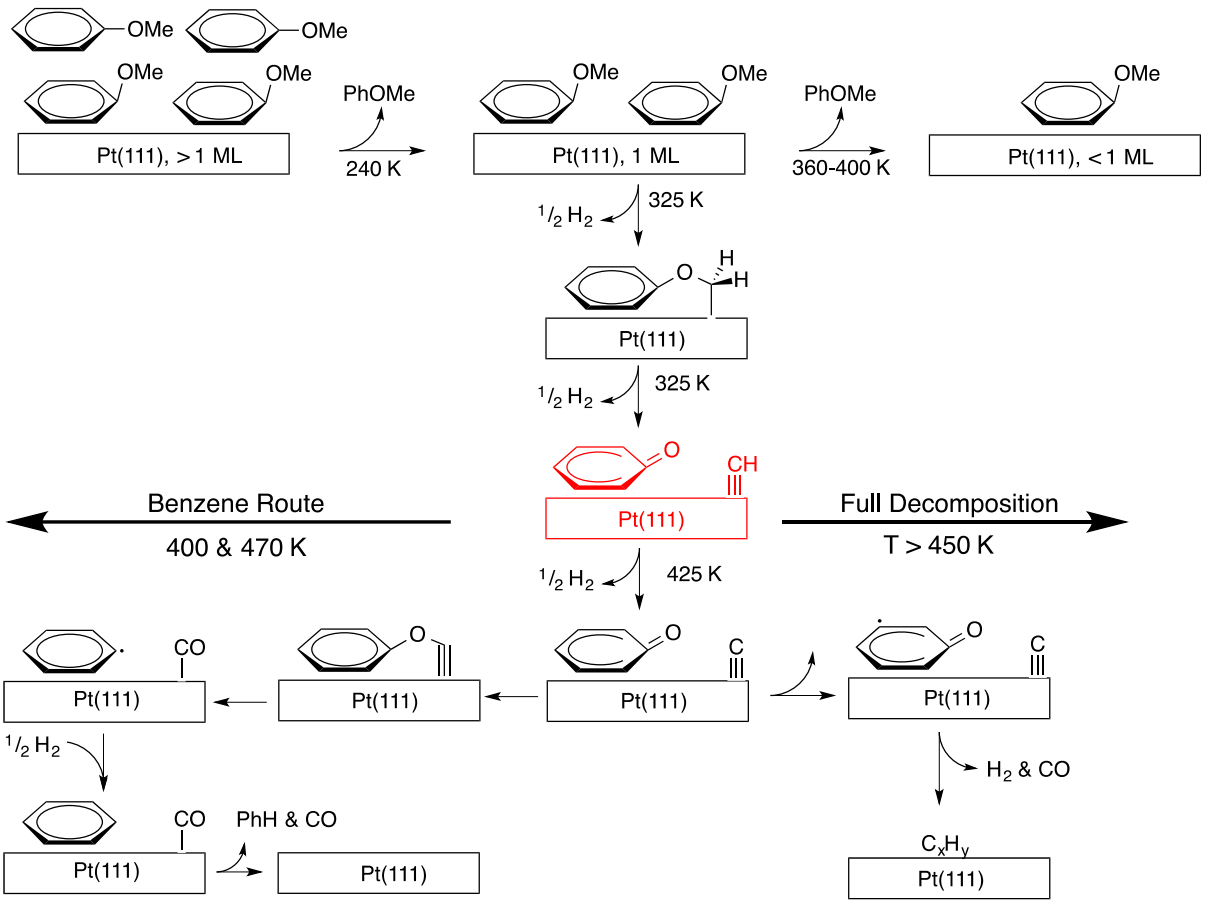

Figure 3.12: Proposed mechanism for anisole decomposition under UHV conditions on Pt(111) built form our DFT calculations and surface science experiments (the temperatures correspond to the TPD peaks).

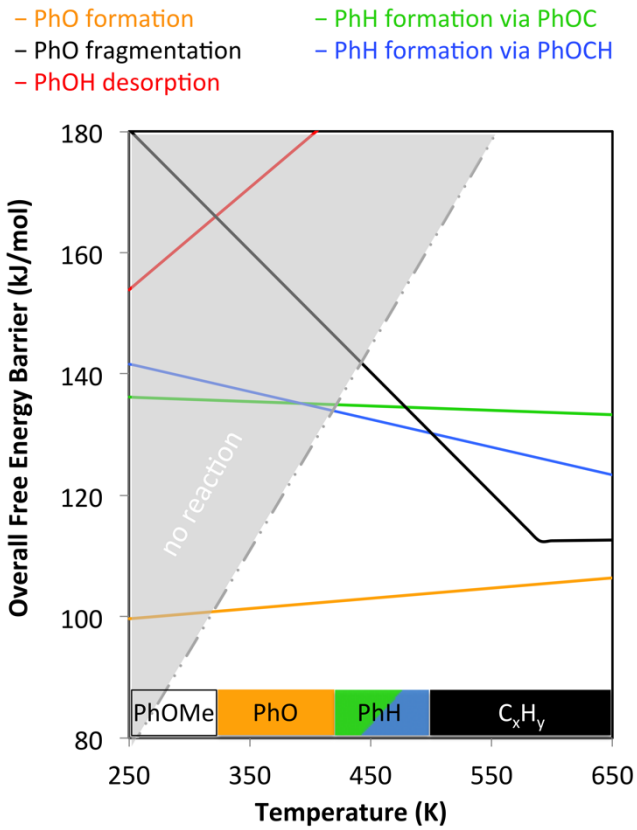

Figure 3.13: Free energy barriers as a function of temperature of the rate-determining steps associated to the four proposed mechanisms, after phenoxy formation (orange). The dotted curve splits the diagram in a kinetically forbidden and a kinetically allowed domain under the TPD conditions. The molar entropies were calculated at 400 K and assumed constant over the temperature range (Ellingham Approximation).

Our DFT investigation has lead us to consider many reactions. From the easy production of the pivotal phenoxy PhO intermediate, we have proposed two routes for benzene formation and one for phenol production. The competing fragmentation of phenoxy into carbonaceous species and carbon monoxide has also been described. Even if this whole inspection allows us to explain qualitatively the selectivity for benzene over phenol and the large amount of hydrogen released at higher temperatures, the comparison between DFT and TPD results remains, as things stand, out of range, since TPD gives temperatures and DFT free energies. To overcome this issue we plotted, see Figure 3.13, the overall barrier of free energy of each process as a function of temperature (solid curves). The dotted gray line splits the diagram into two domains: the upper gray half-space corresponds to kinetically difficult processes, and the lower white half-space shows kinetically

crossable barriers (see Appendix F for the mathematical development). With this new tool that we introduced, one can now give a detailed comparison between DFT and TPD to support the scheme given in Figure 3.12.

In Figure 3.13, the lowest barrier corresponds to the dehydrogenation of anisole PhOMe into {$PhOCH_2$+H} (orange line). This barrier is not much temperature-dependent and remains about 100 kJ/mol over the whole temperature range. Nonetheless, such a barrier is too high to be crossed at temperatures around 250 K, where anisole is predicted to be kinetically stable. When the temperature reaches 320 K, the orange curve crosses the kinetically forbidden gray domain to enter the kinetically allowed white half-space: the associated dehydrogenation of the methoxy substituent starts being effective. It is readily followed by a C*-O cleavage and another dehydrogenation process to yield phenoxy, methylidene and dihydrogen {$PhO+CH+H_{2(g)}$}, a state showing a particular stability ($\Delta_r F = -121$ kJ/mol at 400K). This is in excellent agreement with the TPD experiments that show one peak for hydrogen desorption at 325 K. This peak is particularly intense since it is associated to the desorption of two hydrogen atoms from anisole (over a total of 8 hydrogen atoms available). From the rate-determining intermediate state[66] {$PhO+CH+H_{2(g)}$} the overall free energy barriers to phenol (red curve), benzene (blue and green curves since two mechanisms have been studied), and coke formation (black curve) are also reported in Figure 3.13. The required adsorption of hydrogen (which is particularly endergonic under UHV conditions) for phenol production makes the phenolic route more and more difficult with the increase of temperature. This explains why no signal corresponding to phenol could have been detected in the TPD experiments.

Above 420 K, the overall barrier of benzene production via the rate-determining transition state {$PhO+[C\cdots H]^{\ddagger}+H_{2(g)}$} intersects the limit between the kinetically forbidden and kinetically allowed domains. We note that the other mechanism via the rate-determining transition state {$[Ph\cdots OCH]^{\ddagger}+H_{2(g)}$} is also possible from our DFT calculations. Nonetheless the shoulder at 425 K in the TPD of hydrogen seems to be consistent with the path through {$PhO+[C\cdots H]^{\ddagger}+H_{2(g)}$}. Therefore, hydrogen is produced from methylidene and further reaction steps readily follow and yield benzene. It agrees well with the TPD results that show a small hydrogen peak at 425 K and also a broad peak for benzene desorption at about 400 K (left path in Figure 3.12).

Above 450 K, the rate-determining transition state associated to the *ipso-ortho* C-C cleavage starts being reachable with the increased exergonicity resulting from the desorption of

hydrogen and yield carbonaceous species (black curve in Figure 3.13). According to those DFT predictions, phenoxy can indeed undergo a dehydrogenation at the *meta* position, which seems to open up the route to the total decomposition of phenoxy into carbon monoxide, hydrogen, and carbonaceous species. This route becomes predominant over 500 K (lower barrier than phenol and benzene productions). This is consistent with the TPD experiments that show the formation of hydrogen at 460 K and carbon monoxide at 470 K. This is supported by the XPS experiments that show the disappearing of the peak associated to carbon atoms bound to oxygen atoms: a C-O bond(s) containing species desorbs upon heating leaving hydrogenated carbonaceous fragments behind on the surface. The TPD of hydrogen is also to be compared with the one *Ihm et al.* [28] obtained when they studied the TPD of phenol on Pt(111). They show the same "peak-shoulder-band" pattern for hydrogen desorption over 460 K, which was attributed to the decomposition of phenoxy into $\{C_3H_3+CO+C_2+H_{2(g)}\}$ (460 K peak) and then $\{Cx+5/2H_{2(g)}+CO_{(g)}\}$ (600 K band). The shoulder was interpreted by *Ihm et al.*[28] as being the superposition of the peak at lower temperatures and the band at higher temperatures. It stands as an indirect evidence that phenoxy is indeed produced on the surface in our TPD experiments of anisole on Pt(111). They also estimated the overall barrier of this decomposition mechanism at 128 kJ/mol and attributed it to the rate-determining dehydrogenation of phenoxy at the *meta* position. Our DFT calculations suggest indeed that the barrier lies between 110 to 130 kJ/mol when the fragmentation of phenoxy becomes predominant. For temperature above 600 K, the rate-determining step is also predicted to be the *meta*-dehydrogenation (black curve in Figure 3.13).

All in all, the chemically relevant regime under TPD conditions is then between 420 and 490 K. At low temperatures, the productions of benzene and phenol compete, but the surface is not hot enough to have the aromatic compounds desorb. When the temperature increases, hydrogen desorption gets more and more exergonic. It therefore favors the dehydrogenation processes and disfavors the hydrogenation processes. That is why the production of phenol through phenoxy hydrogenation gets more and more difficult with the increase of temperature, whereas benzene production is almost not impacted by the temperature variations. Eventually large amounts of hydrogen can be produced upon coke formation: even if this route is particularly difficult energetically, it is entropically aided and becomes the predominant path above 500 K.

Although realistic catalytic conditions are far from the TPD conditions, this study points out the central role of phenoxy and methylidene, on the one hand, and hydrogen desorption, on the other hand, in hydrodeoxygenation reactions of aromatic oxygenates extracted from lignin.

The kinetically favored initial reaction is the dehydrogenation of the methyl group followed by the C*-O bond cleavage to yield phenoxy. In lieu of getting hydrogenated, it reacts with the carbonaceous species generated from the methyl group of anisole itself. The actual reducing agents are hence adsorbed atomic carbon atoms or methylidene (depending on the considered mechanism) and not hydrogen. This "hook-back" mechanism, performed by atomic carbon atoms adsorbed on the surface, is especially favored since it leads to the particularly stable carbon monoxide adsorbate. This chemistry is to be compared to the oxygen removal from furfural on Pt(111) mediated with an atomic zinc co-adsorbate that stands as the actual reducing agent.[68]

Even though hydrogen might not be as crucial as expected to deoxygenate aromatic compounds, it still plays a key role. At a slightly higher temperature, the dehydrogenation of the adsorbates does not only affect the methyl group but also the aryl moieties. This results in the total decomposition of the organic compounds into coke. Under catalytic conditions, the hydrogen pressure (ranging from about one atmosphere to tens of bars) prevents this aryl decomposition. Nonetheless hydrogen desorption is much less favored and the selectivity of benzene over phenol is lost. Moreover a methane production pathway may also be possible under catalytic conditions, so that the reducing carbonaceous species get removed from the surface. All in all, phenolic derivatives indeed turn out to be the main products in hydrodeoxygenation performed over Pt/Al_2O_3 under catalytic conditions.[10,69]

3.7 Conclusion

In this article, we carefully studied the decomposition of anisole at a Pt(111) surface, a platform molecule in the transformation of lignin into valuable compounds. From surface science experiments (TPD and XPS), we showed that the anisole decomposition in ultra high vacuum experiments yields mainly benzene and not phenol, in contrast with the catalytic tests performed with supported Pt catalysts under a H_2 atmosphere.

To rationalize those observations, we performed an extensive analysis of the reaction mechanism based on DFT using the optPBE functional and a periodic slab model. We carefully assessed the adsorption of anisole at various coverages from 0.6 ML to the physisorbed second

layer. Then, a kinetic analysis based on our DFT data shows an excellent agreement with the TPD spectra we obtained experimentally, validating the reaction mechanism we proposed here. The critical intermediate is phenoxy PhO co-adsorbed with methylidene CH. As far as we understand the system, the pressure of hydrogen tunes the selectivity of the subsequent branching reactions. Under UHV conditions, the hydrogenation reactions are all extremely difficult and phenol is therefore not produced. Carbonaceous species, which cannot be hydrogenated into methane for example, remain on the surface and efficiently perform the deoxygenation of phenoxy around 400 K. Above 450 K, phenoxy gets even more dehydrogenated leading to the full decomposition of phenoxy into coke and carbon monoxide.

Based on this study, we can now propose a better design of hydrodeoxygenation catalysts. To prevent the formation of coke, a sufficient pressure of H_2 is required. However to facilitate the formation of benzene over phenol, we need to promote the Ph-O breaking with a reducing agent able to stabilize the liberated oxygen atom. Promoters such as atomic zinc adsorbed on the platinum surface have been successful in the deoxygenation of furfural and very recently anisole.[68,70] In addition to the stabilization of the oxygen atom, it weakens the C=O double bond: this might explain why it works with the deoxygenation of phenolics since phenoxy, the rate determining intermediate, has a strong C-O bond that structurally looks like a double bond.

References

(1) Zakzeski, J.; Bruijnincx, P. C. A.; Jongerius, A. L.; Weckhuysen, B. M. *Chem. Rev.* **2010**, *110*, 3552–3599.

(2) Ragauskas, A. J.; Beckham, G. T.; Biddy, M. J.; Chandra, R.; Chen, F.; Davis, M. F.; Davison, B. H.; Dixon, R. a; Gilna, P.; Keller, M.; Langan, P.; Naskar, A. K.; Saddler, J. N.; Tschaplinski, T. J.; Tuskan, G. a; Wyman, C. E. *Science (80-.).* **2014**, *344*, 1246843.

(3) Li, C.; Zhao, X.; Wang, A.; Huber, G. W.; Zhang, T. *Chem. Rev.* **2015**, *115*, 11559–11624.

(4) Laurent, E.; Delmon, B. *Ind. Eng. Chem. Res.* **1993**, *32*, 2516–2524.

(5) Laurent, E.; Delmon, B. *Appl. Catal. A Gen.* **1994**, *109*, 77–96.

(6) Romero, Y.; Richard, F.; Brunet, S. *Appl. Catal. B Environ.* **2010**, *98*, 213–223.

(7) Jongerius, A. L.; Jastrzebski, R.; Bruijnincx, P. C. A.; Weckhuysen, B. M. *J. Catal.* **2012**, *285*, 315–323.

(8) Wang, H.; Male, J.; Wang, Y. *ACS Catal.* **2013**, *3*, 1047–1070.

(9) Wildschut, J.; Mahfud, F. H.; Venderbosch, R. H.; Heeres, H. J. *Ind. Eng. Chem. Res.* **2009**, *48*, 10324–10334.

(10) Nimmanwudipong, T.; Runnebaum, R. C.; Block, D. E.; Gates, B. C. *Energy & Fuels* **2011**, *25*, 3417–3427.

(11) Runnebaum, R. C.; Nimmanwudipong, T.; Block, D. E.; Gates, B. C. *Catal. Letters* **2011**, *141*, 817–820.

(12) Zhu, X.; Lobban, L. L.; Mallinson, R. G.; Resasco, D. E. *J. Catal.* **2011**, *281*, 21–29.

(13) Gao, D.; Xiao, Y.; Varma, A. *Ind. Eng. Chem. Res.* **2015**, *54*, 10638–10644.

(14) Saidi, M.; Rahimpour, M. R.; Raeissi, S. *Energy & Fuels* **2015**, *29*, 3335–3344.

(15) Zhu, X.; Nie, L.; Lobban, L. L.; Mallinson, R. G.; Resasco, D. E. *Energy & Fuels* **2014**, *28*, 4104–4111.

(16) Foo, G. S.; Rogers, A. K.; Yung, M. M.; Sievers, C. *ACS Catal.* **2016**, *6*, 1292–1307.

(17) Pepper, J. M.; Fleming, R. W. *Can. J. Chem.* **1978**, *56*, 896–898.

(18) Pepper, J. M.; Lee, Y. W. *Can. J. Chem.* **1969**, *47*, 723–727.

(19) Honkela, M. L.; Björk, J.; Persson, M. *Phys. Chem. Chem. Phys.* **2012**, *14*, 5849–5854.

(20) Lee, K.; Gu, G. H.; Mullen, C. A.; Boateng, A. A.; Vlachos, D. G. *ChemSusChem* **2015**, *8*, 315–322.

(21) Gu, G. H.; Mullen, C. A.; Boateng, A. A.; Vlachos, D. G. *ACS Catal.* **2016**, *6*, 3047–3055.

(22) Lu, J.; Heyden, A. *J. Catal.* **2015**, *321*, 39–50.

(23) Chiu, C.; Genest, A.; Borgna, A.; Rösch, N. *Phys. Chem. Chem. Phys.* **2015**, *17*, 15324–15330.

(24) Chiu, C.; Genest, A.; Borgna, A.; Rösch, N. *ACS Catal.* **2014**, *4*, 4178–4188.

(25) Lu, J.; Behtash, S.; Mamun, O.; Heyden, A. *ACS Catal.* **2015**, *5*, 2423–2435.

(26) Xu, X.; Friend, C. M. *J. Phys. Chem.* **1989**, *93*, 8072–8080.

(27) Serafin, J. G.; Friend, C. M. *Surf. Sci.* **1989**, *209*, 163–175.

(28) Ihm, H.; White, J. M. *J. Phys. Chem. B* **2000**, *104*, 6202–6211.

(29) Tan, Y. P.; Khatua, S.; Jenkins, S. J.; Yu, J.-Q.; Spencer, J. B.; King, D. a. *Surf. Sci.* **2005**, *589*, 173–183.

(30) Norton, P. R.; Davies, J. A.; Jackman, T. E. *Surf. Sci.* **1982**, *122*, 593–600.

(31) Kresse, G.; Hafner, J. *Phys. Rev. B* **1993**, *47*, 558–561.

(32) Kresse, G.; Furthmüller, J. *Phys. Rev. B* **1996**, *54*, 11169–11186.

(33) Kresse, G.; Furthmüller, J. *Comput. Mater. Sci.* **1996**, *6*, 15–50.

(34) Dion, M.; Rydberg, H.; Schröder, E.; Langreth, D. C.; Lundqvist, B. I. *Phys. Rev. Lett.* **2004**, *92*, 246401.

(35) Klimeš, J.; Bowler, D. R.; Michaelides, A. *J. Phys. Condens. Matter* **2010**, *22*, 022201.

(36) Yildirim, H.; Greber, T.; Kara, A. *J. Phys. Chem. C* **2013**, *117*, 20572–20583.

(37) Gautier, S.; Steinmann, S. N.; Michel, C.; Fleurat-Lessard, P.; Sautet, P. *Phys. Chem. Chem. Phys.* **2015**, *17*, 28921–28930.

(38) Kresse, G.; Joubert, D. *Phys. Rev. B* **1999**, *59*, 1758–1775.

(39) Monkhorst, H. J.; Pack, J. D. *Phys. Rev. B* **1976**, *13*, 5188–5192.

(40) Henkelman, G.; Uberuaga, B. P.; Jónsson, H. *J. Chem. Phys.* **2000**, *113*, 9901.

(41) Sheppard, D.; Terrell, R.; Henkelman, G. *J. Chem. Phys.* **2008**, *128*, 134106.

(42) Henkelman, G.; Jónsson, H. *J. Chem. Phys.* **1999**, *111*, 7010.

(43) Heyden, A.; Bell, A. T.; Keil, F. J. *J. Chem. Phys.* **2005**, *123*, 224101.

(44) Kästner, J.; Sherwood, P. *J. Chem. Phys.* **2008**, *128*, 014106.

(45) Gottfried, J. M.; Vestergaard, E. K.; Bera, P.; Campbell, C. T. *J. Phys. Chem. B* **2006**, *110*, 17539–17545.

(46) Köhler, L.; Kresse, G. *Phys. Rev. B* **2004**, *70*, 165405.

(47) Jugnet, Y.; Loffreda, D.; Dupont, C.; Delbecq, F.; Ehret, E.; Cadete Santos Aires, F. J.; Mun, B. S.; Aksoy Akgul, F.; Liu, Z. *J. Phys. Chem. Lett.* **2012**, *3*, 3707–3714.

(48) Christmann, K.; Ertl, G.; Pignet, T. *Surf. Sci.* **1976**, *54*, 365–392.

(49) Lu, K. E.; Rye, R. R. *Surf. Sci.* **1974**, *45*, 677–695.

(50) Steininger, H.; Lehwald, S.; Ibach, H. *Surf. Sci.* **1982**, *123*, 264–282.

(51) Norton, P. R.; Goodale, J. W.; Selkirk, E. B. *Surf. Sci.* **1979**, *83*, 189–227.

(52) Nieskens, D. L. S.; van Bavel, A. P.; Niemantsverdriet, J. W. *Surf. Sci.* **2003**, *546*, 159–169.

(53) Campbell, C. T.; Árnadóttir, L.; J. R. V. Sellers. *Zeitschrift für Phys. Chemie* **2013**, *227*,

1435–1454.

(54) Campbell, C. T.; Sellers, J. R. V. *J. Am. Chem. Soc.* **2012**, *134*, 18109–18115.

(55) Campbell, C. T.; Sellers, J. R. V. *J. Am. Chem. Soc.* **2013**, *135*, 13998–13998.

(56) Chase, Jr., M. W.; Davies, C. A.; Downey, Jr., J. R.; Frurip, D. J.; McDonald, R. A.; Syverud, A. N. *NIST JANAF thermodynamical tables 1985*; National Institue of Standard and Technology, 1986.

(57) Ihm, H.; Ajo, H. M.; Gottfried, J. M.; Bera, P.; Campbell, C. T. *J. Phys. Chem. B* **2004**, *108*, 14627–14633.

(58) McEwen, J.-S.; Payne, S. H.; Kreuzer, H. J.; Kinne, M.; Denecke, R.; Steinrück, H.-P. *Surf. Sci.* **2003**, *545*, 47–69.

(59) Bonalumi, N.; Vargas, A.; Ferri, D.; Baiker, A. *J. Phys. Chem. B* **2006**, *110*, 9956–9965.

(60) Réocreux, R.; Huynh, M.; Michel, C.; Sautet, P. *J. Phys. Chem. Lett.* **2016**, *7*, 2074–2079.

(61) Bonalumi, N.; Vargas, A.; Ferri, D.; Bürgi, T.; Mallat, T.; Baiker, A. *J. Am. Chem. Soc.* **2005**, *127*, 8467–8477.

(62) Liu, B.; Greeley, J. *J. Phys. Chem. C* **2011**, *115*, 19702–19709.

(63) Ferrin, P.; Simonetti, D.; Kandoi, S.; Kunkes, E.; Dumesic, J. a.; Nørskov, J. K.; Mavrikakis, M. *J. Am. Chem. Soc.* **2009**, *131*, 5809–5815.

(64) Karp, E. M.; Silbaugh, T. L.; Campbell, C. T. *J. Phys. Chem. C* **2013**, *117*, 6325–6336.

(65) Wolcott, C. A.; Green, I. X.; Silbaugh, T. L.; Xu, Y.; Campbell, C. T. *J. Phys. Chem. C* **2014**, *118*, 29310–29321.

(66) Kozuch, S.; Martin, J. M. L. *ChemPhysChem* **2011**, *12*, 1413–1418.

(67) Chickos, J. S.; Acree, W. E. *J. Phys. Chem. Ref. Data* **2003**, *32*, 519–878.

(68) Shi, D.; Vohs, J. M. *ACS Catal.* **2015**, *5*, 2177–2183.

(69) Saidi, M.; Rostami, P.; Rahimpour, H. R.; Roshanfekr Fallah, M. A.; Rahimpour, M. R.; Gates, B. C.; Raeissi, S. *Energy and Fuels* **2015**, *29*, 4990–4997.

(70) Shi, D.; Arroyo-Ramírez, L.; Vohs, J. M. *J. Catal.* **2016**, *340*, 219–226.

Chapter 4:
Adsorption and Decomposition of a Lignin β-O-4 Linkage Model, 2-phenoxyethanol, on Pt(111): Combination of Experiments and First Principles Calculations

I performed all the XPS and TPD experiments, and XPS prediction by density functional theory calculations for the reactivity of 2-phenoxyethanol on Pt(111). I performed all the analysis and interpretation related to the experimental results. Romain Réocreux performed all the DFT calculations (except the XPS predictions) and related analysis.

4 Adsorption and Decomposition of a Lignin β-O-4 Linkage Model, 2-phenoxyethanol, on Pt(111): Combination of Experiments and First Principles Calculations

Cherif A. Ould Hamou,[†,§] Romain Réocreux,[‡] Philippe Sautet,[‡,&] Carine Michel,[‡,*] Javier B. Giorgi,[†,‖,*]

[†] Centre for Catalysis Research and Innovation, [§] Department of Physics, [‖] Department of Chemistry and Biomolecular Sciences, University of Ottawa, 10 Marie Curie Pvt., Ottawa, Ontario, Canada. K1N 6N5.
[‡] Univ Lyon, Ens de Lyon, CNRS UMR 5182, Université Claude Bernard Lyon 1, Laboratoire de Chimie, F-69342, Lyon, France
[&] Department of Chemical and Biomolecular engineering, University of California, Los Angeles, Los Angeles, CA 90095, United States

Abstract

To sustain the current attempts in valorizing lignin-based derivatives, this study focuses on the decomposition upon a temperature ramp of 2-phenoxyethanol, a model for the β-O-4 linkage in lignin, on a Pt(111) surface. Under ultra-high vacuum conditions, benzene, hydrogen and carbon monoxide are the main desorbing products. Although benzene is the only aromatic desorbed product at low initial molecular coverages, very small amounts of phenol can be detected at higher initial coverage. Combining X-ray photoelectron spectroscopy and temperature programmed desorption experiments together with density functional theory calculations, a reaction mechanism is suggested, starting with the OH bond scission. Phenoxy, PhO, is proposed as a key surface intermediate that preferentially deoxygenates rather than desorbs as phenol, similarly to the case of anisole. This behavior, typical of ultra-high vacuum conditions, is attributed to the reducing properties of carbonaceous surface species that efficiently deoxygenate phenoxy and afford the formation of the very stable carbon monoxide.

Key-words: 2-phenoxyethanol, mechanism, decomposition, TPD, DFT, XPS, lignin

4.1 Introduction

Biomass is a sustainable and renewable feedstock for potentially high value chemicals that, due to its abundance, could theoretically supply the world demand.[1] Alternatively it could produce up to 10%-14% of the world's energy usage.[2] Lignin, an important biomass component, is the second most abundant polymer in wood and represents up to 40% of the dry biomass weight. While the lignin specific formulation is variable,[3–5] each of its monomers consists of one aromatic oxygenate unit. The removal of oxygen to produce higher value compounds is a necessity but it still remains one of the challenging tasks for lignin exploitation (via pyrolysis, hydrolysis, oxidation, etc).[6,7] Pyrolysis is the most studied method for conversion of lignin and removal of oxygen linkages. It is an effective method to liquefy lignin in order to produce bio-oils.[8,9] However, the separation of the products can be challenging and costly. In contrast, heterogeneous catalysis seems to be the key solution for the conversion of lignin, as the products and the catalyst can be easily separated. Regardless, since thermal decomposition leads to a variable and often uncontrolled product range of the target products, catalysis plays an essential role in making biomass conversion viable for valorization by reducing activation energies for reaction and guiding product selectivity. 2-phenoxyethanol (2-PE), with its aryl and alkyl ether function, is used here as a model of the quintessential β-O-4 linkage, one of lignin's dominant structural motifs which provides more than half of the linkage structures. In this study that combines surface science and modeling, its reactivity is investigated on the platinum Pt(111) model surface as a model catalyst in order to compare the facility of the C-H versus C-O versus C-C bonds cleavage (Figure 4.1).

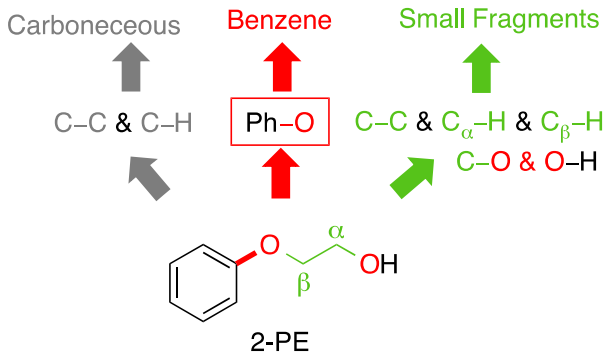

Figure 4.1: Potential decomposition pathways 2-phenoxyethanol (2-PE): in grey, the fragmentation of the aromatic ring; in red the targeted Ph-O cleavage; in green, the decomposition of the ethanol arm.

As a substituted aromatic compound, 2-PE can undergo a decomposition scheme that is, in principle, related to simpler aromatics like phenol, anisole, etc. Single crystal investigations of aromatic oxygenates on transition metal surfaces have shown different preferences in C-H, C-O and C-C bond cleavage.[10–13] The decomposition pathways of aromatics are strongly dependent on the coverage of adsorbed molecules on the surface and the interaction strength of the aromatic ring with the catalyst.[10–13]

In the study of the binding of lignin model molecules such as 2-PE to a metal surface, the importance of the aromatic ring is affected by the binding of the phenyl group to oxygen. Molecules with this phenoxy moiety could be expected to behave differently from non oxygenated-aromatics. As such, previous studies of phenol-catalyst interactions are relevant. Phenol has been widely studied on different noble metals. On Pt(111), phenol in a multilayer desorbs from the surface at 195 K while in the second layer at 225 K.[11] Between 0.7 to 1 ML, the O-H bond cleavage occurs below 200 K and phenoxy is subject to a competitive reaction pathway. It either generates benzene and surface oxygen, or it decomposes into CO, H_2 and hydrocarbons. Below 0.7 ML coverage, C-C and C-H bond cleavages are more favorable than C-O bond cleavage resulting in a total decomposition into CO, H_2 and graphitic carbon. Upon adsorption of Phenol on Rh(111), the multilayer molecularly desorbs at 210 K. Part of the saturated surface undergoes molecular desorption at 240 K and the remaining molecules on the surface decompose into phenoxy via O-H bond cleavage at temperatures below 300 K.[13] The C-H bond cleavage is observed at 350 K and above. Observable products of desorption are CO and H_2. Whereas on Mo(110), the multilayer desorbs at 210 K and a weakly bond layer desorbs at 240 K. Desorption competes with reaction on the surface, where a phenoxy species is formed below 300 K and subsequently decomposes into H_2, surface oxygen and hydrocarbon fragments. All C-O bond cleavages occur by 450 K[14] (no molecular desorption of CO is observed). No formation of benzene has been reported from the decomposition of phenol on Rh(111) or Mo(110). Similarly, on Ni(110) the phenol multilayer desorbs at 200 K and a non-reactive second layer is observed to desorb at 224 K. The first layer totally decomposes into phenoxy between 250-350 K.[10] Further decomposition of phenoxy leads to the formation of H_2 and CO as the only observed byproducts. Those studies demonstrate the intrinsic differences between the first, second and multilayer behavior, and the presence of phenoxy as an intermediate.

Phenoxy also seems to be a key intermediate in the decomposition of more complex oxygenated aromatics.[12,15–17] As an example, Vohs and co-workers and King and co-workers propose the formation of the phenoxy species as the main intermediate for anisole decomposition on Pt(111) and Pt(100)hex.[15,18] Combining surface science experiments and periodic DFT computations,[12] Réocreux et al. showed that anisole on Pt(111) reaches a saturation coverage of one monolayer (1 ML) corresponding to 7 carbon atoms per 10 platinum atoms on the surface, 7C/10Pt. For a coverage below 1 ML, a small fraction of anisole molecularly desorbs from the surface at 360 K while the majority decomposes into phenoxy via a C-H bond cleavage on the methyl group below 325 K. At higher temperatures, there is a competition between Ph-O bond cleavage, forming phenyl then benzene, and a complete decomposition of the aromatic ring. These results showed that under UHV conditions, the formation of benzene is dominant and it desorbs from the surface at 400 K. Above 450 K, the remaining phenoxy completely decomposes into CO and H_2.

Several studies also demonstrated that the introduction of specific additives promotes the decomposition of oxygenated aromatics. Vohs and co-workers have shown that the introduction of Zn to enhance binding through the oxygen group leads to the preferential breaking of the Ph-O bond.[19] A similar behavior was seen for benzaldehyde on Pt(111).[15] On H_2 pre-covered Pt(111), part of the benzaldehyde molecularly desorbs from the surface at 200K while the rest completely decomposes into CO, H_2 and CH_4, keeping the C-O bond intact. In contrast, on H_2 pre-covered Zn/Pt(111), upon heating to 200 K, part of the benzaldehyde molecularly desorbs from the surface and part of it reacts by breaking the C-O bond and leads to toluene and other compounds. Due to the bonding of the carbonyl oxygen with Zn sites, the C-O bond cleavage is facilitated. In addition, Medlin's group investigated the interaction of benzyl alcohol on Pt(111) and Pt(111)/Mo surfaces using a combination of TPD experiments and DFT calculations.[20] On clean Pt(111), benzyl alcohol mainly decomposes into benzene, CO and H_2. Here also C-C and C-H bond cleavage are favorable. However, upon depositing benzyl alcohol on the Mo modified Pt(111) surface, the decomposition of benzyl alcohol into benzene, CO and H_2 decreases and the production of toluene is observed. The presence of Mo subsurface atoms decreases the strong adsorption of the aromatic ring on the surface, leading to a change in the adsorption geometry of benzyl alcohol that favors the C-O bond cleavage. This example shows that changing the electronic structure of the Pt(111) surface can influence the adsorption energy and geometry of the aromatic molecules. A less strongly adsorbed

aromatic group on the Pt(111) surfaces tends to make C-O bond cleavage accessible. All these examples demonstrate the need for a deoxygenating species on the Pt(111) to break the Ph-O or the C-O bond. In the case of anisole, it has been shown recently that surface carbonaceous species can play this role explaining the formation of benzene under ultra high vacuum conditions[12] in contrast with the selectivity towards phenolics under hydrogenolysis conditions of related molecules.[21–28]

Although the dominant binding of 2-PE to the surface is through the benzene ring, it is expected that at low temperature the aromatic ring remains intact.[11,12,18,19] The early reactivity might therefore be governed by the substituent. In other words, at low temperature, 2-PE can be thought of as a substituted ethanol. The reactivity of such C2 flexible adsorbates (like ethanol or ethylene glycol) has already been reported in the literature.[29,30] Although it depends on both the nature of the surface and the substrate, C-H cleavages are usually rather easy. At a certain dehydrogenation level, the C2 oxygenates can undergo a C-C cleavage. As for the C-O bond, a higher dehydrogenation level is required for the cleavage to proceed on Pt(111).[29,30]

Overall, to understand the different reaction pathways of lignin decomposition, it is important to systematically increase the level of complexity of the model molecules used, as it has recently been reported.[26–28] This work provides a detailed description of the interaction and decomposition pathways of 2-PE on a Pt(111) surface. The focus is on the mutual influence of the arm and the aromatic moiety in regards to the reaction selectivity (in particular, the influence of this flexible oxygenated arm on the Ph-O bond breaking). It will combine detailed DFT calculations with experimental techniques focusing on the 1st layer reactivity of 2-PE on the surface. Experimental results will be presented for X-ray photoelectron spectroscopy (XPS) and temperature programmed desorption (TPD).

4.2 Experimental

Experiments were performed under ultra high vacuum (UHV) in a stainless steel analysis chamber with a base pressure of 5×10^{-10} mbar. The Pt(111) crystal surface was cleaned by repetitive cycles of 15 min of sputtering (1.5 keV, 1×10^{-5} mbar Ar^+) at 600 K, followed by annealing to 1100 K, described in details previously.[12]

2-phenoxyethanol (+99% purity, Sigma Aldrich) was introduced to the UHV chamber through a leak valve that was connected to a gas manifold with an attached 2-PE reservoir. The

reservoir was heated to 435 K to increase the vapor pressure and ensure the purity of the deposition. The gas manifold was heated accordingly to prevent condensation and allow a constant, stable flux of 2-PE gas into the chamber. Exposure of 2-PE to the surface was typically performed at $1x10^{-8}$ mbar pressure and the dosage measured in Langmuirs (1 L = $1.33x10^{-6}$ mbar ● s).

The carbon coverage was determined by calibration with the C 1s XPS signal of the CO saturation coverage on Pt(111) at 300 K. Under these conditions, CO is known to saturate with a coverage of C/Pt = 0.49 ± 0.02 (1 CO molecule for every 2 Pt atoms).[31] Comparison of this saturation with the intensity dependence of the carbon signal from 2-PE allowed us to determine the amount of deposited carbon per platinum atoms. Every Dosage of 2-PE on Pt(111) and its corresponding C/Pt ratio can be found in table G1 (Appendix G). We define the coverage as the amount of carbon per Platinum atoms.

XPS

XPS spectra were recorded on a Specs GmbH system (XR50 X-ray source and Phoibos 100 SCD analyzer) using a standard Al Kα source (1486.7 eV) operated at 380 W (14.6 kV, 26 mA). Selected peaks were obtained in high resolution spectra using 0.1 eV step size, 0.5 second dwell time, and pass energy of 20 eV. For the C 1s and O 1s regions three scans were acquired to increase the signal to noise ratio. The spectra were then fit using CasaXPS analysis software using a mixed Gaussian-Lorentzian function and Shirley background subtractions for the C 1s region while a Linear background subtraction was used for the O 1s region.

For the experiments, 2-phenoxyethanol was dosed on the clean sample at 110 K and then heated up to the desired temperature of observation to acquire the spectrum. Once the acquisition was done, the sample was subject to a cleaning cycle (Ar sputtering followed by annealing to 1100 K) to remove all the residual carbon on the surface. The cleanness of the sample surface was verified by LEED and XPS.

TPD

The TPD experiments require the placing of the sample in front of a differentially pumped quadrupole mass spectrometer (QMS) and ramping up the sample temperature while monitoring the fragments of interest. For our experiments, the Pt(111) sample was dosed with varying exposures of 2-phenoxyethanol at 110 K and placed 1 mm below a 1 mm diameter hole leading to the differentially pumped QMS. The temperature controlled heating ramp was programmed in LabView and designed to provide and record a linear temperature ramp in the range of 120 K to

800 K, with a ramp rate of 6 K/s. the sample was subject to one cleaning cycle (Ar sputtering followed by annealing to 1100 K) to insure the cleanness of the surface before each dosage. A total of 13 channels corresponding to m/z values of 138, 122, 108, 94, 78, 77, 65, 45, 33, 32, 31, 28 and 2, were monitored for the 2-PE TPD experiments. The selected m/z values correspond to the expected species and their respective fragmentation patterns.

4.3 Computation Details

The plane-wave periodic DFT calculations were performed using the Vienna Ab initio Simulation Package (version 5.3).[32–34] The energies were computed using the optPBE[35,36] exchange correlation function that was proven to account accurately for the interactions of aromatics on metal surfaces.[37,38] The core electrons were treated using the Projector Augmented Wave (PAW) method.[39] The valence electron density was developed on a plane wave basis set truncated at 400 eV. All the structures were considered optimized for forces less than 0.02 eV/A.

Unless defined otherwise, four-layer p(4x4) slabs were considered. The Pt atoms of the down most two layers were held fixed at the bulk position. The metallic surface was then surmounted with a 5 layer void (counted in units of Pt interlayers) in order to minimize the unphysical interactions arising from the 3D periodicity of the calculation. The integration over the Brillouin zone was performed using a Γ-centered 3x3x1 Monkhorst-Pack k-point mesh.[40] Gas phase structures were optimized in a 20x20x20 $Å^3$ cell computing the energy at the Γ point only.

Transition state structures were first interpolated from the structures of the reactant and the product using the Opt'n'Path program.[41] They were then pre-optimized using the CI-NEB algorithm[42,43] and finally fully optimized using a quasi-Newton algorithm or the Dimer Method.[44–46]

We performed a frequency calculation for each structure in order to, first, check the first-order saddle point property of the transition states, and second, calculate the Zero-Point Energy correction (ZPE) and the vibrational entropy (calculation at 400 K supposed constant). For slab structures, only the uppermost layer was included in the finite difference scheme of the frequency calculations. The two weakest modes associated to the global horizontal motion of the platinum atoms along the cell vectors were moreover removed before the calculation of the entropic contributions as in our previous work.[12] The rotational and translational entropies (the latter depending on the partial pressure of the gas) were also taken into account for gas phase hydrogen.

We assumed for hydrogen a partial pressure of 10^{-10} mbar, corresponding to the order of magnitude of the pressure inside the UHV chamber. It only concerns hydrogen since the partial pressure of the other desorbing products is zero and the associated chemical potential is therefore ill defined. All the entropic contributions were evaluated using the equations of statistical mechanics for a free particle in a box, a rigid rotator and a harmonic oscillator.

4.4 Results and Discussion

(a) XPS and TPD

The identification of surface species upon dosing 2-phenoxyethanol on Pt(111) was initially performed by monitoring the carbon and oxygen environment of species on the surface as a function of temperature. Figure 4.2 shows C 1s and O 1s photoelectron spectra after deposition of 1.5 L of 2-PE on Pt(111) at 110K, with spectra acquired at varying temperatures. Upon deposition, at 120K, 2-PE shows two peaks in the C 1s spectra, one at 285.3 eV, which is attributed to carbon bound to an oxygen atom (labeled C-O), and the other one at 283.5 eV which is attributed to carbon atoms bound only to other carbons or hydrogens (labeled C-C).[11] The binding energy difference between the carbon peaks is 1.8 eV. After flashing to 260K, the C-C and C-O peak areas decrease in intensity as some desorption takes place and only the C-O peak shifts to lower binding energy (285.1 eV). Then, the binding energy difference of the C 1s signals of the C-C and C-O peaks reduces from 1.8 eV to 1.6 eV, suggesting a decomposition of the parent molecule. At 300 K, the C-C and C-O areas decrease in intensity as desorption of the byproducts takes place. At 360K, the C-O peak area vanishes. Upon heating to 460 K, the remaining C 1s area peak decreases as only adventitious carbon remains on the surface.

Observations of the O 1s region after depositing 1.5L of 2-PE at 110 K on Pt(111) correlates with observations in the C 1s region. Upon deposition, at 120 K, 2-PE shows one peak at 532.2 eV. After flashing to 260K, the peak area intensity decreases and shifts to lower binding energy of 531.5 eV as some desorption and decomposition takes place. This is consistent with the observations made on the C 1s region. At 300 K, the peak area decreases in intensity as some anisole and phenol start desorbing from the surface (see TPD data below). At 360 K, the peak area vanishes.

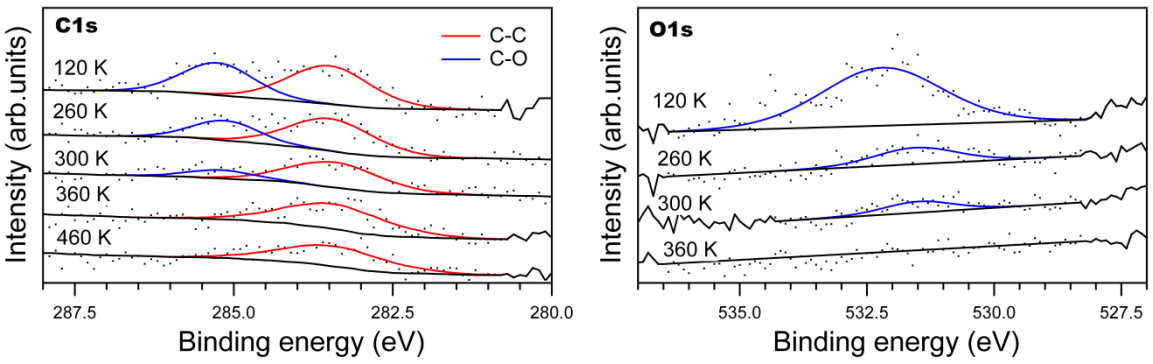

Figure 4.2: XPS spectra acquired at different temperatures for 1.5L of 2-phenoxyethanol deposited at 110 K.

Integrating the area of the C 1s region gives insight on how the coverage changes as a function of temperature (Figure 4.3). A dose of 1.5 L, which corresponds to one molecule of 2-PE per 10 Pt atoms (as determined by XPS intensities, see Appendix G, Table G1), corresponds to the onset of multilayers on the surface. The large drop in C 1s peak area between 240 K and 260 K corresponds to desorption of the multilayer as will be further discussed in comparison with TPD results.

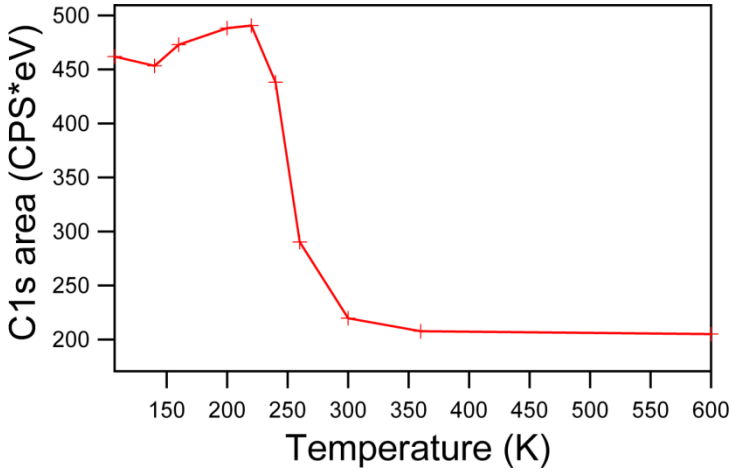

Figure 4.3: Analysis of XPS spectra acquired at different temperatures for 1.5L of 2-phenoxyethanol deposited at 110 K. The peak area decreases drastically between 240-260K, which corresponds to desorption of the multilayer.

Turning now to the TPD experiments, molecular desorption of the parent 2-PE molecule was monitored for multiple coverages as a function of temperature (Figure 4.4). The data shows

no molecular desorption of 2-PE at low coverages (0.85 L and below). As the coverage increases and a dose of 1.12 L is reached, the second layer of 2-phenoxyethanol is seen to molecularly desorb with a peak at 256 K. Assignment of these desorbing molecules to the second layer (rather than generically from multilayers) was made not only by the quantification of molecules, but also by comparison of the desorption energy values with DFT calculations (see below, Figure 4.8). A low temperature peak appears at 238 K for higher doses and does not saturate within the range of our measurements. This 238 K peak is attributed to the multilayer desorption. Studies on phenol have reported a similar behavior for the multilayer.[10,14]

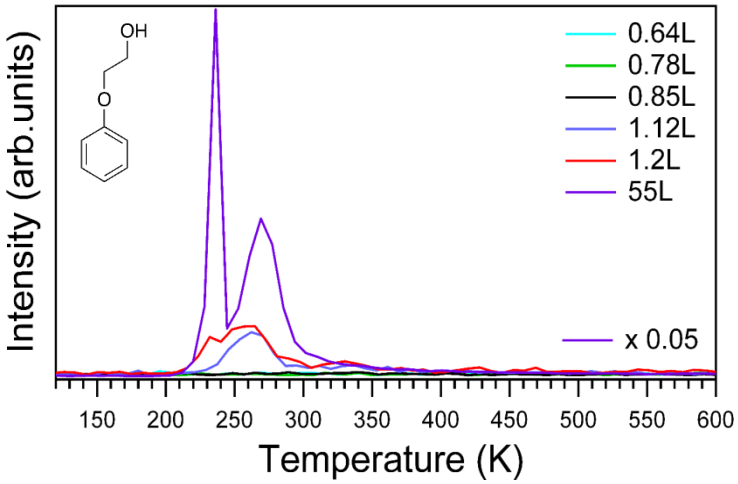

Figure 4.4: TPD spectra after several 2-phenoxyethanol exposure at 110K on Pt(111)and desorption rates are measured using a linear temperature ramp of 6 K/s

Three primary reaction products result from the decomposition of 2-PE on the surface, namely anisole, phenol and benzene. The TPD for these species are shown in Figure 4.5. By far, the highest intensity was observed for benzene, making it the primary desorbing aromatic product as discussed below. The TPD spectrum for the benzene fragments (mass 78) shows that for 0.78 L coverage, benzene molecularly desorbs from the surface with a peak at 380 K and keeps desorbing up to 520 K. As the coverage increases, the peak centers at 360 K. Phenol and anisole desorb in small quantity in a peak centered at 360 K, but only for initial coverage of 0.85 L or higher. The dosage dependence, particularly the lack of observed desorbing aromatics at lower coverages, is in agreement with previous literature where it was also shown that aromatics such as

benzene, phenol and anisole decompose completely on the Pt(111) surface for coverages below 0.6 ML.[11,12,47,48]

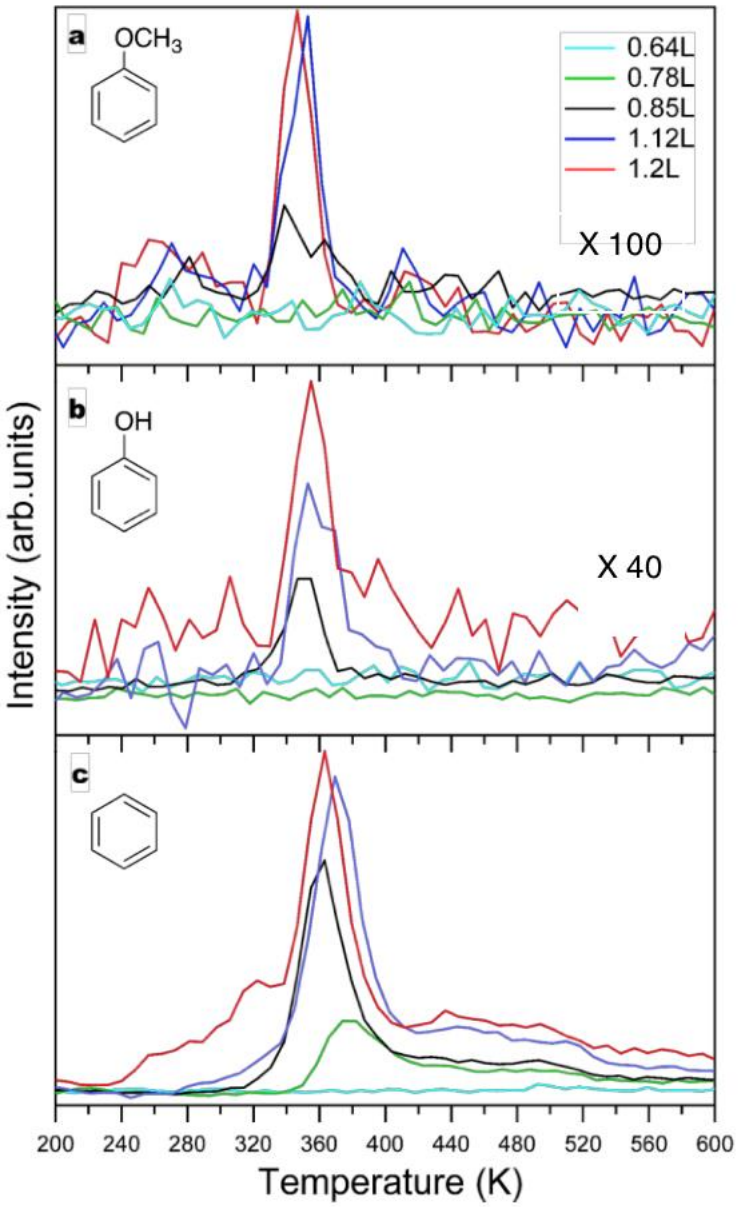

Figure 4.5: TPD spectra after several 2-phenoxyethanol exposures at 110K on Pt(111). Monitored masses 108, 94 and 78 correspond to Anisole, Phenol and Benzene respectively. The contribution of the parent molecule from the fragmentation pattern in the gas phase has been subtracted so as to show only desorbing species (see Appendix G for subtraction procedure). Desorption rates are measured using a linear temperature ramp of 6 K/s.

The only other observed reaction products of the decomposition of 2-PE are H_2 and CO (Figure 4.6). Hydrogen shows peaks at 334 K, 438 K and 555 K with two shoulders at 357 K and 520 K after dosing 0.85 L of 2-PE. For comparison, the associative desorption of hydrogen from Pt(111) has been previously observed in the temperature interval between 290-375 K.[49,50] The dot-dash line in Figure 4.6, which matches the observed peak in these experiments, corresponds to the reported dosage of 2L of H_2 on clean Pt(111).[49] Above 375 K the hydrogen peaks might correspond to the decomposition of the phenoxy species on the surface as observed with phenol and anisole on Pt(111).[11] The additional high temperature hydrogen peaks in Figure 4.6 have been assigned to subsequent surface reactions yielding H_2 as a product. In an attempt to quantify the origin of the hydrogen products, fitted Gaussians have been used to estimate the area ratio between the desorption peaks (see Appendix G, Figure G2). The desorption spectra can be fitted with 5 peaks (centered at 335 K, 357 K, 438 K, 520 K, and 554 K respectively) with a corresponding area ratio of approximately 2:1:5:1:1. This qualitative ratio, normalized to the smallest peak as 1, correlates with the number of 10 hydrogen atoms in the 2-PE molecules. The corresponding sequence of dehydrogenation will be discussed below using DFT calculations.

In contrast with the rich hydrogen spectra, only one broad peak of CO is observable at 404K with a shoulder at 438 K. The dashed line for CO corresponds to molecular desorption of pure CO from Pt(111) with 0.5 ML coverage.[51] No other molecular products have been observed.

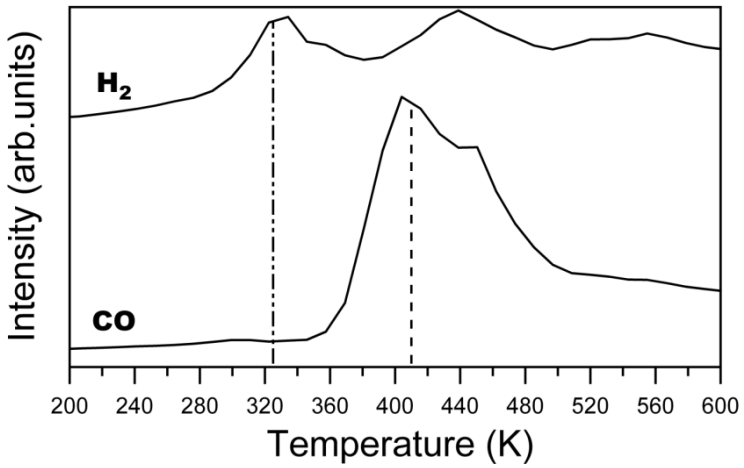

Figure 4.6: TPD spectra after 0.85 L exposure of 2-phenoxyethanol on Pt(111) and selecting formed byproducts Hydrogen and Carbon-monoxide (Mass 2 and 28). Desorption rates are measured using a linear temperature ramp of 6 K/s. The dashed line for CO corresponds to molecular desorption of pure CO from Pt(111) with 0.5 ML coverage.[51] The dot-dashed line for H_2 corresponds to desorption temperature of Hydrogen with 2 L coverage from Pt(111).[49,50]

Analysis of the TPD data allows the experimental determination of desorption energies E_{des} for each species and it can also provide information on the activation energy associated with surface reactions (Table 4.1). The analysis is performed based on the general rate law for desorption by the simple approach of Redhead[52] with appropriately corrected frequency factors. The calculated frequency factors **ν** are presented in Table 4.1 as obtained using the Campbell approach for molecular or associative desorption[53–55] and temperature corrected entropy values from the Yaw's Handbook.[56,57] The only exception is for 2-phenoxyethanol, where the entropy value for anisole was used as an approximation (the entropy value for 2-phenoxyethanol is not available). Further details on the choice of the approach method have been previously described.[12]

The high temperature peaks in the hydrogen TPD spectrum correspond to H_2 generated at a temperature above its normal desorption temperature and hence the associated activation energy calculated corresponds to the process that generates the additional H atoms. This quantity is labeled as the apparent activation energy E_a^{app}.

Table 4.1: Desorption energies of observed species, calculated by Redhead analysis of the TPD data.

Species	**Observations**	**Temperature (K)**	**ν^a (s^{-1})**	**E_{des} (kJ/mol)**	**E_a^{app} (kJ/mol)**
2-phenoxyethanol	2nd Layer	256	5.4×10^{16}	81	-------
	Multilayer	238	3.5×10^{16}	75	-------
Anisole	Molecular desorption	355	2.2×10^{17}	119	------
	Literature				-------
	2nd layer	260[12]	5.4×10^{16}	83	-------
	saturated 1st layer	360[12]	2.4×10^{17}	121	
Phenol	Molecular desorption	355	3.9×10^{16}	-------	114
	Literature	225[11]	-------	57	-------
Benzene	Molecular desorption	363	8.0×10^{15}	112	-------
		510	2.2×10^{18}	182	
	Literature	400-550[48]	-------	133-200[47]	-------
Carbon monoxide	Molecular desorption	404	7.7×10^{14}	117	-------
		438	8.5×10^{14}	128	
	Literature	410[58]	-------		-------
Hydrogen	Analyzed as molecular desorption	335	1.9×10^{14}		93
		357	1.9×10^{14}		100
		438	2.0×10^{14}		123
		520	2.1×10^{14}		147
		554	2.1×10^{14}		157

Analyzed as	335	1.05×10^{9}	-------	54
associative	357	9.92×10^{8}	-------	58
desorption	438	8.62×10^{8}	-------	72
	520	7.66×10^{8}	-------	85
	554	7.20×10^{8}		91
Literature	293-375[49]	-------	-------	39.7[49]
	330[50]	-------	-------	73[50]

Since decomposition of 2-phenoxyethanol and its fragments is significant, even at relatively low temperatures, we have quantified the amount of carbon left on the surface at different stages using the C 1s XPS signal. Figure 4.3 shows an example of the C 1s intensity upon dosage of 1.5 L of 2-phenoxyethanol and the decrease in signal due to multilayer desorption, yielding a residual carbon signal corresponding to decomposition species. To assess the relative yield of the decomposition vs intact desorption pathways during reaction, the C 1s intensity for one monolayer had to be estimated. This was done by comparison of the XPS signal for several doses as well as by determination of the XPS intensity at a temperature where the multilayer has desorbed (as determined by TPD). In Figure 4.3, the monolayer intensity was determined at T = 260 K (lowest temperature to allow second layer desorption prior to XPS data collection) and the residual carbon intensity at T = 360 K. From this analysis, it was determined that approximately 29% of the monolayer desorbs as molecular fragments, while 71% decompose into carbonaceous species.

Now getting back to the TPD data, one can correlate the peak area of the desorbing fragments to the amount of desorbed byproducts (see Table 4.2). At low coverages such as 0.64 L, 1 molecule per 23 Pt atoms (C/Pt=8/23), no desorption of byproducts is observed. The decomposition of the aromatic ring in 2-phenoxyethanol is dominant due to the availability of many unoccupied sites. At 0.78 L, 1 molecule per 19 Pt atoms, only benzene is observed as a byproduct. As the carbon coverage on the surface increases to 1 molecule per 16 Pt atoms (0.85 L), a competitive reaction pathway is observed with desorption of phenol and anisole. As the

surface gets more crowded, part of the Ph-O bond cleavage is inhibited. The ratio of desorption of the byproducts is maintained at a higher coverage of 1 molecule per 12 Pt atoms (1.2 L).

Table 4.2: Analysis of the TPD spectra after different dosages of 2-phenoxyethanol on Pt(111) at 110K. As the carbon coverage increases anisole and phenol desorption is observed.

Exposure (L)	Molecule/Pt	Anisole (%)	Phenol (%)	Benzene (%)
0.64	1/23	0	0	0
0.78	1/19	0	0	100
0.85	1/16	0.2	4.8	95
1.12	1/13	0.1	6	93.9
1.20	1/12	0.3	6.5	93.2

(b) Proposed pathway combining XPS and TPD.

From XPS and TPD experimental results, a schematic of the reaction and decomposition of 2-phenoxyethanol on Pt(111) is proposed in Figure 4.7. Upon dosing, 2-phenoxyethanol adsorbs on the Pt(111) surface at 110 K. Then, when heating, the multilayer molecularly desorbs at 238 K followed by desorption of the second layer at 254 K. The desorption energies are measured as 75 kJ/mol for the multilayer in reasonable agreement with the enthalpy of vaporization of 66 kJ/mol[57] of 2-phenoxyethanol, and 81 kJ/mol for the second layer molecules in good agreement with the DFT calculated adsorption energy of 85 kJ/mol (see below, Figure 4.8).

The first saturated layer totally decomposes on the surface. The only observed byproducts are anisole, phenol, benzene, CO and H_2. At 260K, the C 1s binding energy difference between the C-C and C-O XPS peaks reduces to 1.65 eV, suggesting the onset of decomposition of the parent molecule. This is comparable with the difference of 1.6 eV and 1.7eV C 1s binding energy of pure anisole and phenoxy on Pt(111)[11,12] suggesting these two species may be produced on the surface. The associative desorption of H_2 at 335K (which corresponds to "usual' temperature desorption of H_2) is another clear indication of the decomposition of the parent molecule. Literature suggests that this first hydrogen desorption comes from the cleavage of the O-H bond,[10,11,13,14] but a more detailed discussion of the origin of H at the different stages of reaction will be explored using mechanistic DFT calculations. Upon heating to 360 K, aromatics derived from the 2-phenoxyethanol, start to desorb: traces of anisole, few percent of phenol and a majority

as benzene. Anisole is known to decompose into phenoxy and to yield benzene and not phenol, as its been reported in a previous study.[12] Thus, the benzene that starts desorbing at 363K could be obtained through the following sequence: C-C bond breaking, generation of anisole and/or phenoxy, decomposition into benzene.

The additional presence of non-negligible amount of phenol questions the role of the glycoxy arm in the selectivity of the decomposition. Since phenol completely decomposes in the first layer before reaching its desorption temperature,[11] the observed phenol from 2-PE decomposition must be formed at a temperature that is higher than its desorption temperature. Therefore, the observed molecular desorption of phenol at 355 K has to be reaction limited, that is, as soon as it is formed it already has enough energy to desorb and hence the measured E_a^{app} should be comparable to the activation energy of the reaction that produces it. Desorption of oxygen containing species (anisole, phenol, carbon monoxide, etc.) correlates with the disappearance of the C-O peak in C 1s and in the O 1s region at 360 K and only hydrocarbons and adventitious carbon remains on the surface at 460 K.

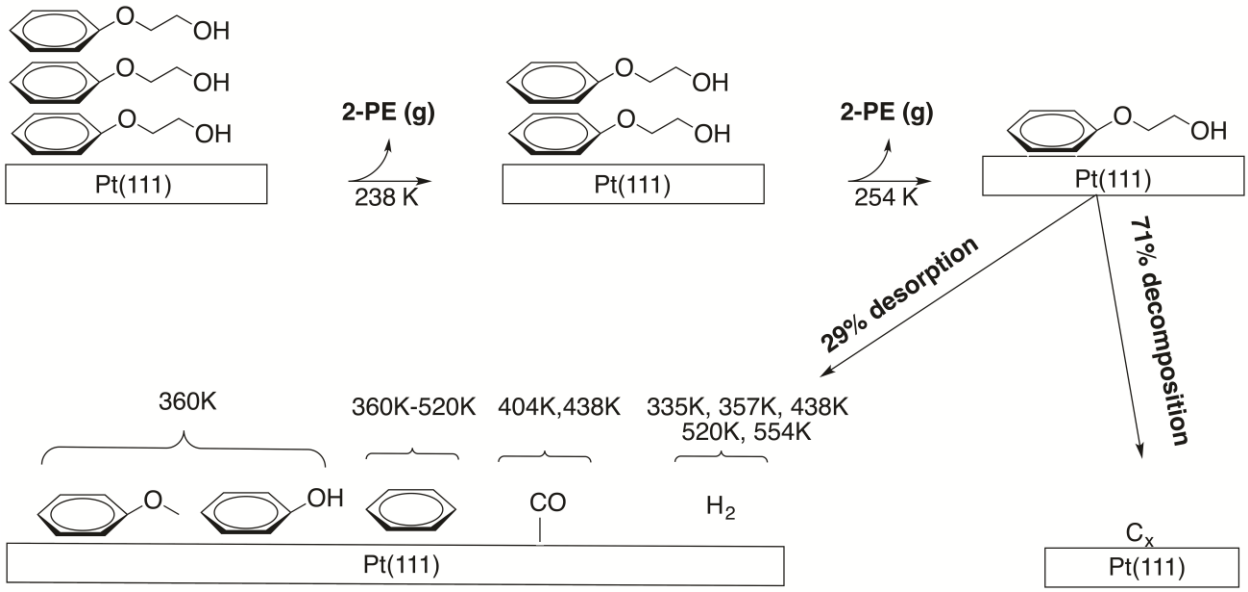

Figure 4.7: Proposed pathway of 2-phenoxyethanol (2-PE) decomposition under UHV conditions on Pt(111) built form surface science experiments (the temperatures correspond to the TPD peaks).

To achieve additional insight into the selectivity toward the different bond cleavage mechanisms (shown in Figure 4.1) involved in 2-phenoxyethanol decomposition on Pt(111), the

different reaction steps associated with the experimentally obtained pathway (Figure 4.7) have been calculated. In the following section, we use periodic DFT calculations to not only corroborate some of the experimental conclusions, but also to propose the reasons for the formation of benzene, phenol and anisole as products and particularly for the coverage dependence of their appearance.

(c) Mechanistic insight from DFT calculations

i. 2-phenoxyethanol (2-PE) desorption

TPD experiments show that the molecular desorption of 2-PE occurs at both 238 K and 256 K (see Table 4.1) at a dosage above 1.12L. To assess the structure in function of coverage, the adsorption structure and energy are computed on different sized slabs (see Figure 4.8). The most stable structure on the p(4x4) slab is found at the bri30 site in agreement with our previous study on the adsorption of oxygenated aromatics on Pt(111)[59] and with previous studies on related adsorbates.[26,27,59,60] The desorption energy at such a coverage (1 molecule:16 Pt) is computed at 200 kJ/mol, much larger than the one expected from the TPD (see Table 4.1, 81 kJ/mol). The structure expands on three Pt atoms in one direction and four in the other one (12 Pt atoms in total) suggesting that this structure – on the 16 Pt atoms of a p(4x4) slab – does not model a saturated monolayer of 2-phenoxyethanol. We were able to put this adsorbate on a smaller p(3x3) slab (9 Pt atoms). The desorption energy decreases to 175 kJ/mol. This coverage effect can safely be attributed to the increased lateral interactions and the reorganization of the glycoxy substituent that has to fit in this smaller p(3x3) cell. In spite of the increased coverage, the interaction of the adsorbate with the metallic surface remains very strong and desorption appears as being a very unlikely process. Increasing the coverage to the second layer gave a desorption energy of 85 kJ/mol. This was modeled using a p(3x3) slab with an extra molecule on top of a chemisorbed 2-PE and was confirmed on several configurations using a p(4x4) slab. For this calculation only, the void thickness was increased to 14 layers (in units of Pt layers). For the second layer, only weak physical interactions ensure the stability of the two-layered system which explains why the desorption energy has been more than halved on going from the first to the second layer. The calculated value of 85 kJ/mol matches well with the desorption energy obtained experimentally (see Table 4.1, 81 kJ/mol). Consequently, it is the first layer, which cannot desorb, that contributes most significantly to subsequent reaction products.

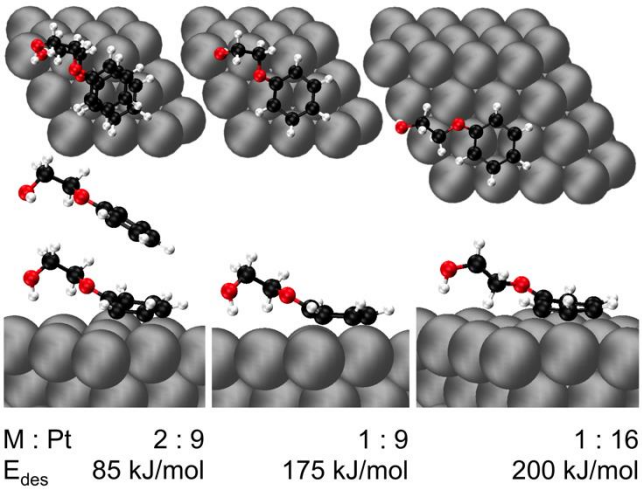

Figure 4.8: Adsorption geometries of 2-phenoxyethanol at different coverages on Pt(111) (M designates the number of organic molecules and Pt the number of surface platinum).

ii. Low coverage reactivity

Since it is extremely complex to tackle coverage effects for coverages close to saturation using only DFT and geometry optimization (many very specific geometrical configurations would need to be tested), we focused on the reactivity study using the large enough p(4x4) slab on which the lateral interactions are not too important and less likely to be specific.

2-PE has twenty bonds and as many first reactions possible. This means that there is, in principle, a very large reaction network to study. However, from previous experimental and theoretical studies, it is known that the first bonds to be broken are unlikely to be on the aromatic moiety, without yielding coke.[11,12] In other words, although the dominant binding of 2-PE to the surface is through the benzene ring, in terms of initial reactivity we can think of the molecule as a phenoxy substituted ethanol. Comparing the substituent to the numerous studies on oxygenated C2 organic compounds suggests that the C-C and C-O bonds cannot be cleaved unless a certain level of dehydrogenation has been reached.[29,30] Therefore, the early reactivity should be governed by C-H and O-H cleavages. Among the O-H and C-H bonds (see Table 4.3 for the activation parameters), the α hydrogen appears as being the easiest cleavage in ethanol ($\Delta^{\ddagger}U$ = 58 kJ/mol). In 2-PE however, this is the most recalcitrant to abstraction with a barrier of $\Delta^{\ddagger}U$ = 119 kJ/mol. This difference in activation energies ($\Delta\Delta^{\ddagger}U$ = 61 kJ/mol) illustrates that the adsorption through the aromatic moiety can exert a strong constraint on the reactivity of the C2 fragment; and this, in spite of the distance of the C_{α} carbon to the aromatic group. In the transition state of ethanol

dehydrogenation, the C_α is on top of a Pt atom at a height of 2.63 Å from the surface (see Figure 4.9) and can easily take the ideal and classic triangular shape. Because of the phenoxy group that acts as a real anchor at the bri30 site, 2-PE does not have the same capability to adapt to this 3-center transition state. Although the C_α manages to get even closer to the surface (2.57 Å), it does not lie over a Pt atom and the hydrogen reaches a bridge position, in a strongly distorted 4-center transition state. Despite a reduce distance between the aromatic and the C_β, the C_β-H is impacted to a lesser extent ($\Delta\Delta^{\ddagger}U$ = 28 kJ/mol). The corresponding transition state appears as less strained since it manages to reach the sTable 4.3-center configuration (see Figure 4.10). Lastly, the O-H bond seems to be less impacted energetically ($\Delta\Delta^{\ddagger}U$ = 9 kJ/mol) than entropically ($\Delta\Delta^{\ddagger}S$ = -46 $J.K^{-1}.mol^{-1}$). Unlike ethanol, which directly interacts via its oxygen in both the initial state and the transition state, 2-PE indeed undergoes a bigger conformation restriction from a free –OH group to the 4-center transition state (see Figures 8 and 10).

In short, the 2-PE decomposition starts with the O-H scission. This detailed comparison between the 2-PE and the simple ethanol molecule shows that the bond scission in the pending arm can be strongly affected by the presence of the aromatic moiety, and that they are systematically destabilized. In the following analysis of the reaction network, this will be used as a general behavior to avoid exploring the entire reaction network.

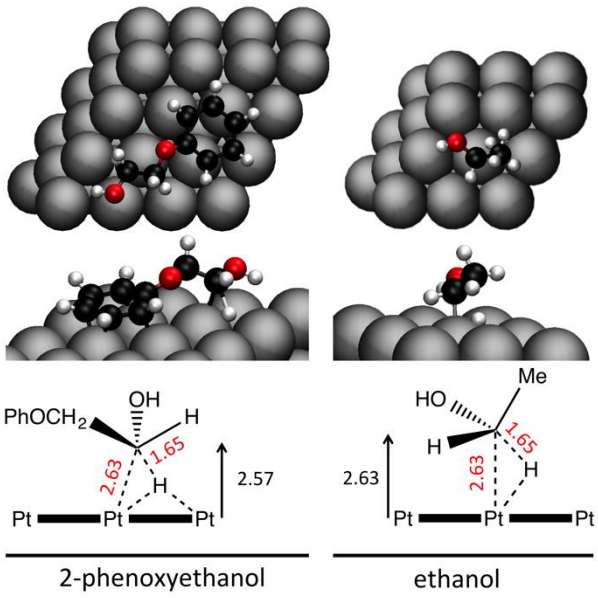

Figure 4.9: Structures of the transition states associated to the C_α-H cleavage on 2-phenoxyethanol (left panels) and ethanol (right panels). Distances are reported in Å.

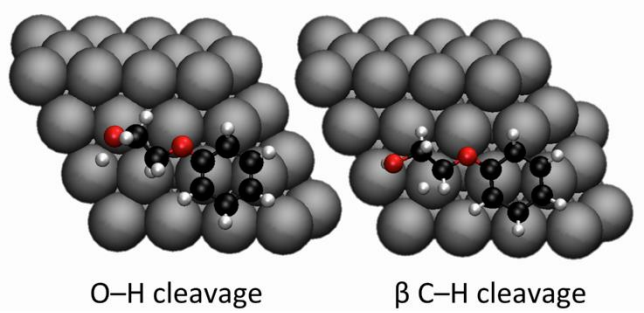

Figure 4.10: Structures of the transitions states associated to the O-H and C_β -H cleavages on 2-phenoxyethanol.

Table 4.3: Comparison of the reactivity of ethanol and 2-phenoxyethanol (2-PE) for the different O-H and C-H cleavages. These DFT data were computed on a p(4x4) slab for 2-PE and a p(3x3) slab for ethanol. The internal energy U includes the zero point energy (ZPE) contribution. The entropy contribution includes only the vibrational entropy based on harmonic frequencies since those are surface steps with no rotational or translational degrees of freedom. More details can be found in the computational details section.

	2-phenoxyethanol		**Ethanol**	
	$\Delta^{\ddagger}U$ ($kJ.mol^{-1}$)	$\Delta^{\ddagger}S$ ($J.K^{-1}.mol^{-1}$)	$\Delta^{\ddagger}U$ ($kJ.mol^{-1}$)	$\Delta^{\ddagger}S$ ($J.K^{-1}.mol^{-1}$)
O-H	84	− 65	75	−19
C_α-H	119	−19	58	−10
C_β-H	112	−10	84	−31
PhO-C & C_α-H	129	+2	—	—

The reaction profile of the 2-PE decomposition is reported in Figure 4.11, free energy F being computed at 400K. As detailed above, the first step is the breaking of the O-H bond. With a barrier of 110 kJ/mol, it easily competes with the desorption of 2-PE at low coverage. This first process is quite endergonic ($\Delta_r F$=+65 kJ/mol) but is readily followed by the desorption of hydrogen ($\Delta_r F$=-40 kJ/mol), pushing the dehydrogenation forward and making the reverse process unlikely. The subsequent α-dehydrogenation reaction is indeed very slightly activated ($\Delta^{\ddagger}F$=26 kJ/mol) and happens selectively compared to the backward reaction ($\Delta^{\ddagger}F$=85 kJ/mol) and the β-

dehydrogenation ($\Delta^{\ddagger}F$=125 kJ/mol). The result of the dehydrogenation at the O-H and C_{α}–H sites affords the corresponding aldehyde (2-phenoxyethanal in conformation A, Figure 4.12) and hydrogen {$PhOCH_2CHO+H_2(g)$} at F=-71 kJ/mol (see Figure 4.11). The subsequent α and β dehydrogenations ($\Delta^{\ddagger}F$=73 kJ/mol and 98 kJ/mol respectively) cannot compete with the conformational change to a second conformer labeled B (see Figure 4.12). This conformational change is admittedly slightly endergonic (Δ_rF=14 kJ/mol) but proceeds though a low barrier of 45 $kJ.mol^{-1}$. In addition B is very reactive towards the second α-dehydrogenation with a barrier of only $\Delta^{\ddagger}F$=31 k/mol (*ie* an overall barrier of $\Delta^{\ddagger}F$=45 kJ/mol from conformer A). As a consequence of the Curtin-Hammett principle, we obtain 2-phenoxyacetyl $PhOCH_2CO$ in a B conformation. After desorption of hydrogen, this step (at F=−149 kJ/mol in Figure 4.11) becomes irreversible with a reverse barrier of $\Delta^{\ddagger}F$=133 kJ/mol.

The 2-phenoxyacetyl appears as a key intermediate along the reaction path. After the large amount of hydrogen released (3 atoms for one 2-PE molecule), further dehydrogenation appears as kinetically blocked ($\Delta^{\ddagger}F$=160 kJ/mol). In line with the reactivity of ethanol[29] and anisole,[12,15,18] the cleavage of the PhO-C and C-C bonds should be now affordable. The barriers are $\Delta^{\ddagger}F$=92 kJ/mol and $\Delta^{\ddagger}F$=116 kJ/mol respectively, suggesting that the PhO-C cleavage is the most accessible. The products are the phenoxy fragment PhO and the ketene CH_2CO that further decomposes into methylene CH_2 and adsorbed carbon monoxide CO with a barrier of $\Delta^{\ddagger}F$=86 kJ/mol. Further, methylene readily evolves into methylidene CH (see gray part of the diagram) yielding an additional H atom. Then methylidene (or carbon after an extra dehydrogenation step) can snatch the oxygen atom from phenoxy to produce benzene with an overall barrier of $\Delta^{\ddagger}F$=135 kJ/mol around 400 K, as we have recently shown for the anisole/Pt(111) system.

Overall, the production of {$PhO+CH+2CO+2H_2(g)$} can be considered to proceed with a relatively low overall barrier of $\Delta^{\ddagger}F$=110 kJ/mol and should therefore appear at moderate temperatures under TPD conditions (in the 320-380 K range). It is associated to four dehydrogenations directly followed by hydrogen desorption (see downward arrows in Figure 4.11). Although, the last dehydrogenation might be a bit delayed by two barriers of $\Delta^{\ddagger}F$=92 kJ/mol and $\Delta^{\ddagger}F$=86 kJ/mol (the associated transition states of which being at F=−57 kJ/mol and F=−118 kJ/mol respectively in Figure 4.11) to afford methylene CH_2. If the decomposition of 2-PE followed the mechanism proposed in Figure 4.11 with a selectivity of 100%, one would expect a ratio of approximately 3:1 for the first two peaks in the TPD of H_2 in the 300-400 K range.

However, the DFT calculations have shown that the C_β-H cleavage, although not preferential, is also possible for the first dehydrogenation ($\Delta^{\ddagger}F$ = 116 kJ/mol at 400 K, calculated from the data given in Table 4.3). This might open a competitive route that could alter the 3:1 ratio, potentially leading to an observed TPD ratio of approximately 2:1 (Figure 4.6). At higher temperature, the production of benzene competes with the decomposition of PhO, which can form carbonaceous species. As shown previously, such a process starts with the CH dissociation in meta of the oxy substituent and becomes more favorable than the benzene production at temperature higher than 450K.[12,47] This explains the large production of hydrogen and the shoulder in CO above 400K.

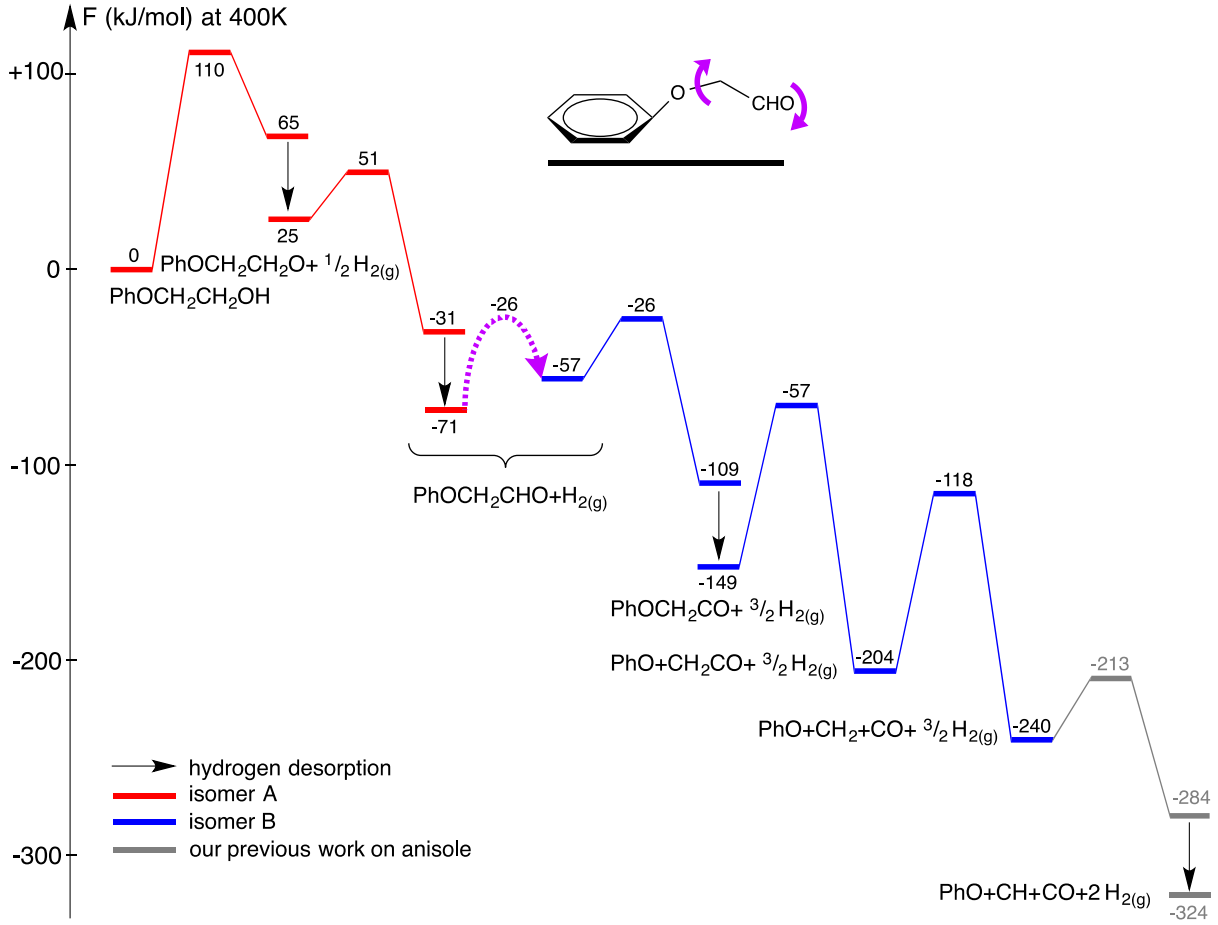

Figure 4.11: Free Energy profile of 2-phenoxyethanol decomposition into phenoxy, methylidene, carbon monoxide, and gas phase hydrogen. The free energy was computed at 400 K as described in Computational Details.

(iii) Towards higher coverages

The proposed mechanism has been derived for low to moderate coverages. However, the TPD experiments show that an increase in the coverage (up to 1 molecule per 12 Pt) yields to a small production of phenol (PhOH) and negligible traces of anisole (see Table 4.2). The increase of the coverage is expected to favor steps that require a reduced amount of surface Pt at the expense of steps that necessitate more.

The first transition state, corresponding to the dehydrogenation of the alcohol has a geometry where 2-phenoxyethanol lies down on three Pt atoms in one direction and four on the other (see Figure 4.10). This means that approximately twelve Pt atoms are needed for this step to proceed easily. If the coverage increases, the energy of this transition state should increase. At higher coverages, 2-phenoxyethanol might even lack space to have the alcohol function interact with the surface.

So far, only classic sequential cleavages were considered, following the Langmuir-Hinshelwood mechanism for surface reactions. However, at high coverage, an Eley-Rideal mechanism could be more favorable, the bond cleavage being synchronous with the ejection of one of the products. The simultaneous cleavage of the PhO-C and the C_α-H bonds produces phenoxy PhO, hydrogen and the hydroxyethylene (CH_2CHOH) that is directly ejected in the gas phase (see Figure 4.13). The free energy barrier is $\Delta^{\ddagger}F$=128 kJ/mol at 400 K on a p(4x4) slab (calculated from the data given in Table 4.3, entry PhO-C & C_α-H). This barrier is too high to be relevant at low coverages. However, the ejection of the enol makes this alternative competitive at higher coverages with the increase of the other barriers. It leaves locally only phenoxy and hydrogen. In absence of CH_x species, the deoxygenation is unlikely since the Ph-O bond dissociation in phenoxy is highly endothermic ($\Delta_r F$=124 kJ/mol at 400 K) and strongly activated ($\Delta^{\ddagger}F$=225 kJ/mol at 400 K). Then, the hydrogen surface diffusion is hindered by the high surface coverage, opening the door to the PhO+H recombination into PhOH instead of {PhO+½H_2(g)}, which would lead to the small yield of phenol observed.

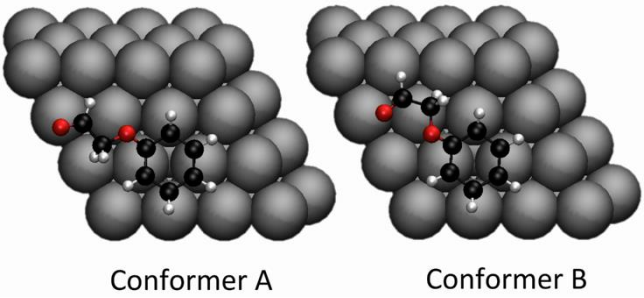

Figure 4.12: Conformers A & B of 2-phenoxyethanal.

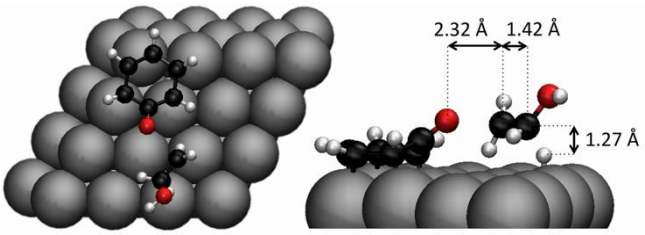

Figure 4.13: Transition state structure associated to the concerted formation of enol.

4.5 Conclusion

In ultra-high vacuum conditions, the 2-phenoxyethanol (2-PE) desorbs from the Pt(111) surface in two stages: (i) desorption of the multilayer (ii) desorption of the second layer. The strongly chemisorbed first layer decomposes in coke (71%) and aromatic compounds (29%). The decomposition of the pending arm and the deoxygenation of the aromatic moiety is effective since the main product is benzene and only ~5% of phenol is observed at a higher coverage.

Despite its flexibility, the pending arm of 2-PE is highly constrained by the strong adsorption of the aromatic ring and it does not react as a simpler alcohol such as ethanol. The reaction starts with the O-H scission, followed by two successive C_α-H scissions, yielding the $PhOCH_2CO$ intermediate and 3/2 H_2(g). The alkyl arm of this intermediate cannot be easily dehydrogenated further and undergoes a C-C scission. Falling back to the reaction network of the anisole decomposition, the phenoxy intermediate is obtained and yields benzene thanks to the presence of numerous carbonaceous species.

A higher coverage yields to a higher fraction of oxygenated aromatics (mainly phenol). The DFT calculations suggest that this can be related to the existence of a synchronous step that does not require the adsorption of all the products. The CH_2CHOH fragment is ejected in gas phase as a stable molecule, leaving behind the phenoxy intermediate and one hydrogen atom. Locally,

without CH_x species, the deoxygenation is unlikely. In addition, the higher coverage probably limits the H diffusion, allowing the recombination into phenol.

This study opens the road to a better design of metallic based catalysts aiming at lignin deoxygenation. A strong pressure in hydrogen is to be avoided to prevent the formation of phenol from phenoxy. The reluctant Ph-O cleavage requires the presence of reductive species such as CHx or promoters such as Zinc.[19] Without promoters, the formation of reductive carbonaceous species necessitates a low enough coverage of reactants.

References

(1) Popp, J.; Lakner, Z.; Harangi-Rákos, M.; Fári, M. The Effect of Bioenergy Expansion: Food, Energy, and Environment. *Renew. Sustain. Energy Rev.* **2014**, *32*, 559–578.

(2) Peter, M. Energy Production from Biomass (part 1): Overview of Biomass. **2002**, *83*, 37–46.

(3) Pettersen, R. The Chemical Composition of Wood. *Chem. solid wood* **1984**, 1–9.

(4) Zakzeski, J.; Bruijnincx, P. C. A.; Jongerius, A. L.; Weckhuysen, B. M. The Catalytic Valorization of Ligning for the Production of Renewable Chemicals. *Chem. Rev.* **2010**, *110*, 3552–3599.

(5) Ragauskas, A. J.; Beckham, G. T.; Biddy, M. J.; Chandra, R.; Chen, F.; Davis, M. F.; Davison, B. H.; Dixon, R. a; Gilna, P.; Keller, M.; et al. Lignin Valorization: Improving Lignin Processing in the Biorefinery. *Science* **2014**, *344*, 1246843.

(6) Pandey, M. P.; Kim, C. S. Lignin Depolymerization and Conversion: A Review of Thermochemical Methods. *Chem. Eng. Technol.* **2011**, *34*, 29–41.

(7) Huber, G. W.; Iborra, S.; Corma, A. Synthesis of Transportation Fuels from Biomass: Chemistry, Catalysts, and Engineering. *Chem. Rev.* **2006**, *106*, 4044–4098.

(8) Mohan, D.; Pittman, C. U.; Steele, P. H. Pyrolysis of Wood/biomass for Bio-Oil: A Critical Review. *Energy and Fuels* **2006**, *20*, 848–889.

(9) Bridgwater, a. V. Review of Fast Pyrolysis of Biomass and Product Upgrading. *Biomass and Bioenergy* **2012**, *38*, 68–94.

(10) Russell, J. N.; Sarvis, S. S.; Morris, R. E. Adsorption and Thermal Decomposition of Phenol on Ni(110). *Surf. Sci.* **1995**, *338*, 189–203.

(11) Ihm, H.; White, J. M. Stepwise Dissociation of Thermally Activated Phenol on Pt(111). *J. Phys. Chem. B* **2000**, *104*, 6202–6211.

(12) Réocreux, R.; Ould Hamou, C. A.; Michel, C.; Giorgi, J. B.; Sautet, P. Decomposition Mechanism of Anisole on Pt(111): Combining Single-Crystal Experiments and First-Principles Calculations. *ACS Catal.* **2016**, *6*, 8166–8178.

(13) Xu, X.; Friend, C. M. The Role of Coverage in Determining Adsorbate Stability: Phenol Reactivity on rhodium(111). *J. Phys. Chem.* **1989**, *93*, 8072–8080.

(14) Serafin, J. G.; Friend, C. M. Carbon-Oxygen Bond Strength as a Control of Reaction Kinetics: Phenol on Mo(110). *Surf. Sci.* **1989**, *209*, 163–175.

(15) Shi, D.; Vohs, J. M. Lignin-Derived Oxygenate Reforming on a Bimetallic Surface: The Reaction of Benzaldehyde on Zn/Pt(111). *Surf. Sci.* **2016**, *650*, 161–166.

(16) Bonalumi, N.; Vargas, A.; Ferri, D.; Baiker, A. Theoretical and Spectroscopic Study of the Effect of Ring Substitution on the Adsorption of Anisole on Platinum. *J. Phys. Chem. B* **2006**, *110*, 9956–9965.

(17) Bonalumi, N.; Vargas, A.; Ferri, D.; Bürgi, T.; Mallat, T.; Baiker, A. Competition at Chiral Metal Surfaces: Fundamental Aspects of the Inversion of Enantioselectivity in Hydrogenations on Platinum. *J. Am. Chem. Soc.* **2005**, *127*, 8467–8477.

(18) Tan, Y. P.; Khatua, S.; Jenkins, S. J.; Yu, J.-Q.; Spencer, J. B.; King, D. a. Catalyst-Induced Changes in a Substituted Aromatic: A Combined Approach via Experiment and Theory. *Surf. Sci.* **2005**, *589*, 173–183.

(19) Shi, D.; Arroyo-Ramírez, L.; Vohs, J. M. The Use of Bimetallics to Control the Selectivity for the Upgrading of Lignin-Derived Oxygenates: Reaction of Anisole on Pt and PtZn Catalysts. *J. Catal.* **2016**, *340*, 219–226.

(20) Robinson, A. M.; Mark, L.; Rasmussen, M.; Hensley, J. E.; Medlin, J. W. Surface Chemistry of Aromatic Reactants on Pt and Mo-Modified Pt Catalysts. *J. Phys. Chem. C* **2016**, *in review.*

(21) Nimmanwudipong, T.; Runnebaum, R. C.; Block, D. E.; Gates, B. C. Catalytic Conversion of Guaiacol Catalyzed by Platinum Supported on Alumina: Reaction Network Including Hydrodeoxygenation Reactions. *Energy & Fuels* **2011**, *25*, 3417–3427.

(22) Runnebaum, R. C.; Nimmanwudipong, T.; Block, D. E.; Gates, B. C. Catalytic Conversion of Anisole: Evidence of Oxygen Removal in Reactions with Hydrogen. *Catal. Letters* **2011**, *141*, 817–820.

(23) Zhu, X.; Lobban, L. L.; Mallinson, R. G.; Resasco, D. E. Bifunctional Transalkylation and Hydrodeoxygenation of Anisole over a Pt/HBeta Catalyst. *J. Catal.* **2011**, *281*, 21–29.

(24) Zhu, X.; Nie, L.; Lobban, L. L.; Mallinson, R. G.; Resasco, D. E. Efficient Conversion of M -Cresol to Aromatics on a Bifunctional Pt/HBeta Catalyst. *Energy & Fuels* **2014**, *28*, 4104–4111.

(25) Gao, D.; Xiao, Y.; Varma, A. Guaiacol Hydrodeoxygenation over Platinum Catalyst: Reaction Pathways and Kinetics. *Ind. Eng. Chem. Res.* **2015**, *54*, 10638–10644.

(26) Lee, K.; Gu, G. H.; Mullen, C. A.; Boateng, A. A.; Vlachos, D. G. Guaiacol Hydrodeoxygenation Mechanism on Pt(111): Insights from Density Functional Theory and Linear Free Energy Relations. *ChemSusChem* **2015**, *8*, 315–322.

(27) Lu, J.; Behtash, S.; Mamun, O.; Heyden, A. Theoretical Investigation of the Reaction Mechanism of the Guaiacol Hydrogenation over a Pt(111) Catalyst. *ACS Catal.* **2015**, *5*, 2423–2435.

(28) Lu, J.; Wang, M.; Zhang, X.; Heyden, A.; Wang, F. B-O-4 Bond Cleavage Mechanism for Lignin Model Compounds over Pd Catalysts Identified by Combination of First-Principles Calculations and Experiments. *ACS Catal.* **2016**, *6*, 5589–5598.

(29) Ferrin, P.; Simonetti, D.; Kandoi, S.; Kunkes, E.; Dumesic, J. a.; Nørskov, J. K.; Mavrikakis, M. Modeling Ethanol Decomposition on Transition Metals: A Combined Application of Scaling and Brønsted−Evans−Polanyi Relations. *J. Am. Chem. Soc.* **2009**, *131*, 5809–5815.

(30) Liu, B.; Greeley, J. Decomposition Pathways of Glycerol via C–H, O–H, and C–C Bond Scission on Pt(111): A Density Functional Theory Study. *J. Phys. Chem. C* **2011**, *115*, 19702–19709.

(31) Norton, P. R.; Davies, J. A.; Jackman, T. E. Absolute Coverages of CO and O on Pt(111); Comparison of Saturation CO Coverages on Pt(100), (110) and (111) Surfaces. *Surf. Sci.* **1982**, *122*, 593–600.

(32) Kresse, G.; Hafner, J. Ab Initio Molecular Dynamics for Liquid Metals. *Phys. Rev. B* **1993**, *47*, 558–561.

(33) Kresse, G.; Furthmüller, J. Efficiency of Ab-Initio Total Energy Calculations for Metals and Semiconductors Using a Plane-Wave Basis Set. *Comput. Mater. Sci.* **1996**, *6*, 15–50.

(34) Kresse, G.; Furthmüller, J. Efficient Iterative Schemes for Ab Initio Total-Energy Calculations Using a Plane-Wave Basis Set. *Phys. Rev. B* **1996**, *54*, 11169–11186.

(35) Dion, M.; Rydberg, H.; Schröder, E.; Langreth, D. C.; Lundqvist, B. I. Van Der Waals Density Functional for General Geometries. *Phys. Rev. Lett.* **2004**, *92*, 246401.

(36) Klimeš, J.; Bowler, D. R.; Michaelides, A. Chemical Accuracy for the van Der Waals Density Functional. *J. Phys. Condens. Matter* **2010**, *22*, 022201.

(37) Yildirim, H.; Greber, T.; Kara, A. Trends in Adsorption Characteristics of Benzene on Transition Metal Surfaces: Role of Surface Chemistry and van Der Waals Interactions. *J. Phys. Chem. C* **2013**, *117*, 20572–20583.

(38) Gautier, S.; Steinmann, S. N.; Michel, C.; Fleurat-Lessard, P.; Sautet, P. Molecular Adsorption at Pt(111). How Accurate Are DFT Functionals? *Phys. Chem. Chem. Phys.* **2015**, *17*, 28921–28930.

(39) Kresse, G.; Joubert, D. From Ultrasoft Pseudopotentials to the Projector Augmented-Wave Method. *Phys. Rev. B* **1999**, *59*, 1758–1775.

(40) Monkhorst, H. J.; Pack, J. D. Special Points for Brillouin-Zone Integrations. *Phys. Rev. B* **1976**, *13*, 5188–5192.

(41) Fleurat-Lessard, P.; Dayal, P. http://perso.ens-lyon.fr/paul.fleurat-lessard/ReactionPath.html.

(42) Henkelman, G.; Uberuaga, B. P.; Jónsson, H. A Climbing Image Nudged Elastic Band Method for Finding Saddle Points and Minimum Energy Paths. *J. Chem. Phys.* **2000**, *113*, 9901.

(43) Sheppard, D.; Terrell, R.; Henkelman, G. Optimization Methods for Finding Minimum Energy Paths. *J. Chem. Phys.* **2008**, *128*, 134106.

(44) Henkelman, G.; Jónsson, H. A Dimer Method for Finding Saddle Points on High Dimensional Potential Surfaces Using Only First Derivatives. *J. Chem. Phys.* **1999**, *111*, 7010.

(45) Heyden, A.; Bell, A. T.; Keil, F. J. Efficient Methods for Finding Transition States in Chemical Reactions: Comparison of Improved Dimer Method and Partitioned Rational Function Optimization Method. *J. Chem. Phys.* **2005**, *123*, 224101.

(46) Kästner, J.; Sherwood, P. Superlinearly Converging Dimer Method for Transition State Search. *J. Chem. Phys.* **2008**, *128*, 014106.

(47) Ihm, H.; Ajo, H. M.; Gottfried, J. M.; Bera, P.; Campbell, C. T. Calorimetric Measurement of the Heat of Adsorption of Benzene on Pt(111). *J. Phys. Chem. B* **2004**, *108*, 14627–14633.

(48) Campbell, J. M.; Seimanides, S.; Campbell, C. T. Probing Ensemble Effects in Surface Reactions. 2. Benzene Adsorption on Clean and Bismuth-Covered platinum(111). *J. Phys. Chem. B* **1989**, *92*, 815.

(49) Christmann, K.; Ertl, G.; Pignet, T. Adsorption of Hydrogen on a Pt(111) Surface. *Surf. Sci.* **1976**, *54*, 365–392.

(50) Lu, K. E.; Rye, R. R. Flash Desorption and Equilibration of H2 and D2 on Single Crystal Surfaces of Platinum. *Surf. Sci.* **1974**, *45*, 677–695.

(51) Steininger, H.; Lehwald, S.; Ibach, H. On the Adsorption of CO on Pt(111). *Surf. Sci.* **1982**, *123*, 264–282.

(52) Redhead, P. a. Thermal Desorption of Gases. *Vacuum* **1962**, *12*, 203–211.

(53) Campbell, C. T.; Sellers, J. R. V. Correction to "The Entropies of Adsorbed Molecules." *J. Am. Chem. Soc.* **2013**, *135*, 13998–13998.

(54) Campbell, C. T.; Sellers, J. R. V. The Entropies of Adsorbed Molecules. *J. Am. Chem. Soc.* **2012**, *134*, 18109–18115.

(55) Campbell, C. T.; Árnadóttir, L.; Sellers, J. R. V. Kinetic Prefactors of Reactions on Solid Surfaces. *Zeitschrift für Phys. Chemie* **2013**, *227*, 1–20.

(56) Chase, Jr., M. W.; Davies, C. A.; Downey, Jr., J. R.; Frurip, D. J.; McDonald, R. A.; Syverud, A. N. *NIST JANAF Thermodynamical Tables 1985*; National Institue of Standard and Technology, 1986.

(57) Stephenson, R. M.; Malanowski, S. *Handbook of the Thermodynamics of Organic Compounds*; Springer Netherlands, 1987.

(58) McEwen, J.-S.; Payne, S. H.; Kreuzer, H. J.; Kinne, M.; Denecke, R.; Steinrück, H.-P. Adsorption and Desorption of CO on Pt(111): A Comprehensive Analysis. *Surf. Sci.* **2003**, *545*, 47–69.

(59) Réocreux, R.; Huynh, M.; Michel, C.; Sautet, P. Controlling the Adsorption of Aromatic Compounds on Pt(111) with Oxygenate Substituents: From DFT to Simple Molecular Descriptors. *J. Phys. Chem. Lett.* **2016**, *7*, 2074–2079.

(60) Honkela, M. L.; Björk, J.; Persson, M. Computational Study of the Adsorption and Dissociation of Phenol on Pt and Rh Surfaces. *Phys. Chem. Chem. Phys.* **2012**, *14*, 5849–5854.

Chapter 5:
Direct observation of phenoxy as the key and common intermediate for the decomposition of lignin fragments containing the beta-O-4 linkage

Ould Hamou, C. A.; Giorgi, J.B. Direct observation of phenoxy as the key and common intermediate for the decomposition of lignin fragments containing the beta-O-4 linkage. S*ubmitted to J. Phys. Chem. C*

I performed all the RAIRS experiments and analysis of the reactivity of phenol, anisole and 2-phenoxyethanol on Pt(111). I performed all the analysis and interpretation related to the experimental results.

5 Direct Observation of Phenoxy as the Key and Common Intermediate for the Decomposition of Lignin Fragments Containing the Beta-O-4 Linkage

Cherif A. Ould Hamou,[†,§] Javier B. Giorgi,[†,‖,*]

[†] Centre for Catalysis Research and Innovation, [§] Department of Physics, [‖] Department of Chemistry and Biomolecular Sciences, University of Ottawa, 10 Marie Curie Pvt., Ottawa, Ontario, Canada. K1N 6N5.

Abstract

The decomposition of phenol, anisole and 2-phenoxyethanol on Pt(111) in ultra-high vacuum is studied as models to understand the reactivity of the β-O-4 linkage in lignin. Desorption of multilayer and monolayer is observed as well as the generation of decomposition products. Using RAIRS to monitor the vibrational signatures of all the species we observed the appearance of the characteristic 1480 cm^{-1} vibration for the phenoxy group. This in conjunction with changes in other bands is used to identify the phenoxy species (as opposed to the oxocyclohexadienyl moiety) as the common key in the decomposition of the three molecules. The nature of the phenoxy species is discussed in comparison with previous literature and may lead to insight into the reaction-product selectivity of the decomposition.

Keywords: Lignin, Pt(111), anisole, phenol, 2-phenoxyethanol, RAIRS

5.1 Introduction

As the world's population increases, sustainability is a growing concern in areas ranging from energy to chemicals and other resources.[1] New alternative ways must be found to supply the growing world demands. Biomass conversion seems to be an ideal candidate to be used in chemical production since it is inexpensive, renewable and readily available.[2,3] and thus the conversion of biomass into high value products is an important target both economically and socially. Lignin, an important biomass component, is the second most abundant polymer in wood and represents up to 40% of the dry biomass weight.[4,5] Lignin conversion has significant potential as a source for the sustainable production of fuels and bulk chemicals.[2,4,6,7] With its unique structure and chemical properties, a wide variety of bulk and fine chemicals, particularly aromatic and alcohol compounds are potentially obtainable from lignin.[6] As of today, lignin is usually a byproduct of paper and pulp industries; and it is mainly recycled as low-grade fuel to generate heat.[5] The degradation of lignin into value added compounds has been studied by hydrothermal conversion, pyrolysis, catalysis, enzymatic degradation, etc.[5,8–11] The use of heterogeneous catalysis for lignin conversion is a promising method as the products and the catalyst can be easily separated. Moreover, catalysis plays an essential role in making biomass conversion viable for valorization by reducing activation energies for reaction and guiding product selectivity.

Lignin can be simplistically described as a large molecule consisting of aromatic rings linked together by various forms of oxygen links. The most abundant link is the β-O-4 which constitutes up to 60% of all the lignin linkages (Figure 5.1 shows a small lignin fragment where the β-O-4 link is showcased). Because of the complexity of the lignin molecule and the difficulty in handling it for fundamental studies (due to its high viscosity, low vapor pressure, immiscibility, etc), it is important to start with simple model molecules that identify key features. Surface studies with smaller key molecular fragments allow a better understanding of the bond breaking steps of these moieties in a catalytic environment.[12,13] Since lignin is defined by aromatic groups bound to oxygen, the simplest model molecule to consider is phenol, and from it we can bridge the level of complexity by considering more complex ligands in the arm moiety to anisole and 2-phenoxyethanol (Figure 5.1). The reactivity of such lignin fragments has been explored on different catalysts, including sulfides and noble metals for hydrodeoxygenation. Metals such as Ru and Pd are quite efficient, but Pt which produces compounds less deoxygenated has even higher conversion. In this work, the molecular reactivity of phenol, anisole, and 2-phenoxyethanol is

investigated on the Pt(111) surface as a model catalyst in order to compare the relative facility of the C-H, C-O, and C-C bond cleavages.

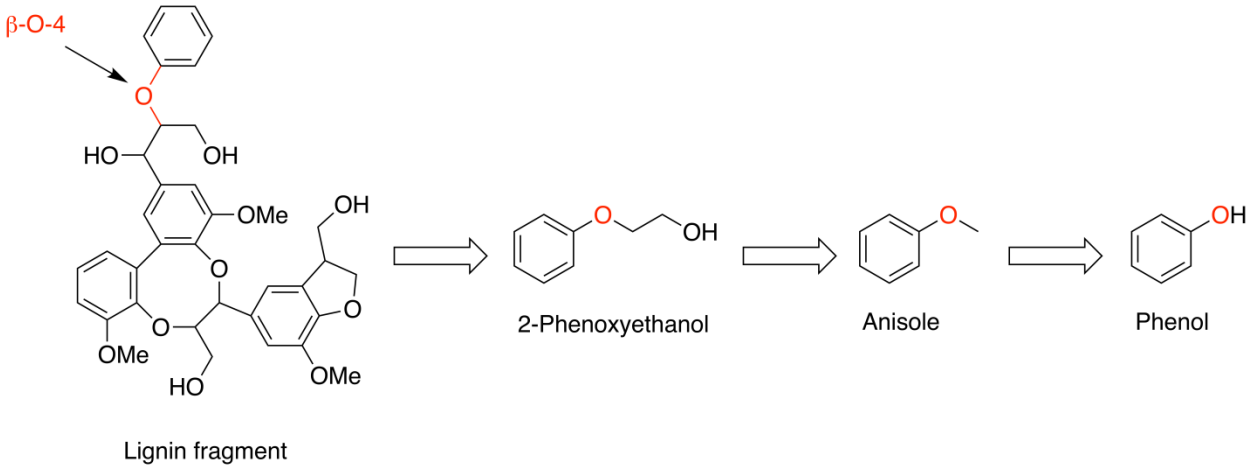

Figure 5. 1: *Small Lignin fragment and the identification of suitable small-molecule fragments: 2-phenoxyethanol, anisole and phenol.*

Single crystal investigations of aromatic oxygenates on transition metal surfaces have shown different preferences in C-H, C-O and C-C bond cleavage.[11,14–18] The decomposition pathways of aromatics seem to be strongly dependent on the coverage of adsorbed molecules on the surface and the interaction strength of the aromatic ring with the catalyst.[14,19–21] Previous studies of phenol-Pt(111) interactions are relevant.[14,22–24] On Pt(111), phenol multilayers have been reported to desorb from the surface at 195 K while the second layer would desorb at 225 K.[14] The adsorption geometry of phenol on Pt(111) has been reported to be lying with the ring flat and parallel to the surface.[14,22,23,25–27] As one would expect for phenol, the O-H bond cleavage seems to occur first and the resulting phenoxy is subject to decomposition via two competitive reactions: generation of benzene and surface oxygen, or decomposition into CO, H_2 and hydrocarbons. Zhuang studied phenol on Pt(111) by HREELS showing that upon heating to 225 K the multilayer of phenol desorbs from the surface and the first layer starts decomposing by O-H bond cleavage, which they see as a weak shoulder in the 3300-3350 cm^{-1} region, leading to the formation of phenoxy on the surface.[22] No C-O stretching peak was observed in the expected region of 1800-2100 cm^{-1}, hence the reported CO formation is reaction limited (it is formed above the natural desorption temperature, and therefore it desorbs as soon as it is formed). The general conclusion

was that phenoxy is the intermediate specie in the decomposition of phenol and that O-H bond cleavage is more favorable than C-O, C-H and C-C bond cleavage.

Phenoxy also seems to be a key intermediate in the decomposition of more complex oxygenated aromatics.[16,19,21,28,29] King and co-workers proposed the formation of the phenoxy species as the main intermediate for anisole decomposition on Pt(111) and Pt(100)hex. Vohs and co-workers[30] went a step further suggesting the formation of cyclohexadienone as a subsequent intermediate.[30,31] Combining surface science experiments and periodic DFT computations,[21] Réocreux et al. showed that anisole on Pt(111) reaches a saturation coverage of one monolayer (1 ML) corresponding to 7 carbon atoms (one molecule) per 10 platinum atoms on the surface, 7C/10Pt. For a coverage below 1 ML, a small fraction of anisole molecularly desorbs from the surface at 360 K while the majority decomposes into phenoxy with a mechanism initiated via a C-H bond cleavage on the methyl group below 325 K. Anisole further decomposes via O-C bond cleavage to form phenoxy (PhO), methylidyne (CH) and hydrogen on the surface. At higher temperatures, there appears to be a competition between Ph-O bond cleavage, forming phenyl then benzene, and a complete decomposition of the aromatic ring. The formation of benzene was proposed to occur through two different pathways. The first one consists of further decomposition of methylidyne to form carbon and hydrogen on the surface. The carbon would eventually react with the phenoxy to form PhOC that further reacts to form benzene and CO. The second pathway consists of the reaction of methylidyne with phenoxy to form PhOCH that keeps reacting to form benzene. The estimated energy barriers for the start of the 1st and 2nd pathways are 135 and 133 kJ/mol, respectively. These results showed that under UHV conditions, the formation of benzene is dominant, and it desorbs from the surface at 400 K. Above 450 K, the remaining phenoxy completely decomposes into CO and H_2.

Increasing the complexity of the model molecule, Ould Hamou et al. showed that 2-phenoxyethanol (2-PE) on Pt(111) desorbs from the surface in two stages, the multilayer at 238 K and the second layer at 256 K.[19] For the monolayer, the major desorption products of the decomposition are benzene, CO, H_2, a small fraction of phenol and traces of anisole. The 2-PE decomposition was proposed to start with the O-H scission below 325 K, followed by successive C-H scissions, yielding the $PhOCH_2CO$ intermediate. The alkyl arm of this intermediate cannot be easily dehydrogenated further and undergoes C-C or PhO-C scission. The decomposition barriers are 92 and 116 kJ/mol, respectively, suggesting that the C-C and PhO-C cleavage are both

accessible. If $PhOCH_2CO$ undergoes C-C bond cleavage, it will fall back to the reaction network of the anisole and if it undergoes PhO-C bond cleavage the products are the phenoxy fragment, PhO, and the ketene CH_2CO.

Overall, to understand the different reaction pathways of lignin decomposition, it is important to systematically increase the level of complexity of the model molecules used, as it has recently been reported.[19,21] Despite the general acceptance of the phenoxy radical as an important intermediate, its observation has not been without controversy. In particular, the formation of phenoxy is the cornerstone of the proposed decomposition pathways of anisole and 2-phenoxyethanol on Pt(111), but no direct observation has been reported. This work focuses on the identification of specific bonds being broken during the decomposition of phenol, anisole and 2-phenoxyethanol on Pt(111). The study is focused on the commonality of the mechanisms and the direct identification of key intermediates of the decomposition of the parent molecules.

5.2 Experimental

Experiments were carried out in a UHV chamber with a base pressure of 7×10^{-10} mbar achieved by a combination of a mechanical pump and a turbo molecular pump. The chamber is dedicated for reflection absorption infrared spectroscopy (RAIRS) and contains a low energy electron diffraction (LEED) to verify surface cleanness, a quadrupole mass spectrometer for residual gas analysis and a sputtering gun used in sample cleaning. The chamber is equipped with a main manipulator allowing 500 mm linear transfer of the sample in the z direction with 360° rotational range. The manipulator is also mounted on an x-y stage which allows the arm to move within 25 mm range in the x and y directions.

The RAIRS experiments were performed with a Bruker Equinox 55 FT-IR spectrometer coupled to the UHV chamber. The IR beam is redirected from the spectrometer to a flat mirror that reflects the beam at a 90° angle to a parabolic mirror (90° off-axis, 30 cm focal length) which focuses the beam on the sample with an angle of incidence of 3° inside of the UHV chamber and onto the surface. After reflection from the surface of the sample, a second parabolic mirror focuses the beam to a liquid-nitrogen cooled mercury-cadmium-telluride (MCT) detector (InfraRed associates, model D315/6). Two differentially pumped windows are mounted on opposite sides of the UHV chamber. These windows have 2.75” CF flanges and use KBr 38 x 6mm optical crystals

with a 1/4" tube for differential pumping. Fluorocarbon O-rings are used as seals between the chamber and the windows. The entire optical pathway outside UHV is purged with dry air.

The 8 mm diameter and 0.5 mm thick platinum single crystal sample with purity of 99.999% was purchased from Princeton Scientific. The Pt(111) crystal surface was cleaned by repetitive cycles of 30 min of sputtering (1.5 keV, 1 x 10^{-5} mbar Ar^{+}) at 600 K, followed by annealing to 1100 K for 2 min. The efficiency of the cleaning cycle was periodically confirmed by XPS, where no carbon peaks were observed, and by LEED verifying spot sharpness. In addition, each RAIRS experiment was preceded by LEED verifying spot sharpness. The sample was heated by electron bombardment and the temperature was measured by a chromel-alumel (K-type) thermocouple in contact with the edge of the sample.

Phenol (+99% purity, Sigma Aldrich), anisole (+99% purity, Sigma Aldrich) and 2-phenoxyethanol (+99% purity, Sigma Aldrich) were introduced to the UHV chamber through a leak valve that was connected to a gas manifold with an attached reservoir. The reservoir was heated to increase the vapor pressure and ensure the purity of the deposition. The gas manifold was heated accordingly to prevent condensation and allow a constant, stable flux of gas into the chamber. Exposure of the molecules to the surface was typically performed by background dosing at 1x10^{-6} mbar pressure and the dosage measured in Langmuirs (1 L = 1.33x10^{-6} mbar ● s). The gas purity was monitored by a quadrupole mass spectrometer.

The RAIRS experimental spectra were collected at 4 cm^{-1} resolution with 1000 scans. The molecules were dosed on the clean sample at 130 K and then heated up to the desired temperature of observation to acquire the spectrum. For temperatures above 360 K, the sample was heated to the desired temperature and then cooled down to 360 K to acquire the spectrum. The spectra were manipulated using OPUS analysis software by performing a baseline correction and an atmospheric compensation for the CO_2 and H_2O regions.

5.3 Results

RAIRS spectra were obtained for phenol, anisole and 2-phenoxyethanol upon the adsorption of a multilayer on Pt(111). Data was then obtained as a function of temperature and the spectra were analysed in detail. A summary of all peak positions at various temperatures is provided in Appendix H, together with quantification of selected relevant peaks.

Phenol

The identification of surface species upon dosing phenol on Pt(111) was initially performed by monitoring vibrational modes of species on the surface using RAIRS. Attribution of the different vibrational modes of the as-deposited phenol is best performed by comparison with the spectra of liquid phenol, since it is expected that on the surface at low temperature the molecules will condense but not in a typical crystalline form. Additionally, vibrational modes can be compared with experimental vapor data and computed modes (see Appendix H, Table H1). There are small shifts between the vibrational modes of liquid phenol and the ones observed upon adsorption of 100 L of phenol on the Pt(111) surface at 130 K, which indicates that the surface influences the adsorption geometry of the molecules even in the multilayer regime.

Figure 5.2 shows the vibrational spectra of phenol after deposition of 100 L of phenol at 130 K, with spectra acquired at varying temperatures. This dosage produces multilayers of phenol on the surface. As the temperature is increased, desorption and reaction are expected to occur.

Upon deposition, at 130 K, we can center our attention on the 5 major peaks in the spectra at 758, 1244, 1480, 1501 and 1598 cm^{-1}, which can be used to assess qualitative evidence of the arrangement of the molecules. The peaks at 1480, 1501 and 1598 cm^{-1} are assigned to C-C stretches whereas the peaks at 758 and 1244 cm^{-1} are assigned to C-H out of plane bending and Ph-OH stretching, respectively (Table 5.1). Because of the surface selection rules, only the modes that have vibrational dipole moments perpendicular to the surface can be observed, and therefore the observation of the C-H stretching peaks indicates that phenol is tilted from the surface, as it has been reported previously for coverages above 2 ML, that is, non-parallel orientations become important.[14] This is in direct contrast with the predicted adsorption geometry of isolated phenol on the surface, which would have an almost flat phenyl group.[32,33]

Additionally, weak peaks corresponding to C-H bending modes are also observed at 889, 1025, 1072, 1154 and 1169 cm^{-1}. Very weak C-H stretching modes are observed at 3026, 3049 and 3093 cm^{-1}. However no conclusive O-H stretch peak can be attributed in the acquired spectrum (data not shown), in agreement with the extremely weak signals observed by HREELS.[14] Details of the band assignments and comparison to the vibrational frequencies of liquid phenol are presented in Table 5.1.

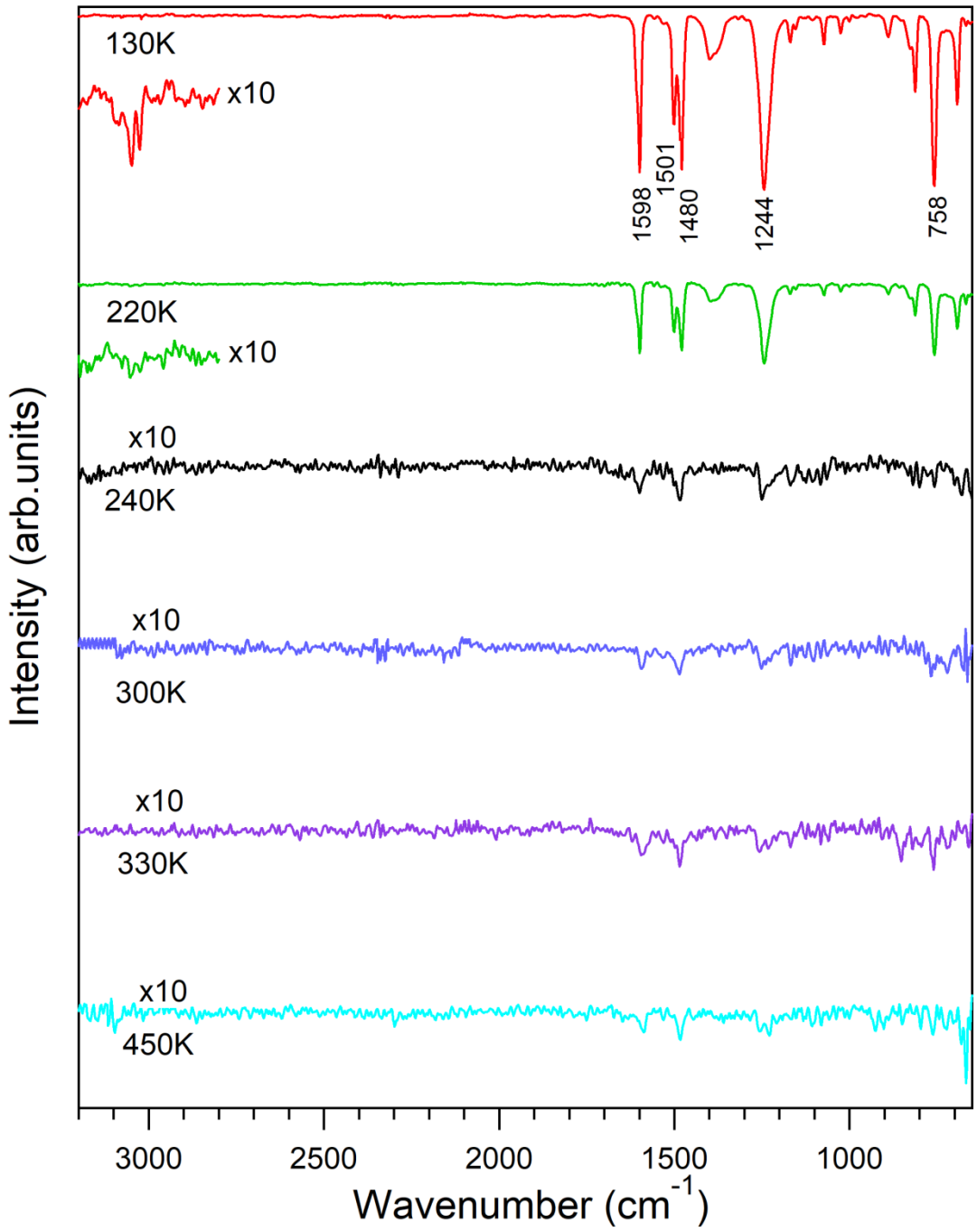

Figure 5.2: RAIRS spectra acquired at different temperatures for 100L of Phenol deposited at 130 K. Spectra have been offset for clarity.

After increasing the temperature to 220 K, the IR peak intensities diminish as some desorption takes place. This correlates with the desorption temperature of the multilayer of phenol

on Pt(111). Upon reaching 240 K and subsequently 300 K, the IR peaks further decrease in intensity which is in agreement with the molecular desorption of the second layer of phenol on Pt(111).[14,22] The CO bond in phenol (Ph-OH), observed at 1244 cm^{-1}, experiences a "blue shift" to 1250 cm^{-1} together with the disappearance of most of the C-C and C-H stretching modes indicating a possible rearrangement of the phenyl ring and/or the onset of decomposition of the molecule. Of particular interest is the apparent shift of the peaks at 758, 889 and 1480 to 768, 852 and 1484 cm^{-1}, and the appearance of peak at 1233 cm^{-1} as the temperature is increased. As will be discussed below, these are uniquely indicative of the interaction between the phenoxy radical and the surface, and its subsequent decomposition. The nature and orientation of the phenoxy group on the surface will be discussed in the Discussion in conjunction with the observations for anisole and 2-phenoxyethanol.

At 450 K, the peaks at 758 and 852 cm^{-1} disappear indicating the eventual full decomposition on the surface. No molecular CO stretching peak has been observed in the 1800-2100 cm^{-1} region, which suggests that the reported desorption of CO from phenol decomposition is reaction limited; that is, as soon as it forms, it desorbs. This is in agreement with the previously reported results.[14,22]

Table 5. 1: Vibrational modes and peak assignments of Phenol on Pt(111) at 130 K.

Vibrational mode[a]	Pt(111)	Phenol liquid (exp)[34]
C-H stretch (20a)	**3093**	**3070**
C-H stretch (13)	**3049**	**3044**
C-H stretch (2)	**3026**	**3020**
C-C stretch (8a)	**1598**	**1597**
C-C stretch (19b)	**1501**	**1500**
C- C stretch (8b)	**1480**	**1474**
Ring stretch (19a)	**1398**	**1362**
C-O stretch (7a)	**1244**	**1228**
C-H bend (9a)	**1169**	**1168**
C-H bend (15)	**1154**	**1152**
C-H bend (9b)	**1072**	**1072**
C-H bend (12)	**1025**	**1025**
Ring breathing (18a)	**1000**	**981**
C-H bend (17b)	**889**	**888**
X2 sensitive (1)	**812**	**812**
C-H bend (4)	**758**	**752**

[a]Approximate mode description. Wilson's notation in parenthesis.[39]

Anisole

As the natural increase in complexity of model molecules toward lignin, anisole provides a methyl group as the shortest aliphatic group attachment to the phenolic oxygen. Since in phenol the O-H bond is the first to cleave, this replacement poses the question as to whether the O-C bond will follow suit for anisole.

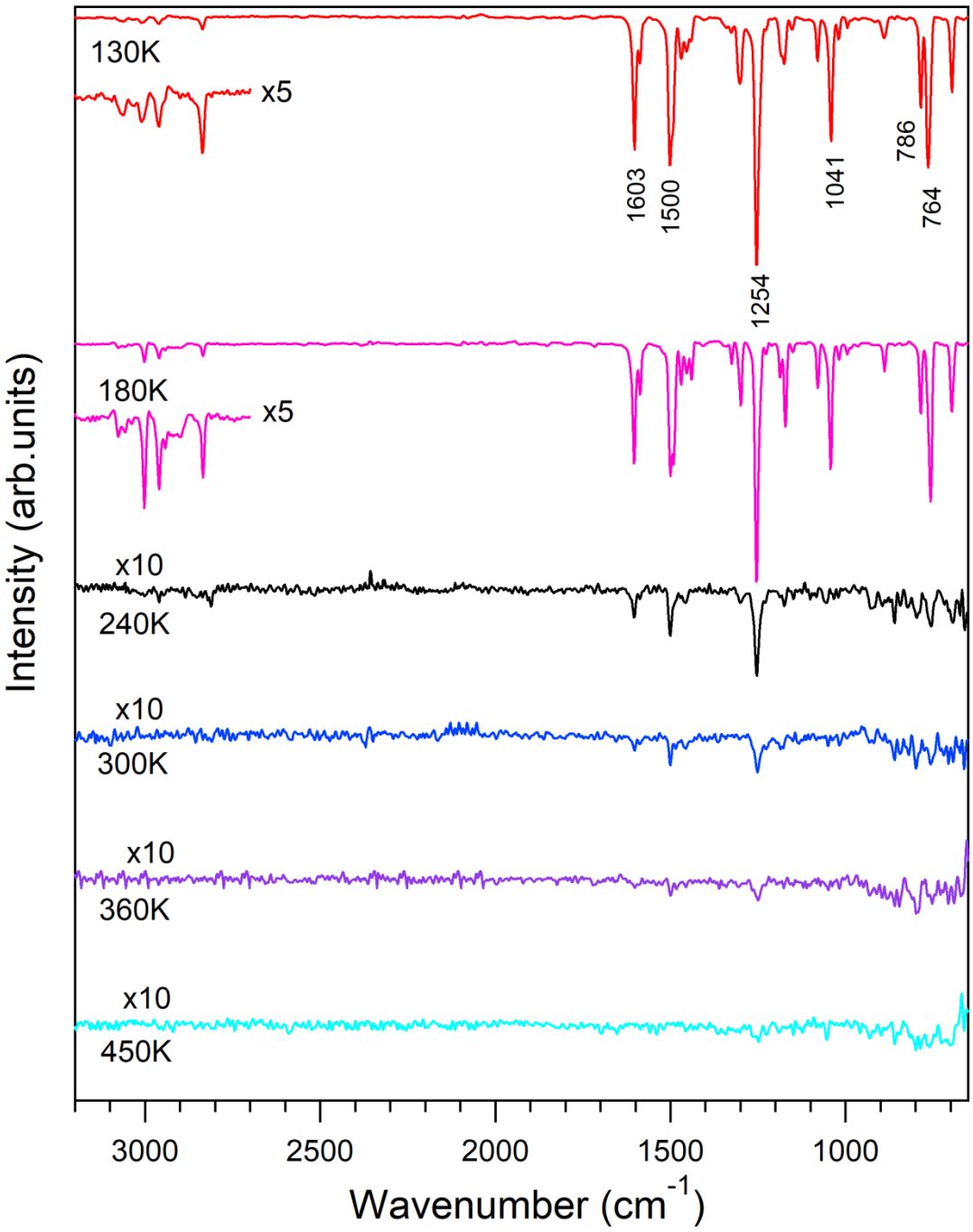

Figure 5.3: RAIRS spectra acquired at different temperatures for 100 L of Anisole deposited at 130 K. Spectra have been offset for clarity.

The identification of surface species upon dosing multilayers of anisole on Pt(111) was performed by monitoring vibrational modes of species on the surface as a function of temperature.

Details of the band assignments and comparison to the vibrational frequencies of liquid anisole are presented in Table 5.2.

Figure 5.3 shows the vibrational spectra of anisole after deposition of 100 L of anisole at 130 K, with spectra acquired at varying temperatures. Upon deposition, at 130 K, anisole shows six major peaks in the spectra at 764, 786, 1041, 1254, 1500 and 1603 cm^{-1}. The peaks at 1500 and 1603 cm^{-1} are assigned to C-C stretches, 764 cm^{-1} to C-H bending out of plane and 768 cm^{-1} to ring breathing. The more relevant peaks at 1041 and 1254 cm^{-1} are assigned to O-CH_3 stretching and Ph-OR stretching, respectively. Weak peaks corresponding to CH_3 stretching modes are observed at 2836, 2960 and 3009 cm^{-1}, whereas CH_3 deformation modes are observed at 1441 and 1469 cm^{-1}. Finally, a very weak C-H stretching is also observed at 3063 cm^{-1}.

There are small shifts between the vibrational modes of liquid anisole and the ones observed on Pt(111) mainly due to surface/metal interaction. As above, due to metal surface selection rule, only the modes that have vibrational dipole moments perpendicular to the surface can be observed and this gives us an insight about the adsorption geometry of the molecule on the surface. The observation of strong C-H bending peaks at 764, 890 and 1301 cm^{-1} indicates that anisole adsorbs on the surface primarily via a π-interaction between the phenyl ring and the surface. Furthermore, the observation of O-CH_3, Ph-OR and C-H stretching peaks at 1041, 1254 and 3063 cm^{-1}, respectively, indicates that the methoxy group of the anisole is tilted from the surface. These observations are in agreement with previous suggestions for anisole adsorption on Pt(111).[21,31] After increasing the temperature to 180 K, the majority of the IR peak intensities remains the same except for the peaks at 1175, 1441, 1587, 2960 and 3009 cm^{-1}. These peaks shift and become stronger and sharper. This behavior is attributed to the rearrangement of molecules in the adsorbed layer to a more thermodynamically stable geometry.

Upon reaching 240 K, the IR peaks decrease in intensity which is in agreement with the molecular desorption of the multilayer of anisole from Pt(111), as previously reported.[21] As in the case of phenol, the shift of the C-H bend (764 cm^{-1} out of plane) peak and the appearance of the new peak at 861 cm^{-1} (likely shifted from its 890 cm^{-1} initial position) are associated with the strong interaction of the molecule with the surface on the first layer suggesting that the adsorption geometry of the monolayer is different from the multilayer.

As the temperature reaches 300 K, the IR peaks further decrease in intensity and the CH_3 vibrations at 1441, 1469, 2836, 2960 and 3009 cm^{-1} vanish. In addition, the O-CH_3 peak at 1041

cm^{-1} disappears indicating the rupture of that bond. These observations lead to the conclusion that the anisole molecule follows a decomposition path that includes the dissociation of the C-H bonds in the methyl group and the formation of a phenoxy species. Direct confirmation of the phenoxy species is provided by the appearance of a peak at 1485 cm^{-1}. In addition, the peak at 1254 cm^{-1} (which in anisole is due to the Ph-OR bond) is shifted to 1251 cm^{-1}; and the C-H stretching peaks at 3026, 3049 and 3093 cm^{-1} and C-C peak at 1501 cm^{-1} vanish.

The phenoxy species seems to be stable up to 360 K. At 450 K, we clearly observe a small peak appear at 1261 cm^{-1} (initially a shoulder next to the 1251 cm^{-1} peak), and the C-C peak at 1603 cm^{-1} vanishes as the aromatic ring breaks down as the molecule completely decomposes. The spectra at 360 and 450 K are very similar to the spectra observed for phenol at 330 and 450 K, respectively, which suggests that anisole decomposes by forming phenoxy on the surface. The subsequent steps are similar to the phenol case. In addition, no molecular CO stretching peak has been observed in the 1800-2100 cm^{-1} region, this suggests that the reported desorption of CO from anisole decomposition is reaction limited.

Table 5.2: Vibrational modes and peak assignments of Anisole on Pt(111).

Vibrational mode [a]	**Pt(111)**	**Liquid Phase (exp)**[35]
(a) arm vibrations		
CH_3 antisym. str.	**3009**	**3004**
CH_3 antisym. str.	**2960**	**2942**
CH_3 sym. str.	**2836**	**2834**
CH_3 antisym. def.	**1469**	**1469**
CH_3 sym. def.	**1441**	**1442**
CH_3 rock	**1175**	**1180**
O-CH_3 str.	**1041**	**1039**
(b) ring vibrations		
C-H stretch	**3063**	**3062**
C-C stretch	**1603**	**1599**

C-C stretch	**1587**	**1588**
C-C stretch	**1500**	**1497**
C-C stretch	**1453**	**1455**
C-C stretch	**1326**	**1332**
C-H bend	**1301**	**1292**
Ph-O stretch	**1254**	**1247**
C-H bend	**1153**	**1151**
C-H bend	**1080**	**1073**
C-H bend	**1019**	**1019**
Ring breathing	**994**	**992**
C-H bend	**890**	**880**
Ring breathing	**786**	**785**
C-H bend (out of plane)	**764**	**752**
X-sensitive	**696**	**690**

[a]Approximate mode description.

Overall, the data supports the C-H bond cleavage in the methyl group as the onset of decomposition and provides direct identification of the phenoxy intermediate on the surface, in good agreement with predictions provided by DFT calculations.[21]

2-Phenoxyethanol

With better understanding of the reactivity of phenol and anisole on the Pt(111) surface, 2-phenoxyethanol provides a further increase in the complexity of the arm moiety. 2-phenoxyethanol is an important part of the lignin model, it provides a β-O-4 linkage and it allows a comparison of reactivity for different types of bonds, namely: Ph-O, C-C, C-O, C-H and O-H. A simple comparison with phenol and anisole suggests that there will be a competition between the O-H and C-H bond cleavage.

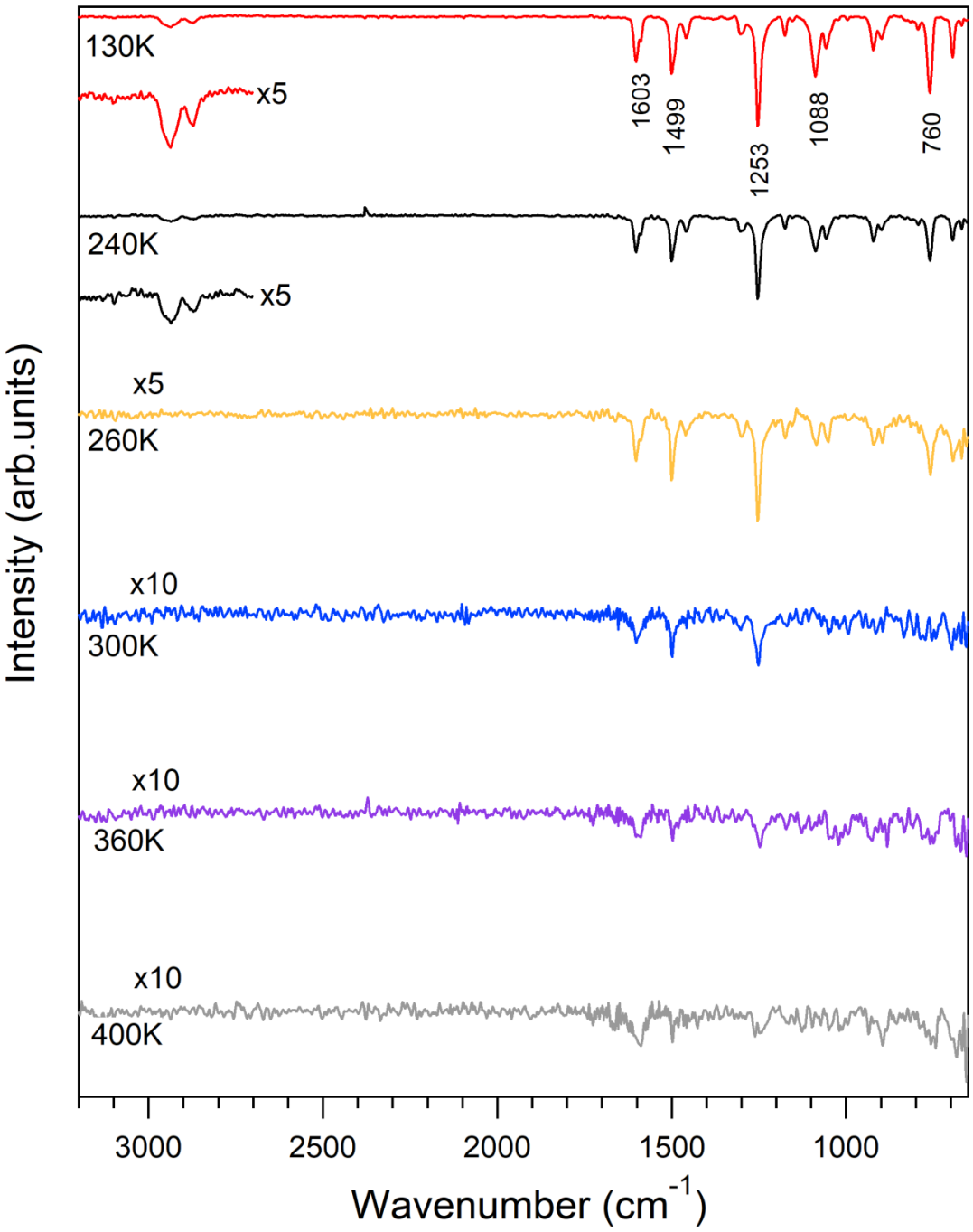

Figure 5.4: RAIRS spectra acquired at different temperatures for 100 L of 2-phenoxyethanol deposited at 130 K. Spectra have been offset for clarity.

Table 5.3: Vibrational modes and peak assignments of 2-Phenoxyethanol on Pt(111).

Vibrational mode[a]	**Pt(111)**	**Liquid Phase (exp)[36]**
(a) arm vibrations		
CH_2-CH_2 antisym str	**2938**	**2930**
CH_2-CH_2 sym str	**2876**	**2873**
CH_2 scissor	**1499**	**1491**
CH_2 twist + C-H ring bends	**1303**	**1296**
O-C + C-C + C-O str	**1088**	**1078**
O-C + C-O str	**1057**	**1042**
O-C-C + C-C-O def	**922**	**914**
(b) ring vibrations		
C-H ring bends	**1603**	**1594**
C-H ring bends	**1588**	**1584**
C-H ring bends	**1459**	**1454**
Ph-O + O-C str + O-H bend	**1253**	**1240**
C-H ring bends	**1175**	**1172**
C-H ring bends	**1153**	**1150**
Ring breathing		**996(cal)**
C-H ring bends	**899**	**892**
C-H ring bends	**817**	**822**
Ph-O-C def	**793**	**789**
C-H ring bends	**760**	**750**
C-H ring bends	**694**	**688**

[a] Abbreviations used : str, stretch; def, deformation. Approximate mode description.

The identification of surface species upon dosing 2-phenoxyethanol on Pt(111) was initially performed by monitoring vibrational modes of species on the surface at low temperature and then increasing the temperature to induce desorption and reaction. Details of the band assignments and comparison to the vibrational frequencies of liquid 2-phenoxyethanol are presented in Table 5.3.

Figure 5.4 shows the vibrational spectra of 2-phenoxyethanol after deposition of 100 L of 2-PE at 130 K, with spectra acquired at varying temperatures. Upon deposition, at 130 K, 2-PE shows five major peaks in the spectra at 760, 1088, 1253, 1499 and 1603 cm^{-1}. The peaks at 1088 and 1253 cm^{-1} are assigned to O-C + C-C + C-O str and Ph-O + C-O strs + O-H bend, respectively whereas the peak at the peak at 1499 cm^{-1} is assigned to CH_2 scissor bending mode. The peak at 760 cm^{-1} is assigned to C-H bending and the peak at 1603 cm^{-1} is assigned to C-C stretch in the phenyl. The remaining peaks are assigned as follows. Weak peaks corresponding to CH_2-CH_2 stretching modes are observed at 2876 and 2938 cm^{-1} whereas C-H bending modes are observed at 694, 817, 899, 1153, 1175, 1459 and 1588 cm^{-1}. However no conclusive O-H stretch peak can be attributed in the acquired spectrum. There are small shifts between the vibrational modes of liquid 2-phenoxyethanol and the ones observed on the Pt(111) surface,[36] especially for the Ph-OR+ O-C + O-H peak that is shifted from 1240 to 1253 cm^{-1} which indicates that the surface influences the adsorption geometry of the molecule. The aromatic ring is expected to lay parallel to the surface,[33] but the observation of the ring stretching frequencies suggest some degree of tilt. The observation of the strong peak at 1253 cm^{-1} indicates that the linear portion of the molecule is not completely flat on the surface and is probably tilted away from the surface at an angle, hence the observation of vibrations at 1088, 1499, 2876 and 2938 cm^{-1}. These observations are in agreement with the previous study of 2-phenoxyethanol on Pt(111).[19] After increasing the temperature to 240 K, the IR peaks decrease in intensity but no shifts are observed which is in agreement with the molecular desorption temperature of the multilayer of 2-PE on Pt(111).[19] Further heating to 260 K, leads to desorption of the second layer of 2-phenoxyethanol, leaving us with one monolayer that already started decomposing. The disappearance of the CH_2-CH_2 stretching modes at 2876 and 2938 cm^{-1} followed by the shift of Ph-OR + O-C + O-H and O-C + C-C + C-O vibrational modes to 1051 and 1086 cm^{-1} indicate the onset of decomposition of the arm, likely by O-H bond cleavage as it has been previously predicted.[19] The peak at 1499 cm^{-1}

remains since it not only corresponds to the CH_2 scissor mode, but also to ring vibrations (C-C str).

Upon reaching 300 K, the O-C + C-O and O-C + C-C + C-O stretching modes at 1051 and 1086 cm^{-1} vanish, and the Ph-OR + O-C stretching peak at 1253 cm^{-1} shift to 1251 cm^{-1}. The onset of the peak at 1482 cm^{-1} indicates the formation of the phenoxy group. By 400 K, the spectra look like the spectra observed for phenol between 330 K and 450 K, with the two peaks in the oxygen region at 1483 cm^{-1} and 1260 cm^{-1} which confirms that the 2-phenoxyethanol decomposes by forming phenoxy on the surface and falls back to same reactivity. In addition, no molecular CO stretching peak has been observed in the 1800-2100 cm^{-1} region, this suggests that the reported desorption of CO from 2-phenoxyethanol decomposition is reaction limited as well.

5.4 Discussion

Phenol, anisole and 2-phenoxyethanol adsorb on the surface at 130 K. Upon heating, the decomposition pathways of these aromatics undergo several bond cleavages to be able to form a key intermediate which is phenoxy. The phenoxy group, which had been previously suggested, can be clearly identified in our RAIRS spectra. Figure 5.5 shows a summary of the decomposition pathways as determined by combining RAIRS results with previous experimental and first-principles calculations.[14,16,19,21,22,26,31]

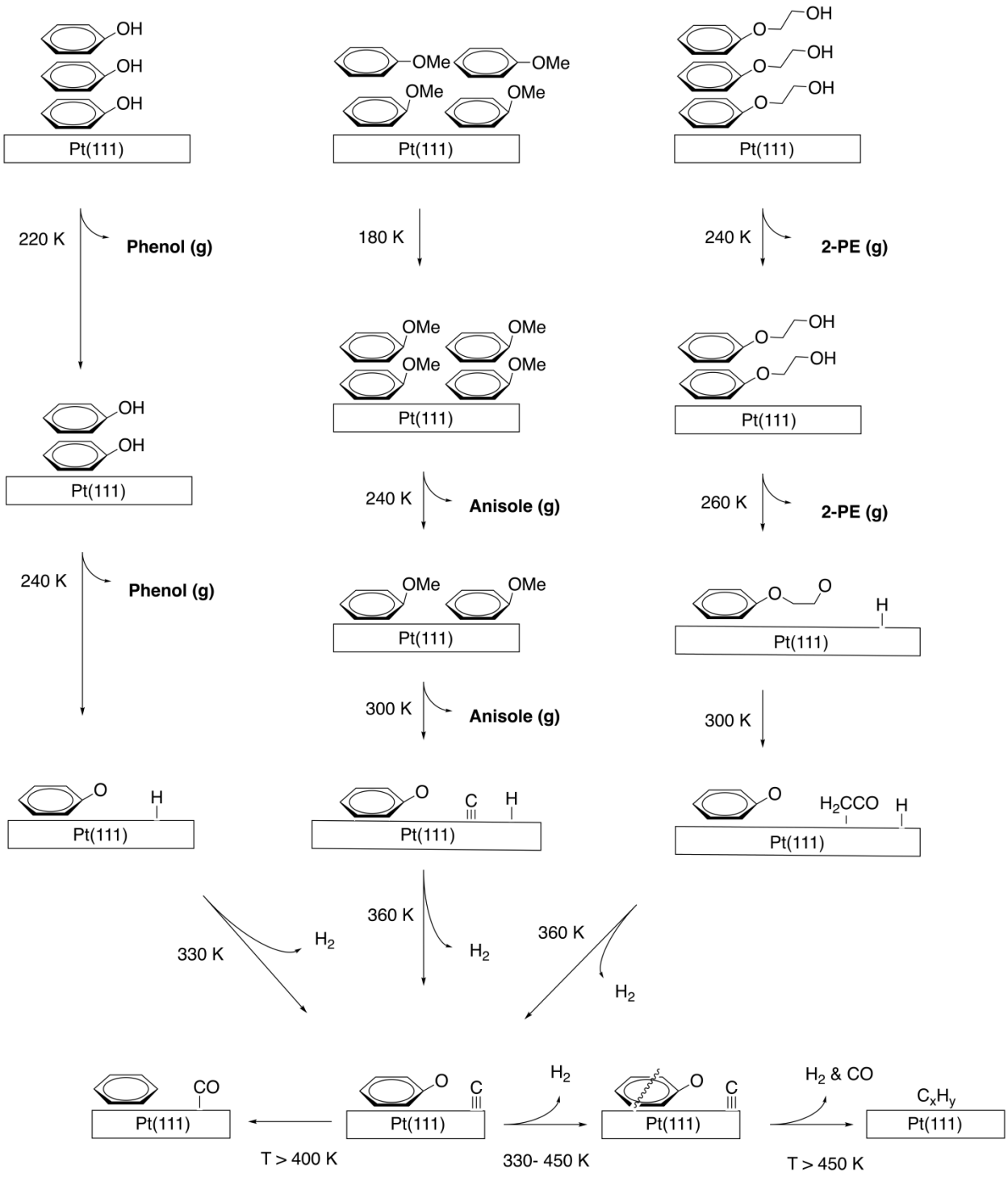

Figure 5.5: Reaction pathways and associated temperatures for phenol, anisole and 2-phenoxyethanol on Pt(111) under UHV conditions. The three molecules decompose via the same key phenoxy intermediate. The wavy line represents the cleavage of the aromatic ring. Molecular fragments are drawn for clarity, and drawing does not imply observed or inferred geometry.

Desorption

Phenol desorbs from the surface in two steps: the multilayer desorption occurs upon reaching 220 K, while the second layer desorbs upon reaching 240 K. These temperatures are consistent with White and co-workers[14] that reported the two step desorption of phenol from Pt (111) at 195 K for multilayers and 225 K for the second layer. Campbell and co-workers[26] used calorimetry to show that initially phenol adsorbs on the Pt(111) surface with a heat of 220 kJ/mol. Upon increasing the coverage, they distinguish a transition layer that binds more strongly compared to the bulk multilayer. The reported heats of adsorption of the second layer and the multilayer are 118 kJ/mol and 73.2 kJ/mol, respectively.

The adsorption geometry of the multilayer of anisole is different from the monolayer. The methyl group peak vibrations get stronger at 180 K. This suggests that upon heating to 180 K the molecule has enough energy to reorient itself on the surface in a more stable configuration. At 240 K, the multilayer desorbs from the surface. Upon reaching 300 K, part of the saturated monolayer desorbs from the surface. Reocreux et al.[21] investigated the reactivity of anisole on Pt(111) by temperature programmed desorption and first-principles calculations. The reported TPD result showed that the multilayer and part of the monolayer desorbs at 260 K and 360 K respectively.

2-phenoxyethanol desorbs from the surface in two steps. The multilayer and the second layer desorb from the surface upon reaching 240 K and 260 K respectively. At this temperature, desorption competes with the onset of decomposition. This is in agreement with the reported TPD and first-principles calculations results from Ould Hamou et al.[19] that showed that the multilayer and the second layer of 2-phenoxyethanol desorb from the surface at 238 K and 254 K respectively.

Decomposition

The decomposition of the three molecules can be followed by the disappearance of the the PhO-C peak at ~1040 cm^{-1} in the parent species and the appearance of the characteristic Ph-O vibration in the phenoxy radical at 1480 cm^{-1}. Figure 5.6 shows the intensity behaviour of these bands together with the most intense 1250 cm^{-1} band characteristic of the three parent molecules which allows the observation of the desorption process. The onset of formation of the phenoxy species is around 200 K and above ~400 K we observed its complete decomposition. The phenoxy species arising from phenol seems to linger to higher temperatures (~550K). This may be explained by the lack of carbon-containing fragments on the surface which have been proposed to catalyze

the decomposition. Quantification of the Ph-O peak arising from phenol decomposition is difficult because of the overlapping peaks, and therefore the data shown in Figure 5.6 for this peak contain a large error. Nevertheless, the peak is clearly visible as shown in Figure 5.7.

Although the reaction takes place sufficiently fast to prevent us from determining which bond will cleave first, for anisole/Pt(111), Reocreux et al.[21] showed by first-principles calculations results that the first reaction starts with C-H bond cleavage followed by the PhO-CH_2 bond cleavage (O-C) and further dehydrogenation of the methyl group to form phenoxy and carbon on the surface. For 2-phenoxyethanol, decomposition was proposed to start by O-H bond cleavage forming $PhOCH_2CH_2O$ followed by two consecutive C-H bond cleavages and then formation of phenoxy. Overall, the decomposition of all three molecules leads to the formation of phenoxy on the surface.

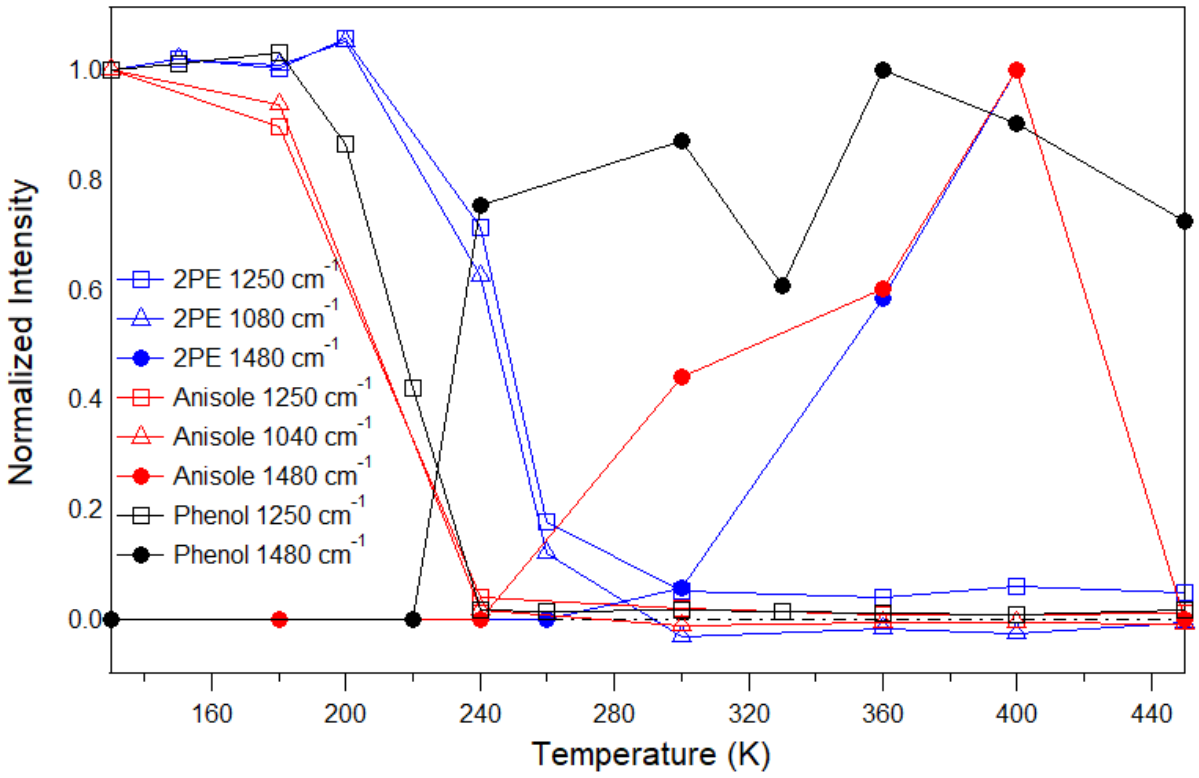

Figure 5.6: Decomposition of phenol; anisole; and 2-phenoxyethanol. Peaks at ~1250 cm^{-1} are associated with the parent molecule (ring plus Ph-OR), 1040 and 1080 cm^{-1} corresponds to the PhO-C bond and 1480 cm^{-1} shows the Ph-O bond in the phenoxy radical. Intensities have been normalized to the value at 130 K for the parent molecules and to their highest value for the Ph-O peak.

The nature of the key phenoxy intermediate

The formation of the phenoxy intermediate can be inferred for the decomposition of the three molecules studied here. White and co-workers[14] and Zhuang[22] showed that phenol decomposes into phenoxy by O-H bond cleavage above 225 K. We have inferred the formation of phenol from anisole by the disappearance of the O-CH_3 vibration at ~1040 cm^{-1} in agreement with Vohs and co-workers[30] and King and co-workers[31] who also proposed the formation of the phenoxy species as the main intermediate for anisole decomposition on Pt(111) and Pt(100)hex. Similarly the formation of phenoxy was proposed by DFT by comparison with TPD and XPS data.[21]

The phenoxy intermediate has been predicted to bind to the Pt(111) surface via a η^5-π adsorption geometry, effectively as an oxocyclohexadienyl radical.[37] Such a π adsorption is calculated to be more stable than a physisorbed geometry by approximately 0.9 eV, with an overall adsorption energy of ~2.7 eV, depending on binding site. It is therefore no surprise that when any evidence of phenoxy is inferred, the assumption is made that the species will have a η^5-π geometry. However, in this species, the C-O bond has some double bond character, and its vibrational frequency is expected in the 1600-1650 cm^{-1} rang and has been predicted at 1616 cm^{-1} by DFT calculations for phenoxy/Pt(111).[21]

The results shown above do not show a peak in the 1616 region for any of the molecules studied. Instead, peaks characteristic of the phenoxy radical have been observed. Figure 5.7 shows the appearance of the Ph-O peak for phenoxy at ~1480 cm^{-1} during the decomposition of the three molecules. The complete identification of the vibrational structure of the phenoxy species is obtained by comparison with experimental data obtained for phenoxy supported in an argon matrix and computational data.[38] In Table 5.4 we compare the phenoxy vibrational frequencies with those observed by the decomposition of the three target molecules as measured here. Through this comparison, phenoxy can be clearly identified. The evolution of all the peaks with temperature is provided in the Appendix H.

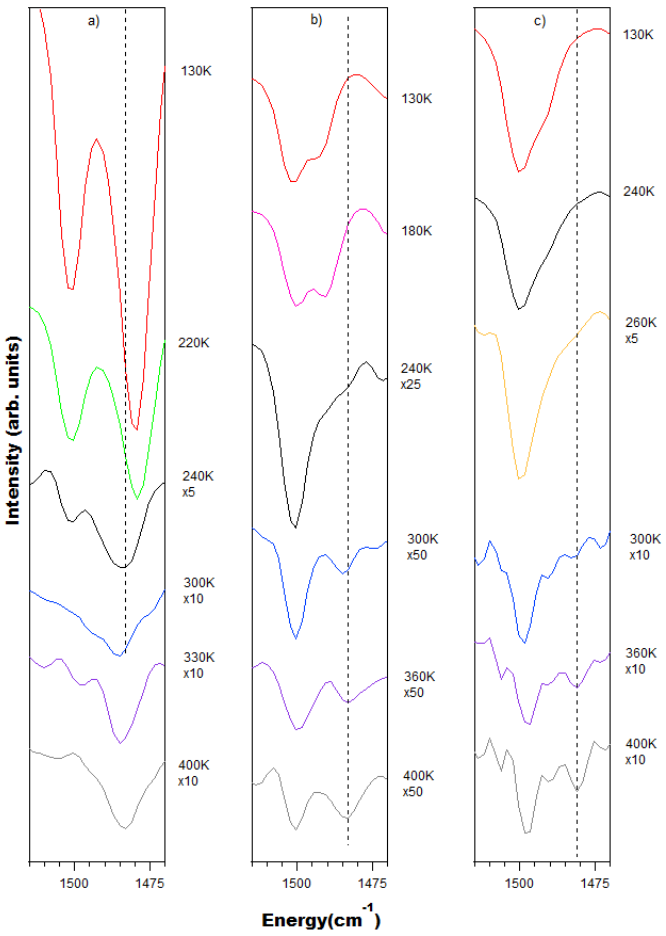

Figure 5.7: Direct observation of the peak at ~1480 cm^{-1} during the decomposition of a) phenol; b) anisole; and c) 2-phenoxyethanol.

Table 5.4: Assignment of the phenoxy vibrations during decomposition of phenol, anisole and 2-phenoxyethanol on Pt(111).

Mode[a]	**Phenoxy Matrix[b]**	**Phenol[c] Pt(111) 300K**	**Anisole[c] Pt(111) 300K**	**2PE[c] Pt(111) 300K**
C-H str (20a)	3090			
C-H str (13)	3065			
C-H str (2)	3018			
C-C str (8a)	1550	1593	1603	1602
			1589	1586
C-C stretch/C-H bend (19b)	1515		1500	
C-C str/C-H bend (8b)	1441		1457	
C-H bend/ C-C str (19a)	1397			
C-C str/C-H bend (14)	1318			
C-O stretch (7a)	**1481**	**1483**	**1485**	**1482**
C-C str/C-H bend (3)	1266	1251[d]	1251[d]	1251[d]
C-H bend	1167			
C-H bend/ C-C str (8b)	1441			
C-H bend/ C-C str (9b)	1072			
C-H bend + ring breathing (12)	1038		1016	
C- C- C bend (18a)	977		930	
C-H wag + boat def (17b)	898		860	

Chair def + CO/CH wag (4)	784	768

[a]Approximate mode description based on phenoxy. Wilson's notation in parenthesis.[39] [b]Spanget-Larsen experimental data.[38] [c]At this temperature the molecule has mostly reacted to produce phenoxy. [d]Peak shifts to 1261 at higher temperature.

The formation of the phenoxy species (and not the oxocyclohexadienyl) can be easily explained by the surface coverage. In these experiments the surface is dosed with multilayer quantities of the molecule of interest (phenol, anisole or 2-phenoxyethanol) with a relatively high flux. Under these conditions, the molecules are crowded on the surface and upon reaction there is not enough space for a rearrangement of the phenoxy radical into its preferred geometry. The phenomenon of molecular crowding for these type of molecules has been predicted since the decomposition leads to multiple fragments.[19,21] A tilted or perpendicular orientation has also proposed for high coverages[14] and it is the norm for other transition metals.[15,40–42] The explanation of our observations as arising from a phenoxy radical is actually consistent with the previously published data where the oxocyclohexadienyl species is logically proposed but not clearly observed when the dose exceeds a monolayer.[14,19,21,30,31] In fact, the only clear observation of the oxocyclohexadienyl radical is seen in the data of Vohs et al.[30] for an experiment in which less than a monolayer is deposited on the surface with low flux and then the sample is heated. The HREELS data for anisole/Pt(111) shows a peak at 1630 cm^{-1} between that starts to appear before 250 K and disappears by 350 K. This peak, which was not identified by the authors, is consistent with the formation and decomposition of the oxocyclohexadienyl radical, emphasizing that this species can only be observed at low coverage. Interestingly, Vohs et al[30] report the formation of H_2 and CO as the only reaction products arising from the oxocyclohexadienyl intermediate, while we have previously reported[19,21] the formation of benzene which is consistent with a tilted/perpendicular geometry of the phenoxy species as intermediate.[18,40]

5.5 Conclusion

Under ultra-high vacuum conditions, the lignin model molecule, phenol, anisole and 2-phenoxyethanol (2-PE) adsorbed on the Pt(111) surface decompose via several complex and simultaneous reaction mechanisms. Despite increasing the arm complexity, the models of β-O-4 linkages seems to eventually fall back to the formation of phenoxy as the key intermediate in the

decomposition process. Upon dosing in the multilayer regime, we measure the vibrational spectra of each molecule in the adsorbed state and monitor the desorption and decomposition by the changes in characteristic vibrational modes of each species. The appearance of a peak at ~1480 cm^{-1} indicates the formation of the phenoxy species.

This study provides direct evidence of the phenoxy species (as opposed to the oxocyclohexadienyl moiety) and further insights in the order of bond cleavage of lignin models on Pt(111).

References

(1) Goklany, I. Have Increases in Population, Affluence and Technology Worsened Human and Environmental Well-Being? *Electron. J. Sustain. Dev.* **2009**, *1*, 3–28.

(2) Demirbaş, A. Biomass Resource Facilities and Biomass Conversion Processing for Fuels and Chemicals. *Energy Convers. Manag.* **2001**, *42*, 1357–1378.

(3) Peter, M. Energy Production from Biomass (part 1): Overview of Biomass. **2002**, *83*, 37–46.

(4) Pettersen, R. The Chemical Composition of Wood. *Chem. solid wood* **1984**, 1–9.

(5) Kang, S.; Li, X.; Fan, J.; Chang, J. Hydrothermal Conversion of Lignin: A Review. *Renew. Sustain. Energy Rev.* **2013**, *27*, 546–558.

(6) Zakzeski, J.; Bruijnincx, P. C. a; Jongerius, A. L.; Weckhuysen, B. M. The Catalytic Valorization of Ligning for the Production of Renewable Chemicals. *Chem. Rev.* **2010**, *110*, 3552–3599.

(7) Huber, G. W.; Iborra, S.; Corma, A. Synthesis of Transportation Fuels from Biomass: Chemistry, Catalysts, and Engineering. *Chem. Rev.* **2006**, *106*, 4044–4098.

(8) Jahirul, M. I.; Rasul, M. G.; Chowdhury, A. A.; Ashwath, N. Biofuels Production through Biomass Pyrolysis- A Technological Review. *Energies* **2012**, *5*, 4952–5001.

(9) Bridgwater, a. V. Review of Fast Pyrolysis of Biomass and Product Upgrading. *Biomass and Bioenergy* **2012**, *38*, 68–94.

(10) Mohan, D.; Pittman, C. U.; Steele, P. H. Pyrolysis of Wood/biomass for Bio-Oil: A Critical Review. *Energy and Fuels* **2006**, *20*, 848–889.

(11) Yan, N.; Zhao, C.; Dyson, P. J.; Wang, C.; Liu, L. T.; Kou, Y. Selective Degradation of Wood Lignin over Noble-Metal Catalysts in a Two-Step Process. *ChemSusChem* **2008**, *1*, 626–629.

(12) Zakzeski, J.; Bruijnincx, P. C. A.; Jongerius, A. L.; Weckhuysen, B. M. The Catalytic Valorization of Ligning for the Production of Renewable Chemicals. *Chem. Rev.* **2010**, *110*, 3552–3599.

(13) Mobley, J. K.; Yao, S. G.; Crocker, M.; Meier, M. Oxidation of Lignin and Lignin B-O-4 Model Compounds via Activated Dimethyl Sulfoxide. *RSC Adv.* **2015**, *5*, 105136–105148.

(14) Ihm, H.; White, J. M. Stepwise Dissociation of Thermally Activated Phenol on Pt(111). *J. Phys. Chem. B* **2000**, *104*, 6202–6211.

(15) Richardson, N. V.; Hofmann, P. A Spectroscopic Investigation of the Adsorption of Phenol on Cu{110}. *Vacuum* **1983**, *33*, 793–796.

(16) Shi, D.; Vohs, J. M. Lignin-Derived Oxygenate Reforming on a Bimetallic Surface: The Reaction of Benzaldehyde on Zn/Pt(111). *Surf. Sci.* **2016**, *650*, 161–166.

(17) Russell, J. N.; Sarvis, S. S.; Morris, R. E. Adsorption and Thermal Decomposition of Phenol on Ni(110). *Surf. Sci.* **1995**, *338*, 189–203.

(18) Serafin, J. G.; Friend, C. M. Carbon-Oxygen Bond Strength as a Control of Reaction Kinetics: Phenol on Mo(110). *Surf. Sci.* **1989**, *209*, 163–175.

(19) Ould Hamou, C. a.; Réocreux, R.; Sautet, P.; Michel, C.; Giorgi, J. B. Adsorption and Decomposition of a Lignin B-O-4 Linkage Model, 2-Phenoxyethanol, on Pt(111): Combination of Experiments and First-Principles Calculations. *J. Phys. Chem. C* **2017**, *121*, 9889–9900.

(20) Ihm, H.; Ajo, H. M.; Gottfried, J. M.; Bera, P.; Campbell, C. T. Calorimetric Measurement of the Heat of Adsorption of Benzene on Pt(111). *J. Phys. Chem. B* **2004**, *108*, 14627–14633.

(21) Réocreux, R.; Ould Hamou, C. A.; Michel, C.; Giorgi, J. B.; Sautet, P. Decomposition Mechanism of Anisole on Pt(111): Combining Single-Crystal Experiments and First-Principles Calculations. *ACS Catal.* **2016**, *6*, 8166–8178.

(22) Zhuang, S. X.; Wei, X. M.; Wang, Y. S.; Zhai, R. S. A HREELS Study of the Interaction of Cyclohexanone and Phenol with Pt(111) Surface. *Chinese Chem. Lett.* **1996**, *7*, 661–662.

(23) Lu, F.; Salaita, G. N.; Laguren-Davidson, L.; Stern, D. a.; Wellner, E.; Frank, D. G.; Batina, N.; Zapien, D. C.; Walton, N.; Hubbard, A. T. Characterization of Hydroquinone and Related Compounds Adsorbed at Pt(111) from Aqueous Solutions: Electron Energy-Loss Spectroscopy, Auger Spectroscopy, LEED, and Cyclic Voltammetry. *Langmuir* **1988**, *4*, 637–646.

(24) Kahn, B. E.; Chaffins, S. a.; Gui, J. Y.; Lu, F.; Stern, D. a.; Hubbard, A. T. Surface Vibrational Spectroscopy. A Comparison of the EELS Spectra of Organic Adsorbates at Pt(111) with IR and Raman Spectra of the Unadsorbed Organics. *Chem. Phys.* **1990**, *141*, 21–39.

(25) Li, G.; Han, J.; Wang, H.; Zhu, X.; Ge, Q. Role of Dissociation of Phenol in Its Selective Hydrogenation on Pt(111) and Pd(111). *ACS Catal.* **2015**, *5*, 2009–2016.

(26) Carey, S. J.; Zhao, W.; Mao, Z.; Campbell, C. T. Energetics of Adsorbed Phenol on Ni(111) and Pt(111) by Calorimetry. *J. Phys. Chem. C* **2018**, acs.jpcc.8b03155.

(27) Cheng, J.; Hu, P. Theory of the Kinetics of Chemical Potentials in Heterogeneous Catalysis. *Angew. Chemie - Int. Ed.* **2011**, *50*, 7650–7654.

(28) Bonalumi, N.; Vargas, A.; Ferri, D.; Bürgi, T.; Mallat, T.; Baiker, A. Competition at Chiral Metal Surfaces: Fundamental Aspects of the Inversion of Enantioselectivity in Hydrogenations on Platinum. *J. Am. Chem. Soc.* **2005**, *127*, 8467–8477.

(29) Bonalumi, N.; Vargas, A.; Ferri, D.; Baiker, A. Theoretical and Spectroscopic Study of the Effect of Ring Substitution on the Adsorption of Anisole on Platinum. *J. Phys. Chem. B* **2006**, *110*, 9956–9965.

(30) Shi, D.; Arroyo-Ramírez, L.; Vohs, J. M. The Use of Bimetallics to Control the Selectivity for the Upgrading of Lignin-Derived Oxygenates: Reaction of Anisole on Pt and PtZn Catalysts. *J. Catal.* **2016**, *340*, 219–226.

(31) Tan, Y. P.; Khatua, S.; Jenkins, S. J.; Yu, J.-Q.; Spencer, J. B.; King, D. a. Catalyst-Induced Changes in a Substituted Aromatic: A Combined Approach via Experiment and Theory. *Surf. Sci.* **2005**, *589*, 173–183.

(32) Honkela, M. L.; Björk, J.; Persson, M. Computational Study of the Adsorption and Dissociation of Phenol on Pt and Rh Surfaces. *Phys. Chem. Chem. Phys.* **2012**, *14*, 5849–5854.

(33) Réocreux, R.; Huynh, M.; Michel, C.; Sautet, P. Controlling the Adsorption of Aromatic Compounds on Pt(111) with Oxygenate Substituents: From DFT to Simple Molecular Descriptors. *J. Phys. Chem. Lett.* **2016**, *7*, 2074–2079.

(34) Evans, J. C. The Vibrational Spectra of Phenol and Phenol-OD. *Spectrochim. Acta* **1960**, *16*, 1382–1392.

(35) Balfour, W. J. The Vibrational Spectrum of Anisole. *Spectrochim. Acta* **1983**, *39A*, 795–800.

(36) Badawi, H. M. Vibrational Spectra and Assignments of 2-Phenylethanol and 2-Phenoxyethanol. *Spectrochim. Acta - Part A Mol. Biomol. Spectrosc.* **2011**, *82*, 63–68.

(37) Peköz, R.; Donadio, D. Effect of van Der Waals Interactions on the Chemisorption and Physisorption of Phenol and Phenoxy on Metal Surfaces. *J. Chem. Phys.* **2016**, *145*.

(38) Spanget-Larsen, J.; Gil, M.; Gorski, a.; Blake, D. M.; Waluk, J.; Radziszewski, J. G. Vibrations of the Phenoxyl Radical. *J. Am. Chem. Soc.* **2001**, *123*, 11253–11261.

(39) Wilson, E. B. The Normal Modes and Frequencies of Vibration of the Regular Plane Hexagon Model of the Benzene Molecule. *Phys. Rev.* **1934**, *45*, 706–714.

(40) Xu, X.; Friend, C. M. The Role of Coverage in Determining Adsorbate Stability: Phenol Reactivity on rhodium(111). *J. Phys. Chem.* **1989**, *93*, 8072–8080.

(41) Guo, X. C.; Madix, R. J. Monolayer Structure of Phenoxy Species on Cu(110): An STM Study. *Surf. Sci.* **1995**, *341*.

(42) Solomon, J. L.; Madix, R. J.; Stöhr, J. Orientation and Absolute Coverage of Benzene, Aniline, and Phenol on Ag(110) Determined by NEXAFS and XPS. *Surf. Sci.* **1991**, *255*, 12–30.

Chapter 6:

Adsorption and Decomposition of a Lignin β-O-4 Linkage Model: Reactivity of Veratrol on Pt(111) by Combination of XPS, TPD and RAIRS Experiments.

I initiated and supervised the project related with the reactivity of Veratrol on Pt(111). Kusuma Virginna Adiningtyas helped me perform the XPS and TPD experiments as part of fulfillment of her coop term. I trained Mohammed Asiri in performing the RAIRS experiments and analysis. I interpreted all the results and wrote the draft article.

Draft Manuscript in preparation for submission to Surface Science.

6 Adsorption and Decomposition of a Lignin β-O-4 Linkage Model: Reactivity of Veratrol on Pt(111) by Combination of XPS, TPD and RAIRS Experiments

Cherif A. Ould Hamou,[†,§] Mohammed Z. Asiri,[†,§] Kusuma V. Adiningtyas, [†,‖] Javier B. Giorgi.[†,‖,*]

[†] Centre for Catalysis Research and Innovation, [§] Department of Physics, [‖] Department of Chemistry and Biomolecular Sciences, University of Ottawa, 10 Marie Curie Pvt., Ottawa, Ontario, Canada. K1N 6N5.

Abstract

To sustain the current attempts in valorizing lignin-based derivatives, the adsorption and decomposition of veratrol on a Pt(111) surface is studied as a model to understand the reactivity of the β-O-4 linkage in lignin. The results showed that under ultra-high vacuum conditions, hydrogen and carbon monoxide are the main desorbing products. Combining X-ray photoelectron spectroscopy, reflection absorption infrared spectroscopy and temperature programmed desorption experiments, a reaction mechanism is suggested, starting with the desorption of the multilayer around 215 K, followed by the decomposition of the monolayer through C-H and O-C bonds cleavage on the methoxy groups. 1,2-Benzoquinone is proposed to exist as a key surface intermediate that keeps decomposing to form H_2 and CO that desorb at 315 K and 420 K respectively.

Key-words: Veratrol, mechanism, decomposition, TPD, DFT, XPS, lignin

6.1 Introduction

Lignin is one of the most abundant polymer in wood and consists of network of aromatics that are linked with each other by oxygenate groups.[1] Lignin is a sustainable and renewable feedstock that could provide an infinite supply of valuable chemicals. Among the potential routes for production of chemicals, heterogeneous catalysis is regarded as the key for lignin conversion by reducing the activation energies for reaction and targeting products selectively. In the lignin valorization quest, it becomes important to always increase the complexity of the lignin model used to have a better overall understanding of the reactivity of lignin itself. In previous published work, we started with a simple lignin model such as anisole and gradually increased the complexity of the arm moiety towards 2-phenoxyethanol.[2,3] The aromatic molecules within lignin are cross-linked with each other by more than one arm moiety and this opens new sight for investigation. Veratrol, with its two methoxy functional groups on the 1,2 positions, is used here as a model of the substituted β-O-4 linkage type (Figure 6.1).

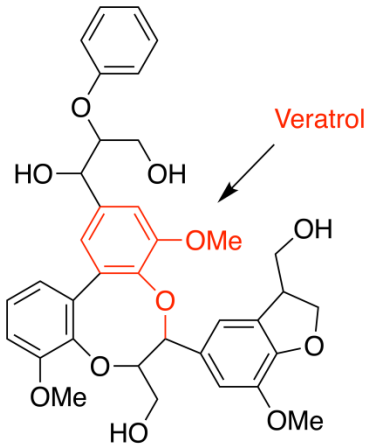

Figure 6.1: Small lignin fragment with highlighted veratrol molecule in red.

No experimental or theoretical studies on the reactivity of veratrol on single crystal catalysts had yet been published. In terms of reactivity, veratrol can undergo a decomposition scheme that is, in principle, related to aromatics containing similar functional groups, such as anisole and guaiacol (2-Methoxyphenol). As such, previous studies of the reactivity of anisole and guaiacol on Pt(111) are relevant.

The reactivity of anisole on Pt(111) has been studied by means of temperature programmed desorption, X-ray photoelectron spectroscopy and reflection absorption infrared spectroscopy. In summary, anisole desorbs from the Pt(111) surface in two stages, the multilayer at 260 K and small fraction of the monolayer at 360 K.[2] The core level binding energies of C 1s showed two major peaks at 283.7 and 285.3 eV that were attributed to carbon species bound to a carbon atom and carbon species bound to an oxygen atom respectively. Most of the monolayer decomposes into phenoxy via a C-H bond cleavage on the methyl group below 325 K. At higher temperatures, there is a competition between Ph-O bond cleavage, forming phenyl then benzene, and a complete decomposition of the aromatic ring. These results showed that under UHV conditions, the formation of benzene is dominant and it desorbs from the surface at 400 K. Above 450 K, the remaining phenoxy completely decomposes into CO and H_2.[2,4,5]

The reactivity of Guaicol has been studied on Pt(111) by means of surface science technique and first principle calculations. The decomposition of the guaiacol starts with the dehydrogenation of the arm moieties.Vohs and coworkers[6] studied the reactivity of guaiacol on Pt(111) by means of temperature programmed desorption and high energy electron loss spectroscopy. On Pt(111), the physisorbed layer of guaiacol desorbs from the surface at 225 K. The chemisorbed layer simply decomposes by dehydrogenation of the hydroxyl group to form 2-methoxy-2,5-cyclohexadien-1-one as key intermediate. Further heating to 285 K, the intermediate starts to decompose and the observed desorption byproducts are CO that desorbs at 435 K and H_2 that desorbs at 340 K and 435 K. Upon reaching 485 K, only hydrocarbons remain on the surface.

McEwen and coworkers[7], on the other hand, studied the reactivity of guaiacol on Pt(111) by means of a temperature programmed X-ray photoelectron spectroscopy and first principles calculations. Guaiacol was adsorbed on the surface at 170 K and two major signals in the C 1s region corresponding to hydrocarbons/aromatic carbon species and carbon bound to oxygen species are found at 284.4 and 286.2 eV respectively. The desorption of the physisorbed layer was observed at 240 K. Although the overall binding energies remain unchanged, the use of synchrotron based XPS allowed to distinguish the different carbon species and it was reported that the saturation of the monolayer does not occur without some decomposition of guaiacol. At 170 K, the physisorbed and chemisorbed layers, in addition to some decomposed guaiacol are simultaneously present on the surface. Upon heating to 375 K, guaiacol decomposes by either the dehydrogenation of the hydroxyl group or the methyl group to eventually form 1,2-benzoquinone

as key intermediate. Above 375 K, the 1,2-benzoquinone keeps decomposing to form carbonaceous species and CO that quickly desorb from the surface.

Vlachos and coworkers[8], studied the reaction mechanism of guaiacol hydrogenation on Pt(111) by means of density functional theory calculations and linear free energy relations. guaiacol adsorbs flat on the surface via all the carbon atoms in the aromatic ring. The decomposition of guaiacol starts with the dehydrogenation of the methyl group. The intermediate specie can undergo two distinct reaction pathways to form a quinone radical specie as a key intermediate specie that will eventually get hydrogenated to form catechol. The first reaction pathway involves further dehydrogenation of the methyl group or demethylation. The second pathway will undergo O-H bond cleavage followed by dehydrogenation of the methyl group. The formation of phenol is speculated on further decomposition of the catechol on the surface.

Heyden and coworkers[9], studied the reaction mechanism of guaiacol hydrogenation on Pt(111) by means of density functional theory calculations and microkinetic modeling. guaiacol decomposes into two different reaction pathways that involve either the dehydration of the methyl group or the hydroxyl group to eventually form 2-Hydroxyphenolate as a key intermediate. Then the intermediate specie gets hydrogenated to form catechol as the major byproduct. The formation of anisole and phenol is proposed as well but the deoxygenation of the intermediate specie is 4 orders magnitude slower than production of catechol.

Building on previous experiments with anisole and 2-phenoxyethantol, but considering the uncertainty in reaction pathways and intermediates observed for guaiacol, similar but more complex molecules require detail study. This work provides a detailed description of the interaction and decomposition of veratrol on a Pt(111) surface. The focus is on the influence of the second arm moiety with regard to the reaction selectivity. The study is conducted by means of X-ray photoelectron spectroscopy (XPS), reflection absorption infrared spectroscopy (RAIRS) and temperature programmed desorption (TPD).

6.2 Experimental

XPS and TPD experiments were performed under ultrahigh vacuum (UHV) in a stainless steel analysis chamber with a base pressure of 5×10^{-10} mbar. The Pt(111) crystal surface was cleaned by repetitive cycles of 15 min of sputtering (0.5 keV, 1×10^{-5} mbar Ar^{+}) at 600 K, followed by annealing to 1100 K, described in details previously.[2]

RAIRS experiments were carried out in another UHV chamber dedicated for reflection absorption infrared spectroscopy where the base pressure is 7 x 10^{-10} mbar. The Pt (111) crystal surface was cleaned by repetitive cycles of 30 mins of sputtering (1.5 keV, 1 x 10^{-5} mbar Ar^{+}) at 600 K, followed by annealing to 1100 K for 2 mins. The sample cleanness was confirmed by LEED. Detailed description of the chamber can be found in chapter 5.

Veratrol (+99% purity, Sigma Aldrich) was introduced to the UHV chamber through a leak valve that was connected to a gas manifold with an attached veratrol reservoir. The reservoir was heated to 473 K to increase the vapor pressure and ensure the purity of the deposition. The gas manifold was heated accordingly to prevent condensation and allow a constant, stable flux of veratrol gas into the chamber. Exposure of veratrol to the surface was typically performed at 1x10^{-7} mbar pressure and the dosage measured in Langmuirs (1 L = 1.33x10^{-6} mbar ● s).

XPS

XPS spectra were recorded on a Specs GmbH system (XR50 X-ray source and Phoibos 100 SCD analyzer) using a standard Al Kα source (1486.7 eV) operated at 380 W (14.6 kV, 26 mA). Selected peaks were obtained in high resolution spectra using 0.1 eV step size, 0.5 second dwell time, and pass energy of 30 eV. For the C 1s and O 1s regions 6 scans were acquired to increase the signal to noise ratio. The spectra were then fit using CasaXPS analysis software using a mixed Gaussian-Lorentzian function and Shirley background subtractions for the C 1s region while a Linear background subtraction was used for the O 1s region.

For the experiments, veratrol was dosed on the clean sample at 130 K and then heated up to the desired temperature of observation to acquire the spectrum. Once the acquisition was done, the sample was subject to a cleaning cycle (Ar^{+} sputtering followed by annealing to 1100 K) to remove all the residual carbon on the surface. The cleanness of the sample surface was verified by LEED and XPS.

TPD

The TPD experiments require the placing of the sample in front of a differentially pumped quadrupole mass spectrometer (QMS) and ramping up the sample temperature while monitoring the fragments of interest. For our experiments, the Pt(111) sample was dosed with varying exposures of veratrol at 110 K and placed 1 mm below a 1 mm diameter hole leading to the differentially pumped QMS. The temperature-controlled heating ramp was programmed in LabView and designed to provide and record a linear temperature ramp in the range of 120 K to

800 K, with a ramp rate of 6 K/s. The sample was subject to one cleaning cycle (Ar^+ sputtering followed by annealing to 1100 K) to ensure the cleanness of the surface before each dosage. A total of 11 channels corresponding to m/z values of 138, 110, 108, 94, 78, 32, 31, 28, 16, 14 and 2, were monitored for the veratrol TPD experiments. The selected m/z values correspond to the expected species and their respective fragmentation patterns.

Analysis of the TPD data allows the experimental determination of desorption energies E_{des} for veratrol. The analysis is performed based on the general rate law for desorption by the simple approach of Redhead[10] with appropriately corrected frequency factors. The calculated frequency factors **ν** are presented in Table 1 as obtained using the Campbell approach[11,12] for molecular desorption and temperature corrected entropy values from the Knovel's Database.[13] The entropy of veratrol is not available; the entropy value for guaiacol was used as an approximation. Further details on the choice of the approach method have been previously described.

RAIRS

The RAIRS experimental spectra were collected at 4 cm^{-1} resolution with 1000 scans. The molecules were dosed on the clean sample at 130 K and then heated up to the desired temperature of observation to acquire the spectrum. For temperatures above 400 K, the sample was heated to the desired temperature and then cooled down to 400 K to acquire the spectrum. The spectra were manipulated using OPUS analysis software by performing a baseline correction and an atmospheric compensation for the CO_2 and H_2O regions. Due to geometry and different setup, the dosage in the RAIRS chamber is different from the analysis chamber of the TPD and XPS. Dosage values are reported and the discussion is performed in terms of comparable relative coverage.

6.3 Results

XPS

The identification of surface species upon dosing veratrol on Pt(111) was initially performed by monitoring the carbon and oxygen environment of species on the surface as a function of temperature. Figure 6.2 shows C 1s and O 1s photoelectron spectra after deposition of 20 L of veratrol on Pt(111) at 130 K, with spectra acquired at varying temperatures. Upon deposition, at 130 K, veratrol shows two peaks in the C 1s spectra, one at 285.2 eV, which is attributed to carbon atoms bound to an oxygen atom (labeled C-O), and the other one at 283.5 eV which is attributed to carbon atoms bound only to other carbon or hydrogen atoms (labeled C-C).

The binding energy difference between the carbon peaks is 1.7 eV. After flashing to 260 K, the C-C and C-O peak areas decrease in intensity as some desorption takes place and the binding energy difference of the C 1s signals of the C-C and C-O peaks remain the same. At 300 K, the C-C and C-O areas decrease in intensity and shift to lower binding energies of 283.1 and 284.7 eV respectively. The difference in binding energy is 1.6 eV. At 360 K, the C-O peak area vanishes. Upon heating to 450 K, the remaining C 1s area peak decreases as only adventitious carbon remains on the surface.

Observations of the O 1s region after depositing 20 L of veratrol at 130 K on Pt(111) correlates with observations in the C 1s region. Upon deposition, at 130 K, veratrol shows one peak at 531.7 eV. After flashing to 260 K, the peak area intensity decreases and shifts to lower binding energy of 531.5 eV as some desorption and decomposition takes place. This is consistent with the observations made on the C 1s region. At 300 K, the peak area intensity decreases and shifts to a lower binding energy of 531.3 eV, as some desorption and decomposition occur from the surface. At 360 K, the peak area vanishes.

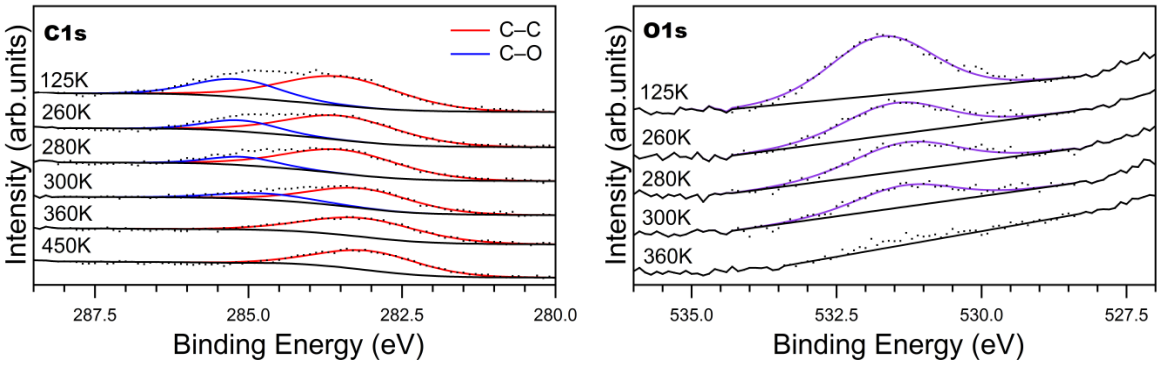

Figure 6.2: XPS spectra acquired at different temperatures for 20 L of veratrol deposited at 130 K.

Integrating the area of the C 1s region gives insight on how the coverage changes as a function of temperature (Figure 6.3). The drop in C 1s peak area above 220 K corresponds to desorption of the multilayer as will be further discussed in comparison with TPD results.

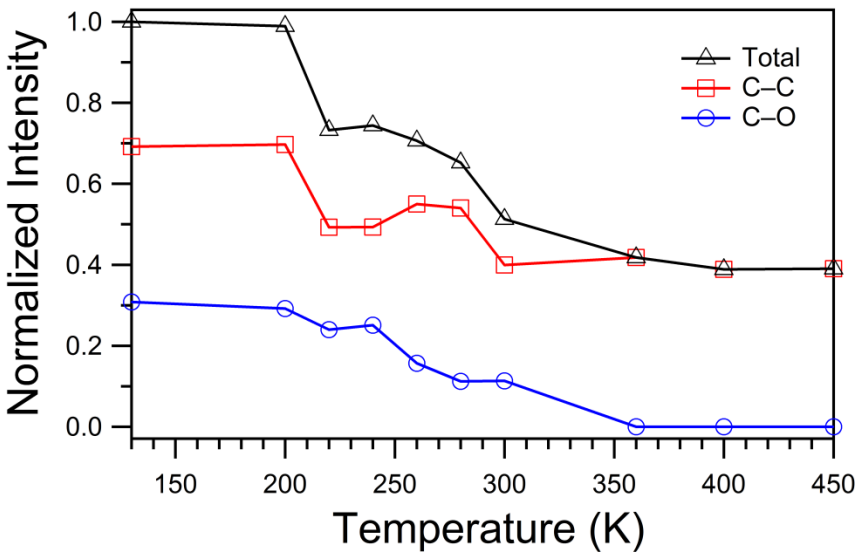

Figure 6.3: Analysis of XPS spectra acquired at different temperatures for 20 L of veratrol deposited at 130 K. The peak area decreases after 220 K, which corresponds to desorption of the multilayer.

RAIRS

The geometry and setup of the RAIRS chamber is different from the analysis one, hence the dosage between the two chambers cannot be directly compared.

Figure 6.4 shows the vibrational spectra of veratrol after deposition of 200 L of veratrol at 130 K, with spectra acquired at varying temperatures. Upon deposition, at 130 K, veratrol shows seven major peaks in the spectra at 758, 1033, 1127, 1261, 1467, 1515 and 1595 cm^{-1}. The peaks at 1515 and 1595 cm^{-1} are assigned to C-C ring + CCO stretches and the peak at 758 cm^{-1} to C-H bending out of plane. The more relevant peaks assigned to O-CH_3 stretching are observed at 1033 and 1055 cm^{-1} whereas the Ph-O + C-C stretches are assigned at 1233 and 1261 cm^{-1}. Weak peaks corresponding to CH_3 stretching modes are observed at 2836, 2958, 3004 cm^{-1} whereas CH_3 scissor modes are observed at 1443 and 1467 cm^{-1}. Finally, a very weak C-H stretching peak is also observed at 3064 cm^{-1}.

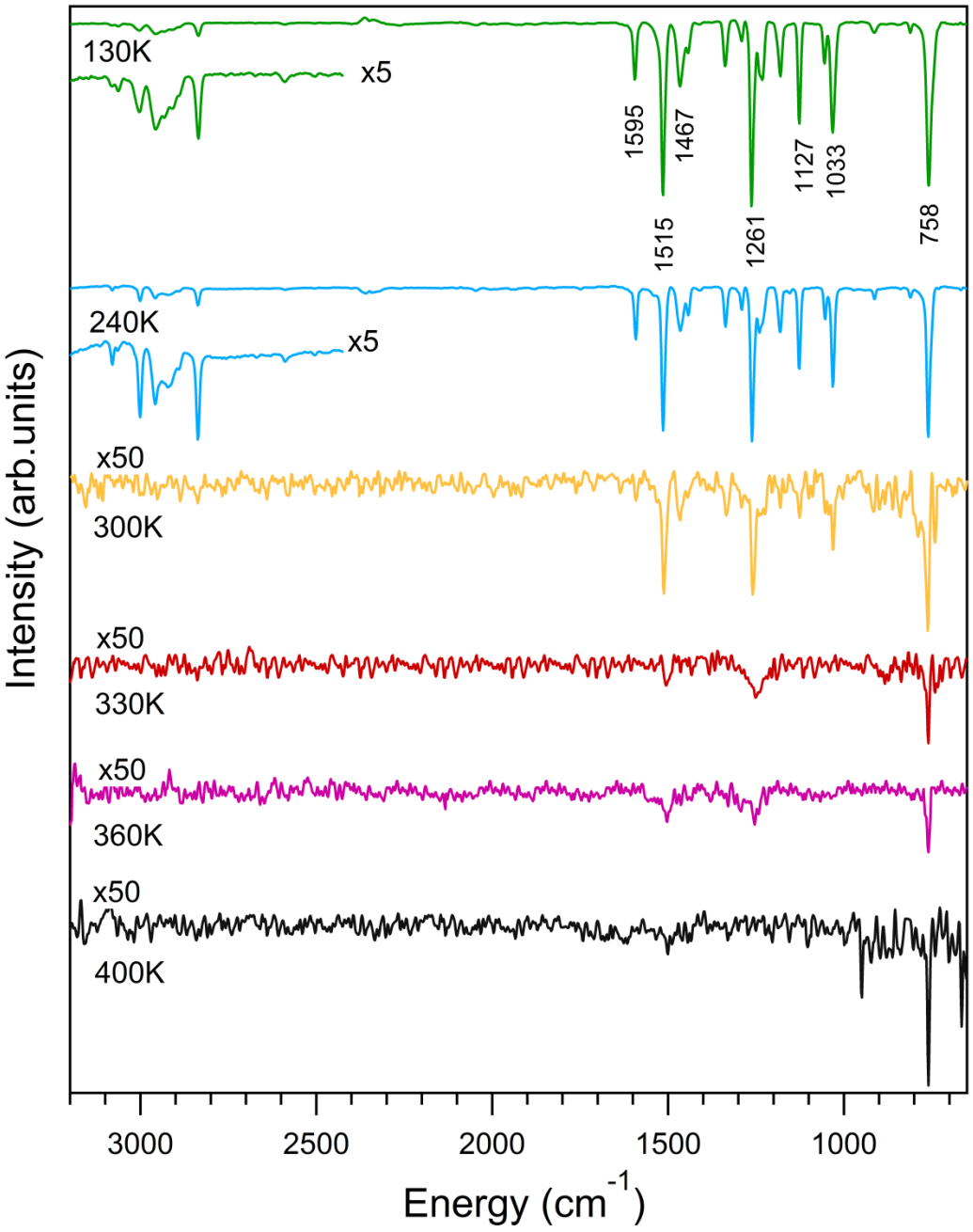

Figure 6.4: RAIRS spectra acquired at different temperatures for 200 L of Vertarol deposited at 130 K. Spectra have been offset for clarity.

The identification of surface species upon dosing multilayers of veratrol on Pt(111) was performed by monitoring vibrational modes of species on the surface as a function of temperature. Details of the band assignments and comparison to the vibrational frequencies of liquid anisole are presented in Table 6.1.

Table 6.1: Vibrational modes and peak assignments of veratrol on Pt(111).

Vibrational mode [a]	Pt(111)	Gas Phase (exp)[14]	Calculated[14]
(a) arm vibrations			
CH3 asym. ip. str.	**3004**	**3000**	**3039**
CH3 asym. op. str.	**2958**	**2954**	**2971**
CH3 sym. op. str.	**2836**	**2835**	**2898**
HCH (CH_3) scissor	**1467**	**1463**	**1457**
HCH (CH_3) scissor	**1443**	**1442**	**1435**
CH_3 scissor	**1335**	**1330**	**1421**
CH_3 rock	**1181**	**1176**	**1157**
O-CH_3 str.	**1055**	**1052**	**1042**
O-CH_3 str.	**1033**	**1028**	**1019**
(b) ring vibrations			
C-H str.	**3064**	**3064**	**3065**
C-C ring + CCO str.	**1595**	**1592**	**1563**
C-C ring + CCO str.	**1515**	**1506**	**1480**
Ph-O sym. + C-C str. + CH bend	**1261**	**1254**	**1255**
Ph-O asym. + C-C str. + C-H bend	**1233**	**1230**	**1211**
C-H bend	**1127**	**1123**	**1096**
C-H bend	**915**	**------**	**------**
Ring breathing	**810**	**------**	**------**
C-H bend (out of plane)	**758**	**------**	**------**

[a]Approximate mode description; str, stretching; sym/asym, symmetric/asymmetric; ip, in plane; op, out of phase.

There are small shifts between the vibrational modes of gas phase veratrol and the ones observed on Pt(111) mainly due to surface/metal interaction. As above, due to metal surface selection rules, only the modes that have vibrational dipole moments perpendicular to the surface can be observed and this gives us an insight about the adsorption geometry of the molecule on the surface. The observation of strong C-H bending peaks at 758, 915, and 1127 cm^{-1} indicates that veratrol adsorbs on the surface primarily via carbon atoms of the aromatic ring. Furthermore, the observation of O-CH_3, Ph-O + C-C, C-C ring + CCO stretches and C-H stretching peaks indicates that the methoxy groups of the veratrol are tilted away from the surface. These observations are in agreement with previous suggestions for anisole and guaiacol adsorption on Pt(111).[2,4,8,9,15] After increasing the temperature to 240 K, the majority of the IR peak intensities remain the same except for the peaks at 2958, 3004 and 3064 cm^{-1}. These peaks become stronger and sharper. This behavior is attributed to the rearrangement of molecules in the adsorbed layer to a more thermodynamically stable geometry.

Upon reaching 300 K, the IR peaks decrease in intensity which is in agreement with the temperature range of the molecular desorption of the multilayer observed in the XPS. The peaks corresponding to C-H stretching modes in the CH_3 fragment, observed at 2836, 2958, 3004 cm^{-1}, vanish and the constant presence of the 1033 and 1261 cm^{-1} assigned to O-CH_3 stretching and Ph-O + C-C stretching suggest that the veratrol started decomposing by C-H bond cleavage on the methyl group. Further heating to 330 K leads to the disappearance of the peaks at 1033, 1335 and 1467 cm^{-1} corresponding to O-CH_3 stretching, CH_3 rocking and HCH scissoring respectively. These observations clearly indicate the cleavage of the methyl group, inferring the formation of quinone-like species on the surface. Furthermore, the peaks at 758, 1261 and 1515 cm^{-1} shift and the disappearance of the C-H bending mode at 1127 cm^{-1} are associated with the loss of aromaticity in the ring which emphasizes the formation of quinone-like species.

The intermediate specie seems to be stable up to 360 K. At 400 K, the peak at 1261 cm^{-1} vanish while a new peak emerges at 950 cm^{-1} and the peak at 758 cm^{-1} gets stronger which suggests that the ring breaks down as the molecule completely decomposes. In addition, no molecular CO stretching peak has been observed in the 1800-2100 cm^{-1} region, which suggests that the reported desorption of CO from veratrol decomposition is reaction-limited.

TPD

Turning now to the TPD experiments, molecular desorption of the parent veratrol molecule was monitored at a high coverage as a function of temperature (Figure 6.5). The data shows that, at early temperatures, the molecular desorption peak of veratrol occurs at 215 K. This peak is attributed to the desorption of the multilayer. Previous studies of closely related aromatics have reported similar temperatures and behavior for the physisorbed layer.[2,6,7,16,3]. The only other observed reaction products of the decomposition of veratrol are H_2 and CO.

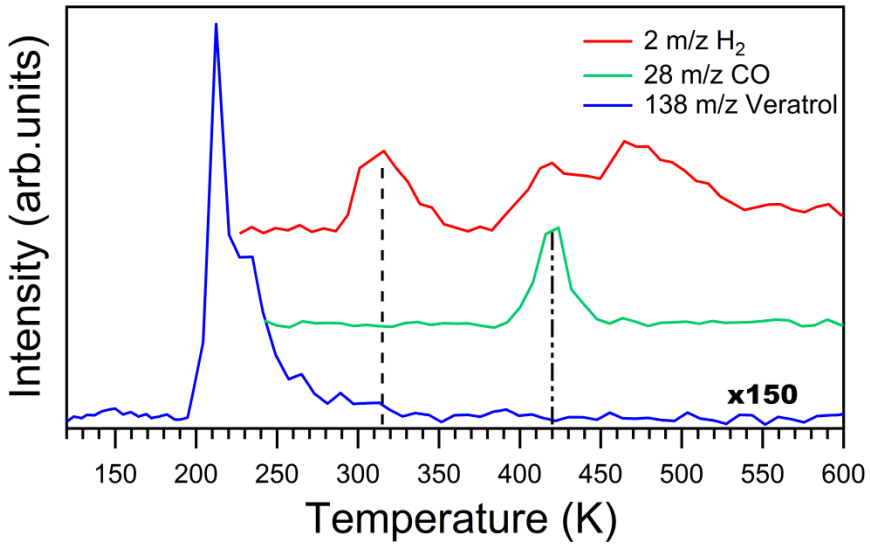

Figure 6.5: TPD spectra after 20 L exposure of veratrol at 130 K on Pt(111). Monitored masses 138, 28 and 2 correspond to veratrol, CO and H_2 respectively and desorption rates are measured using a linear temperature ramp of 4 K/s. The dot-dashed line for CO corresponds to molecular desorption of pure CO from Pt(111) with 0.33 ML coverage.[17,18]The dashed line for H_2 corresponds to desorption temperature of Hydrogen with 2 L coverage from Pt(111).[19,20]

Hydrogen shows peaks at 315 K, 420 K and 470 K. In comparison, the associative desorption of hydrogen from Pt(111) has been previously observed in the temperature interval between 290-375 K.[19,20] This suggests that the desorption peak at 315 K is more likely to be desorption-limited and the peaks at 420 K and 470 K are reaction-limited. In contrast, CO desorbs with one peak at 420 K and this corresponds to the molecular desorption of pure CO from Pt(111) with a 0.33 ML coverage.[17,21] The coincidence of the desorption temperature and the sharpness of the CO peak and the second hydrogen peak suggest that the desorption of CO is also reaction-

limited and that they are the byproduct of a common intermediate species. At this point it is more likely that the aromatic ring is starting to decompose on the surface. Similar behavior has been observed with oxygenated aromatic molecules (anisole, 2-phenoxyethanol and phenol) adsorbed on Pt(111).[2,4,16,3] No other molecular products have been observed.

6.4 Discussion

From RAIRS, XPS and TPD experimental results, a schematic of the reaction and decomposition of veratrol on Pt(111) is proposed in Figure 6.6. Upon dosing, veratrol adsorbs on the Pt(111) surface at 130 K. Upon heating, the physisorbed layer molecularly desorbs at 215 K. The desorption energy of the multilayer is 64.8 kJ/mol and it is agreement with the enthalpy of vaporization of 68.1 kJ/mol of veratrol.[22]

The first saturated layer totally decomposes on the surface as the temperature is increased and the only observed byproducts are CO and H_2. At 260 K, the C 1s binding energy difference between the C-C and C-O XPS peaks reduces to 1.6 eV, suggesting the onset of decomposition of the parent molecule. The associative desorption of H_2 at 315 K (which corresponds to "usual' temperature desorption of H_2) is another clear indication of the decomposition of the parent molecule. Furthermore, The peaks corresponding to CH_3 stretching modes observed at 2836, 2958, 3004 cm^{-1} at 300 K, clearly indicate that the dehydrogenation occurred on the methyl group. This is in agreement with previously published studies of phenol, anisole, 2-phenoxyethanol and guaiacol on Pt(111) showing that the first reaction step starts with the dehydrogenation of the arm below 300 K.[2,4,6–9,16,3] Upon heating to 330 K, we observe further changes in the IR spectrum, the disappearance of the peaks at suggests that the molecule lost its aromaticity but the presence of the peaks at 760 and 1250 cm^{-1}. The IR spectrum of 1,2-benzoquinone has vibrational peaks at 739, 1262 and 1734 cm^{-1} which are attributed to C-H wag, C-C stretch + C-H bend and C–C=O stretch respectively. Heyden and coworkers[9] studied guaiacol on Pt(111) and suggested that 1,2-benzoquinone to be an intermediate in the possible decomposition pathways of guaiacol on Pt(111). They showed that the adsorption energy of 1,2-benzoquinone is ~397 kJ/mol and the most stable adsorption geometry to be flat with two oxygen atoms parallel to the surface. Thus, the peak at 1734 cm^{-1} cannot be observed in our study due to metal selection rules. In fact, a clear observation of the C–C=O stretch is seen in the data of Vohs et al.[6] The HREELS data for guaiacol/Pt(111) shows that the intermediate species of the decomposition loses its aromaticity at

285 K. A peak at ~1740 cm^{-1} starts to appear at 285 K and disappears between 400-480 K. This peak, which was not identified by the authors, is consistent with the formation of 1,2-benzoquinone, emphasizing that this species adsorbs in a flat geometry on the surface and keeps decomposing above 400 K. Desorption of carbon monoxide correlates with the disappearance of the C-O peak in C 1s and in the O 1s region at 360 K, and the appearance of a new peak at 950 cm^{-1} indicates further decomposition of the 1,2-benzoquinone. This is in agreement with the strong adsorption energy of ~397 kJ/mol reported previously, suggesting that 1,2-benzoquinone is more likely to start decomposing on surface rather than molecularly desorbing from it. Only hydrocarbons and adventitious carbon remains on the surface at 450 K. This is consistent with the previous reported results of the decomposition of 1,2-benzoquinone on Pt(111) surface.

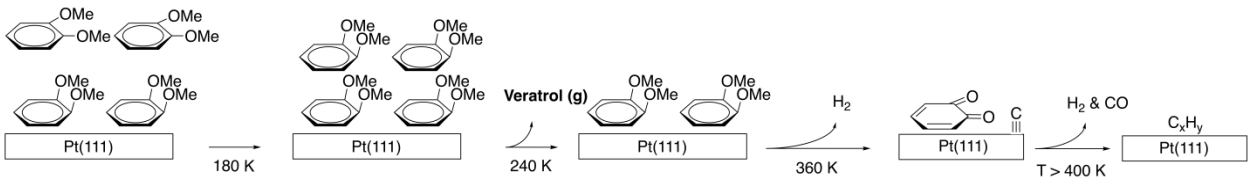

Figure 6.6: Proposed pathway of veratrol decomposition under UHV conditions on Pt(111) built from surface science experiments.

6.5 Conclusion

In ultra-high vacuum conditions, veratrol adsorbs on the surface at 130 K. The multilayer desorbs at 230 K and the monolayer starts decomposing by dehydrogenation of the methyl group below 300 K. The only observed decomposition by products H_2 and CO. 1,2-Benzoquinone seems to be key intermediate in the decomposition pathway of veratrol. It seems that increasing the complexity by having a methoxy arm attached in the ortho position didn't change the first reaction steps of these aromatics. The cleavage of C-H on the arm is still preferred, but the intermediate species of the decomposition is more likely to simply keep decomposing as no other aromatic species have been observed during the desorption process.

References

(1) Zakzeski, J.; Bruijnincx, P. C. A.; Jongerius, A. L.; Weckhuysen, B. M. The Catalytic Valorization of Ligning for the Production of Renewable Chemicals. *Chem. Rev.* **2010**, *110*, 3552–3599.

(2) Réocreux, R.; Ould Hamou, C. a.; Michel, C.; Giorgi, J. B.; Sautet, P. Decomposition Mechanism of Anisole on Pt(111): Combining Single-Crystal Experiments and First-Principles Calculations. *ACS Catal.* **2016**, *6*, 8166–8178.

(3) Ould Hamou, C. a.; Réocreux, R.; Sautet, P.; Michel, C.; Giorgi, J. B. Adsorption and Decomposition of a Lignin B-O-4 Linkage Model, 2-Phenoxyethanol, on Pt(111): Combination of Experiments and First-Principles Calculations. *J. Phys. Chem. C* **2017**, *121*, 9889–9900.

(4) Shi, D.; Arroyo-Ramírez, L.; Vohs, J. M. The Use of Bimetallics to Control the Selectivity for the Upgrading of Lignin-Derived Oxygenates: Reaction of Anisole on Pt and PtZn Catalysts. *J. Catal.* **2016**, *340*, 219–226.

(5) Tan, Y. P.; Khatua, S.; Jenkins, S. J.; Yu, J.-Q.; Spencer, J. B.; King, D. a. Catalyst-Induced Changes in a Substituted Aromatic: A Combined Approach via Experiment and Theory. *Surf. Sci.* **2005**, *589*, 173–183.

(6) Shi, D.; Vohs, J. M. TPD and HREELS Study of the Reaction of Guaiacol on Zn-Decorated Pt(111). *Catal. Today* **2018**, *302*, 272–276.

(7) Hensley, a. J. R.; Wöckel, C.; Gleichweit, C.; Gotterbarm, K.; Papp, C.; Steinrück, H.-P.; Wang, Y.; Denecke, R.; McEwen, J.-S. Identifying the Thermal Decomposition Mechanism of Guaiacol on Pt(111): An Integrated X-Ray Photoelectron Spectroscopy and Density Functional Theory Study. *J. Phys. Chem. C* **2017**.

(8) Lee, K.; Gu, G. H.; Mullen, C. A.; Boateng, A. A.; Vlachos, D. G. Guaiacol Hydrodeoxygenation Mechanism on Pt(111): Insights from Density Functional Theory and Linear Free Energy Relations. *ChemSusChem* **2015**, *8*, 315–322.

(9) Lu, J.; Behtash, S.; Mamun, O.; Heyden, A. Theoretical Investigation of the Reaction Mechanism of the Guaiacol Hydrogenation over a Pt(111) Catalyst. *ACS Catal.* **2015**, *5*, 2423–2435.

(10) Redhead, P. A. Thermal Desorption of Gases. *Vacuum* **1962**, *12*, 203–211.

(11) Campbell, C. T.; Sellers, J. R. V. Correction to "The Entropies of Adsorbed Molecules." *J. Am. Chem. Soc.* **2013**, *135*, 13998–13998.

(12) Campbell, C. T.; Sellers, J. R. V. The Entropies of Adsorbed Molecules. *J. Am. Chem. Soc.* **2012**, *134*, 18109–18115.

(13) Knovel Critical Tables (2nd Edition).

(14) Lucarelli, C.; Giugni, a.; Moroso, G.; Vaccari, a. FT-IR Investigation of Methoxy Substituted Benzenes Adsorbed on Solid Acid Catalysts. *J. Phys. Chem. C* **2012**, *116*, 21308–21317.

(15) Réocreux, R.; Huynh, M.; Michel, C.; Sautet, P. Controlling the Adsorption of Aromatic Compounds on Pt(111) with Oxygenate Substituents: From DFT to Simple Molecular Descriptors. *J. Phys. Chem. Lett.* **2016**, *7*, 2074–2079.

(16) Ihm, H.; White, J. M. Stepwise Dissociation of Thermally Activated Phenol on Pt(111). *J. Phys. Chem. B* **2000**, *104*, 6202–6211.

(17) Steininger, H.; Lehwald, S.; Ibach, H. On the Adsorption of CO on Pt(111). *Surf. Sci.* **1982**, *123*, 264–282.

(18) Norton, P. R.; Davies, J. A.; Jackman, T. E. Absolute Coverages of CO and O on Pt(111); Comparison of Saturation CO Coverages on Pt(100), (110) and (111) Surfaces. *Surf. Sci.* **1982**, *122*, 593–600.

(19) Christmann, K.; Ertl, G.; Pignet, T. Adsorption of Hydrogen on a Pt(111) Surface. *Surf. Sci.* **1976**, *54*, 365–392.

(20) Lu, K. E.; Rye, R. R. Flash Desorption and Equilibration of H2 and D2 on Single Crystal Surfaces of Platinum. *Surf. Sci.* **1974**, *45*, 677–695.

(21) Norton, P. R.; Goodale, J. W.; Selkirk, E. B. Adsorption of Co on Pt(111) Studied by Photoemission, Thermal Desorption Spectroscopy and High Resolution Dynamic Measurements of Work Function. *Surf. Sci.* **1979**, *83*, 189–227.

(22) Matos, M. A. R.; Miranda, M. S.; Morais, V. M. F. Calorimetric and Theoretical Determination of Standard Enthalpies of Formation of Dimethoxy- and Trimethoxybenzene Isomers. *J. Phys. Chem. A* **2000**, *104*, 9260–9265.

Chapter 7:
Summary and outlook

7 Summary and outlook

To gain insights into the reactivity of aromatic oxygenates that relates to the β-O-4 lignin models, a study of combination of single crystal experiments and first principles calculation was proposed.

In this thesis, we carefully studied the decomposition of β-O-4 lignin models such as anisole, 2-phenoxyethanol and veratrol on Pt(111) surface by means of X-ray photoelectron spectroscopy, Temperature programmed desorption, Reflection adsorption infrared spectroscopy and Density functional theory calculations.

From surface science experiments, we showed that the β-O-4 lignin models such as Anisole and 2-Phenoxyethanol decompose in ultrahigh vacuum and leads mainly to the formation of benzene as byproduct. The decomposition always starts on the arm attached to the aromatic ring, the preference in the bond cleavage (when available) are in this following order O-H, C-H then C-O or C-C. The decomposition pathways of these molecules lead to the formation of Phenoxy as common key intermediate. The presence of carbonaceous species from the initial decomposition of the parent molecules act as reducing agent in the deoxygenation of phenoxy, thus allowing the formation of benzene.

The reaction pathways of these aromatics strongly depend on the coverage. For the submonolayer regime, these molecules tend to completely decompose into CO and H2. Close to the monolayer regime, lateral interactions become important allowing product selectivity. For a monolayer coverage of anisole, 20% leads to the formation of benzene while 80% simply decomposes into carbonaceous species. Similar results are observed for 2-Phenoxyethanol where only 29% leads to the formation of benzene and 71% leads to the formation of coke. Combining experimental techniques and first principal calculation showed to be a powerful tool to investigate the reaction pathway of these oxygenated aromatics.

Moving towards a more complex lignin model such as veratrol showed a different reaction intermediate. At a very high coverage, veratrol simply desorbs from the surface at 215 K while the monolayer simply decomposes into CO, H2 and coke. Even though we expect that the lateral interaction of the saturated monolayer to influence the product selectivity, the adsorption energy of the key intermediate 1,2-benzoquinone is still very high and favors the formation of coke.

Setting up a new surface science technique (RAIRS) helped to provide further insights into the decomposition pathway of these aromatics.

Near future studies should involve further investigation of veratrol at submonolayer coverage. As mentioned before lateral interactions play an important role in the guidance of product selectivity and it is important to investigate the reactivity of veratrol for very low coverages. It will be also important to extract more conclusions and exploit the experimental data at its full potential by conducting a more substantial analysis.

Moreover, it would be interesting to see the influence of the second methoxy group on the meta and para sites. It is worthwhile studying the reactivity of 1,3 and 1,4-Dimethoxybenzene.

We also noticed that in the case of phenol and 2-Phenoxyethanol the existence of a second layer that is more strongly bound than the bulk layer suggests that there is an interaction between the 1st and the 2nd layer. It may be that the hydroxyl groups create a sort of dimer making the adsorption energy of the second layer stronger compared to the bulk one. Investigating molecules such as phenylmethanol, phenoxymethanol and 2-Phenylethan-1-ol with a hydroxyl group termination on the arm moieties will give us a better insight into the proposed hypothesis.

Overall, to understand the different reaction pathways of lignin decomposition, it is important to systematically increase the level of complexity of the model molecules used by increasing the complexity of the arm, increasing the number of the attached arm moieties to the aromatic ring and/or probing the relative sites of the attached arm.

Appendix A

Pump's specifications

The UHV conditions is achieved by a combination of a different type of pumps : mechanical pump, turbo molecular pump, ion pump and a titanium sublimation pump . In this appendix, general information about the models and their technical data will be presented.

Table A1: Technical data of the turbomolecular pumps used in the laboratory. Provided by Pfeiffer.

Model	**TMU 071P**	**TMU 261 P**	**TPH 180 H**
Manufacturer	Pfeiffer	Pfeiffer	Pfeiffer
Rotation speed (rpm)	90000	60000	50000
Max Temperature (°C)	80	90	80
Cooling	Water	Water	Air
Location(Chamber)	Load-lock	Analysis	RAIRS
Final pressure (mbar)	$< 5x10^{-10}$	$< 5x10^{-10}$	$5x10^{-11}$
Backing pump (mbar)	< 10	< 5	< 5
Volume flow rate (l/s)			
N_2	60	210	180
He	55	220	170
H_2	45	175	140

Table A2: Technical data of the mechanical pumps used in the laboratory. Provided by Edwards, Varian and Leboyd.

Model	**RV3/RV5**	**SH-110**	**D4A**
Manufacturer	Edwards	Varian	Leboyd
Rotation speed (rpm) 60Hz	1760	1725	1725
Max Temperature (°C)	70	60	40
Location(Chamber)	Load-lock/Analysis	Dosing lines	RAIRS
Cooling	Not required	Air	Not required
Final pressure (mbar)	$2x10^{-3}$	$6.6x10^{-2}$	$3x10^{-4}$
Oil Capacity (l)	0.7	Not required	0.7
Volume flow rate (l/min)	75/117	110	127

Table A3: Technical data of the ion pump used in the laboratory. Provided by Varian.

Model	**Valcon Plus 300 (Starcell)**
Manufacturer	Varian
Rotation speed (rpm)	90000
Max Temperature (°C)	350
Location(Chamber)	Analysis and RHK
Final pressure (mbar)	$< 10^{-11}$
Magnet	Ferrite
Volume flow rate N_2 (l/s)	240

Table A4: Technical data of the TSP pump used in the laboratory. Provided by Varian.

Model	**916-0061**
Manufacturer	Varian
Max operating current (A)	50
Volume flow rate (l/s) at 20°C	
N_2	516
H_2	1205
H_2O	578
Volume flow rate (l/s) at -195°C	
N_2	555
H_2	1706
H_2O	696

Appendix B

Heating and cooling

In this appendix, a general information about the heating and cooling procedure, and the filament preparation will be addressed. It is important to follow the instructions to be able to heat and cool down the sample without damaging the equipment. Reference data will be shown to keep track of the efficiency of the filament and cooling power.

Heating Procedure :

1. **Main Chamber**

    1. Make sure that the wire connections are set for the filament of the main chamber
    2. Make sure the filament is approached toward the sample and is inside the puck
    3. Turn on the SH 100 power supply
    4. Make sure the temperature stabilisation knob is on manual
    5. Gradually increase the accelerating voltage to 800 V
    6. Gradually increase the current from 0 to 1A, then by 0.05A steps every 5 seconds until the desired temperature is reached (Max: 2.4A)

Note: The filament needs to be retracted before moving the sample inside of the chamber. Hence, the heating should be turned off.

Table B1: Increasing the filament current and its corresponding emission, temperature and pressure. The measurements have been taken every 5 seconds during the cooling process and with an accelerating voltage of 800 V.

Filament current (A)	Emission current (mA)	Temperature (K)	Pressure (mbar)
0.5	0.8	123	8.9×10^{-10}
1.0	5.7	127	1.4×10^{-9}
1.5	7	200	2.1×10^{-9}
1.8	8.2	550	4×10^{-9}
2.0	9.6	880	6.8×10^{-9}
2.2	21.7	1114	1.2×10^{-8}

2. RAIRS Chamber

1. Make sure that the wire connections are set for the filament of the RAIRS chamber
2. Turn on the SH 100 power supply
3. Make sure the temperature stabilisation knob is on manual
4. Gradually increase the accelerating voltage to 800 V
5. Gradually increase the current from 0 to 1A, then by 0.05A steps every 5 seconds until the desired temperature is reached (Max: 2.4A)

Table B2: Increasing the filament current and its corresponding emission, temperature and pressure. The measurements have been taken every 5 seconds during the cooling process and with an accelerating voltage of 800 V.

Filament current (A)	Emission current (mA)	Temperature (K)	Pressure (mbar)
0.5	0.1	130	5.1×10^{-10}
1.0	0.2	160	5.6×10^{-10}
1.5	0.5	245	1.2×10^{-9}
1.6	1.0	310	2.9×10^{-9}
1.7	3.1	440	1.0×10^{-8}
1.8	8.7	620	3.2×10^{-8}
1.9	18.7	900	7.2×10^{-8}
1.95	26.7	1100	1.1×10^{-7}

Cooling Procedure :

1. Connect the dry air line to the coolant lines of the main manipulator for at least 1 hour (Ideally overnight) to remove the moisture and avoid the formation of ice inside the coolant lines.
2. Disconnect the dry air line and connect the coolant tube to the liquid nitrogen dewar and open the valve

Note: In the main chamber, it takes around 30min to cool down the sample stage to 90-95K and 45min to 1h to cool down the sample to 110-130K. In the RAIRS chamber, it takes around 30 min to cool down the sample to 130K.

Heating without cooling can be done but the temperature reading should never exceed 400K. Above this temperature cooling is mandatory. Ideally before performing an experiment that requires heating above 400 K, it is important to first cooldown the arm to 130K then heat to the desired temperature. During the experiment, the temperature of the sample stage needs to be stable (90-110K) and if it is not the case, it means that the cooling power is not sufficient. Increasing the inlet pressure from the dewar should resolve the issue.

Filament preparation Procedure :

1. Cut 10 cm of the tungsten wire (0.005” and 99.98% purity)
2. Take a M1.6 screw size and gently wrap the wire around the grooves to make sur the loops are equally spaced. 13 turns should generate 11 loops with a 1.5 mm diameter (Figure B1).
3. Put the filament in a beaker full of methanol then put the beaker inside of the ultrasonic bath and let it sonicate for at least 30 min to clean the filament.
4. After taking it out, let the filament dry and assemble it on the sample stage.
5. Once the filament is put back into the UHV chamber and UHV condition are achieved, degassing should be performed by passing a current through the filament.

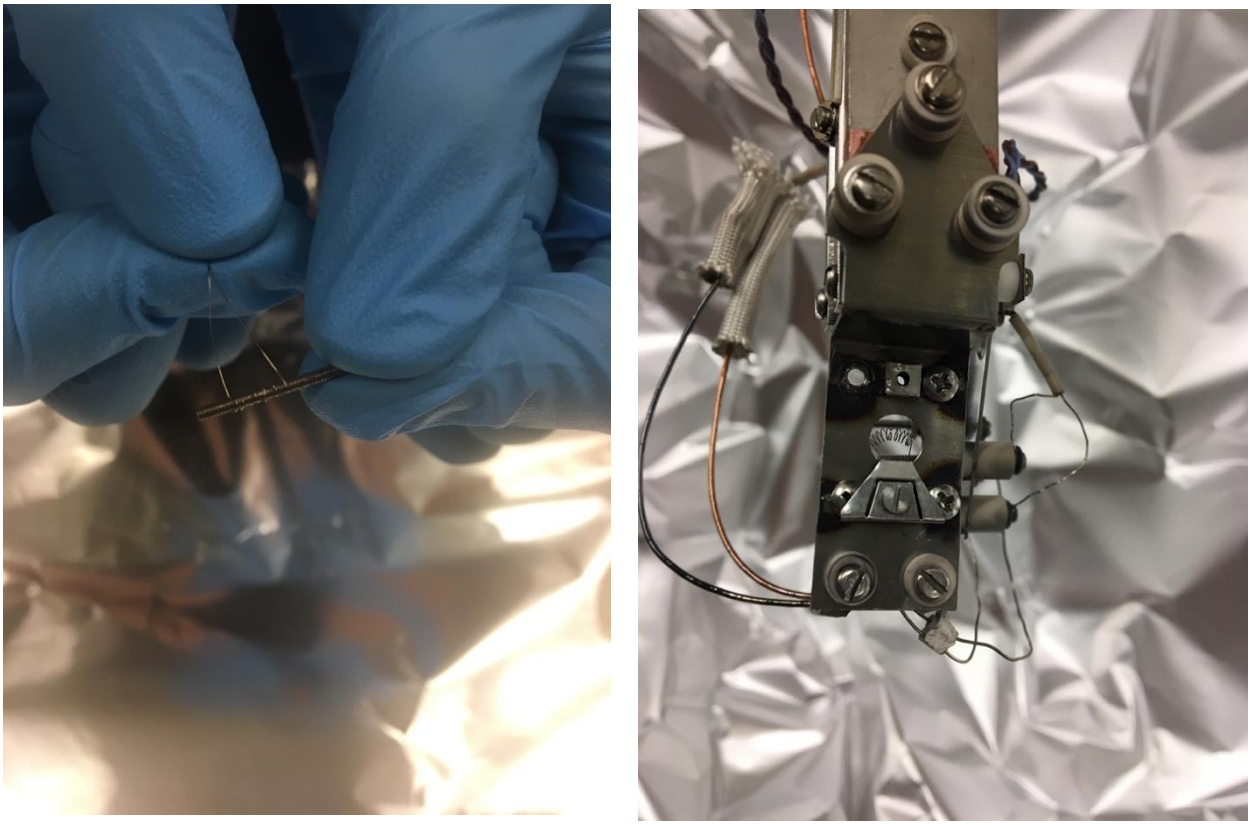

Figure B1: On the left, photograph of the filament preparation. On the right, Photograph of the filament mounted on the sample holder of the RAIRS chamber manipulator.

Resistance readings :

Table B3: Measurements of the resistance of different components of the RAIRS manipulator.

Measurements	Resistance (Ω)	
	20°	245°
Filament feed through to filament feed through	1.16	1
Filament feed through to sample holder (Mo plate)	0	0
Voltage feed through to sample	1.04	1.05
Voltage feed through to sample holder (Mo plate)	0	0
Sample to sample holder (Mo plate)	0	0
Voltage feed through to filament feed through	0	0

Appendix C

Sample cleaning

In this appendix, sample preparation and cleaning procedure of the Pt(111) will be presented. It is important to follow the instructions to be able to clean the sample without distorting the surface.

Cleaning Procedure :

1. **Main Chamber**

   Sample Preparation

   Sample preparation is carried inside the main chamber and requires intensive sputtering and annealing to be able to clean the Pt(111) sample.

   1. Assuming the sample is on the main manipulator, move the sample to the sputtering position $x = 60.9, y = 25, z = 13.5, \theta = 240°$
   2. Cool down the sample to 110-130K
   3. Purge the argon gas lines 3 times to ensure the purity of the dosed argon.
   4. Before turning on the Ion source IQ 11-A controller make sure the knob is on **standby**
   5. Wait 20 seconds for the electronics and emission filament to warm up
   6. Open the leak valve and introduce argon inside the chamber to a pressure of $1x10^{-5}$ mbar
   7. Set the mode on **operate** and slowly increase the energy up to 1.5 KeV and leave it for 30 minutes
   8. After 30 minutes, reduce the energy to 0 KeV and close the leak valve
   9. Repeat steps 5 to 7 multiple times and verify with the XPS that the amount of carbon and oxygen decreased between the cycles.
   10. Repeat steps 5 to 7 but this time at a temperature 600K
   11. Anneal to 1100K for 2 minutes
   12. Decrease the temperature to 900K and introduce oxygen inside the chamber to a pressure of $1x10^{-7}$ mbar for 2 minutes
   13. Reduce the temperature to 600 K
   14. Repeat the steps 9 to 12 until the cleanness of the sample can be verified with the XPS and LEED.

Sample Cleaning

After the sample has been prepared for the first time, the cleaning cycle requires less time and less intensive treatments. The procedure as follow:

1. Assuming the sample is on the main manipulator, move the sample to the sputtering position $x = 60.9\,cm\,, y = 25mm\,, z = 13.5mm\,, \theta = 240°$
2. Purge the argon gas lines 3 times to ensure the purity of the dosed argon.
3. Before turning on the Ion source IQ 11-A controller make sure the knob is on **standby**
4. Wait 20 seconds for the electronics and emission filament to warm up
5. Anneal to 600K and open the leak valve and introduce argon inside the chamber to a pressure of $1x10^{-5}$ mbar
6. Set the mode on **operate** and slowly increase the energy up to 1.5 KeV and leave it for 15 minutes
7. After 15 minutes, reduce the energy to 0 KeV and close the leak valve
8. Anneal to 1100K for 2 minutes
9. Reduce the temperature to 600 K
10. Repeat the steps 5 to 9 two more times to be able to have a clean sample

2. RAIRS Chamber

Sample Cleaning

1. Move the sample to the sputtering position $x = 15.05mm, y = 7mm, z = 26.6mm, \theta = 228°$
2. Purge the argon gas lines 3 times to ensure the purity of the dosed argon.
3. Before turning on the Ion source Perkin-Elmer 20-045 controller make sure the beam voltage is at 5 kV and emission current is at zero.
4. Turn on the power and wait 20 seconds for the electronics to warm up
5. Anneal to 600K and open the leak valve and introduce argon inside the chamber to a pressure of $1x10^{-5}$ mbar
6. Gradually increase the beam voltage to 1.5 kV and slowly increase the emission current to 25 mA and leave it for 15 minutes
7. After 15 minutes, reduce the emission current to 0 mA and close the leak valve
8. Anneal to 1100K for 2 minutes
9. Reduce the temperature to 600 K
10. Repeat the steps 5 to 9 two more times to be able to have a clean sample

After following the cleaning procedure, the surface structure can be verified with the LEED. Figure C1 show the diffraction pattern of the reflected electrons from the Pt(111) surface. The sharpness of the peak, the hexagonal shape indicates that the surface is well ordered and relatively clean. Further verification of the surface cleanness can be conducted by XPS. Figure C2 shows the C1s region before and after cleaning. Before cleaning, the presence of the peak at 284.4 eV is a clear indication of presence of adventitious carbon on the surface. After three cleaning cycles, the peak vanishes indicating that the surface is carbon free.

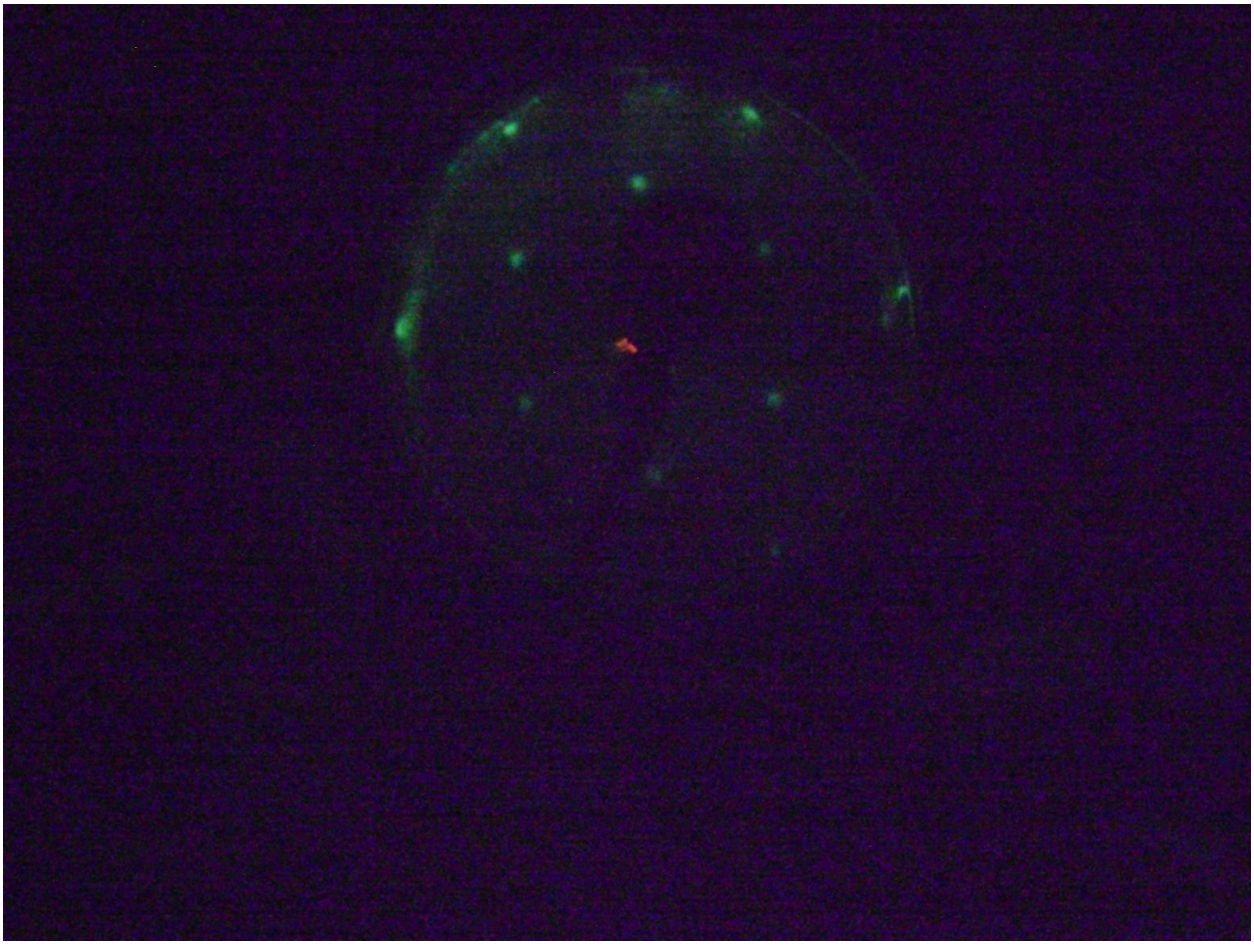

Figure C1: A photograph of the LEED diffraction pattern after 3 cleaning cycles. The energy of the incident electrons is 133 eV.

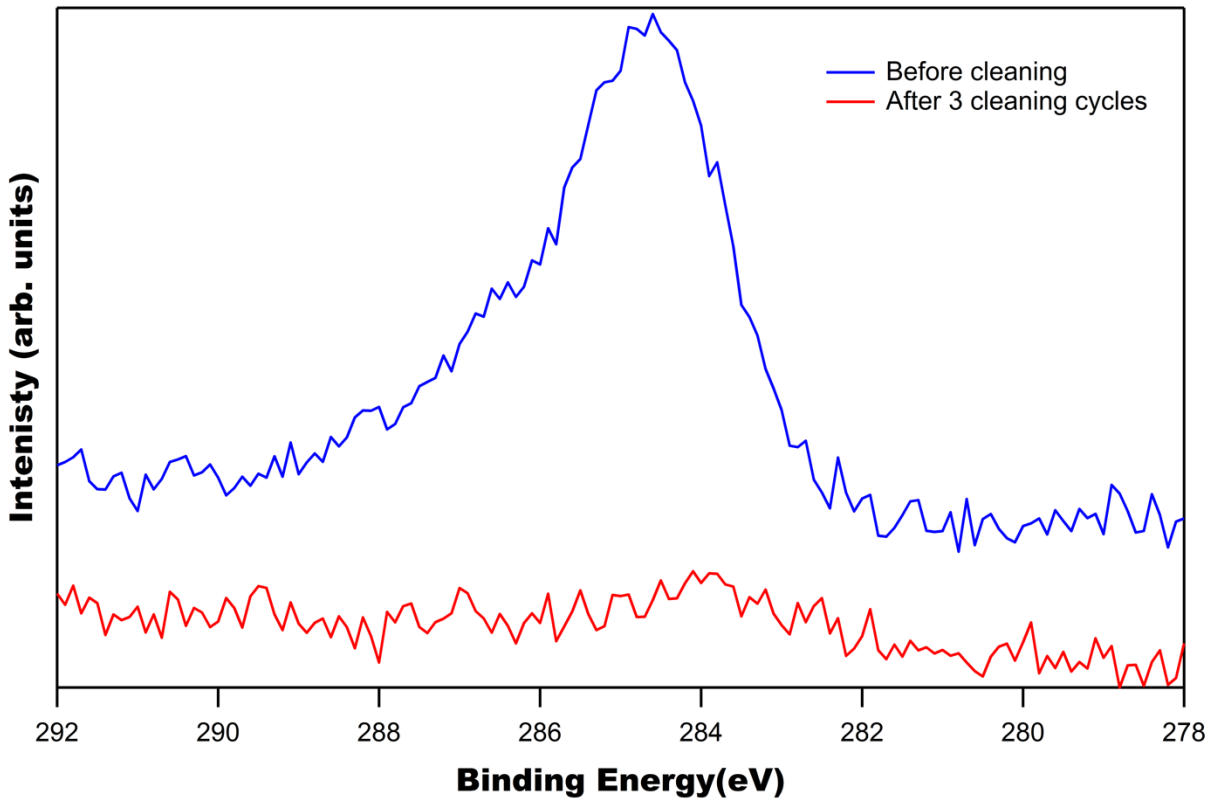

Figure C2: XPS spectra of the C1s region acquired before and after 3 cleaning cycles.

Appendix D

UHV techniques instructions

In this appendix, instruction on how to operate the techniques will be presented. It is important to follow the steps to avoid breaking parts in the UHV chamber.

X-ray photoelectron spectroscopy instructions :

1. Turning on the X-ray photo electron spectroscopy

1. Assuming the sample is on the main manipulator, move the sample to the XPS position $x = 69.6, y = 12.5, z = 11.7, \theta = 294°$
2. Make sure the sample is centered by looking through the apparatus window.
3. Make sure the sample is grounded either through the filament or the puck. A diagram of the ground connections is attached on the electronics side panel. Any charging on the sample will cause a shift in the spectrum and will increase the noise level.
4. Approach the X-ray gun at 15 mm
5. Turn on the XRC 1000 control unit then the HSA 3500 power supply and Wait 20 seconds for the electronics.
6. Press the water button on the XRC 1000 control unit to allow the water to flow though the lines and cool down the X-ray source.
7. Open Specslab2 software and select in the analyzer drop box PHOIBOS-HAS 3500. This should establish the connection between the computer and XPS and if successful the indicator lights CAN and HV on the HSA 3500 should light up in green and orange respectively. If an Error message appears, make sure that the internet connection is disabled and restart the software.
8. On the specslab2 software, set the desired acquisition parameters and region of interest. Please refer to Table 1 of section 2.6.2.3.
9. Once the regions and acquisition parameters are validated, press on the standby button then on HV (high voltage) button located on the XRC 1000 control unit.
10. The voltage should ramp up to 14.6 kV and a red light indicator should blink up during this step.
11. Once the voltage stabilises, the red light should be on and constant. You can now press on the operate button.
12. Click on acquire in specslab2.

Note: The high voltage should always be on standby if no acquisition is performed and during the dosing process as well. This will prolong the filament life. Once ready to perform a scan, click on the operate button.

2. **Turning off the X-ray photo electron spectroscopy**

    1. Press on the standby button then on the HV button.
    2. On the Specslab2 software unselect PHOIBOS-HAS 3500 from the analyzer drop box. This will terminate the connection between the computer and XPS and the CAN on the HAS 3500 should be blinking in green.
    3. Wait 3 minutes to allow the voltage to drop down, then retract the X-ray gun at 40 mm.
    4. Keep the water flowing between 5 and 10 minutes to cool down the completely the X-ray source.
    5. Turn off the XRC 1000 control unit and the HSA 3500 power supply.

Low Energy Electron Diffraction instructions :

Main UHV chamber

1. **Turning on the LEED**

    1. Assuming the sample is on the main manipulator, move the sample to the LEED position $x = 51.7, y = 1, z = 10.6, \theta = 86°$
    2. Make sure the sample is centered by looking through the LEED window. The sample should be facing the electron gun.
    3. Make sure the sample is grounded either through the filament or the puck. Charging on the sample will prevent the observation of the diffraction pattern.
    4. Approach the LEED towards the sample at ~ 1 mm.
    5. Turn on the erLEED 1000-A control unit then gradually increase the screen voltage to 7 kV.
    6. Gradually increase the cathode current to 2.4 A.
    7. Once set, make sure that the initial parameters of table 2 in section 1.6.2 are the same.
    8. All light should be turned off including the ion gauge. To turn off the ion gauge, click on the interlock button. A red-light indicator on the interlock bridge should turn on. You can now turn off the ion gauge.

9. Position yourself in front of the LEED screen and increase the kinetic energy of the electrons until you see a diffraction pattern.

2. Turning off the LEED

1. Decrease the energy of the electrons until you reach zero.
2. Turn on the ion gauge, wait until the pressure reading stabilises then click on the interlock button. The red-light indicator should turn off.
3. Gradually decrease the cathode current to zero then decrease the screen voltage to zero as well.
4. Turn off the erLEED 1000-A control unit
5. Retract the LEED screen.

Temperature programmed desorption instructions :

1. How to collect TPD data (Desorption rate vs T)

1. Assuming the sample is on the main manipulator, move the sample to the TPD position $x = 40.55, y = 11.375, z = 19.6, \theta = 86°$
2. Make sure the sample is centered by looking through the several windows. The use of a cell phone to zoom in can be quite useful to make sure the sample is centered.
3. Approach the QMS towards the sample until the molybdenum cone is at ~ 1 mm form the surface.
4. Open TPD software in LabVIEW. Select the temperature ramp, the maximum recording temperature and the initial current for the recording to start. Rename the pathway files according to the experiment.
5. Turn on the XRC 1000 control unit and Wait 20 seconds for the electronics to warm up.
6. Select the Filament current external on the Temperature stabilisation knob (XRC 1000 control unit).
7. Set the accelerating voltage to 800V and turn the filament current 8 turns. Turning the filament current 8 times, will allow the current to reach a maximum of 2.4A.

Note: The filament current should not increase while turning the knob, at this point it is the software that controls the current.

8. Open the QMS software (called measure), then select setup on the toolbar and open the SEM/Emission control. A window appears, make sure that SEM and Emission are checked to be able to turn on the mass spectrometer.

9. Select MID on the toolbar then click on versus time. This will prompt you to choose a file that will measures the ion current versus time for different mass to charge ratios. Once a file is selected, click on parameters than channel to be able to select different mass to charge ratios. The dwell time and the resolution as well can be modified in the parameters.

10. When ready, save the pressure reading as cycles on the QMS software then click on start on the TPD software. The current should increase according to the software parameters.

11. Once the desired maximum temperature is reached, slowly decrease the current of the filament to zero, then stop saving the pressure reading in the QMS software.

12. Open the TPD excel macro and click run, it will prompt to select the temperature file which corresponds to the saved ramp file by the TPD software. Then, it will prompt you to select ASCII pressure file. By doing so, you will obtain the plot of pressures as a function of temperature.

Note: The pressure file saved by the QMS software needs to be converted into ASCII format by using Display software.

2. Turning off the TPD equipment

1. Gradually decrease the current and voltage to zero. Set back the Temperature stabilisation knob to manual then turn off the XRC 1000 control unit .

2. Turn on off the QMS by selecting setup then SEM/Emission control. A window will appear, make sure to uncheck the SEM and the Emission than click on OK. You can now, close the software.

3. Retract the QMS.

Reflection Adsorption Infrared Spectroscopy instructions :

1. Turning on the RAIRS

1. After cleaning the sample, move it to the RAIRS position $x = 22.17, y = 15.39, z = 16, \theta = 217°$

2. Fill up the MCT detector reservoir with liquid nitrogen and wait few minutes until it cools down.

3. Open OPUS software, it will prompt to enter a password : OPUS.

4. Click on advanced data collection, a Measurement window will appear with different tab parameters.
5. Select the Optic tab and make sure the source setting is set to MIR-Source, the beam splitter to KBr , measurement and background channel to external right and finally the detector set to External A.
6. Select the Check Signal tab, to make sure the interferogram is properly displayed and the intensity is maximised.
7. Select the Advanced tab, to choose your resolution, the number of scans and type of spectrum you want to save during the acquisition process.
8. Once the desired parameters are set, select the Basic tab and click on Background Single Channel. This will acquire the background spectrum which become you reference spectrum.
9. One the background spectrum is acquired simply click on Sample Single Channel to acquire the single beam spectrum.

Note: The liquid nitrogen reservoir will stay cold for 6-7 hours. A refill may be necessary if the experiment lasts more than 7 hours.

2. Turning off the RAIRS

1. If the heating is on, please turn it off first.
2. Click on setup then select logout to close the software.

Appendix E

XPS simulations

In this appendix, details about the optimisation of the XPS simulations parameters are described.

X-ray photoelectron spectroscopy simulations :

The binding energy of the core electrons can be described as the following:

$$E_b = E(n-1) - E(n)$$
$$= \underbrace{-\varepsilon_k}_{Koopmans} + \underbrace{\Delta_{relax}}_{\substack{Electronic \\ relaxation}} + \underbrace{\Delta_{corr}}_{\substack{Electronic \\ correlation}} + \underbrace{\Delta_{vibr}}_{\substack{vibrational \\ correction}} + \underbrace{\Delta_{relat}}_{\substack{Relativistic \\ correction}}$$

Unfortunately, the method implemented in VASP for XPS simulation takes into account the calculation in which the valence electrons relax in the presence of the core hole, but the other core electrons are fixed in their ground state configuration. It does not take into account the other correction factors meaning that the binding energy is approximated as the following :

$$E_b \approx -\varepsilon_k + \Delta_{relax}$$

Before starting to calculate the binding energy of the aromatic molecules adsorbed on the Pt(111) surface, it is important to understand and to find the optimal parameters for the calculations of the core level binding energies. In this part, we will start to calculate the binding energy of C1s for Carbon monoxide by varying different parameters such as the K points, the number of adsorbed molecules and the number of electrons excited. Then we will increase the complexity towards Ethanol, to see how the geometry of adsorption can influence the core level binding energies. At the end, we will calculate the core level binding energies of phenol anisole and 2-phenoxyethanol and try to correlate them to experimental observations.

Carbon monoxide

Carbon monoxide has been adsorbed on a Pt(111) 4x4 slab with 3 layers thickness. Figure E1 and Figure E2 show the core level binding energy of Carbon monoxide adsorbed on different sites on the Platinum surface and by varying the number of adsorbed molecules. All the carbon atoms have been excited individually with K(3x3x1) and the following parameters:

ICORELEVEL = 2 Final approximation
CLNT = 2 corresponds to Carbon specie
CLN = 1 main quantum number of the excited core electron
CLL = 0 angular quantum number of the exited core electron
CLZ = 0.5 or 1 electron count

Adsorbing one CO on different sites on the Pt (111) surface shows a difference in binding between the top, hcp, fcc and bridge positions. It seems that the adsorption site of the molecule influences the core level binding energy and this correlates with our predictions. A less coordinated atom on the surface will tend to react more strongly with the adsorbed molecule. Hence the binding energy is expected to be stronger for the top atom surface compared to the more coordinated atoms in the hcp and fcc positions. For 1 CO, the difference in binding energy between the top and bridge position for the full 1 electron and 0.5 partial electron excitation are 0.2 eV and 0.65 eV respectively. By adding several CO monoxides on the surface, the binding energy difference between the top and the other positions becomes smaller for the 1 electron excitation. Upon 4 CO adsorbed on the surface, it seems to be impossible to distinguish between the species adsorbed on the top positions and the ones adsorbed on top position and those adsorbed on hcp and bridge positions. In comparison to the 0.5 partial electron excitation, the difference in binding energy remains relatively stable. For a monolayer or sub-monolayer regime, we would expect to have the same difference in the binding energy. It seems that the 0.5 partial electron excitation is a more sensible choice.

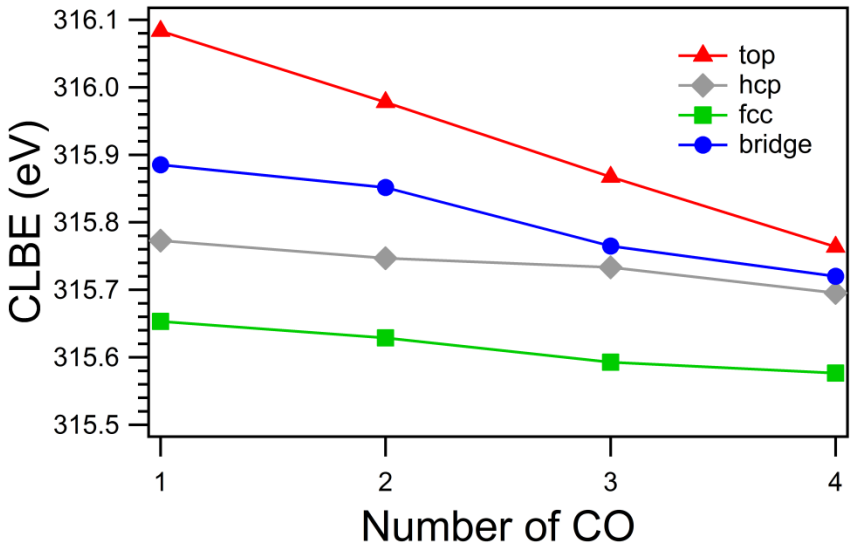

Figure E1: Carbon monoxide adsorbed on Pt(111) surface (4x4 slab). For a full electron excitation, as the increase of the number of adsorbed CO increases on the surface the difference in the core level energies decreases.

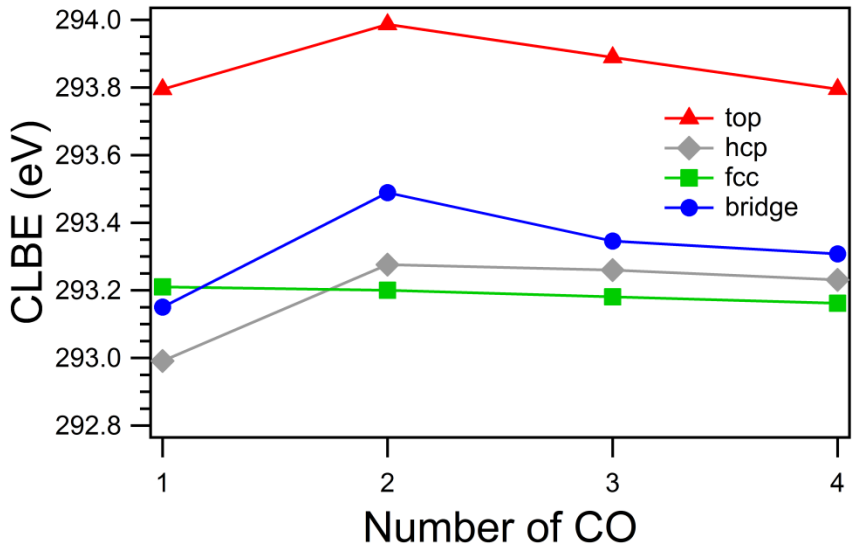

Figure E2: Carbon monoxide adsorbed on Pt(111) surface (4x4 slab). For a partial (0.5) electron excitation, as the increase of the number of adsorbed CO increases on the surface the difference in the core level energies remains relatively stable.

Rosei and coworkers[1] experimentally showed that CO adsorbs preferentially on the top site of Pt(111) surface. When the top atoms on the surface are saturated, its second preferential adsorption site is the bridge position. The difference in binding energy between the top and the bridge site for a 4x2 cell is 0.7 eV. This is in agreement with the binding energy difference of 0.742 eV obtained with the calculations (Table E1).

Table E1: Difference in core electron binding energies of the C1s for CO adsorbed on 4x2 platinum slab.

	Adsorption site	**$\Delta C_{1}s$ (eV)**		**Experimental[1]**
		0.5e	**1e**	**(eV)**
4 CO Pt(111)(4x2)	2CO top +2CO bridge	0.742	0.354	0.7

Another parameter that we can test is the K-points. The K-points rises from Bolch's theorem and corresponds to sampling points in the Brillouin zone. For an infinite system, the integral of the real space is replaced by several integrals over the Brillouin zone. The choice of sufficient K-points for the integration is crucial for the convergence of the results and is therefore one of the major objectives when performing convergence tests. In Figure E3, the same parameters described above has been used, except that this time the number of K-points is increased. It seems that the number of sampling points does not have any effect on the core level binding energies and the shift remains the same.

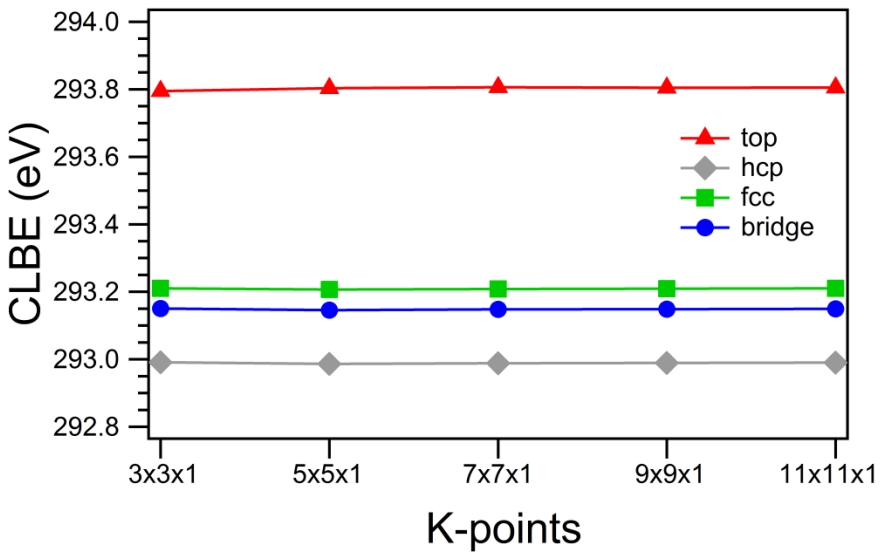

Figure E3: Influence of K-points in the core binding level energies of Carbon monoxide adsorbed on Pt(111) surface (4x4 slab) with a partial electron excitation.

Ethanol

Ethanol has been adsorbed on a Pt(111) with different slabs and different layers. Figure E4 and Figure E5 show the two different stable adsorption geometries of the ethanol on 3x3 slab with 3 layers thickness. All the carbon atoms have been excited individually with K(3x3x1) and the following parameters:

ICORELEVEL = 2 Final approximation

CLNT = 2 corresponds to Carbon specie

CLN = 1 main quantum number of the excited core electron

CLL = 0 angular quantum number of the exited core electron

CLZ = 0.5 or 1 electron count

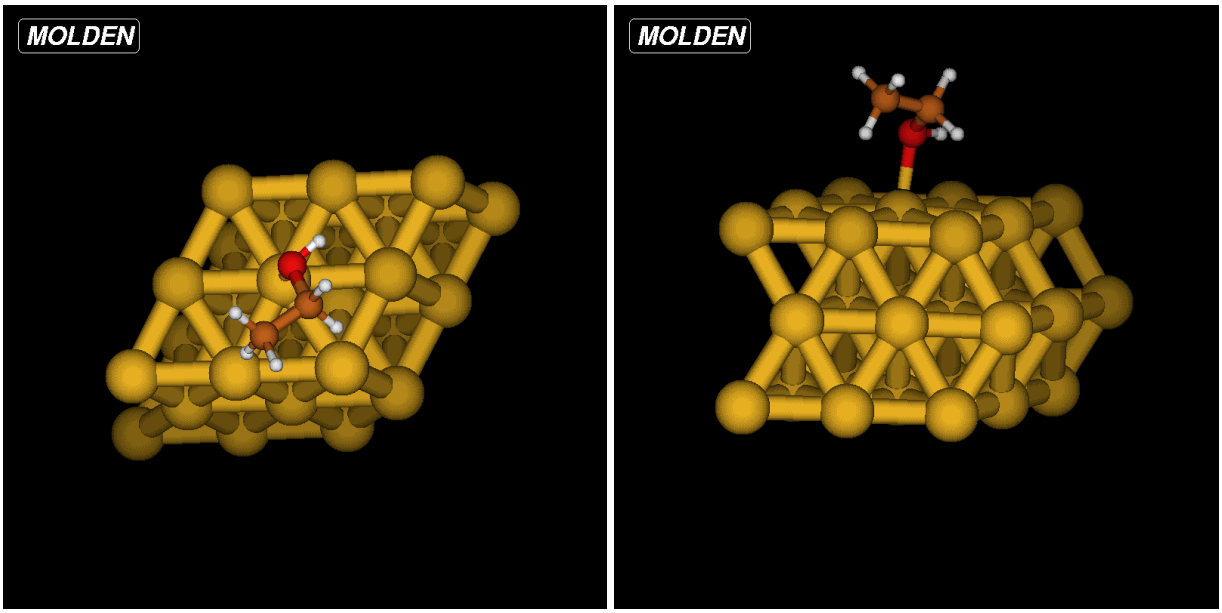

Figure E4: Ethanol adsorbed on the Pt(111) surface (3x3 slab) with a parallel geometry. The side view is shown on the left and the top view is shown on the right.

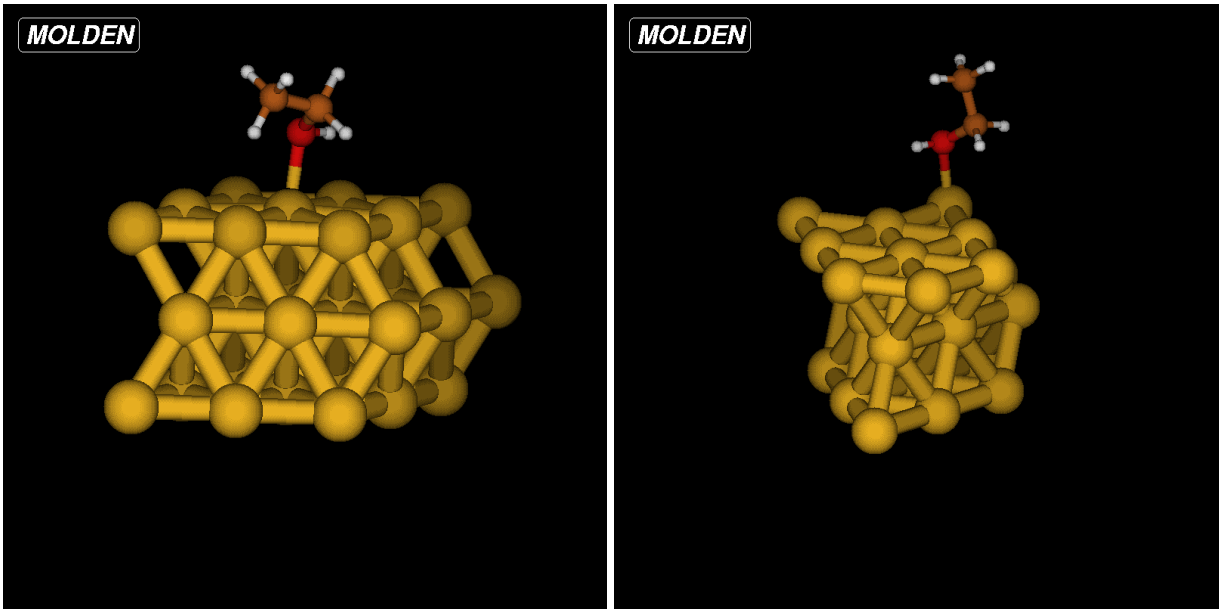

Figure E5: Ethanol adsorbed on the Pt(111) surface (3x3 slab) with a perpendicular geometry. The side view is shown on the left and the top view is shown on the right.

For the Ethanol parallel to the surface, a full electron and partial electron excitation showed a difference in binding energies between the C*H_2 and C*H_3 of 0.75 and 1.5 eV respectively. In comparison to perpendicular ethanol on the surface, a full electron and partial electron excitation showed a difference in binding energies between the C*H_2 and C*H_3 of 0.1 and 0.86 eV. As

expected, it seems that the adsorption geometry influences the binding energy. In the case of a full core electron excitation, we can distinguish both carbon species for the perpendicular ethanol while the carbon species for the parallel ethanol seem to be indistinguishable. In partial electron excitation, regardless of the adsorption geometry both species are distinguishable. Increasing the slab size of the Pt(111) from 3x3 to 3x6 allowed the adsorption 2 ethanol molecule in both stable geometries. The interaction between the two different geometries of the ethanol adsorbed on the surface didn't affect much the shift in the core level binding energies. Although, the difference in binding energies are off by 0.2-0.4 eV from the experimental value, the partial electron excitation seems to be the best choice (Table E2).

Increasing the slab layers didn't change much the shift between the core level binding energies for the ethanol. The change is less than 0.03 eV and therefore it can be neglected (Table E2).

Table E2: Influence of geometry and slab layers in the core electron binding energies of the C1s for ethanol adsorbed on Pt(111) slab.

Slab	**Pt Layers**	**Adsorption geometry**	**ΔC_1s (eV)**		**Experimental[2] (eV)**
			0.5e	**1e**	
3x3	3	Perpendicular	0.86	0.1	1.1
3x3	3	Parallel	1.5	0.7	1.1
3x3	4	Perpendicular	0.83	0.11	1.1
3x3	4	Parallel	1.48	0.67	1.1
3x6	3	Parallel	0.95	0.65	1.1
		+Perpendicular	1.5	0.1	

Phenol, Anisole and 2-phenoxyethanol

Phenol, Anisole and 2-phenoxyethanol have been adsorbed on a Pt(111) 4x4 slab with 4 layers. The most stable adsorption geometry is used for this calculation and they are described in Chapter 5, 6. In this case the C1s atoms have been excited simultaneously and individually using a full electron and partial electron excitations. A summary of the shift between the carbon species bound to an oxygen and carbon species bound to a carbon can be found in Table *E3*.

Table E3: The core electron binding energies of the C1s for phenol, anisole and 2-phenoxyethanol adsorbed on Pt(111) slab.

Molecule	**Excitation type**	**ΔC_1s (eV)**		**Experimental (eV)**
		0.5e	**1e**	
Phenol	Individual	1.6	1.1	1.7[3]
Anisole	Individual	1.6	2.95	1.6[4]
2-phenoxyethanol	Individual	1.5	2.5	1.8[5]
2-phenoxyethanol	Simultaneous	0.7	2.3	1.8[5]

In conclusion it seems that the XPS simulations are in agreement with the experimental results. The best parameters are when 0.5 partial excitation is used and each individual atom is excited separately. Especially for these parameters, the number of slab layers and adsorbates on the surface doesn't influence much the shift in the core level binding energies. It also to be noted that the core level binding energies are sensitive to the adsorption site and the geometry, for this reason it is best if these are known experimentally to facilitate the comparison.

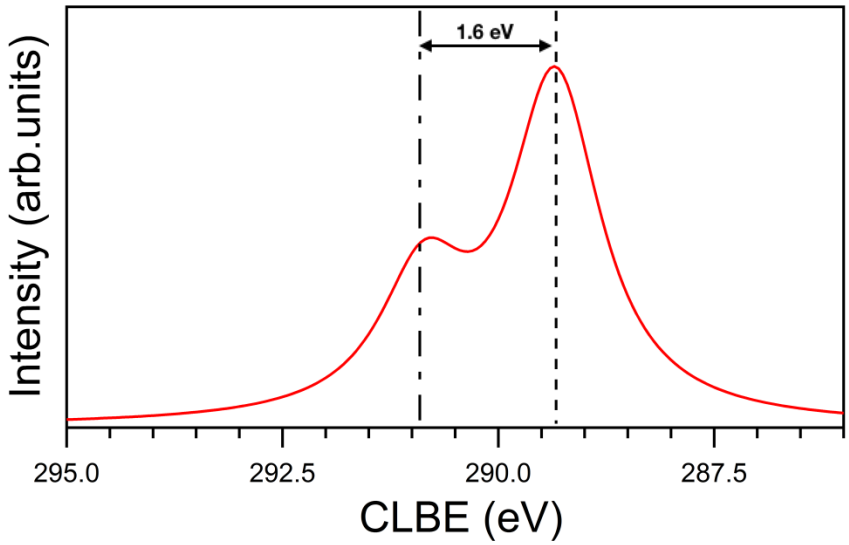

Figure E6: Anisole adsorbed on the Pt(111) surface 4x4 slab. The spectrum was generated using co-added Gaussians with FWHM of 1.5.The dashed line in the spectra corresponds the position of the carbon species bound to a carbon and the dot dashed line corresponds the carbon species bound to an oxygen. The positions of the lines are taken from fitted peaks (not shown).

References

(1) Bondino, F.; Comelli, G.; Esch, F.; Locatelli, a.; Baraldi, a.; Lizzit, S.; Paolucci, G.; Rosei, R. Structural Determination of Molecules Adsorbed in Different Sites by Means of Chemical Shift Photoelectron Diffraction: c(4×2)-CO on Pt(111). *Surf. Sci.* **2000**, *459*, 467–474.

(2) Lee, A. F.; Gawthrope, D. E.; Hart, N. J.; Wilson, K. A Fast XPS Study of the Surface Chemistry of Ethanol over Pt{1 1 1}. *Surf. Sci.* **2004**, *548*, 200–208.

(3) Ihm, H.; White, J. M. Stepwise Dissociation of Thermally Activated Phenol on Pt(111). *J. Phys. Chem. B* **2000**, *104*, 6202–6211.

(4) Réocreux, R.; Ould Hamou, C. A.; Michel, C.; Giorgi, J. B.; Sautet, P. Decomposition Mechanism of Anisole on Pt(111): Combining Single-Crystal Experiments and First-Principles Calculations. *ACS Catal.* **2016**, *6*, 8166–8178.

(5) Ould Hamou, C. a.; Réocreux, R.; Sautet, P.; Michel, C.; Giorgi, J. B. Adsorption and Decomposition of a Lignin B-O-4 Linkage Model, 2-Phenoxyethanol, on Pt(111): Combination of Experiments and First-Principles Calculations. *J. Phys. Chem. C* **2017**, *121*, 9889–9900.

Appendix F

Supporting information for the article presented in chapter 3:

Decomposition Mechanism of Anisole on Pt(111):
Combining Single-Crystal Experiments and First-Principles Calculations

Romain Réocreux,[‡] Cherif A. Ould Hamou,[†,§] Carine Michel,[‡] Javier B. Giorgi,[†,‖,*] Philippe Sautet[‡,&,*]

[‡] Univ Lyon, Ens de Lyon, CNRS UMR 5182, Université Claude Bernard Lyon 1, Laboratoire de Chimie, F-69342, Lyon, France
[†] Centre for Catalysis Research and Innovation, [§] Department of Physics, [‖] Department of Chemistry and Biomolecular Sciences, University of Ottawa, 10 Marie Curie Pvt., Ottawa, Ontario, Canada. K1N 6N5.
[&] Department of Chemical and Biomolecular engineering, University of California, Los Angeles, Los Angeles, CA 90095, United States

Coverage Calibration with C 1s XPS

The C 1s XPS signal was monitored for different exposures of anisole on Pt(111) at 115K. The C1s area reaches a plateau which correspond to the saturation of the monolayer. Coverage calibration was achieved by comparison with CO saturation coverage at room temperature. Dashed line in figure S1 indicates the area of the C 1s peak from a CO coverage surface which is known to correspond to one CO molecule per two Pt atoms on the surface. That is, C/Pt atomic ratio of 0.5. Upon monolayer coverage of anisole, a C/Pt ratio of 0.7 is achieved which corresponds to one molecule of anisole (7 carbon atoms) for each 10 Pt atoms on the surface.

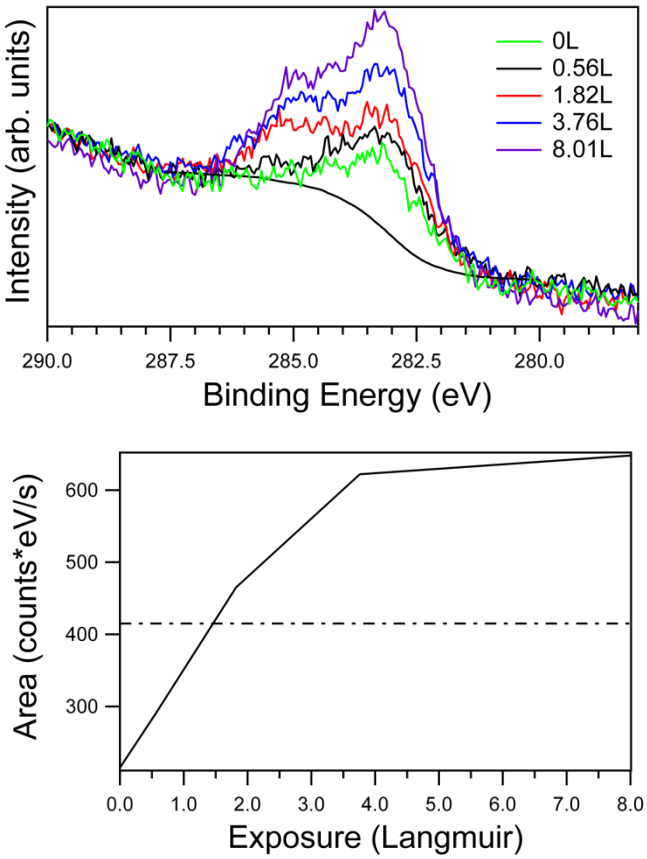

Figure F1: C1s spectra and corresponding integrated area after several exposures of anisole at 115K on Pt(111). The C1s starts reaching a plateau around 2.8 Langmuir corresponding to the saturation of the 1st layer of anisole on the platinum surface. Dash line correspond to calibration point from CO adsorption on Pt(111).

Oxygen XPS

The O 1s XPS signal was monitored for all measurements. Disappearance of the oxygen signal matches the disappearance of the C 1s species assigned to oxygen bound carbons species (C-O labeled peaks).

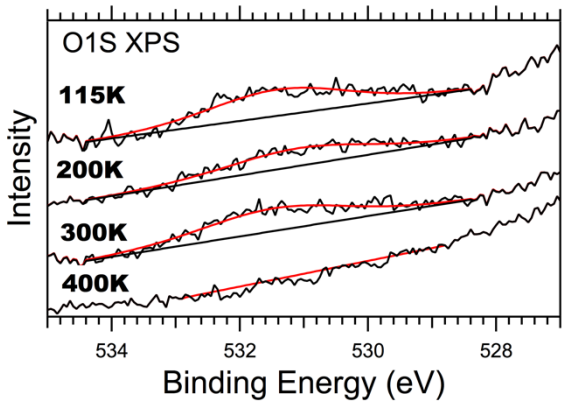

Figure F2: XPS spectra for the O 1s peak acquired at different temperature for 0.5ML of anisole deposited at 115K.

Correction of TPD signal due to fragmentation of species in the mass spectrometer

Because all organic species fragment during the ionization process in the mass spectrometer, it is necessary to identify the fraction of signal at specific mass to charge intensities corresponding to species desorbing from the surface versus those that arise from fragmentation. To perform the correction, appropriate parent molecules (for example anisole) are dosed into the chamber in the gas phase and the mass spectrum is obtained to identify the corresponding fragmentation pattern specific to the instrument (Figure F3a). In this case the ratio of intensities of masses 78/108 was determined as 2.6. Since we monitor TPD of the masses simultaneously, this allows us to quantify the fraction of m/z=78 corresponding to fragmentation of anisole in the QMS and subtract it from the overall benzene signal. The result is the identification of benzene arising from surface desorption (Figure F3b).

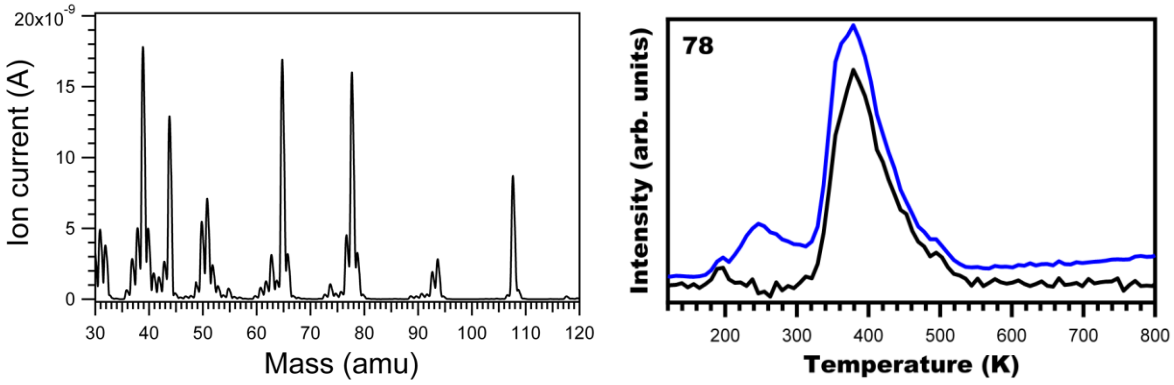

Figure F3: a) Mass spectrum of gas phase anisole illustrating the instrument specific fragmentation pattern. b) TPD spectra after multilayer exposure of anisole at 115K on Pt(111) using a linear temperature ramp of 7 K/s. The blue line corresponds to benzene raw data as measured by the mass-spectrometer. The black line corresponds to benzene produced from the surface (data obtained after the subtraction of contribution of the gas phase fragmentation pattern of anisole in the mass spectrometer).

XPS vs TPD consistency.

To justify that the TPD analysis is consistent with the XPS interpretation of the experiment we calculated, from the TPD-determined frequency factors and activation energies, the expected half-lives (in hour) as a function of temperature. The processes can be considered as kinetically blocked when the half-lives are greater than an hour (blue values) and kinetically possible when the half-lives are much smaller than an hour. From this, we can calculate the expected temperature at which a process will happen during the XPS measurement that lasts one hour. The half-lives presented here were calculated assuming a first-order Arrhenian process with the associated TPD-determined parameters.

Table F1: Half-lives of 4 given processes, namely anisole decomposition, physisorbed anisole desorption and chemisorbed anisole desorption, and carbon monoxide desorption. The half-lives, calculated from TPD-determined parameters, are given as a function of temperature.

	Anisole decomposition	physiorption PhOMe	chemisorption PhOMe	CO desorption
frequency (s-1)	1.70E+14	5.40E+16	2.40E+17	8.30E+14
TPD barrier (kJ/mol)	89	83	121	137
T (K)	half life (hour) for a 1st order process			
100	5.08E+26	8.10E+22	1.29E+42	8.50E+52
115	4.38E+20	1.79E+17	7.35E+33	3.94E+43
150	1.62E+11	2.86E+08	1.10E+21	1.19E+29
200	2.89E+03	1.70E+01	3.22E+10	1.40E+17
210	2.26E+02	1.58E+00	1.01E+09	2.78E+15
220	1.54E+03	1.82E-01	4.31E+07	7.84E+13
230	1.85E+02	2.53E-02	2.43E+06	3.02E+12
240	2.66E+01	4.14E-03	1.74E+05	1.53E+11
250	4.47E+00	7.85E-04	1.54E+04	9.80E+09
260	8.61E-01	1.69E-04	1.64E+03	7.76E+08
270	1.87E-01	4.07E-05	2.06E+02	7.42E+07
280	4.55E-02	1.09E-05	3.01E+01	8.40E+06
290	1.22E-02	3.18E-06	5.01E+00	1.10E+06
300	3.56E-03	1.01E-06	9.40E-01	1.66E+05
310	1.12E-03	3.45E-07	1.97E-01	2.82E+04
320	3.82E-04	1.26E-07	4.53E-02	5.36E+03
330	1.39E-04	4.90E-08	1.14E-02	1.13E+03
340	5.34E-05	2.01E-08	3.12E-03	2.59E+02
350	2.17E-05	8.70E-09	9.19E-04	6.49E+01
360	9.29E-06	3.94E-09	2.89E-04	1.76E+01
370	4.16E-06	1.86E-09	9.71E-05	5.09E+00
380	1.94E-06	9.16E-10	3.45E-05	1.58E+00
390	9.43E-07	4.67E-10	1.29E-05	5.19E-01

400	4.75E-07	2.46E-10	5.08E-06	1.80E-01
450	2.43E-08	1.54E-11	8.92E-08	1.86E-03
500	2.25E-09	1.67E-12	3.51E-09	4.77E-05
550	4.77E-09	2.72E-13	2.49E-10	2.38E-06
600	8.64E-10	6.00E-14	2.75E-11	1.96E-07
XPS temperature (K)	270	220	310	390

DFT predicted infrared spectrum of phenoxy PhO

The RAIRS simulated spectrum was generated from a VASP frequency calculation by computing the contribution of the dipole moment along the direction perpendicular to the surface (RAIRS selection rule) at each displacement. The associated matrix was diagonalized and the intensity of each normal mode was determined using the squared variation of the dipole moment.

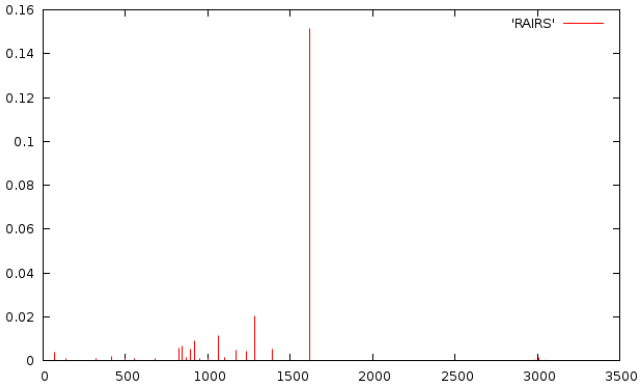

Figure F4: DFT predicted infrared spectrum of phenoxy PhO.

The strong peak at 1616 cm^{-1} corresponds to the stretching mode of the C-O bond. The value of the wave number is typical for a carbonyl function and matches with the experimentally observed cyclohexadienyl structure of "phenoxy" on Pt(111).

Reaction network for phenoxy decomposition.

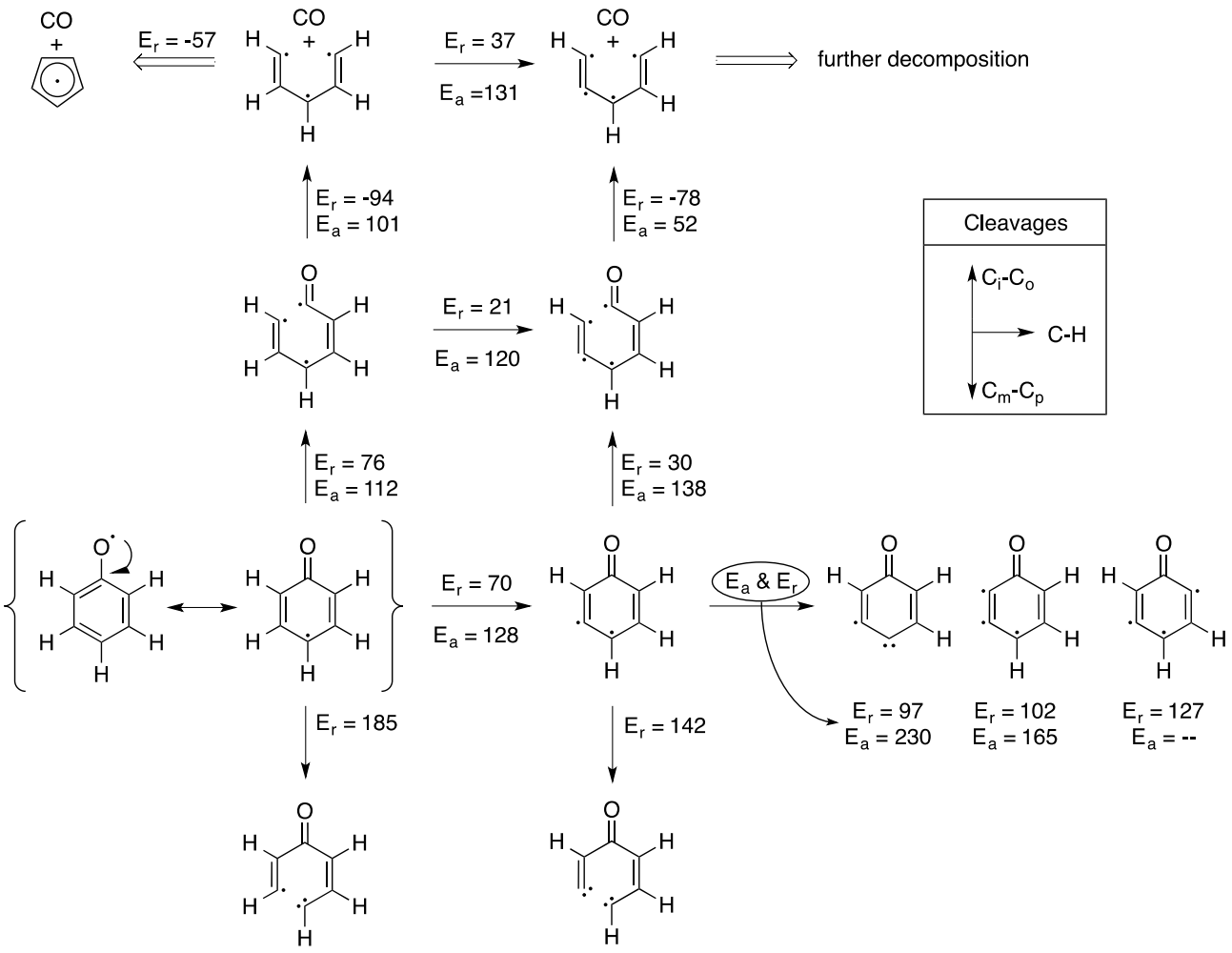

Figure F5: Reaction network of phenoxy decarbonylation to carbonaceous species. Downward, upward and rightward arrows are associated to the meta-para C-C, ipso-para C-C and aromatic C-H cleavages respectively. E_r and E_a stand for reaction and activation energies respectively. The energies are given in kJ/mol and are not ZPE-corrected.

Kinetic analysis of the DFT data.

In a TPD experiment, two time-scales have to be compared: the one imposed by the operator through the choice of the temperature ramp (here $\beta = 7\ K/s$) and the ones that are specific to the reactivity of the chemicals. If the reaction time is smaller than the TPD time-scale T/β, then one can observe the reaction happening. Otherwise, the reaction is to slow to be observed within the time of the TPD experiment. In this work we considered the 1% conversion time $\tau_{1\%}$

since only a small fractions of the initially adsorbed species yield desoring products. A reaction is therefore considered to happen when:

$$\tau_{1\%} < \frac{T}{\beta}$$

Using Eyring's equation for a 1st order process:

$$\tau_{1\%} = \frac{-\ln(0.99)\,h}{k_B T} \exp\left(+\frac{\Delta F^{\ddagger}}{RT}\right) < \frac{T}{\beta}$$

One can then extract the limit we considered in the main text of the article:

$$\Delta F^{\ddagger} \simeq RTln\left(\frac{k_B T^2}{-\ln(0.99)\,h\beta}\right)$$

Intermediates and transition states of the routes to benzene and phenol

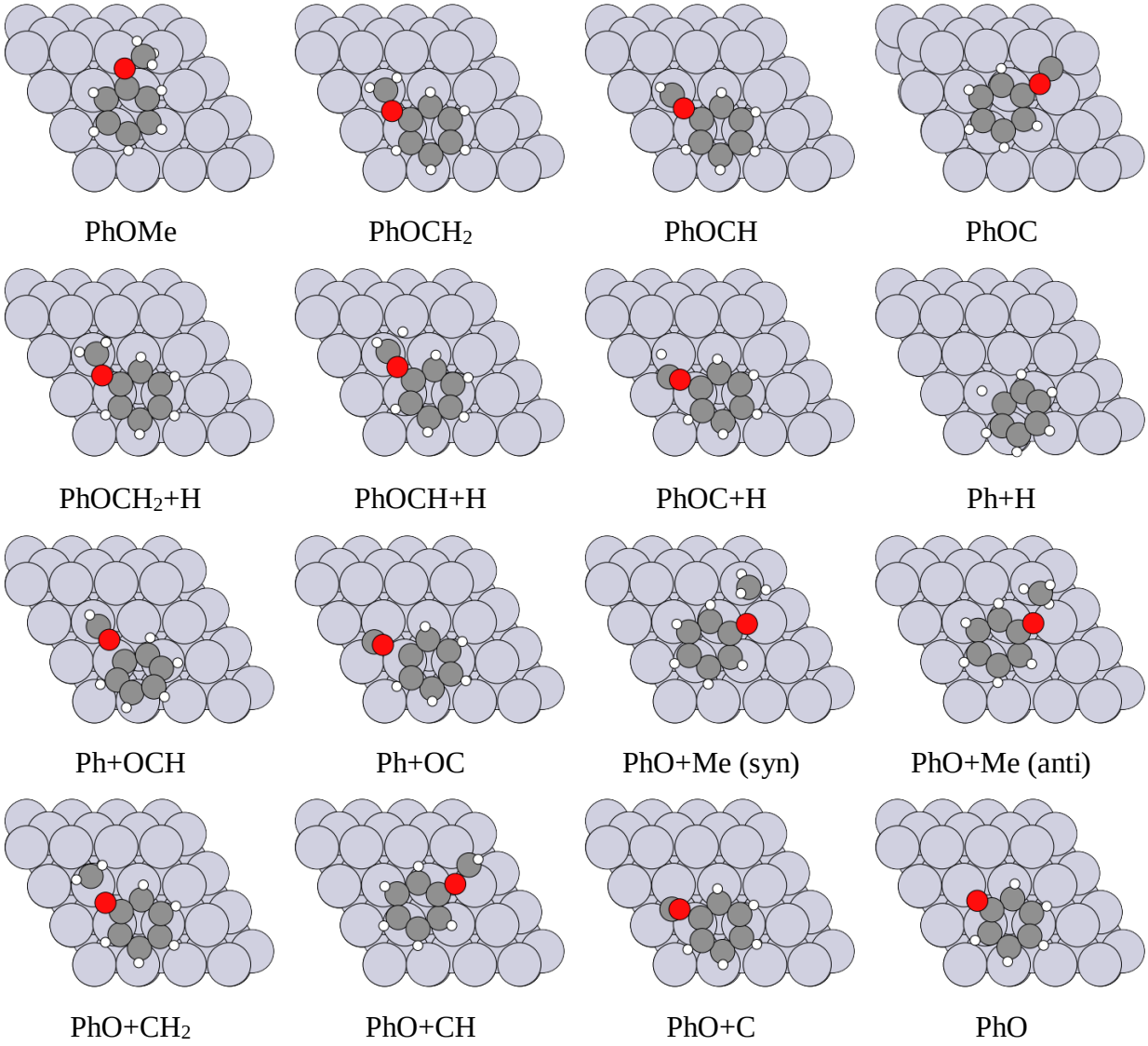

Figure F6: Structures of the intermediates and transition states associated to the benzene and phenol routes.

Intermediates and transitions states of the routes to phenoxy fragmentation.

The structures appear here in the same order as in Figure 3.11 (main article).

Mechanism #1

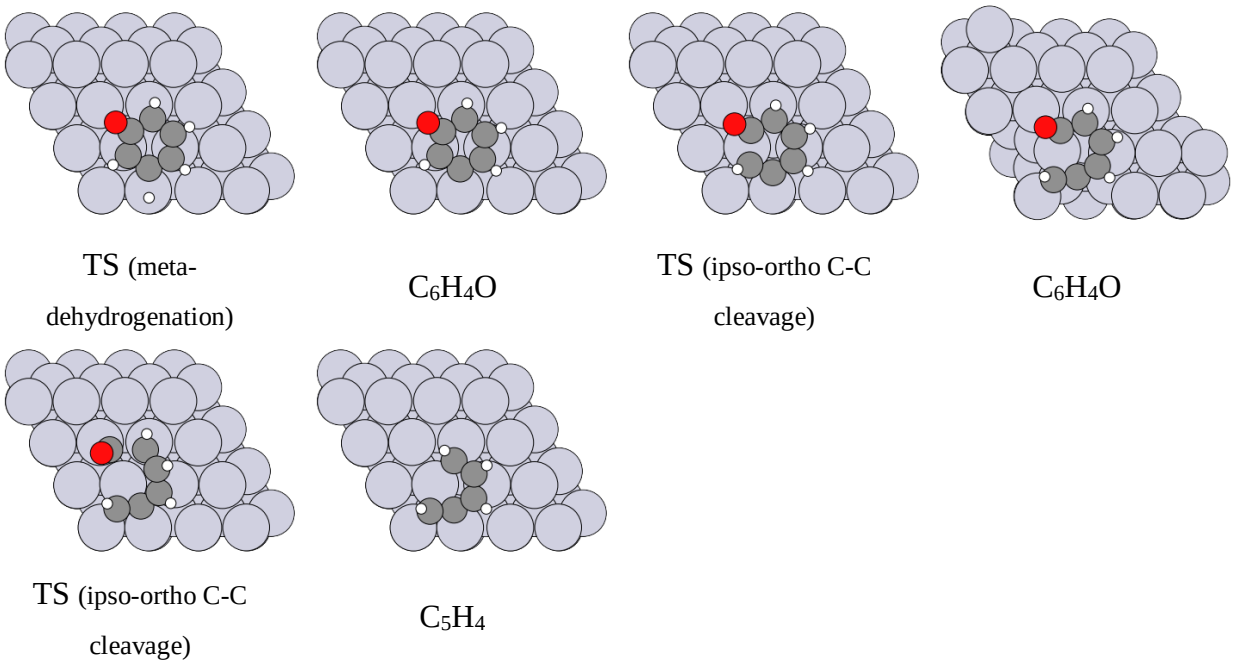

Figure F7: Structures of the intermediates and transition states associated to the 1st mechanism of the fragmentation of phenoxy.

Mechanism #2

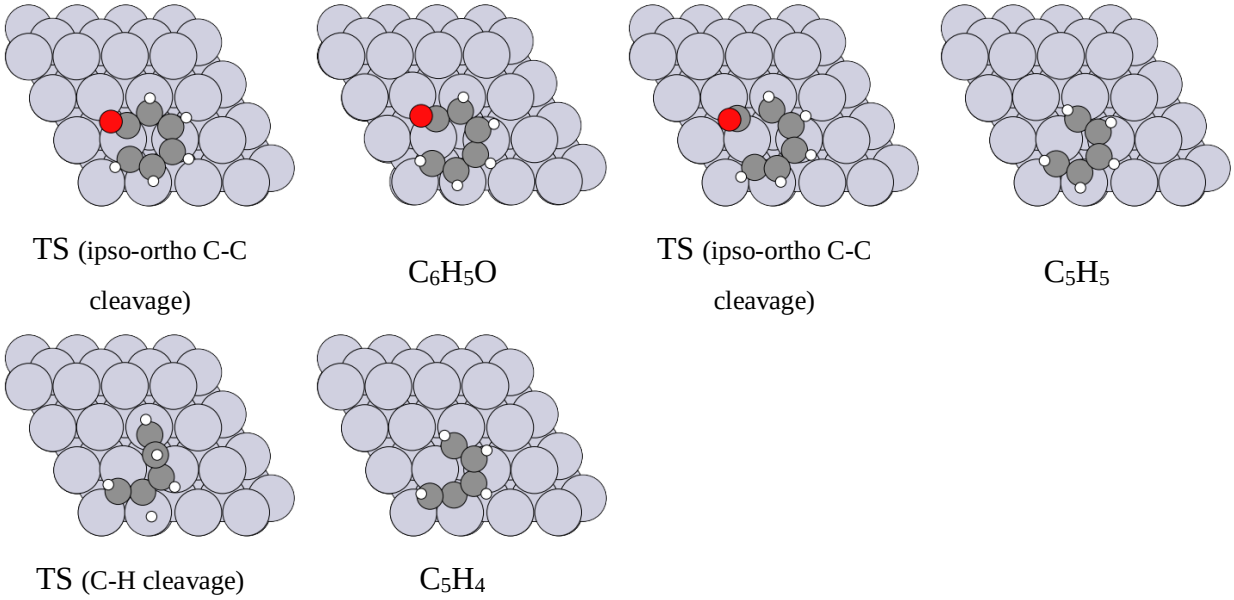

Figure F8: Structures of the intermediates and transition states associated to the 2nd mechanism of the fragmentation of phenoxy.

Appendix G

Supporting information for the article presented in chapter 4:

A Combined DFT Calculations and Experimental Approach of the Adsorption and Decomposition of 2-phenoxyethanol on Pt(111)

Cherif A. Ould Hamou,[†,§] Romain Réocreux,[‡] Carine Michel,[‡] Javier B. Giorgi,[†,‖,*] Philippe Sautet[‡,&,*]

[†] Centre for Catalysis Research and Innovation, [§] Department of Physics, [‖] Department of Chemistry and Biomolecular Sciences, University of Ottawa, 10 Marie Curie Pvt., Ottawa, Ontario, Canada. K1N 6N5.
[‡] Univ Lyon, Ens de Lyon, CNRS UMR 5182, Université Claude Bernard Lyon 1, Laboratoire de Chimie, F-69342, Lyon, France
[&] Department of Chemical and Biomolecular engineering, University of California, Los Angeles, Los Angeles, CA 90095, United States

Table G1: Surface carbon coverage corresponding to several exposures of 2-phenoxyethanol at 110 K.

Dosage (L)	**Carbon Coverage**	
0.64	0.35	1molecule / 23Pt
0.78	0.43	1molecule / 19Pt
0.85	0.51	1molecule / 16Pt
1.2	0.66	1molecule / 12Pt

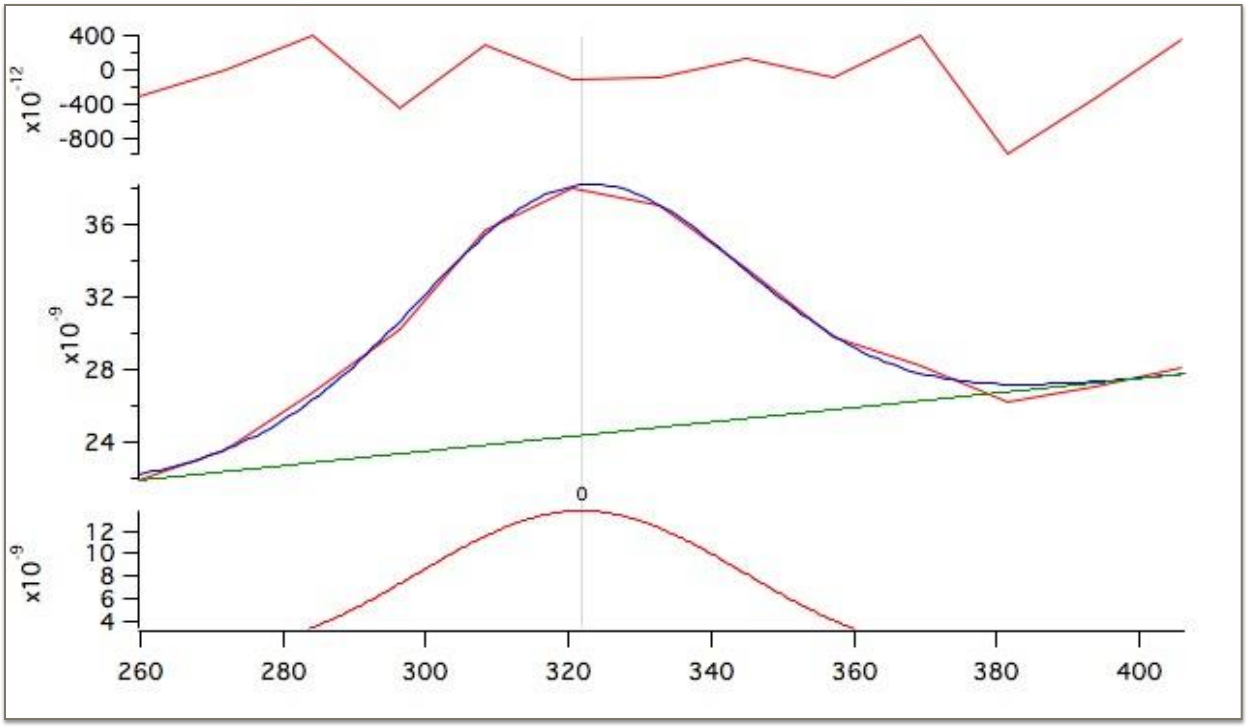

Figure G1: TPD spectra corresponding to Hydrogen contribution from background.

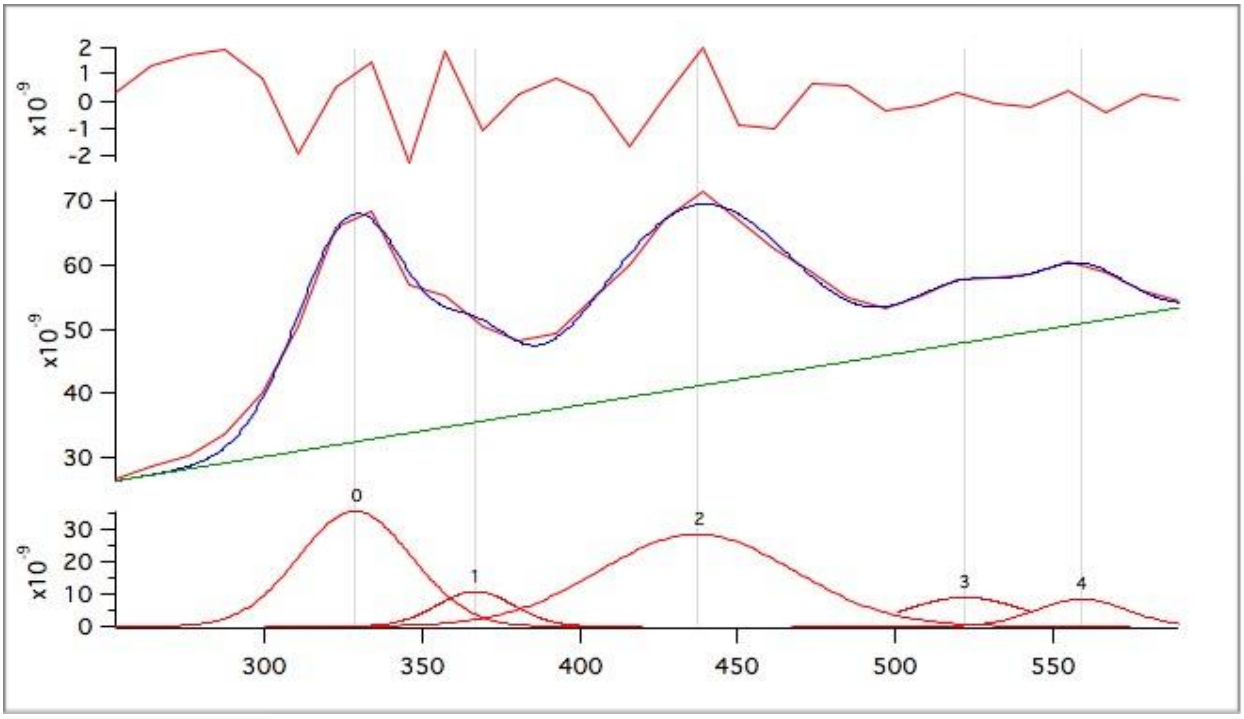

Figure G2: TPD spectra corresponding to desorption of Hydrogen the surface after 0.85L exposure of 2-phenoxyethanol at 110 K with a ramp of 5.8 K/s. The ratio of the peaks are 2:1:5:1:1 respectively

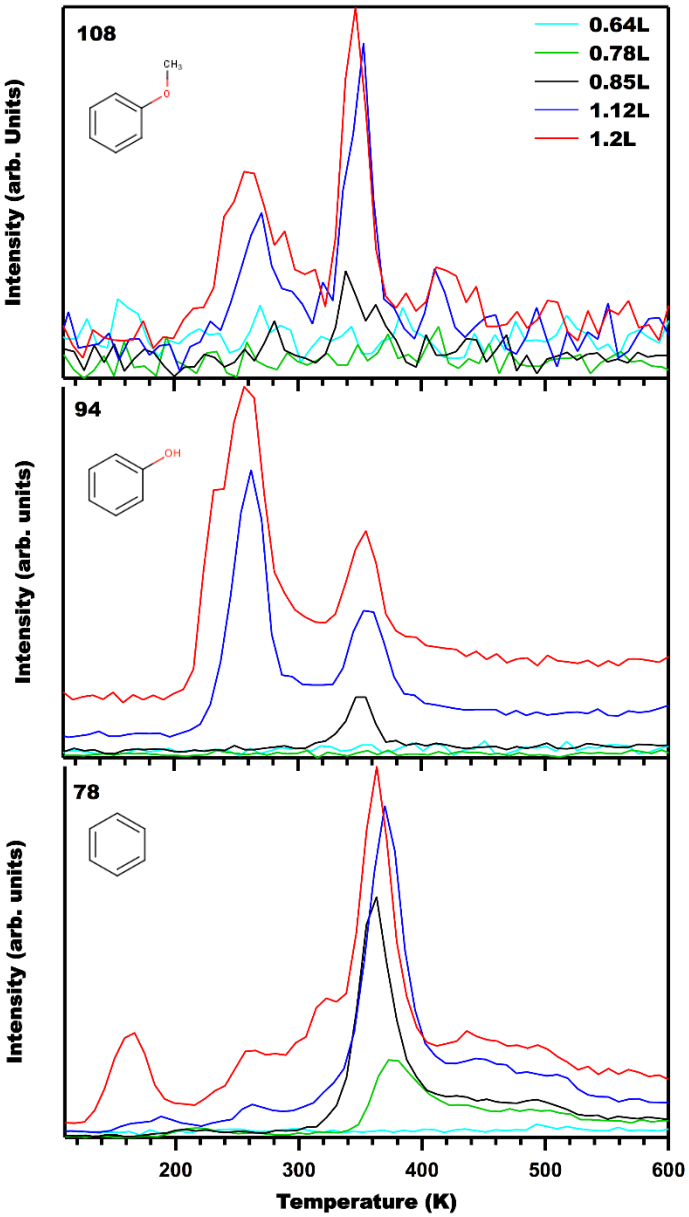

Figure G3: TPD spectra after several 2-phenoxyethanol exposure at 110K on Pt(111). Monitored masses 108,94 and 78 corresponding to Anisole, Phenol and Benzene respectively. Desorption rates are measured using a linear temperature ramp of 5.8 K/s

Appendix H

Supporting information for the article presented in chapter 5:

Ould Hamou, C. A.; Giorgi, J.B. Direct observation of phenoxy as the key and common intermediate for the decomposition of lignin fragments containing the beta-O-4 linkage. S*ubmitted to J. Phys. Chem. C*

Direct Observation of Phenoxy as the Key and Common Intermediate for the Decomposition of Lignin Fragments Containing the Beta-O-4 linkage

Cherif A. Ould Hamou,[†,§] Javier B. Giorgi,[†,‖,*]

[†] Centre for Catalysis Research and Innovation, [§] Department of Physics, [‖] Department of Chemistry and Biomolecular Sciences, University of Ottawa, 10 Marie Curie Pvt., Ottawa, Ontario, Canada. K1N 6N5.

Table H1: Vibrational modes and peak assignments of Phenol on Pt(111).

Vibrational mode[b]	**Pt(111)[a]**	**Phenol vapor[1]**	**Phenol vapor 2[2]**	**Phenol liquid[2]**
C-H stretch (20a)	3093	3087	3078	3070
C-H stretch (13)	3049	3063	3050	3044
C-H stretch (2)	3026	3027		3020
C-C stretch (8a)	1598	1603	1602	1597
C-C stretch (19b)	1501	1501	1501	1500
C- C stretch (8b)	1480		1478	1474
Ring stretch (19a)	1398		1349	1362
C-O stretch (7a)	1244	1261	1260	1228
C-H bend (9a)	1169	1168	1168	1168
C-H bend (15)	1154		1150	1152
C-H bend (9b)	1072		1072	1072
C-H bend (12)	1025	1025	1026	1025
Ring breathing (18a)	1000	999		981
C-H bend (17b)	889		881	888
X2 sensitive (1)	812	823	814	812
C-H bend (4)	758		750	752

[a]Phenol adsorbed on Pt(111), this work.

[b]Approximate mode description. Wilson's notation in parenthesis.

Table H2: Vibrational modes and peak assignments of Phenol on Pt(111) at varying temperatures.

Vibrational mode[a]	**130K**	**220K**	**240K**	**300K**	**330K**	**450K**
C-H stretch (20a)	3093	3078				
C-H stretch (13)	3049	3049				
C-H stretch (2)	3026	3025				
C-C stretch (8a)	1598	1598	1601	1593	1590	1587
C-C stretch (19b)	1501	1501				
C- C stretch (8b)	1480	1479				
Ring stretch (19a)	1398	1398				
C-O stretch (7a)	1244	1243	1250	1251	1257	1257
C-H bend (9a)	1169	1170	1169		1169	
C-H bend (15)	1154	1154				
C-H bend (9b)	1072	1073				
C-H bend (12)	1025	1025				
Ring breathing (18a)	1000	1000				
C-H bend (17b)	889	889				
X2 sensitive (1)	812	813				
C-H bend (4)	758	758		768	761	668
Phenoxy[b]						
CO stretch(7a)			1486	1485	1484	1484
C-C str/C-H bend (3)					1233	1229
C-H bend (17b)					852	

[a]Approximate mode description. Wilson's notation in parenthesis.

[b]Characteristic phenoxy vibrations

Table H3: Vibrational modes and peak assignments of Anisole on Pt(111) at varying temperatures.

Vibrational mode[a]	**130K**	**180K**	**240K**	**300K**	**360K**	**450K**
(a) arm vibrations						
CH_3 antisym. str.	3009	3002	3001			
CH_3 antisym. str.	2960	2960	2960			
CH_3 sym. str.	2836	2835	2812			
CH_3 antisym. def.	1469	1469				
CH_3 sym. def.	1441	1440				
CH_3 rock	1175	1187	1186			
		1171	1175			
O-CH_3 str.	1041	1043	1056			
(b) ring vibrations						
C-H stretch	3063					
C-C stretch	1603	1603	1604	1603	1602	
C-C stretch	1587	1587	1587	1589	1592	
C-C stretch	1500	1499	1501	1500	1500	
		1492				
C-C stretch	1453	1454	1457	1457	1458	
C-C stretch	1326	1325				
C-H bend	1301	1301	1300			
Ph-OR stretch	1254	1255	1254			
C-H bend	1153	1151	1148			
C-H bend	1080	1079				
C-H bend	1019	1018		1016		
Ring breathing	994	995	928	930		

C-H bend	890	889				
Ring breathing	786	785	797	799	797	
C-H bend (out of plane)	764	757	752	756	752	
X-sensitive	696	696	695			
***Phenoxy*[b]**						
CO stretch(7a)				1485	1483	
C-C str/C-H bend (3)				1251	1251	1261
C-H bend (17b)			861	860		

[a]Approximate mode description. Wilson's notation in parenthesis for phenoxy.

[b]Characteristic phenoxy vibrations. Common peaks have not been transferred.

Table H4: Vibrational modes and peak assignments of 2-phenoxyethanol on Pt(111) at varying temperatures.

Vibrational mode[a]	**130K**	**240K**	**260K**	**300K**	**360K**	**400K**
(a) arm vibrations						
CH_2-CH_2 antisym str	2938	2937				
CH_2-CH_2 sym str	2876	2873				
CH_2 scissor	1499	1500	1500	1500		
CH_2 twist + C-H ring bends	1303	1303	1301	1303		
O-C + C-C + C-O str	1088	1087	1086			
O-C + C-O str	1057	1057	1051			
O-C-C + C-C-O def	922	922	920			
(b) ring vibrations						
C-H ring bends	1603	1602	1603	1602	1598	1591

C-H ring bends	1588	1589	1589	1586		
C-H ring bends	1459	1459	1460			
Ph-O + O-C strs + O-H bend	1253	1253	1254	1251	1247	1260 1245
C-H ring bends	1175	1175	1174			
C-H ring bends	1153	1152	1155			
Ring breathing						
C-H ring bends	899	898	896		881	
C-H ring bends	817	814	814			
Ph-O-C def	793	792	972			
C-H ring bends	760	760	758			
C-H ring bends	694	694				
***Phenoxy*[b]**						
CO stretch(7a)				1482	1482	1497

[a]Approximate mode description. Wilson's notation in parenthesis for phenoxy.

[b]Characteristic phenoxy vibrations. Common peaks have not been transferred.

Table H5: Normalized area of the vibrational peaks as a function of temperature after depositing 100L of phenol on Pt (111) at 130K.

Temperature (K)	Ph-O str
130	1
150	1.011
180	1.032
200	0.866
220	0.421
240	0.019
260	0.016
300	0.017
330	0.014
360	0.013
400	0.009
450	0.018

Table H 6: Normalized area of the vibrational peaks as a function of temperature after depositing 100L of Anisole on Pt (111) at 130K.

Temperature (K)	Ph-O str	O-CH_3 str	CH_3 sym	CH_3 a. sym
130	1	1	1	1
180	0.896	0.936	0.867	1.603
240	0.040	0.016	0.592	0.071
300	0.021	-0.008	-0.003	-0.073
360	0.008	-0.004	-0.005	-0.121
400	0.007	-0.004	0.002	0.065
450	0.011	-0.007	-0.004	0.038

Negative numbers are due to noise in the spectra and can be assumed to be zero.

Table H7: Normalized area of the vibrational peaks as a function of temperature after depositing 100L of 2-Phenoxyethanol on Pt (111) at 130K.

Temperature (K)	**Ph-O +C-O strs + O-H bend**	**O-C +C-C + C-O str**	**CH_2-CH_2 sym/a.sym str**	**CH_2 scissor**
130	1	1	1	1
150	1.019	1.021	1.071	1.039
180	1.001	1.009	1.038	1.037
200	1.056	1.051	1.069	1.094
240	0.712	0.625	0.527	0.718
260	0.178	0.120	0.033	0.186
300	0.051	-0.035	-0.002	0.061
360	0.039	-0.019	0.012	0.037
400	0.059	-0.027	0.012	0.033
450	0.048	-0.005	-0.014	0.036

References

(1) Bist, H. D.; Brand, J. C. D.; Williams, D. R. The Vibrational Spectrum and Torsion of Phenol. *J. Mol. Spectrosc.* **1967**, *24*, 402–412.

(2) Evans, J. C. The Vibrational Spectra of Phenol and Phenol-OD. *Spectrochim. Acta* **1960**, *16*, 1382–1392.

Appendix I

Adsorption and Decomposition of Formic Acid on Cobalt (0001)

Although not strictly part of the thesis theme in regards to lignin, this work was part of my graduate work time and learning experience.

Adsorption and Decomposition of Formic Acid on Cobalt (0001)

Jeffrey J. Sims[a,b], Cherif A. Ould Hamou[a,c], Romain Réocreux[e,f], Carine Michel* [e], Javier B. Giorgi* [a,d]

[a]*Centre for Catalysis Research and Innovation,* [b]*Department of Chemical and Biological Engineering,* [c]*Department of Physics,* [d]*Department of Chemistry and Biomolecular Sciences, University of Ottawa, 10 Marie Curie Pvt., Ottawa, Ontario, Canada. K1N 6N5.*

[e]*Univ Lyon, Ens de Lyon, CNRS UMR 5182, Université Claude Bernard Lyon 1, Laboratoire de Chimie, F-69342, Lyon, France*

[f] Current address: *Thomas Young Centre and Department of Chemical Engineering, University College London, Roberts Building, Torrington Place, London WC1E 7JE, United Kingdom*

Abstract

Formic acid can undergo dehydration or dehydrogenation with variable selectivity over a range of metal catalysts. The selectivity among these reactions depends on the reaction mechanism and reaction conditions pertinent on each surface. This work provides mechanistic insight on the decomposition of formic acid on cobalt at high and low temperature regimes. The adsorption and decomposition of formic acid on a Co(0001) single crystal was studied in ultra-high vacuum by X-ray photoelectron spectroscopy (XPS) and temperature programmed desorption (TPD). Insight is provided using DFT calculations. In the low temperature regime, formic acid adsorbs molecularly on the surface at 130 K. Partial decomposition produces CO at 140 K, and at 160 K the decomposition of formic acid into formate, which is a thermodynamic sink, is dominant. Water can be formed at low temperature via bimolecular processes. At high temperature (>400 K) the similar barriers for decomposition of the formate species lead to the concomitant production of CO, CO_2 and H_2. The correlation between experiment and theory provides a framework for the interpretation of surface species and reaction path operating in different regimes.

I1. Introduction

The interaction and reactions of formic acid on transition metal catalysts has been the subject of multiple studies due to the importance of formic acid in a variety of industries.[1–8] Formic acid decomposition possesses similar intermediates as the water-gas shift reaction[9] and methanol oxidation.[10] Additionally, these intermediates are often present in the oxidation of large organic molecules and steam-reforming reactions.[11] As such, formic acid is often a model molecule in the study of bio-oil and biomass applications.[12–14] In addition, formic acid also has been proposed as a hydrogen vector for mobile applications.[15] Hence the importance of understanding and controlling formic acid reactivity has produced a number of fundamental and industrial studies.

Formic acid provides two competing decomposition pathways, namely dehydrogenation and dehydration (eq. I1 and I2). Single crystal investigations of formic acid on transition metal surfaces have shown that not only the ratio of products, but also the mechanism by which they are achieved depends on the nature of the metal and the surface plane involved.[11,16] For example, on Pt(111) formic acid decomposes primarily through the dehydrogenation reaction in UHV[17–19] and the dehydration reaction can only be observed at higher pressures,[20] while on Pt(100) formic acid does not react in UHV conditions.[21] In addition, formic acid has also been suggested to undergo a bimolecular decomposition pathway on Cu,[11,22,23] Ru,[11] and Ni[7,11,23,24] surfaces in addition to or instead of the dehydrogenation and dehydration reactions.

$$HCOOH \rightarrow CO_2 + H_2 \quad \text{(I1)}$$

$$HCOOH \rightarrow CO + H_2O \quad \text{(I2)}$$

The decomposition of formic acid on cobalt surfaces are of particular importance because cobalt is a prevalent catalyst for the water-gas shift reaction,[9] and methanol oxidation reaction,[10] as well as being used as an additive to increase performance and stability of direct formic acid/methanol fuel cell catalysts.[8,25–32] Cobalt has also been suggested as desirable catalyst for steam reforming. Despite its importance, a small number of experimental studies of formic acid decomposition on cobalt have been performed. Inglis and Taylor[23] studied the decomposition of formic acid on 1st row transition metal thin films under 30 Torr of formic acid and temperatures between 100-300 ^{o}C. They report a CO_2:CO ratio of approximately 1:1 on cobalt catalysts. Inglis

and Taylor also found that this ratio was independent of temperature for the temperature range used in their experiments. They postulated that formic acid may decompose through a bimolecular pathway, but no mechanistic information or reaction pathways were proposed. Tang et al.[33] provided insight by measuring reaction products obtained from metallic cobalt powders and performing TPD and IR spectroscopy to show the presence of a monodentate formate species and provide an experimental ratio for the two reaction pathways (CO_2/CO=3.9), although different from those of Inglis and Taylor.

Experimental insight into the reaction pathways is often obtained using single crystal surfaces. Toomes and King explored monolayer and multilayer potassium-promoted synthesis of surface formate and the decomposition of formic acid on Co(1010) by infrared reflective adsorption spectroscopy (IRRAS) and TPD in the temperature range of 160-640 K.[34] They found that formic acid chemisorbed onto the potassium layer forming formate and hydrogen at 160 K. The formate subsequently decomposed to CO, H_2, and atomic O above 250 K. However, surface formate could be synthesized by the reverse process, from CO, O_2, and H_2 at 300 K.

More recently, different groups provided a theoretical study of formic acid decomposition trends for several transition metal surfaces, among them Co(0001).[15,16] They focussed on the relative importance of the formate and carboxylic pathways to determine the CO_2/CO product ratio. Li *et al.* considered the reaction on Co(111) both in vacuum and with solvents[14] and then took it a step further, proposing a microkinetic analysis of the different reaction pathways on a stepped cobalt surface.[12] They found that different reaction pathways were preferred in the different cases. A more detailed discussion of the available theoretical data will be provided in comparison with our DFT calculations.

The present work provides a detailed experimental and theoretical study of the decomposition and adsorption of formic acid on Co(0001) single crystal under ultrahigh vacuum (UHV) conditions. Surface species produced during the interaction and reaction of formic acid with the surface are characterized by low energy electron diffraction (LEED), X-ray photoelectron spectroscopy (XPS) and temperature programmed desorption (TPD). Experimentally determined surface species, decomposition products and desorption energies are compared with a full density functional (DFT) calculations of energetics and transition states of the possible reaction pathways. The combination of experiment and theory is used to obtain insight on this system.

I2. Experimental

Experiments were carried out in a UHV chamber with a base pressure of 3 x 10^{-10} mbar. The chamber contains an XPS, LEED, STM/AFM, mass spectrometer for TPD measurements, and has been described in detail previously.[35]

The 8 mm diameter and 0.5 mm thick cobalt single crystal sample (hcp phase) with purity of 99.999% was purchased from Princeton scientific. The (0001) crystal surface was cleaned by repetitive cycles of 10 mins of sputtering (3 keV, background pressure of 1 x 10^{-5} mbar Ar^+), followed by annealing to 600 K for 5 min. The sample was confirmed clean by LEED, shown in Figure S1 (supporting information). Temperatures above 630 K were avoided due to the Co phase transition from hexagonal closest packing (hcp) to face-centered cubic packing (fcc) at 670 K.[36,37] The sample was heated by electron bombardment and the temperature was measured by a chromel-alumel (K-type) thermocouple.

HPLC-grade formic acid (99% purity) was purchased from Sigma Aldrich. The formic acid was introduced to the UHV chamber through a leak valve that was connected to a gas manifold with a formic acid reservoir. The reservoir underwent a series of freeze-pump-thaw cycles to ensure the pressure of the gas manifold was that of the vapour pressure of formic acid. Formic acid was dosed by backfilling the chamber. The purity of the formic acid dosed was verified by a residual gas analyzer. All exposures are reported in Langmuirs (1 L = 1.0 × 10^{-6} torr s) without corrections for the gauge sensitivity.

I2.1 XPS Measurements

XPS spectra were recorded using a standard Al Kα source (1486.7 eV) operated at 289.7 W (14.2 kV, 20.4 mA) on a Specs GmbH system (XR50 X-ray source and Phoibos 100 SCD analyzer). Selected peaks were obtained in high resolution spectra using 0.1 eV step size, 1 second dwell time, and pass energy of 20 eV. When necessary, each region was scanned 3 times to increase the signal to noise ratio. The spectra were then fit using CasaXPS analysis software using a mixed Gaussian Lorentzian function and Shirley background subtractions. Although it is tempting to consider a large number of species under each spectra, the number of curves fit was limited by the resolving peak width of the instrument (a minimum FWHM of 1.2 eV was used in all fits). The binding energy scale was calibrated using cobalt (Co 2p 3/2 = 777.8 eV).[38]

X-ray exposure was kept to the minimum required to reduce formic acid decomposition due to the X-ray beam. The clean sample was dosed with formic acid at 130 K and then heated up

to the desired temperature of observation; then the spectrum was taken. Once the spectrum was finished, the sample was flashed to 630 K to clean the sample surface and verified clean by LEED. This process was repeated for each temperature of interest.

I2.2 TPD Experiments

The sample surface was dosed with varying exposures of formic acid at 130 K and placed approximately 1 mm below a 1 mm diameter hole leading to a differentially pumped mass spectrometer. The temperature-controlled heating ramp was programmed in LabView and designed to provide and record a linear temperature ramp using a PID controller feedback loop. All experimental ramps started at 130 K and ended at 550 K, with a ramp rate of 4.60 ± 0.15 K/s. The sample was annealed at 630 K for 5 mins after each exposure to clean the sample. A total of 13 channels corresponding to m/z values of 46, 45, 44, 40, 32, 29, 28, 18, 17, 16, 14, 4, and 2, were monitored for the formic acid TPD experiments. These m/z values correspond to the expected species and their respective fragmentation patterns which were measured by background dosing within the instrument. All spectra were thereby correlated during analysis.

I2.3 DFT Calculations

First principle calculations were performed within the framework of Density Functional Theory (DFT) using the dispersion corrected GGA functional PBE+dDsC[39–41] with the Vienna Ab initio Simulation Package software (VASP 5.3) for electronic and geometric optimization.[42–44] The spin-polarized wave-functions were expanded on a periodic plane wave basis set with an energy cut-off of 400 eV and optimized using an energy threshold of 10^{-6} eV. The core electrons were treated using the Projection Augmented Wave (PAW) approach.[45] The electronic energy was integrated over a gamma-centered 3x3x1 Monkhorst-Pack k-point mesh.[46] For gas phase calculations, the gamma point was considered. All geometries were considered optimized when forces were less than 0.02 eV/Å.

The Co(0001) surface was modeled employing a 4 layer 3x3 periodic slab, with 5 layers void. During optimization, only the top two layers were relaxed keeping the position of the other metal atoms fixed at their bulk position. Gas phase structures were optimized in a 20x20x20 $Å^3$ simulation box.

I3. Results

Experimental results will be described for adsorption of formic acid on Co(0001) using XPS, where low temperature species can be identified. Temperature programmed desorption (TPD) was used to directly observe reaction products formed both at low and high temperature. Because of the multiple regimes observed, the DFT calculation results will be presented analyzing separately the different possible reaction pathways.

I3.1 X ray Photoelectron spectroscopy

Figure 1 shows the XP spectra in the carbon and oxygen regions for formic acid upon adsorption on Co(0001) at 130 K. At this temperature, the electron binding energies for the C 1s and O 1s features have been measured at 289.7 and 534.15 eV, respectively. These peak positions are characteristic of molecular formic acid on Co(0001), and are consistent with molecular adsorption at similar low temperatures on potassium-doped Co(1010)[34] and other transition metals.[11] A list of literature values for the different formic acid intermediates species is given in Table J1.

Upon heating the sample to 140 K another carbon peak evolves and the oxygen envelope becomes asymmetric. This can be attributed to the onset of formic acid undergoing decomposition and the formation of carbon monoxide. The binding energy of carbon monoxide in the carbon region is 286.2 eV,[47–49] as observed here. The oxygen peak can be partially deconvoluted taking advantage of the high binding energy component in formic acid and its oxygen stoichiometry. Thus the formic acid contribution can be isolated as shown by the two green curves in Figure I1 O1s at 140 K, with peaks at 534.15 and 533 eV. The remaining species, which include CO and other potential intermediates present, cannot be separated and are thus fitted by a single peak (blue curve in Figure I1).

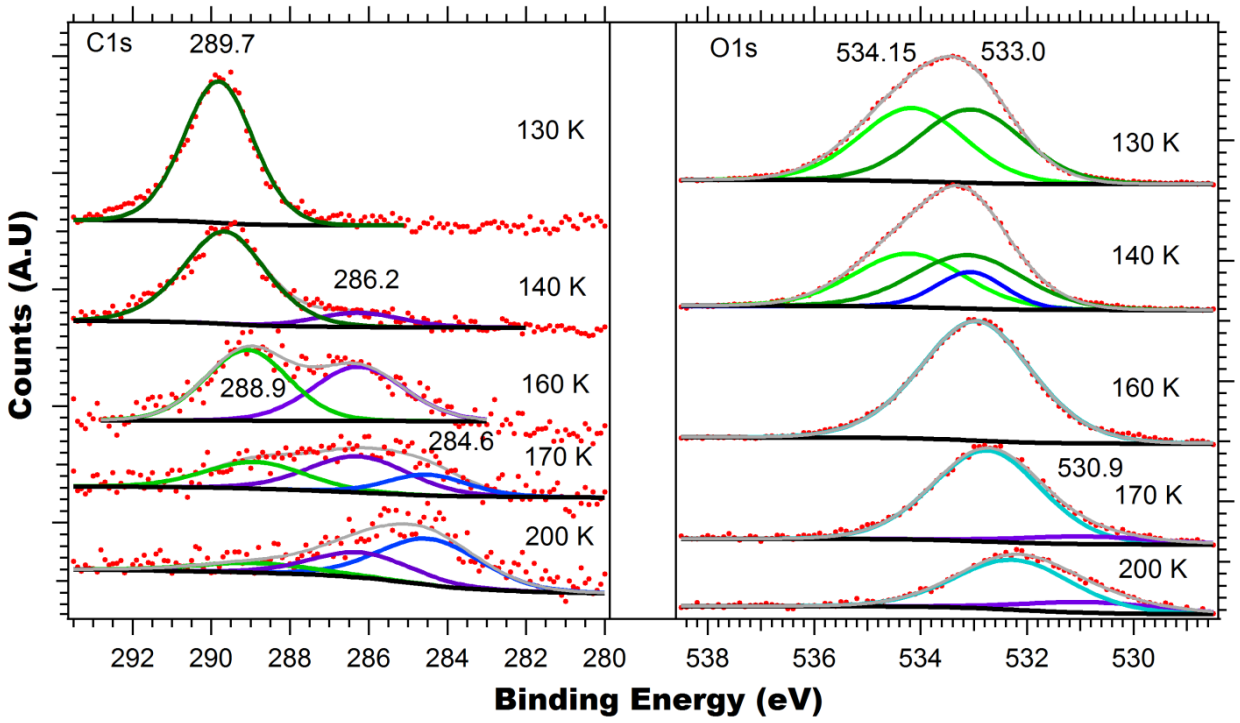

Figure I1: XPS of 1 L formic acid adsorbed at 130 K and subsequent decomposition on Co(0001). C 1s and O 1s regions shown at varying temperatures of interest. Identified peaks correspond to: i) 289.7 eV, molecular formic acid; ii) 288.9 eV, formate; iii) 286.2 eV, carbon monoxide; iv) 284.6 eV, carbon; v) 534.15 and 533 eV formic acid; vi) 530.9 eV, oxygen.

Upon heating to 160 K, there is a shift of 0.8 eV in the carbon peak, to 288.9 eV, with the corresponding disappearance of the higher energy oxygen peak, 534.15 eV, associated with formic acid. The shift in the carbon peak is in agreement with formic acid dissociation to formate and hydrogen,[50–54] and the disappearance of the higher energy oxygen peak indicates the formation of formate binding in either the bidentate or bridged orientation. Due to the disappearance of the higher energy formic acid oxygen peak, the deconvolution of the oxygen peak is no longer possible and therefore the O 1s spectrum likely corresponds to the combined signal of formate, carbon monoxide, and water species.

By 170 K, a third peak in the carbon region is observed at 284.6 eV together with a small peak in the oxygen region at 530.9 eV. At this temperature, carbon monoxide can dissociate to carbon and oxygen on Co(0001), and this process has been reported experimentally with binding energies reported at 284.3 eV and 531.0 eV,[47–49] respectively, in agreement with our observations.

Note that the dissociation of CO on Co(0001) has been predicted as being extremely difficult,[55] but perhaps steps, ad-atoms, defects or a more complex mechanism is involved. Increasing the temperature up to 200 K, there is a decrease in the formate peak and a shift in the oxygen peak to 532.5 eV. The apparent shift in the oxygen peak can be explained by the fact that the adsorbed carbon monoxide to formate ratio is increasing and thus the convoluted oxygen peak is shifting more towards the carbon monoxide binding energies. In addition, the slight decrease in the oxygen signal may be due to desorption of water in this temperature range (see TPD discussion).

Above 200 K desorption of several species becomes significant in the timeframe of XPS measurements. Thus another technique is needed to further the investigation, here temperature programmed desorption (TPD) is used.

I3.2 Temperature Programmed Desorption

Temperature programed desorption spectra were obtained after deposition of formic acid on Co(0001) at 130 K. Since each molecular species produces a characteristic fragmentation pattern (multiple peaks in the mass spectrometer signal), it is possible to correct the mass spectrometer signal to correctly identify species arising from the surface as opposed to those produced by the ionization process in the mass spectrometer. As in previous work,[35,56] we have followed this procedure and all the spectra in Figure I2 have been corrected for the corresponding fragmentation patterns in the mass spectrometer and therefore reflect the actual species desorbing from the surface. The TPD spectrum of molecular formic acid, m/z 46 in Figure I2, shows negligible signal at low doses indicating the tendency of formic acid to decompose on the surface at low temperatures, as discussed above. At doses above 1 L, a very small peak around 174 K is observed, likely due to desorption of unreacted molecular formic acid. However, the main feature of the m/z 46 spectrum is a broad desorption peak with onset at 236 K. Since at this temperature all the formic acid has been decomposed, the observation of this broad peak would indicate a second order (recombination of formate and H) desorption of the molecule. It should be noted that the formate may linger on the surface during the TPD time. Indeed, the variation in temperature observed between XPS and TPD data is taken into account by the different experimental time for each technique and the residence time of species on the surface.

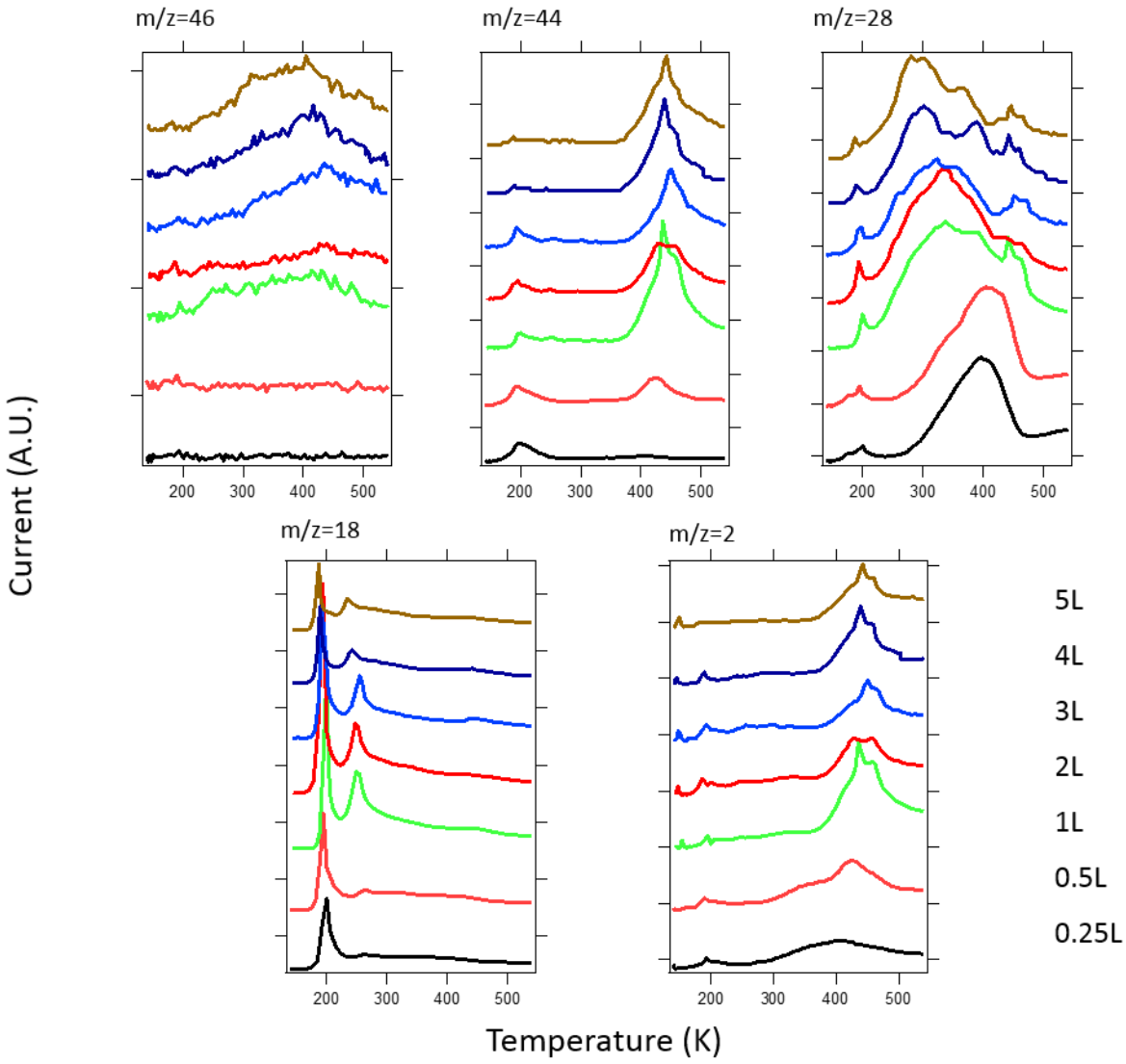

Figure I2: TPD spectra of mass/charge 46, 44, 28, 18, and 2 of increasing exposures of formic acid, dosed at 130 K, on Co(0001) under a linear temperature ramp of 4.6 K up to 550 K

The low temperature regime (below 200 K), also reveals the desorption of molecular water in good agreement with the literature.[57,58] This indicates the formation of water on the surface below the peak temperature of 175 K. Additionally, upon the re-formation of formic acid on the surface at ~236 K, a second peak of water can be observed. This is obviously reaction limited (as soon as water is formed, it desorbs) giving clues for the reaction pathway of water formation (see discussion below).

Carbon monoxide can be observed to desorb in the low temperature regime. This is consistent with on-top or quasi-on-top geometries obtained at high coverages,[49,58] and in this case caused by the constrain of other species present on the surface. However, most of the carbon monoxide, m/z 28, is observed to desorb from the surface in the range of 250 K to 400 K, in agreement with previous CO/Co(0001) studies.[47–49]

As discussed above, formate, carbon monoxide, carbon, oxygen, and water are formed and observed on the surface at low temperature and it is therefore implied that hydrogen must also be a surface species. Molecular hydrogen is expected to desorb from Co(0001) at ~370 K[59] at low coverages in a broad second order desorption peak, with the peak temperature shifting toward lower values as the coverage increases. The TPD data presented here shows a broad peak around 370 K for low coverage, however this can be attributed to ambient hydrogen deposition. No other peaks are observed below 400 K for increasing coverage suggesting that the hydrogen on the surface reacts with other species or remains on the surface below that temperature.

Analysis of all the peaks below 400 K allows for the direct determination of desorption energies at various coverages. Table I1 reports all relevant desorption energies calculated by Redhead analysis and the corrected pre-exponential factors used, calculated by the Campbell *et al.* relation.[60]

Table I1: Desorption energies of observed species, calculated by Redhead analysis.

Species	Temperature (K)	ν_{des} [a] (mbar/s)	E_{des} (kJ/mol)
Formic acid	174[c]	1.1×10^{15}	50.2
	236[b]	1.7×10^{15}	69.5
Water	175[c]	2.6×10^{14}	48.8
Carbon monoxide[c]	275	4.8×10^{14}	79.1
	300	5.2×10^{14}	86.7
	320	5.5×10^{14}	92.8
	380	6.5×10^{14}	111.3
	400[d]	6.9×10^{14}	117.5

[a]Pre-exponential factor derived by the method of Campbell et al.[60] for the corresponding molecular or associative process.
[b]Associative desorption.
[c]Molecular desorption. Molecular carbon monoxide desorption shows multiple peaks in this temperature range.[49,61]
[d]Reported associative desorption.[62,63] Above 400K, desorption of CO is considered as reaction limited, see text.

At temperatures above 400 K, there appears to be a correlation in the observed signal for carbon dioxide, carbon monoxide and hydrogen. As the dose of formic acid increases from 1 to 5 L, the spectra appear to develop a triplet peak shape with main peaks at 415 K, 438 K, and 455 K. As these temperatures are above the desorption temperature of the individual molecules, these signals must be generated by a reaction taking place at that temperature (reaction limited desorption). Comparison of the yields of the three molecules was performed by not only taking into account the fragmentation patterns of all species present, but also compensating for the corresponding ionization cross sections of each species[64] in the mass spectrometer. The overall yield of CO_2:CO:H_2 was estimated as 1:1:1 (see Appendix J). The observation could be explained by a new reaction pathway becoming available (see discussion).

3.3 DFT Calculations

The reaction network for the decomposition of formic acid on Co(0001) has been investigated performing periodic DFT calculations on a p(3x3) slab model of the surface. Formic acid adsorbs on a top site through its carbonyl oxygen in a trans configuration in agreement with previous theoretical studies on roughened Co[12] and other metals.[16,65] The computed adsorption energy (ΔE_{ads} =-66 kJ/mol) is in reasonable agreement with the one measured by TPD (-50.2 kJ/mol, Table 1). We considered three main branches: (i) the carboxyl branch is reached through the C-H bond dissociation (ii) the formate branch through the O-H scission (iii) and the formyl branch through the C-OH bond rupture. Reaction energies and activation energies are gathered in Table I2 and shown in a complete reaction scheme in Figure J2 (Appendix J). Figure 3 shows the most important reaction pathways as discussed in the text.

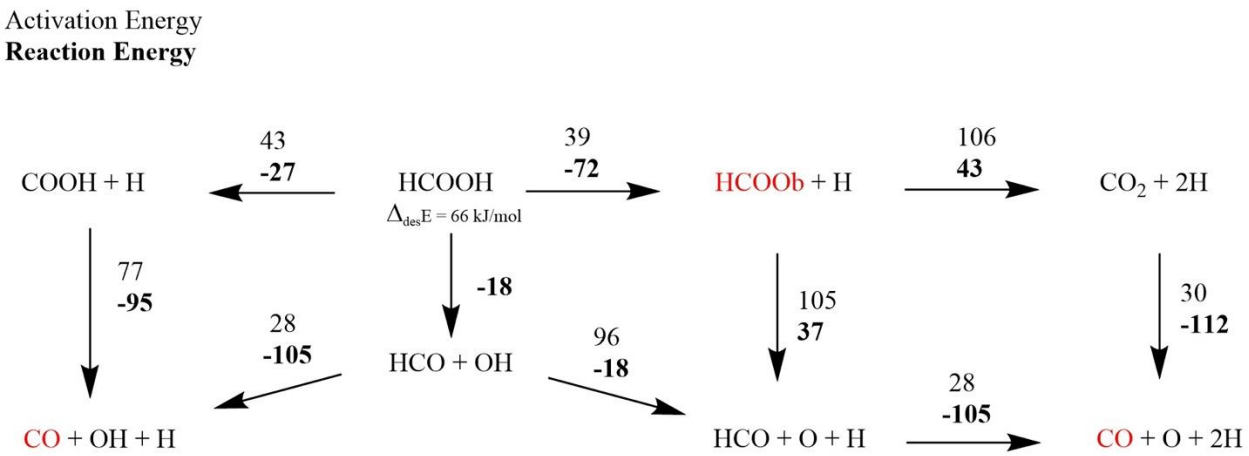

Figure I3: Schematic representation of the most relevant reaction pathways and surface species on Co(0001). Activation and reaction energies are shown. Experimentally observed species are shown in red.

Table I2: Activation and reaction energies for all processed involved in the interaction and decomposition of formic acid on Co(0001)

Label	Reaction	ΔE (kJ/mol)	ΔEa (kJ/mol)
Adsorption	HCOOH → HCOOH*	-66	n/a
	H_2 → 2 H*	-108	n/a
	H_2O → H_2O*	-44	n/a
	CO_2 → CO_2*	-3	12
	CO → CO*	-176	n/a
	O_2 → 2 O*	-495	n/a
Decomposition	HCOOH* → COOH* + H*	-27	43
	HCOOH* → $HCOO_b$* + H*	-72	39
	HCOOH* → HCO* + OH*	-18	75
	COOH* → COH* + O*	-32	89
	COOH* → CO_2* + H*	-1	97
	COOH* → CO* + OH*	-95	77
	$HCOO_b$* → $HCOO_m$*	51	52
	$HCOO_b$* → HCO + O	37	105
	$HCOO_b$* → CO_2 +H	43	106
	HCO → CO +H	-105	28
	HCO →HC + O	-65	71
	CO_2 → CO + O	-112	30
	COH → CO + H	-81	98
	COH → C + OH	10	153
	CO → C + O	73	228
	CH → C + H	32	109
Recombination	O+H → OH	18	114
	OH+H → H_2O	57	144

* indicates chemisorbed species. O2 adsorption was computed using H_2O, H_2 as a reference together with the formation energy of water (241.83 kJ/mol) to avoid using the O_2 energy, which is notoriously badly described at the GGA level.

3.3.1 Carboxyl branch

The carboxyl intermediate (COOH*) can be easily reached through the C-H bond rupture with a barrier of 43 kJ/mol. The reaction is slightly exothermic (-27 kJ/mol) and co-generates a hydrogen atom adsorbed on a hollow site (H*). With its C=O bond adsorbed in a di-sigma mode, COOH* can undergo several decomposition routes. The most accessible one is the C-OH bond rupture with a barrier of 77 kJ/mol. It is strongly exothermic (-95 kJ/mol) and leaves the CO* molecule and the OH* fragment on the surface, both chemisorbed at a hollow site. CO* can hardly be dissociated into C* and O* on Co(0001) since this is a strongly endothermic and highly activated process (228 kJ/mol), in agreement with previous DFT studies.[55] The adsorption energy of CO found by DFT at this low coverage of 1/9 ML (-176 kJ/mol) is in line with previous findings but seems strongly overestimated compared with our TPD data (-117 kJ/mol at most). This discrepancy can be attributed to coverage,[55,66] CO being strongly sensitive to lateral effects.[55,58] Thus, CO* does not dissociate and preferentially desorbs. The other fragment co-generated with CO* is the OH* species, which could be hydrogenated to yield water, recombining with an adsorbed hydrogen H* produced in the first step. But this reaction is endothermic (57 kJ/mol) and its high barrier (144 kJ/mol) renders this process less competitive than H_2 desorption (108 kJ/mol). However, OH* is slightly less difficult to break than CO, with an exothermic reaction (-18 kJ/mol) that requires overcoming a barrier of 96 kJ/mol. Thus OH* tends to generate H* that desorbed as H_2 and O* that remains on the oxophilic Co(0001) surface, chemisorbed at a hollow site. The fate of the O* species is interesting to consider. Adsorbed in a hollow site, the sequential hydrogenation of O* into water is endothermic (75 kJ/mol) with high barriers (>110 kJ/mol), and therefore the process cannot compete with the H_2 desorption, which would in addition benefit from a favorable increase in temperature through a gain in entropy (ΔE_{des} = -108 kJ/mol). This is in agreement with a recent experimental study focusing on water formation on Co(0001) using surface science techniques[67] that have measured an activation energy of water formation from O* and H_2 around 129 ± 7 kJ/mol. In addition, the associative desorption of O* (yielding O_2) is strongly endothermic (495 kJ/mol), in agreement with a recent DFT study[68] on O_2 adsorption on metallic surfaces. Thus, even at a rather high temperature, O* remains on the surface while H_2 and CO desorb.

The next possible decomposition route of the carboxyl is the rupture of the C=O bond. This bond is activated by the chemisorption in a di-sigma geometry, with an elongation of 0.04 Å compared with HCOOH*. This C=O scission yields COH* and O* with a barrier of 89kJ/mol and

an exothermicity of -32 kJ/mol. Then, the COH* fragment would preferentially undergo a CO-H scission, yielding CO* and H* rather than a C-OH scission according to the respective barriers of 98 kJ/mol and 153 kJ/mol. Thus, the resulting fragments are CO*, H* and O*. As already seen, CO* would rather desorb than split into C* and O*, H* will desorb as H_2 and O* will tend to stay on the Co(0001) surface.

The third possible route from COOH* is the O-H scission yielding CO_2 and H*. It is rather unlikely since it necessitates overcoming a barrier that is 20 kJ/mol higher than the C-OH bond rupture. As expected, CO_2* would easily desorb from the Co(0001) surface rather than get dissociated into CO* and O*.

3.3.2 Formate branch

Starting with the chemisorbed formic acid, the formate intermediate HCOO* can be easily reached with a barrier of 39 kJ/mol. Two main configurations of the formate can be found. In the monodentate configuration, HCOOm* is bonded through only one oxygen that bridges two surface atoms (Co-O distance of 2.03 Å). This configuration is slightly less stable that the carboxyl intermediate COOH* with an energy penalty of 21 kJ/mol. However, in its bidentate configuration, $HCOO_b$* is much more strongly stabilized by the formation of two strong Co-O bonds with a short distance of 1.99 Å. The deprotonation of formic acid HCOOH to bidentate formate is therefore particularly exothermic (-72 kJ/mol). This formate route is expected be more competitive than the carboxyl route since the OH scission barrier is slightly lower than the C-H dissociation (by 4 kJ/mol) and the obtained intermediate is much more stable (by 45 kJ/mol). Those conclusions are in line with previous DFT studies that considered the relative stability of the intermediates.[16]

HCOOb* can undergo further reaction through three different paths, however, all of them have high barriers, above 105 kJ/mol, making this intermediate a thermodynamic sink. As discussed later, these paths can only be accessed at higher temperatures. A first possibility is to re-hydrogenate the formate into formic acid with a barrier of 111 kJ/mol. Then, formic acid would easily desorb, especially at a high temperature (ΔE_{des} = 66 kJ/mol). The two others possibilities lead to the decomposition of formate into either HCO* or CO_2* with almost equal barriers (105 kJ/mol and 106 kJ/mol, respectively.). The formation of CO_2 is slightly more endothermic than the formation of HCO*. However, this step would be immediately followed by CO_2 and H_2 desorption that are both less demanding energetically than the previous rupture of the C-H bond in HCOO*. On the other hand, the generation of the formyl intermediate HCO* from $HCOO_b$* is

less endothermic (37 kJ/mol) and is accompanied by the production of O* and H*. As seen previously in the carboxyl route, O* would stay on the surface while H* will desorb as H_2. HCO* would break into CO* and H* rather than CH* and O*, producing finally CO, H_2 and chemisorbed atomic oxygen O*. Indeed, the H-CO scission is easily reached with a barrier of 28 kJ/mol, the lowest of the entire network. Overall, the decomposition of the very stable formate HCOOb* produces O*, CO, H_2 and CO_2 with a limiting barrier around 105 kJ/mol.

3.3.3 Formyl branch

The chemisorbed formic acid can also undergo a C-OH dissociation yielding the formyl intermediate HCO* and OH*. This route was shown to be easily accessible on Co-stepped surface, with a barrier only slightly higher that the formate one while the last possibility, namely the C=O bond breaking was much more difficult.[12] According to our calculations, this process is more demanding on a Co(0001) surface with a barrier of 75 kJ/mol and a slight exothermicity of -18 kJ/mol. As already seen, the as-generated OH* is decomposed into O* and H* but cannot be hydrogenated into water while HCO fragments into H* and CO*. This route finally produces H_2, CO and O*. Importantly, the production of CO* requires to overcome only two low barriers (75 kJ/mol and then 28 kJ/mol).

I4. Discussion

Using DFT calculations we were able to determine the energy requirements for the full reaction network on the flat Co(0001) surface. Moreover, comparison with the experimental data offers insight into the relative importance of the different pathways as conditioned by coverage or temperature. To facilitate the discussion, the results are separated into two regimes of low and high temperature (below and above 200 K) as determined by the different features of the TPD data.

4.1 Low temperature.

Formic acid was dosed on the Co(0001) surface at low temperature, and according to our XPS measurement, molecular formic acid is still the only surface species at 130 K, while chemisorbed CO* appears at a rather low temperature of 140 K and formate only forms at 160 K. The observation of formate at this temperature is consistent with this reaction on other cobalt surfaces and other transition metals[33,69] and with the low barrier in the reaction scheme. Formation of the carboxyl species should be expected at the same time as the formate, since the two paths have similar barriers, however the carboxyl species was not observed experimentally either

because its C 1s signature could not be resolved (Table J1 lists the calculated peak positions for the C 1s photoelectron for all the fragments) or because it decomposes shortly after being produced via CO formation. The disappearance of the high binding energy O 1s peak at 170 K suggests the absence of the carboxyl group. The CO formed at 140 K is seen in our TPD experiments desorbing at a temperature below 200 K. This early temperature of desorption can be related to a strong coverage effect, in this case provided by surrounding molecules and fragments. The production of CO at such low temperatures can be explained by our DFT calculations; CO can be generated together with OH* and ½ H_2 at a low temperature through either the carboxyl or the formyl path. Along the formyl path, the barriers are as low as 75 kJ/mol and the HCO* itself is not visible by XPS (within our sensitivity limits) because of its immediate decomposition to generate CO* with the lowest barrier of the whole scheme, 28 kJ/mol. Note that the HCO C1s peak would be expected at ~287.4 eV.[50,70–72] Li *et al.*[14] also note that HCO would be the preferred reaction pathway on Co(111), although in their calculations HCO was generated from HCOO* and the direct path from HCOOH was not considered. The direct path may be also facilitated by defects since the barrier is predicted to be lower on a Co-stepped surface.[12]

Our TPD experiments showed also a production of water at around 200 K. This production cannot be explained based on our DFT calculations that demonstrate that at low coverage, the formation of water from OH* and H* is very demanding energetically. This high activation energy (144 kJ/mol) might be decreased at a high coverage, however other more energetically favored processes may be at play (see section 4.3).

4.2 High temperature.

The formate species is thermodynamically favoured. That is, considering the first steps in the decomposition of HCOOH, the exothermicity ratios highly favour the HCOOb* species (HCOOb*/COOH*=2.7 and HCOOb*/HCO*=4). These ratios are consistent with previous calculations for Co(0001) (HCOOb*/COOH*=2)[16] and Co(111) (HCOOb*/COOH*=1.7).[14] Chemisorbed in a bidentate configuration, HCOOb*, it is particularly stabilized with the formation of two Co-O bonds. However, further reactions of the formate species are strongly endothermic and activated, making HCOOb* a thermodynamic sink.

The most activated process is the re-generation of formic acid that can be seen in our TPD experiments desorbing around 300-400 K. The two other routes have very close activation energies and thus yield concomitantly CO, CO_2 and H_2. This is in very good agreement with our TPD

experiments that show a very similar pattern in the production of those three molecules above 400 K. As noted in the TPD section, sharp features are observed at 415, 438 and 455K for all three species suggesting that their production is simultaneous. Furthermore, the CO_2:CO ratio was observed as roughly 1:1 for this high temperature range, consistent with the observations of Inglis and Taylor[23] above 100°C.

4.3 Water generation, a bimolecular process?

The formation of water at low temperature could not be directly explained within the reaction scheme we investigated by DFT. For that process, an alternative bimolecular reaction pathway could be the reaction of formic acid with the hydroxyl fragment OH* generated via the formyl path. This reaction would generate formate and water, an exothermic process (by 15 kJ/mol) expected to have an insignificant barrier since it involves proton transfer from a hydrogen bonded species between an acid (formic acid) and a base (adsorbed hydroxyl) The strong interaction of water and OH with formic acid and formate has previously been discussed for platinum and aluminum surfaces.[50,73–75]

An alternative is the dehydration of two formic acid molecules. This bimolecular reaction, which would generate the anhydride in gas phase, could easily produce HCOO*, HCO* and water on the Co(0001) surface (exothermic by 33 kJ/mol). The formation of a formic acid dimer or its anhydride form have been proposed and observed on other surfaces. The anhydride species, HCOOHCO, was calculated here and found to be easily dissociated with a strong exothermicity (-145kJ/mol) into HCOO* and HCO* species. Additionally, no experimental evidence of the anhydride species was observed.

I5. Conclusion

This work provides mechanistic insight on the decomposition of formic acid on cobalt catalysts. Dehydration and dehydrogenation compete in the decomposition of formic acid with the ultimate formation of H_2O, CO, CO_2 and H_2. Selectivity among these products depends on the reaction mechanism and intermediates on the surface. Activation and reaction energies were calculated for the full reaction network on the Co(0001) surface, allowing the interpretation of experimental results. The adsorption and decomposition of formic acid on a Co(0001) single crystal was studied experimentally (in UHV) by XPS and TPD.

Upon adsorption of formic acid on Co(0001), three decomposition pathways have been considered, via formation of a carboxyl, a formyl or a formate species. Carbon monoxide and water are experimentally observed to be formed at low temperature. Calculations suggest that CO is formed via the formyl intermediate while water is not energetically favored on the (0001) terrace and must be produced by a bimolecular process.

The formate species is favored on the surface, being produced in a highly exothermic process and having high barriers for further decomposition. However, at high temperature, above 400 K, these decomposition paths lead to the formation of CO, CO_2 and H_2.

References

(1) Bandara, A. Adsorption and Decomposition of Formic Acid (DCOOD) on NiO(111) and Ni(111) Surfaces Probed by SFG. *Appl. Phys. B Lasers Opt.* **1999**, *68*, 573–578.

(2) Czaun, M.; Goeppert, A.; Kothandaraman, J.; May, R. B.; Haiges, R.; Prakash, G. K. S.; Olah, G. A. Formic Acid As a Hydrogen Storage Medium: Ruthenium-Catalyzed Generation of Hydrogen from Formic Acid in Emulsions. *ACS Catal.* **2014**, *4*, 311–320.

(3) Bulushev, D. A. Vapour Phase Formic Acid Decomposition over PdAu/γ-Al2O3 Catalysts: Effect of Composition of Metallic Particles. *J. Catal.* **2013**, *299*, 171–180.

(4) Xu, J.; Yuan, D.; Yang, F.; Mei, D.; Zhang, Z.; Chen, Y.-X. On the Mechanism of the Direct Pathway for Formic Acid Oxidation at a Pt(111) Electrode. *Phys. Chem. Chem. Phys.* **2013**, *15*, 4367–4376.

(5) Angelucci, C. A.; Varela, H.; Herrero, E.; Feliu, J. M. Activation Energies of the Electrooxidation of Formic Acid on Pt(100). *J. Phys. Chem. C* **2009**, *113*, 18835–18841.

(6) Katano, S.; Kim, Y.; Kagata, Y.; Kawai, M. Vibration-Assisted Rotation and Deprotonation of a Single Formic Acid Molecule Adsorbed on Ni(110) Studied by Scanning Tunneling Microscopy. *J. Phys. Chem. C* **2009**, *113*, 19277–19280.

(7) Luo, Q.; Feng, G.; Beller, M.; Jiao, H. Formic Acid Dehydrogenation on Ni(111) and Comparison with Pd(111) and Pt(111). *J. Phys. Chem. C* **2012**, *116*, 4149–4156.

(8) Olson, T. S.; Pylypenko, S.; Kattel, S.; Atanassov, P.; Kiefer, B. Selectivity of Cobalt-Based Non-Platinum Oxygen Reduction Catalysts in the Presence of Methanol and Formic Acid. *J. Phys. Chem. C* **2010**, *114*, 15190–15195.

(9) Smith R J, B.; Loganathan, M.; Shantha, M. S. A Review of the Water Gas Shift Reaction Kinetics. *Int. J. Chem. React. Eng.* **2010**, *8*.

(10) Zafeiratos, S.; Dintzer, T.; Teschner, D.; Blume, R.; Hävecker, M.; Knop-Gericke, A.; Schlögl, R. Methanol Oxidation over Model Cobalt Catalysts: Influence of the Cobalt Oxidation State on the Reactivity. *J. Catal.* **2010**, *269*, 309–317.

(11) Columbia, M. R.; Thiel, P. A. The Interaction of Formic Acid with Transition Metal Surfaces, Studied in Ultrahigh Vacuum. *J. Electroanal. Chem.* **1994**, *369*, 1–14.

(12) Li, X.; Wang, S.; Zhu, Y.; Lv, C.; Yang, G. Density Functional Theory and Microkinetic Studies of Bio-Oil Decomposition on a Cobalt Surface: Formic Acid as a Model Compound. *Energy and Fuels* **2017,** *31*, 1866-1873.

(13) Li, X.; Wang, S.; Zhu, Y.; Yang, G.; Zheng, P. DFT Study of Bio-Oil Decomposition Mechanism on a Co Stepped Surface: Acetic Acid as a Model Compound. *Int. J. Hydrogen Energy* **2015**, *40*, 330–339.

(14) Li, X.; Zhu, Y.; Chen, G.; Yang, G.; Wu, Z.; Sunden, B. Theoretical Study of Solvent Effects on the Decomposition of Formic Acid over a Co(111) Surface. *Int. J. Hydrogen Energy* **2017,** *42*, 24726-24736.

(15) Yoo, J. S.; Abild-Pedersen, F.; Nørskov, J. K.; Studt, F. Theoretical Analysis of Transition-Metal Catalysts for Formic Acid Decomposition. *ACS Catal.* **2014**, *4*, 1226–1233.

(16) Herron, J. A.; Scaranto, J.; Ferrin, P.; Li, S.; Mavrikakis, M. Trends in Formic Acid Decomposition on Model Transition Metal Surfaces: A Density Functional Theory Study. *ACS Catal.* **2014**, *4*, 4434–4445.

(17) Columbia, M. R.; Crabtree, A. M.; Thiel, P. A. The Temperature and Coverage Dependences of Adsorbed Formic Acid and Its Conversion to Formate on Pt(111). *J. Am. Chem. Soc.* **1992**, *114*, 1231–1237.

(18) Columbia, M. R.; Thiel, P. A. The Reaction of Formic Acid with Clean and Water-Covered Pt(111). *Surf. Sci.* **1990**, *235*, 53–59.

(19) Avery, N. R. Adsorption of Formic Acid on Clean and Oxygen Covered Pt(111). *Appl. Surf. Sci.* **1982**, *11–12*, 774–783.

(20) Jeong, B.; Jeon, H.; Toyoshima, R.; Crumlin, E. J.; Kondoh, H.; Mun, B. S.; Lee, J. Dehydration Pathway for the Dissociation of Gas-Phase Formic Acid on Pt(111) Surface Observed via Ambient-Pressure XPS. *J. Phys. Chem. C* **2018**, *122*, 2064–2069.

(21) Kizhakevariam, N. Coadsorption of Bismuth with Electrocatalytic Molecules: A Study of Formic Acid Oxidation on Pt(100). *J. Vac. Sci. Technol. A Vacuum, Surfaces, Film.* **1990**, *8*, 2557.

(22) Iglesia, E.; Boudart, M. Unimolecular and Bimolecular Formic Acid Decomposition on Copper. *J. Phys. Chem.* **1986**, *90*, 5272–5274.

(23) Inglis, H. S.; Taylor, D. Decomposition of Formic Acid on Titanium, Vanadium, Chromium, Manganese, Iron, Cobalt, Nickel, and Copper. *J. Chem. Soc. A Inorganic, Phys. Theor.* **1969**, *19*, 2985-2987.

(24) Haq, S.; Love, J. G.; Sanders, H. E.; King, D. A. Adsorption and Decomposition of Formic Acid on Ni{110}. *Surf. Sci.* **1995**, *325*, 230–242.

(25) Mohanty, P.; Pant, K. K.; Naik, S. N.; Parikh, J.; Hornung, A.; Sahu, J. N. Synthesis of Green Fuels from Biogenic Waste through Thermochemical Route – The Role of Heterogeneous Catalyst: A Review. *Renew. Sustain. Energy Rev.* **2014**, *38*, 131–153.

(26) Hosseini, H.; Mahyari, M.; Bagheri, A.; Shaabani, A. Pd and PdCo Alloy Nanoparticles Supported on Polypropylenimine Dendrimer-Grafted Graphene: A Highly Efficient Anodic Catalyst for Direct Formic Acid Fuel Cells. *J. Power Sources* **2014**, *247*, 70–77.

(27) Yin, M.; Li, Q.; Jensen, J. O.; Huang, Y.; Cleemann, L. N.; Bjerrum, N. J.; Xing, W. Tungsten Carbide Promoted Pd and Pd–Co Electrocatalysts for Formic Acid Electrooxidation. *J. Power Sources* **2012**, *219*, 106–111.

(28) Stevanović, S.; Babić-Samardžija, K.; Sovilj, S. P.; Tripković, A.; Jovanović, V. M. Oxidation of Formic Acid on Platinum Surfaces Decorated with cobalt(III) Macrocyclic Complexes. *Russ. J. Phys. Chem. A* **2009**, *83*, 1442–1446.

(29) Zhang, L.; Wan, L.; Ma, Y.; Chen, Y.; Zhou, Y.; Tang, Y.; Lu, T. Crystalline Palladium–cobalt Alloy Nanoassemblies with Enhanced Activity and Stability for the Formic Acid Oxidation Reaction. *Appl. Catal. B Environ.* **2013**, *138–139*, 229–235.

(30) Stathi, P.; Deligiannakis, Y.; Louloudi, M. Co-Catalytic Enhancement of H2 Production by SiO2 Nanoparticles. *Catal. Today* **2015**, *242*, 146–152.

(31) Rice, C. Catalysts for Direct Formic Acid Fuel Cells. *J. Power Sources* **2003**, *115*, 229–235.

(32) Zhou, X.; Liu, C.; Liao, J.; Lu, T.; Xing, W. Platinum-Macrocycle Co-Catalysts for Electro-Oxidation of Formic Acid. *J. Power Sources* **2008**, *179*, 481–488.

(33) Tang, Y.; Roberts, C. A.; Perkins, R. T.; Wachs, I. E. Revisiting Formic Acid Decomposition on Metallic Powder Catalysts: Exploding the HCOOH Decomposition Volcano Curve. *Surf. Sci.* **2016**, *650*, 103–110.

(34) Toomes, R.; King, D. Potassium-Promoted Synthesis of Surface Formate and Reactions of Formic Acid on Co {1010}. *Surf. Sci.* **1996**, *349*, 43–64.

(35) Réocreux, R.; Ould Hamou, C. A.; Michel, C.; Giorgi, J. B.; Sautet, P. Decomposition Mechanism of Anisole on Pt(111): Combining Single-Crystal Experiments and First-Principles Calculations. *ACS Catal.* **2016**, *6*, 8166–8178.

(36) Lewis, W. F. Magnetic Domain Behavior during the Hcp-to-Fcc Phase Transition in Cobalt Using Lorentz Electron Microscopy. *J. Appl. Phys.* **1977**, *48*, 2980.

(37) Bidaux, J. E. Study of the H.c.p.-F.c.c. Phase Transition in Cobalt by Acoustic Measurements. *Acta Metall. 37*, 803–811.

(38) McIntyre, N. S.; Johnston, D. D.; Coatsworth, L. L.; Davidson, R. D.; Brown, J. R. X-Ray Photoelectron Spectroscopic Studies of Thin-Film Oxides of Cobalt and Molybdenum. *Surf. Interface Anal.* **1990**, *15*, 265–272.

(39) Perdew, J. P.; Burke, K.; Ernzerhof, M. Generalized Gradient Approximation Made Simple. *Phys. Rev. Lett.* **1996**, *77*, 3865–3868.

(40) Steinmann, S. N.; Corminboeuf, C. A Generalized-Gradient Approximation Exchange Hole Model for Dispersion Coefficients. *J. Chem. Phys.* **2011**, *134*, 44117.

(41) Steinmann, S. N.; Corminboeuf, C. Comprehensive Benchmarking of a Density-Dependent Dispersion Correction. *J. Chem. Theory Comput.* **2011**, *7*, 3567–3577.

(42) Kresse, G.; Hafner, J. Ab Initio Molecular Dynamics for Liquid Metals. *Phys. Rev. B* **1993**, *47*, 558–561.

(43) Kresse, G.; Furthmüller, J. Efficiency of Ab-Initio Total Energy Calculations for Metals and Semiconductors Using a Plane-Wave Basis Set. *Comput. Mater. Sci.* **1996**, *6*, 15–50.

(44) Kresse, G.; Furthmüller, J. Efficient Iterative Schemes for Ab Initio Total-Energy Calculations Using a Plane-Wave Basis Set. *Phys. Rev. B* **1996**, *54*, 11169–11186.

(45) Kresse, G.; Joubert, D. From Ultrasoft Pseudopotentials to the Projector Augmented-Wave Method. *Phys. Rev. B* **1999**, *59*, 1758–1775.

(46) Monkhorst, H. J.; Pack, J. D. Special Points for Brillouin-Zone Integrations. *Phys. Rev. B* **1976**, *13*, 5188–5192.

(47) Habermehl-Cwirzen, K.; Habermehl-Ćwirzeń, K.; Lahtinen, J. Sulfur Poisoning of the CO Adsorption on Co(0001). *Surf. Sci.* **2004**, *573*, 183–190.

(48) Cabeza, G. F.; Légaré, P.; Castellani, N. J. Adsorption of CO on Co (0001) and Pt – Co (0001) Surfaces : An Experimental and Theoretical Study. *Surf. Sci.* **2000**, *465*, 286–300.

(49) Lahtinen, J.; Vaari, J.; Kauraala, K. Adsorption and Structure Dependent Desorption of CO on Co(0001). *Surf. Sci.* **1998**, *418*, 502–510.

(50) Davies, P. R.; Roberts, M. W.; Shukla, N. The Reactive Chemisorption of Formic Acid at A1(111) Surfaces and the Influence of Surface Oxidation and Coadsorption with Water: A Combined XPS and HREELS Investigation. *J. Phys. Condens. Matter* **1991**, *3*, S237-S244.

(51) Mazurkiewicz, M.; Malolepszy, A.; Mikolajczuk, A.; Stobinski, L.; Borodzinski, A.; Lesiak, B.; Zemek, J.; Jiricek, P. Pd/MWCNTs Catalytic Activity in the Formic Acid Electrooxidation Dependent on Catalyst Surface Treatment. *Phys. Status Solidi* **2011**, *248*, 2516–2519.

(52) Cano, E.; Torres, C.; Bastidas, J. An XPS Study of Copper Corrosion Originated by Formic Acid Vapour at 40% and 80% Relative Humidity. *Mater. Corros. UND KORROSION* **2001**, *52*, 667–676.

(53) Ayyoob, M.; Hegde, M. S. Electron Spectroscopic Studies of Formic Acid Adsorption and Oxidation on Cu and Ag Dosed with Barium. *J. Chem. Soc. Faraday Trans. 1 Phys. Chem. Condens. Phases* **1986**, *82*, 1651.

(54) Au, C. T. Adsorption and Interaction of Carbon Dioxide, Formic Acid and Hydrogen/carbon Dioxide Mixtures on (100) Zinc Oxide Surfaces Studied by Photoelectron Spectroscopy (XPS and UPS). *Surf. Sci.* **1988**, *199*, 507–517.

(55) Chen, C.; Wang, Q.; Zhang, R.; Hou, B.; Li, D.; Jia, L.; Wang, B. High Coverage CO Adsorption and Dissociation on the Co(0001) and Co(100) Surfaces from DFT and Thermodynamics. *Appl. Catal. A Gen.* **2016**, *523*, 209–220.

(56) Ould Hamou, C. A.; Réocreux, R.; Sautet, P.; Michel, C.; Giorgi, J. B. Adsorption and Decomposition of a Lignin β-O-4 Linkage Model, 2-Phenoxyethanol, on Pt(111): Combination of Experiments and First-Principles Calculations. *J. Phys. Chem. C* **2017**, *121*, 9889-9900.

(57) Xu, L.; Ma, Y.; Zhang, Y.; Chen, B.; Wu, Z.; Jiang, Z.; Huang, W. Water Adsorption on a Co(0001) Surface †. *J. Phys. Chem. C* **2010**, *114*, 17023–17029.

(58) Jiawei, W.; Chen, J.; Guo, Q.; Su, H. Y.; Dai, D.; Yang, X. H2O and CO Coadsorption on Co (0001): The Effect of Intermolecular Hydrogen Bond. *Surf. Sci.* **2017**, *663*, 56–61.

(59) van Helden, P.; van den Berg, J.-A.; Weststrate, C. J. Hydrogen Adsorption on Co Surfaces: A Density Functional Theory and Temperature Programmed Desorption Study. *ACS Catal.* **2012**, *2*, 1097–1107.

(60) Campbell, C. T.; Árnadóttir, L.; Sellers, J. R. V. Kinetic Prefactors of Reactions on Solid Surfaces. *Zeitschrift für Phys. Chemie* **2013**, *227*, 1435–1454.

(61) Wesner, D. A.; Linden, G.; Bonzel, H. P. Alkali Promotion on Cobalt: Surface Analysis of the Effects of Potassium on Carbon Monoxide Adsorption and Fischer-Tropsch Reaction. *Appl. Surf. Sci.* **1986**, *26*, 335–356.

(62) Nowitzki, T.; Zielasek, V.; Baeumer, M. UHV Studies on CO and Methanol Adsorption and Decomposition on Pristine and Oxidized Alumina-Supported Co Nanoparticles. **2009** *In: Cat D.T., Pucci A., Wandelt K. (eds) Physics and Engineering of New Materials. Springer Proceedings in Physics, vol 127. Springer, Berlin, Heidelberg*.

(63) Cabrera, A. L.; Garrido M, W. H.; Volkmann, U. G. Studies of Carbon Monoxide and Hydrogen Adsorption on Nickel and Cobalt Foils Aimed at Gaining a Better Insight into the Mechanism of Hydrocarbon Formation. *Catal. Letters* **1994**, *25*, 115–126.

(64) Nakao, F. Determination of the Ionization Gauge Sensitivity Using the Relative Ionization Cross-Section. *Vacuum* **1975**, *25*, 431–435.

(65) Mavrikakis, M.; Dumesic, J. A.; Scaranto, J.; Singh, S.; Li, S.; Carrasquillo, R.; Roling, L.; Herron, J. A.; O'Neill, B.; Peng, G. Formic Acid Decomposition on Transition Metal Surfaces: Fundamental Mechanistic Aspects. *Abstr. Pap. Am. Chem. Soc.* **2014**, *247*.

(66) Ma, S. H.; Zu, X. T.; Jiao, Z. Y.; Zhang, X. Z. A Test of Empirical Correction to Site Preference: DFT Calculations for CO Adsorption on Co(0 0 0 1) Surface. *J. Mol. Struct. THEOCHEM* **2008**, *864*, 68–71.

(67) Kizilkaya, A. C. (Ali C.; Niemantsverdriet, J. W. (Hans); Weststrate, C. J. (Kees-J. Oxygen Adsorption and Water Formation on Co(0001). *J. Phys. Chem. C* **2016**, *120*, 4833–4842.

(68) Yan, M.; Huang, Z.; Zhang, Y.; Chang, C.; King, D. A.; Hu, P.; Pei, Y.; Zeng, X. C.; Flytzani-Stephanopoulos, M.; Sykes, E. C. H. Trends in Water-Promoted Oxygen Dissociation on the Transition Metal Surfaces from First Principles. *Phys. Chem. Chem. Phys.* **2017**, *19*, 2364–2371.

(69) Marcinkowski, M. D.; Murphy, C. J.; Liriano, M. L.; Wasio, N. A.; Lucci, F. R.; Sykes, E. C. H. Microscopic View of the Active Sites for Selective Dehydrogenation of Formic Acid on Cu(111). *ACS Catal.* **2015**, *5*, 7371–7378.

(70) Tanaka, K.; Matsuzaki, S.; Toyoshima, I. Photodecomposition of Adsorbed Methoxy Species by UV Light and Formaldehyde Adsorption on silicon(111) Studied by XPS and UPS. *J. Phys. Chem.* **1993**, *97*, 5673–5677.

(71) Bowker, M.; Madix, R. J. XPS, UPS and Thermal Desorption Studies of the Reactions of Formaldehyde and Formic Acid with the Cu(110) Surface. *Surf. Sci.* **1981**, *102*, 542–565.

(72) Frantz, P.; Kim, H. I.; Didziulis, S. V.; Li, S.; Chen, Z.; Perry, S. S. Reaction of Methyl

Formate with VC(1 0 0) and TiC(1 0 0) Surfaces. *Surf. Sci.* **2005**, *596*, 144–162.

(73) Qi, Y.; Zhu, R.; Zhang, D. Adsorption Behaviors of Monomer and Dimer of Formic Acid on Pt (111) in the Absence and Presence of Water. *J. Mol. Model.* **2014**, *20*, 2264.

(74) Silbaugh, T. L.; Karp, E. M.; Campbell, C. T. Energetics of Formic Acid Conversion to Adsorbed Formates on Pt(111) by Transient Calorimetry. *J. Am. Chem. Soc.* **2014**, *136*, 3964–3971.

(75) Akiya, N.; Savage, P. E. Role of Water in Formic Acid Decomposition. *AIChE J.* **1998**, *44*, 405–415.

Appendix J

Supporting information for the article in Appendix I:

Adsorption and Decomposition of Formic Acid on Cobalt (0001)

Jeffrey J. Sims[a,b], Cherif A. Ould Hamou[a,c], Romain Réocreux[e,f], Carine Michel[e], Javier B. Giorgi* [a,d]

[a]*Centre for Catalysis Research and Innovation,* [b]*Department of Chemical and Biological Engineering,* [c]*Department of Physics,* [d]*Department of Chemistry and Biomolecular Sciences, University of Ottawa, 10 Marie Curie Pvt., Ottawa, Ontario, Canada. K1N 6N5.*

[e]*Univ Lyon, Ens de Lyon, CNRS UMR 5182, Université Claude Bernard Lyon 1, Laboratoire de Chimie, F-69342, Lyon, France*

[f] Current address: *Thomas Young Centre and Department of Chemical Engineering, University College London, Roberts Building, Torrington Place, London WC1E 7JE, United Kingdom*

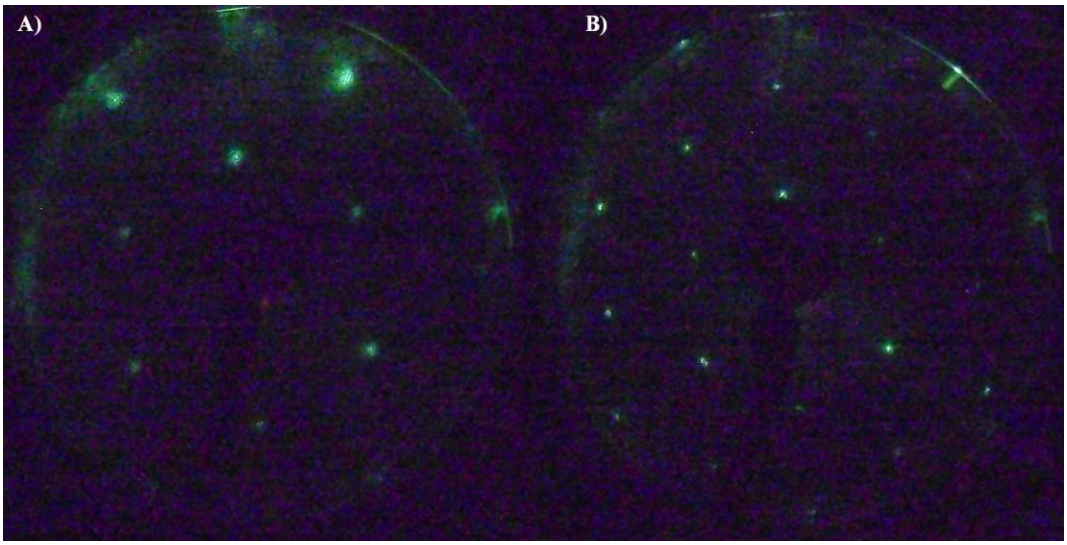

Figure J1: LEED patterns of clean Co(0001) obtained with A) 30 eV and B) 102 eV. The image shows the hexagonal pattern characteristic of the surface.

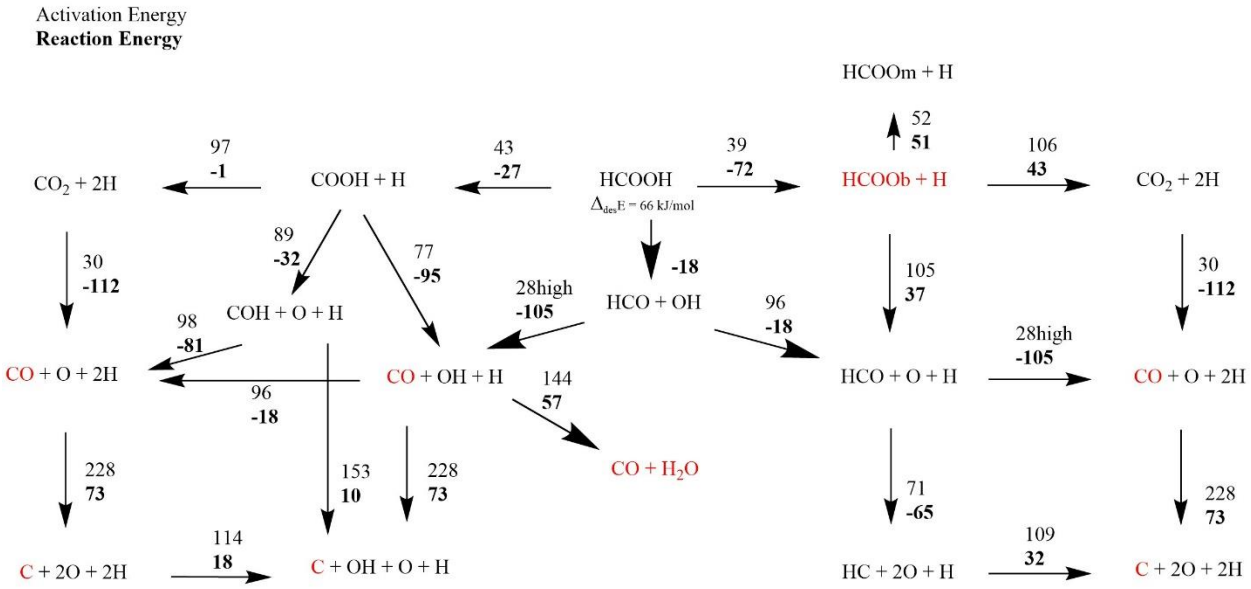

Figure J2: Full reaction scheme for the possible reaction pathways involved in the decomposition of formic acid on Co(0001). Activation and reaction energies are shown. Species identified by either XPS or TPD experiments are shown in red.

Table J1: Literature comparison of C 1s XPS peaks for formic acid

HCOOH	HCOO	COOH	HCO	CO	C	Work
289.7	288.9			286.2	284.6	Co(0001), This work
288.69	288.30b 288.60m	288.06	286.28	286.61	284.80	Co(0001), by DFT.[a] This work
291.0	290.5		287.5[b]		284.0	Al(111),[1]
289.9	289.5					ZnO(1010),[2]
				286.4, 285.8[c]		Co(0001),[3–5]
289.6	287.5			286.6[d]		Cu(110),[6]
	287.4			285.8	284.2	Pt(111),[7]
290.2	289.6					Si(111)7x7,[e,8]
289.5	287.7					Cu(110),[9]

[a]Calculations were performed using the optimized geometries with the final state approximation and excitation of half a core electron, all the remaining core hole electrons were frozen. This method cannot provide absolute core level binding energies, only shifts of the core.[10,11] The values have been corrected using the carbon species (C 1s at 284.8), as it is customary.
[b]Assigned only on the bases of electron density between the other two peaks.
[c]On-top and hollow sites respectively.
[d]Identified as formate in the manuscript.
[e]Peaks identified as chemisorption (289.6) and physisorption (290.2).

Estimation of the product yield for the high temperature reaction

In order to quantify the TPD, deconvolution of the currents for each species in the mass spectrometer signal was achieved by independently measuring the fragmentation patterns of each molecule in the MS and adding the fragmentation patterns of the molecules together until the observed currents were matched. This deconvolution is necessary because many of the m/z are shared by the molecules present such as m/z 46, 45, and 44 values being shared by both formic acid and carbon dioxide, as well as m/z 28, 29, 16, and 14 values being shared by carbon dioxide, carbon monoxide, and formic acid. The deconvoluted currents of each molecule were then corrected by dividing by the relative sensitivity factor of ionization for the relevant molecule. The difference in ionization cross section results in differing current produced for equal amounts of molecules for each species passing through the MS. From this data the stoichiometry of each event

can be gleaned. Figure S3 shows the corrected data for CO, CO_2 and H_2 for the high temperature regime after dosing 2L of formic acid. As can be seen in the figure, not only is there a shape match in the spectra, but also their intensity is very similar. Because of the multiple corrections, absolute quantification would carry a large error, and therefore we use the conservative approach of stating that the ratio of the three species is estimated as 1:1:1.

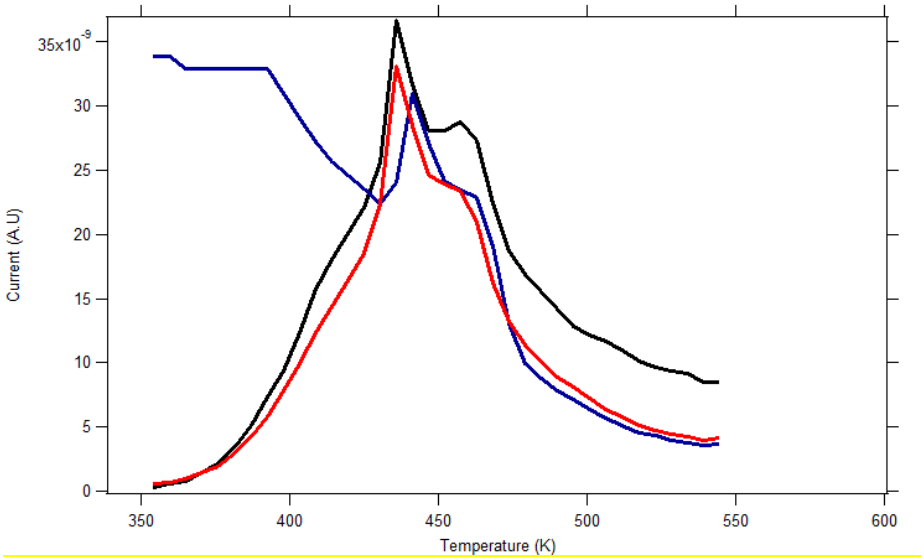

Figure J3: High temperature region of the TPD spectra for CO (blue), CO_2 (red) and H_2 (black). Data corrected for fragmentation patterns of all species and signal cross section in the mass spectrometer.

References

(1) Davies, P. R.; Roberts, M. W.; Shukla, N. The Reactive Chemisorption of Formic Acid at A1(111) Surfaces and the Influence of Surface Oxidation and Coadsorption with Water: A Combined XPS and HREELS Investigation. *J. Phys. Condens. Matter* **1991**, *3* S237-S244.

(2) Au, C. T. Adsorption and Interaction of Carbon Dioxide, Formic Acid and Hydrogen/Carbon Dioxide Mixtures on (100) Zinc Oxide Surfaces Studied by Photoelectron Spectroscopy (XPS and UPS). *Surf. Sci.* **1988**, *199*, 507–517.

(3) Habermehl-Ćwirzeń, K.; Lahtinen, J. Sulfur Poisoning of the CO Adsorption on Co(0001). *Surf. Sci.* **2004,** *573*, 183-190.

(4) Lahtinen, J.; Vaari, J.; Kauraala, K. Adsorption and Structure Dependent Desorption of CO on Co(0001). *Surf. Sci.* **1998**, *418*, 502–510.

(5) Cabeza, G. F.; Légaré, P.; Castellani, N. J. Adsorption of CO on Co (0001) and Pt – Co (0001) Surfaces : An Experimental and Theoretical Study. *Surf. Sci.* **2000**, *465*, 286–300.

(6) Yao, Y.; Zaera, F. Adsorption and Thermal Chemistry of Formic Acid on Clean and Oxygen-Predosed Cu(110) Single-Crystal Surfaces Revisited. *Surf. Sci.* **2016**, *646*, 37–44.

(7) Kaichev, V. V.; Prosvirin, I. P.; Bukhtiyarov, V. I. Decomposition and Oxidation of Methanol on Platinum: A Study by in Situ X-Ray Photoelectron Spectroscopy and Mass Spectrometry. *Kinet. Catal.* **2014**, *55*, 509–519.

(8) Huang, J. Y.; Huang, H. G.; Lin, K. Y.; Liu, Q. P.; Sun, Y. M.; Xu, G. Q. The Structures of Physisorbed and Chemisorbed Formic Acid on Si(1 1 1)-7 × 7. *Surf. Sci.* **2004**, *549*, 255–264.

(9) Bowker, M.; Madix, R. J. XPS, UPS and Thermal Desorption Studies of the Reactions of Formaldehyde and Formic Acid with the Cu(110) Surface. *Surf. Sci.* **1981**, *102*, 542–565.

(10) Köhler, L.; Kresse, G. Density Functional Study of CO on Rh(111). *Phys. Rev. B* **2004**, *70*, 165405.

(11) Jugnet, Y.; Loffreda, D.; Dupont, C.; Delbecq, F.; Ehret, E.; Cadete Santos Aires, F. J.; Mun, B. S.; Aksoy Akgul, F.; Liu, Z. Promoter Effect of Early Stage Grown Surface Oxides: A near-Ambient- Pressure XPS Study of CO Oxidation on PtSn Bimetallics. *J. Phys. Chem. Lett.* **2012**, *3*, 3707–3714.